Thesis

On Quantitative Evaluation of 3-D Histo-pathological Images from Confocal Laser Scanning Microscope

P. S. Umesh Adiga

Computer Vision and Pattern Recognition Unit
Indian Statistical Institute
Calcutta

A thesis submitted to the
Indian Statistical Institute
in partial fulfilment of the requirements for the degree of
Doctor of Philosophy
1999

Acknowledgements

First and foremost I would like to thank my supervisor Prof. B. B. Chaudhuri for his guidance and support in this research project. He was instrumental in getting the data set and all other materials needed to start this ambitious research project. His interest in the project, his ideas to overcome the difficulties, patience and above all the appreciation of the work done is one of the important factors that kept me going during the last four and a half years in this project. I also thank him for sending me to GSF, Germany for getting a first-hand experience of the difficulties involved in the project as well as, for recommending me to attend ICPR-98 at Brisbane, Australia to present some of our work. Though he was very busy in other research areas, he has spent considerable time for discussions on this research and development project. I am very much indebted to him for what he was to me during last four and a half years of research.

Another person whom I would like to thank is Mr. K. Rodenacker, Bio-medical Image analysis Division, Institute of Pathology, GSF-National Research Centre for Health and Environment., Munich, Germany. He has helped me in the beginning of my research career by making me visualize the difficulties and the challenges that may come across in taking up this kind of projects. His constant support, both emotional as well as academic has helped me in realizing this project. I would also like to thank Dr. Hutzler and Dr. Aubele of the same institute for their kindness in giving the large number of data set and the details regarding the specimen preparation and Image acquisition. I also thank Prof. Hofler, Prof. Lutz, Mr. Gais. Ms. Jutting, Mr. Voss and all other staff members of Institute of Pathology, GSF, Munich for providing me a good environment to learn the advancements in quantitative histo-pathology.

I thank Prof. Swapan K. Parui for his kind help and invaluble time he has spent in discussions about the project. His constant support and insight of the problem has helped me to a large extent in achieving the objective. Prof. D. Dutta Majumder has shown keen interest in the progress of the project and helped with constructive suggestions. I thank his support in my research work. I also thank Dr. P. Sengupta, for many discussions we had about the project as well as about general computer related stuff. His very presence in the lab was helpful in confidence building.

I would also like to thank Mr. Arijit Vishnu, Mr. Utpal Garain, Mr. B. Uma Shankar, Dr. Mandar Mitra and Dr. A. Roy Chaudhuri for reading several chapters of this thesis and providing an enjoyable environment in the laboratory. I also thank Dr. U. Pal, Mr. Ujjwal Bhattacharya, Dr. D. Chaudhuri and Dr. Nirupam Sarkar for their help.

I acknowledge with thanks, the academic help and the moral support extended by my friends Dr. Tiziana D'Adda, Dr. Jennifer Pittman, Ms. Marianne Haberbauer, Dr. Sojen Joy and Dr. Natabar Shyam. Their kindness in hearing my non-stop nonsense and prompt replies to put me on the track has helped me in sustaining the highs and lows of research life. My thanks are

also due to Mr. S. Chatterjee Mr. Sounak Mishra, Mr. Ravi Kumar and Mr. J. Biswal for their help, discussions and support during my research days.

The most enjoyable research envoronment in the Computer Vision and Pattern Recognition Unit is one of the most important reasons for the success of this research project. My colleagues Mr. Tamal Taru Pal, Mr. Niladri Shekar Dash, Mr. Anil Chand, Mr. Kirani Singh, Mr. Soumen Chaudhuri, Mr. Sougata Das, Ms. Vidya Chand, Ms. Sucharita Mitra, Ms. Ishita De, Ms. Lidya and Ms. Srirupa Das were responsible for keeping the good research environment in the department. I acknowledge with thanks their help in development of this project.

Most of the time I had a feeling that I am putting pressure on our office staff to do lot of non-academic work to help me in speeding up the completion of my responsibility in the project. It is their patience and acceptance of extra work without any complaints that helped me in concentrating on the research work. I acknowledge with thanks the help rendered by Mrs. Sumita Sen, Mr. Jayanta Das, Mr. Kamal Ghosh, Ms. Shampa Pal, Mr. Buddha, Mr. Vidya Ram, for their help.

Last but not the least, I acknowledge the help of Dean of Studies, Deans' office staff and the staff members of Reprography Unit of Indian Statistical Institute for their cooperation in bringing out this work. I dedicate this thesis to my parents, teachers, brothers, sister and friends.

P. S. Umesh Adiga

Some of the publications related to the thesis work

1. **Adiga P. S. U.** and Chaudhuri B. B., "An Efficient Cell Segmentation Tool for Confocal Microscopy Tissue Images for Quantitative Evaluation of FISH Signals", Int. J. of Microscopy Research and Technique, Vol. 44, (1999), pp. 49-68.

2. Rodenacker K., Aubele M., Hutzler P. and **Adiga P. S. U.**, "Groping for Quantitative 3D Image Analysis: an Approach to Quantitative Evaluation of Fluorescence in situ Hybridization in Thick Tissue Sections of Prostate Carcinoma", Anal. Cell. Pathol., Vol. 15, (1997), pp. 19-29.

3. **Adiga P. S. U.** and Chaudhuri B. B., "Segmentation of Volumetric Tissue Images Using Constrained Active Contour Models", Accepted Subject to Revision in Int. J. of Image and Vision Computing (revised and submitted) (1999).

4. **Adiga P. S. U.** and Chaudhuri B. B., "Deformable Models for Segmentation of CLSM Images and Its Application in FISH Signal Analysis", Accepted subject to revision in Int. J. of Analytical Cellular Pathology (revised and submitted) (1998).

5. **Adiga P. S. U.** and Chaudhuri B. B., "Segmentation and Counting of FISH signals in Confocal Microscopy Images", Accepted for publication in MICRON, Int. J. for microscopy research and review (1998).

6. **Adiga P. S. U.** and Chaudhuri B. B., "Region based Techniques for the Segmentation of Volumetric Histo-Pathological Images Obtained using Confocal Microscope", Accepted subject to minor revision in Int. J. of Computer Methods and Programs in Biomedicine (1999).

7. **Adiga P. S. U.**, Chaudhuri B. B. and Rodenacker K., "Semi-automatic Segmentation of Tissue Cells from Confocal Microscopy Images", In: Proceedings of 13 th Int. Conf. on Pattern Recognition, ICPR-96, 3, (1996), pp. 494-497.

8. **Adiga P. S. U.** and Chaudhuri B. B., "Segmentation of Histo-Pathological Images by Surface Following Using Constrained Snakes", In: Proceedings of 14 th International Conference on Pattern Recognition, ICPR-98, (1998), pp. 1674-1676.

9. **Adiga P. S. U.** and Chaudhuri B. B., "Analysis of Volumetric Images of Filamentous Bacteria in Industrial Sludge", In: Proceedings of 14 th International Conference on Pattern Recognition, ICPR-98, (1998), pp. 1735-1737.

10. **Adiga P. S. U.** and Chaudhuri B. B., "Segmentation of 3-D Histo-Pathological Images Using Snakes and Its Application in Quantitative Evaluation of FISH Signal", In Proceedings of 2 nd International Conference on Medical Image Understanding and Analysis, MIUA-98, (1998).

11. **Adiga P. S. U.** and Chaudhuri B. B., "Automatic Prostate Cancer Grading System Based on 3-D Histo-Pathological Images", In: Proceedings of IAPR workshop on Machine Vision and Applications, MVA-98 to be held in Chiba, Japan, (1998).

12. **Adiga P. S. U.** and Chaudhuri B. B. , "Automatic Segmentation of 3-D Cells from Confocal Microscopy Images and Its Application in FISH Signal Evaluation", In: Proceedings of 16 th International CODATA Conference, CODATA-98, (1998).

13. **Adiga P. S. U.** and Chaudhuri B. B., "Classification of Prostate Tumor Specimen based on Cyto and Histological Features Measured from 3D Images", In: Proceedings of 16 th International CODATA Conference, CODATA-98, (1998).

14. **Adiga P. S. U.** and Chaudhuri B. B., "Quantitative Evaluation of Bacteria in Industrial Sludge by 3-D Image Analysis", In: Proceedings of 16 th International CODATA Conference, CODATA-98, (1998).

15. **Adiga P. S. U.** and Chaudhuri B. B., "Active Surfaces for the segmentation of the Volumetric Histo-pathological Images", In: Proceedings of Indian Conf. on CVGIP, 1998, pp. 28-34.

16. **Adiga P. S. U.** and Chaudhuri B. B., "Active Surfaces as a Direct 3-D approach for Segmentation of Volumetric Histological Images and Its Application in Molecular Pathology", for IEEE trans. on Image Processing (In Preparation) (1999).

17. **Adiga P. S. U.** and Chaudhuri B. B., "Comparative Study of Different Segmentation Techniques for the 3-D Histo-pathological Images" for IEEE Biomedical Engineering (In Preparation) (1999).

Contents

List of Figures

List of Tables

Chapter 1

Introduction

Automation of image analysis in the bio-medical field is one of the important achievements of applied image processing research. The rapid development in the electronic instrumentation during 1960s and 70s made it possible to automate the routine process of diagnosis and prognosis of many diseases. Development of high resolution imaging instruments such as X-ray CT, MRI, etc., for macro imaging and electron microscope, confocal microscope, etc., for micro imaging has given a tremendous boost to the advancement of medical field. Advancement in the field of computing has made it possible to reconstruct the pictures of internal organs of the body in a non-invasive method.

Based on the imaging instrument, we can broadly classify the medical images into two types. They are macro-images obtained by macro-imaging instruments such as MRI, CT-scan, Ultra-sound, etc., and micro-images obtained by micro-imaging instruments such as light microscope, electron microscope, confocal microscope, etc.. This thesis mainly concerns with the analysis of micro-imaging data sets obtained using confocal microscope. More specifically, we consider 3-D histo-pathological images where the aim is to automatically segment the cells and measure the quantitative features of the tissue and the cells of a histo-pathological specimens.

The histo-pathological images are relatively complex in the sense that the cells are arranged in different patterns often touching or overlapping on each other. Moreover, during different pathological disorders, the change in the features of tissue and cells belonging to different organs is different. Even the cells and tissue of the same organ may show different characteristics during different sub-classes of the same disease. Such problems, along with the inconsistency in defining the features by different pathologists as well as lack of standard procedures to define the pathological features make automatic processing of these images more difficult. As a result very few automated systems are found to be successful.

The necessity of automation of the analysis of histo-pathological images stems from the fact that the quantitative study of the tissue specimen by visual approach is very difficult. The visual inspection of the tissue specimen under the microscope depends upon the understanding of the physiological processes and the ability to diagnose by comparing each sample to cases that the expert has seen before. This qualitative or subjective evaluation is appropriate to identify different diseases. The same can not be said while differentiating the different sub-classes of the same disease (Firestone et al., 1996). Visual inspection is less effective in quantification of tissue characteristics. The number of specimens to be inspected, the time factor, consistency and the reproducibility make the automatic quantitative study of the biological specimens, a significant and important part of tissue specimen analysis.

The automation of the quantitative study of histo-pathological images exists in several levels. A completely automatic system is the one where the human interaction may be

needed only for preparing and loading the specimens. In the semi-automatic systems, the human interaction is necessary to feed a priori information for processing the image data. There is a task-specific automation in which only a particular task or the region in the image is subject to automatic image analysis. Full automation exist in the systems such as red blood cell counters, bacterial colony counters, etc.. Complete automation is possible when the cells in the tissue are not arranged compactly and the segmentation of cells is not a difficult problem. One such example is the analysis of blood tissue. Many instruments as well as software are available for the purpose of counting different blood particles and cells in the human blood. In cases where the cells are arranged compactly, the operator or the expert has to interactively intervene in the analysis process either to feed information or to correct the errors. The semi-automation and the task specific automation is applied to a number of cases such as cancer pre-screeners, feature analysis systems, blood inspection, etc.. The review paper by Preston and Bartels (1988) provides many examples of automatic and semi-automatic image processing systems for the analysis of tissue sections.

1.1 Historical Review

The late 1940s and the early 1950s saw the evolution in the utilization of the television microscope for quantitative microscopy. In the 1960s transistorization led to dramatic improvements in automated microscopy, as it did in general purpose computation. The 1970s saw a new era that began with the announcement of the first computerized microscopes that automated the clinical examination of the human blood cells. Mellors et al. (1952), have first reported that cancer cells in cervical smears could be distinguished from normal cells by measurement of nuclear size and optical density. The project on quantification of the structures in tissue and cells by a computer vision and pattern recognition system was taken up in 1960s by Airborne Instrument Lab., under the "Cytoanalyzer" project for pre-screening of the cancer cells. The project was not successful due to several reasons including the difficulties in solving the complex pattern recognition tasks. During approximately same period, a far-sighted idea to obtain a three-dimensional image of tissue specimen as a stack of two-dimensional images was proposed by Marvin Minsky (1961). The basic idea was to vary the focal length of the imaging system and take images at different depths of the specimen. This system, called confocal microscope, came into the market during late 1980s and early 1990s with a laser beam for illuminating the specimen.

Earlier works in histo-pathological image analysis by optical density histogram were reported by Prewitt and Mendelsohn (1966), etc.. Garbay et al. (1981), have shown that the calorimetric and morphological measurements allow the automated recognition of the structures present in the image data. If there are clearly defined modes in the optical density histogram, it is relatively easy to select suitable thresholds and generate masks specific to the major components of the image. When this is not true, more complex methods of gradient tracking may be necessary to find boundaries. Mendelsohn et al. (1971), have worked on boundary detection in chromosome images, and Prewitt (1972) did similar studies on boundaries of images of leukocytes. Some other approaches towards coding the edge and the

boundary were reported by Saraga and Wavish (1971). Rosenfeld and Thurston (1971) have reported work on the problem of locating boundary between different textures. Yosnoff and Bacus (1984) have used array measures for locating boundaries in images of cervical smears.

Not withstanding the problems in ideal specimen preparation, the research efforts were made to correct the imaging artifacts by pre-processing techniques using computers. Though many artifacts can be corrected by designing and adjusting the hardware of the microscope, it is easier to use image processing techniques to correct the images in many cases. Neighborhood averaging filter, directional averaging (Jain, 1995), Gaussian smoothing filter, etc., were used to smooth the noisy images with a minimum loss of information. Adaptive filter for digital image noise smoothing were also discussed (Mastin, 1985). The noise reduction filters such as mode-filter (Davies, 1988), median filter (Huang, 1979; Yang and Huang, 1981), hybrid median or edge-preserving median filter (Niemen et al., 1987) were shown to be useful in reducing different kinds of noise in the histo-pathological images. Some of the major work in noise reduction and correction of confocal images such as reducing out of focus information, etc., can be seen in papers by Roysam et al., (1992, 1994), Rigaut et al., (1992), etc..

Some of the earlier works demonstrating the applications of image processing methodologies in automation of quantitative analysis of histo-pathological images can be seen in the papers by Preston and Onoe (1976), Preston Jr. (1981), Garbay et al., (1982), Garbay (1986; 1995), Acharya (1987), Rodenacker (1987), Carvajal-Gonzalez et al., (1991), Acharya and Wasserman et al., (1995), etc.. Some of the recent works in building the image understanding systems for cancer pre-screening and related studies based on histo-pathological image analysis can be found in the theses and papers by Nardin (1989), Choi (1996), Firestone (1996), etc.. One of the reasons for these systems not to meet the complete success in automation is the less importance given to the segmentation of the cells. Our experience says that even for a same pathological disorder, the images obtained may show vast difference in their properties as well as structure of the cells and tissue. This calls for more research in developing or modifying the existing segmentation techniques to suite the need of automation and precision in segmentation of the cells.

Most of the earlier studies were concentrated on the analysis of two-dimensional histo-pathological images. The late 1980s has heralded a new era in microscopy when the biological application of the confocal microscopy was shown by Amos et al., (1987) and White et al., (1987). This initiated a renewed interest in the study of spatial structures of tissue and cells in biological specimens. Some of the preliminary works on correction, pre-processing, segmentation and reconstruction of the three-dimensional biological specimen images can be found in the papers by Acharya et al., (1990), Hiraoka et al., (1990), Rigaut (1991), Marko and Leith (1992), Bron and Gremillet (1992), etc.. Rigaut et al., (1992), has given a brief study of the advantages of using three-dimensional histo-pathological images. They have also discussed about some of the simple methods that can be used for preliminary analysis of the 3-D images. Several articles on the application of image processing techniques on confocal and other three-dimensional microscopy images can be found in Acharya et al. (Eds.) (1995), Roysam (1994), Acharya et al., (1987), Rodenacker et al. (1997), etc.. Our work on designing the image understanding system for quantitative evaluation of the confocal

microscopy images is unique in the sense, we have tried to build a complete system with more importance given to the segmentation of the 3-D cells rather than the process of classification. This thesis describes the work done by us in this regard. Relatively few studies with practical, biological results from confocal images have been reported. In this regard our work can be considered as new and extensive.

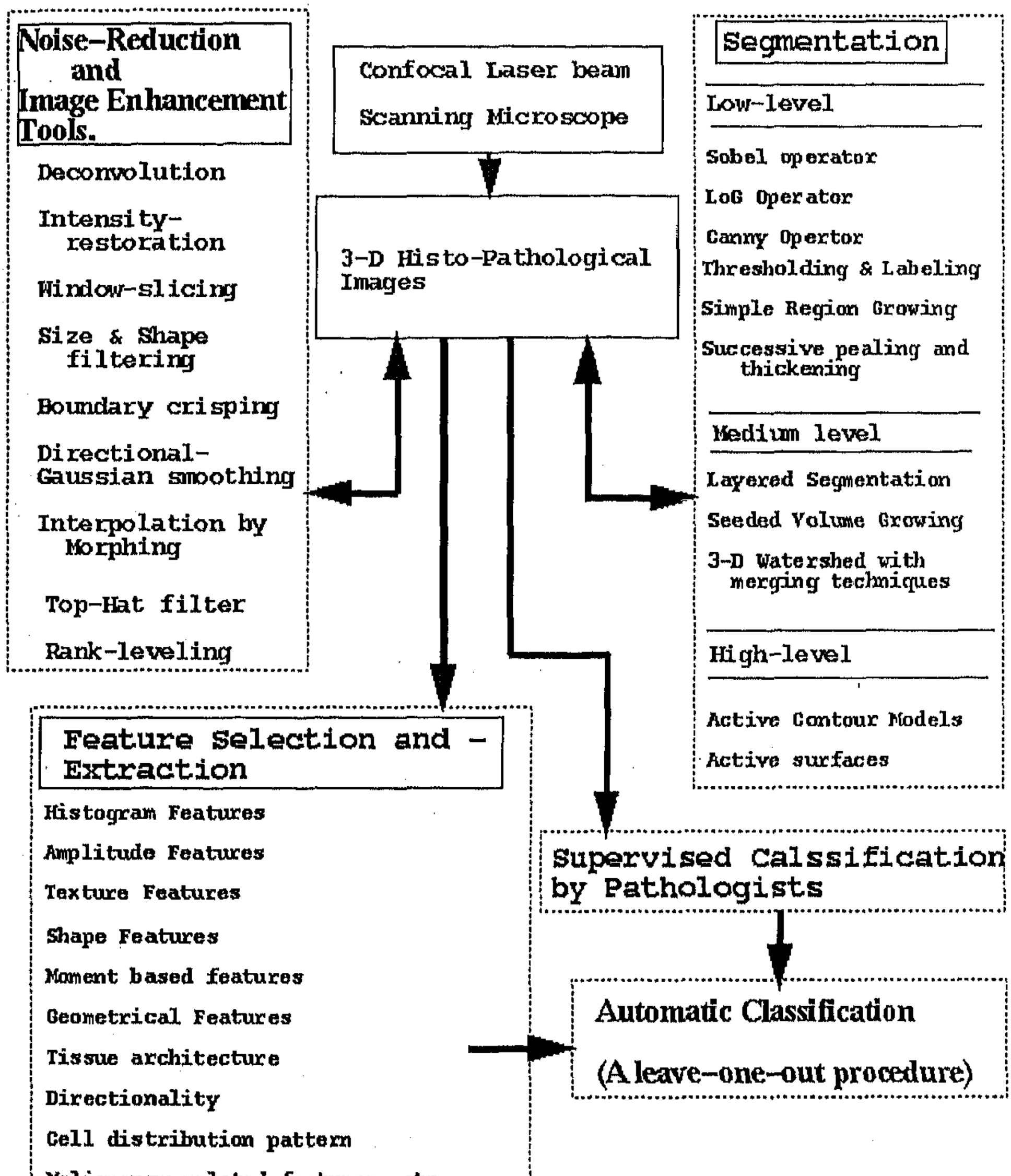

Fig. 1.1: Block diagram of the image understanding system for quantitative evaluation of 3-D tissue images.

1.2 Overview of the Thesis

In this work we have explored the field of three-dimensional histo-pathological image analysis. The quantitative study using the full 3-D image is preferable, as it allows measurement of individual objects and quantitative assessments of their spatial arrangement. This requires the segmentation of all relevant objects and the estimation of various features by image analysis. The two major reasons for using the 3-D images are the possibilities of (i) Three-dimensional visualization of the gray-tone images and of objects reconstructed after segmentation, and (ii) Precise quantification of features.

Measurement of simple shape features such as size and shape based on 2-D images can be erroneous since the 2-D images may not represent the complete cell in its entirety. The significant slicing of the cell nuclei results in under estimation of nuclear DNA content. It has been shown that the 3-D analysis is essential for the measurement of malignancy related features such as Fluorescence in situ Hybridization (FISH) signals in case of prostate cancer (Aubele, 1996). Other than precise quantification of the feature values, the three-dimensional study of the tissue gives an option to evaluate the spatial arrangement of the cells.

We have built an image understanding system capable of providing image correction, enhancement, segmentation, feature measurement and possible decision supporting based on confocal images. In general, this work presents an image understanding system for the quantitative analysis of three-dimensional histo-pathological images. The three-dimensional images of histo-pathological specimens (Prostate cancer tumor), are obtained using Confocal Laser beam Scanning Microscope (CLSM). Results of classification of the specimen images into different grades of cancer based on automatic feature measurement is also presented. Fig.1.1, shows the block diagram of the complete system for quantitative evaluation of the three-dimensional tissue images.

1.2.1 Lay-out of the Thesis

The image understanding system presented in this thesis consists of three main features.

1) Image Enhancement,
2) Image Segmentation,
3) Feature Selection and Extraction.

The image enhancement or image correction is an important step that should be carried out before segmentation and feature extraction. The process of image enhancement involves noise reduction and enhancing the important features in the image. This includes the restoration of degrading light intensity due to photo-bleaching, adaptive smoothing, improving the resolution, reducing the background variation, contrast enhancement, boundary enhancement, scaling, etc.. We have described these steps in **chapter 2**, with respect to

confocal microscopy images. Chapter 2 also includes, brief description of the principles of confocal microscopy, some of the causes for the noise artifacts, specimen preparation, influence of specimen preparation on the image, image acquisition feature set up, etc..

Segmentation of the objects of interest in an image is a key to the success of any computer vision and image understanding system. In analysis of histo-pathological images, segmentation is the most difficult part. The complexity arises due to the compact arrangement of the cells, irregular shape of the objects, presence of dense intra and inter-cellular matters, fine textured cell chromatin, low and uneven intensity gradient depicting the cell boundary, etc.. Most of the earlier works on developing systems have either ignored or over looked the importance of segmentation process while giving more importance to the extraction of features such as textures, etc.. We have given more importance to the segmentation as the precision of feature extraction and classification depends on the accuracy of the segmentation. We have designed and/or implemented several segmentation methods instead of trying to stick to any one global method. We have also presented an integrated approach that can be generally applied on many histo-pathological images for getting reasonably good results.

The segmentation can be broadly classified into two categories. They are (1) Edge based segmentation and (2) Region based segmentation. Some of the early experiments for segmentation of cells is done using local edge-detectors, simple region growing methods, thresholding and labeling, etc.. As these methods have not produced satisfactory results, we have implemented several semi-automatic methods which gives acceptable segmentation. These methods are layered segmentation, active contour models and active surfaces. Layered segmentation and the application of active contour models are considered as 2-D plane-by-plane approaches while the use of active surfaces is a direct 3-D approach. All these methods results in marking of smooth and continuous surface of the cells separating one another in the cluster. These methods, which are generally known as edge based segmentation, is explained in **chapter 3**. Chapter 3 also gives a brief comparison of the performances of these methods on a few 3-D histo-pathological image data.

Chapter 4 explains different region based segmentation techniques. They include seeded volume growing technique, successive pealing-constrained thickening as well as 3-D watershed technique. We have presented a simple pealing or erosion technique to mark the seed inside the cells. Intensity similarity constraints, gradient similarity constraints and several morphological criteria are then used to control the growth of the seeds into immediate neighborhood voxels. The watershed algorithm is extended to work on 3-D images. We have also presented an additional algorithm as an extension to 3-D watershed, for reducing the over-segmentation of the cells. All the three methods are compared and a brief discussion on comparative results is given. Chapter 4 also includes an integrated approach for automatic segmentation of the cells in a tissue. Several techniques such as active models, region growing, watershed, etc., are integrated to develop a complete automatic method which can provide good segmentation.

In molecular pathology, it has been observed that the variation of a chromosome density can indicate the malignancy level of a cancer tumor. Example is the gain or loss of chromosome #7 and #12 in a prostate tumor (Dhingra et al., 1994; Zitzelsberger et al., 1996).

These signals can be seen as fluorescence signals within the cell nuclei. It has been shown that the three-dimensional image analysis is necessary to estimate this gain or loss of a chromosome numbers in a cell nucleus (Aubele et al., 1996). In **chapter 5**, we have described automatic methods for selecting the region of interest in the signal channel, reducing the noise, identifying and segmenting these chromosome signals and counting them. We have also discussed possible errors in automatic evaluation. The results are compared with the signal counting by pathologists as well as with the 2-D evaluation. Effect of different image segmentation techniques on signal counting is also presented.

The main goal of an image understanding system that deals with the histo-pathological images is to quantify the cell and tissue features. Selection of features from the segmented image is an important factor to study the prognostic and diagnostic value of the specimen. In **chapter 6** we have explained various criteria for selecting the features. Methods are explained to measure the standard features of the cells in 3-D image. Many heuristic algorithms are designed and tested to quantify the spatial architecture and the cell arrangement in the tissue. Influence of Image correction, enhancement and segmentation, on the feature extraction is discussed elaborately.

In **chapter 7**, we have implemented a simple two step classification procedure for sub-classifying the specimen images based on the automatically measured features. We have used approximately about one-hundred and sixty data sets. As the number of data sets per sub-class is too low, we have used leave-one-out procedure for designing the classifier. Though the results obtained were encouraging, we found that experiments on large number of data sets is needed before considering the system for routine use. We have designed a simple Graphical User Interface (GUI) so that even the people with little experience in handling the computer can find it easy to apply various segmentation and feature extraction algorithms for the three-dimensional image processing. Though the system is not completely automatic, most of the task specific analysis is done automatically.

In **chapter 8** we have discussed the various problems we have come across in implementing this system and what are the further steps which have to be taken to make the software more reliable. We have also discussed the need of statistical confirmation about the reliability of the image understanding system for prognosis and diagnosis of histo-pathological problems. The system has to be tested on different kinds of data sets from different diseases of various organs and tissues of the human body. We feel that there is much scope to improve the classifier performance. It needs more number of data sets and more pathologists to be involved in setting up the standards for quantitative study.

Chapter 2

Confocal Microscopy and Image Correction

2.1 Introduction

Among recent developments in the visualization of the histo-pathological images, Confocal Laser Scanning Microscopy (CLSM) is one of the most exciting new developments. Confocal Microscope can be considered as a three-dimensional (3-D) imaging instrument for collecting data from spatial structures, especially biological ones. The CLSM technique with its capacity for optical sectioning, high resolution reconstruction and most importantly 3-D imaging of the fluorescence labeled or reflecting structures, allows accurate and detailed information to be gathered on the architecture, directionality, size and shape of the cells in the tissue specimen.

The principle of confocal microscopy was first stated by Marvin Minsky (1961). The object is scanned by fixing the point light source and moving the specimen for a short distance in a raster pattern. This is a stage scanning process. The variation in the amount of light, modulated by the specimen, is captured by a photoelectric cell. The photoelectric current can be subsequently used to reconstruct the image.

Early instruments using a stationary specimen and a scanning laser beam were built by Davidovits and Egger (1971). A few years later, Sheppard and Chaudhury (1977), provided a thorough theoretical analysis on various modes of confocal microscopy. During the following years, Sheppard et al., (1978) and Wilson et al., (1980), described a transmitted light confocal microscope. This microscope was a stage scanning type, equipped with a laser source and a Photo-Multiplier Tube (PMT) as the detector, using a novel specimen holder. The specimen holder supported on four tout steel wires running parallel to the optical axis, allowed precise Z-axis positioning as well as fairly rapid voice coil actuated scanning of the specimen in the XY plane. Instruments employing a stationary laser beam and a moving specimen stage were developed some years later by Barkenhoff et al., (1979).

Cramer and Cramer (1978), of Heidelburg have designed a specimen scanning laser illuminated confocal microscope. A verification of the imaging properties at high numerical apertures was made experimentally by Barckenhoff et al., (1979). The advancement of digital image processing, instrumentation, etc., along with the research on confocal imaging, culminated in a development of the confocal laser scanning microscope (CLSM) (Aslund et al., 1987). The biological applications of the confocal microscopy was first reported by Amos et al., (1987) and White et al., (1987). Fig. 2.1 shows the block diagram of the laser scanning confocal microscope.

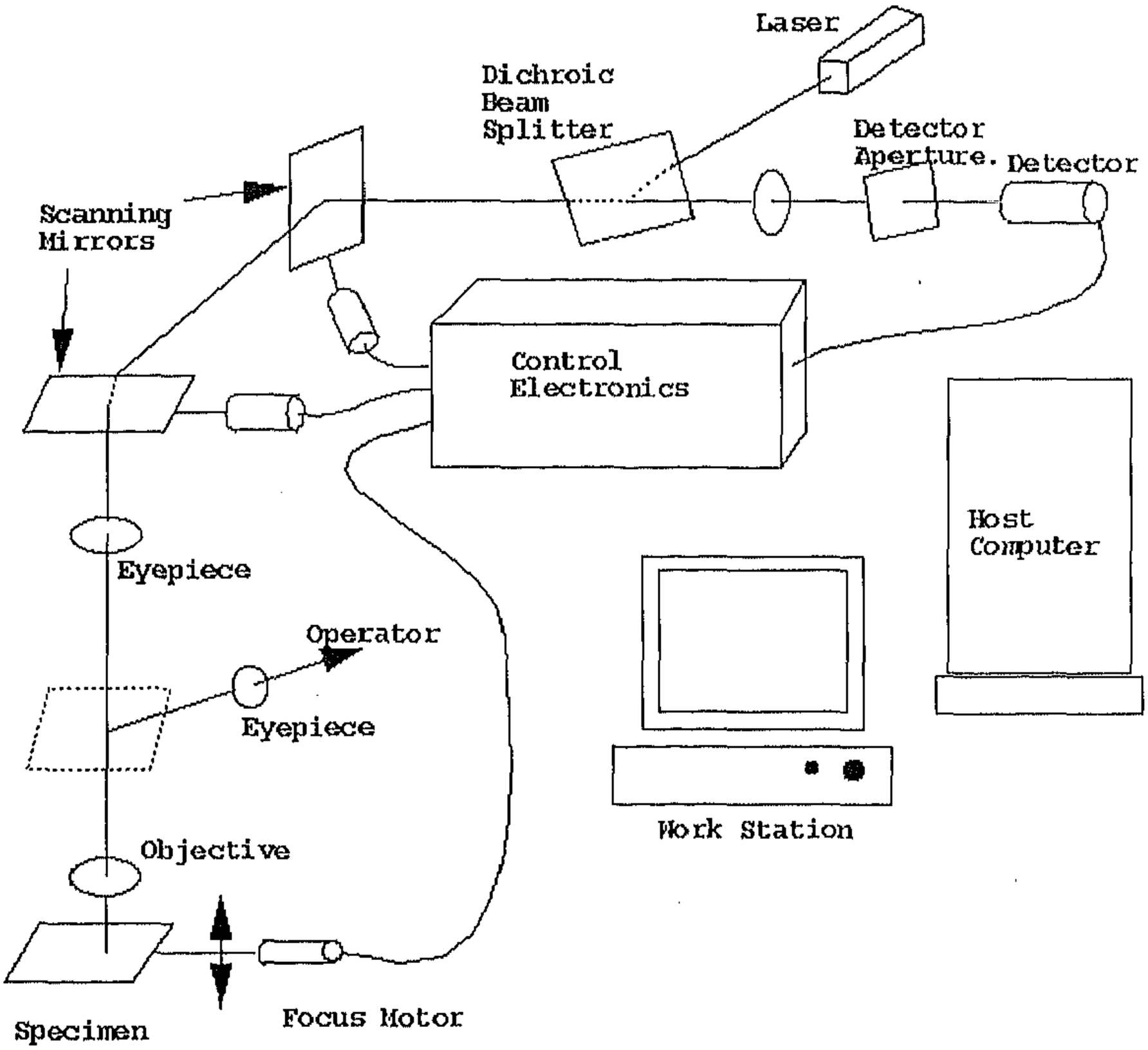

Fig. 2.1: Block Diagram of Confocal Microscope System

Working Principle of CLSM: The working principle of the CLSM can be briefly stated as follows. A sharp laser beam is focussed on a particular point of the focal plane in a thick tissue specimen. The reflected laser beam being modulated by the specimen at the respective focal point, carries information about the specimen at that point. The focal point is moved in a lateral plane in a raster pattern for scanning and the information about the specimen in a corresponding focal plane is obtained. Then the focal plane is varied in the axial direction and next image slice is obtained. The lateral and axial resolutions are controlled with the help of a computer interfaced to the CLSM. In this way a stack of optical sections depicting the 3-D information about the tissue specimen is obtained.

Fig. 2.2 shows a schematic diagram of working principle of the confocal microscope in its simplest form. Confocal Laser Scanning Microscopy uses laser as a light source and the laser beam is focused to a diffraction limited spot within the specimen. The reflected or fluorescent light emanating from this point is separated from the exciting laser by a dichroic mirror and deflected towards a photo-detector. The pinhole aperture placed in front of the photo-detector stops de-focused light from reaching photo-detector. The de-focused light is due to the light reflected from the neighboring optical sections of the specimen. The

photo-detector captures the variation in the amount of light, modulated by the specimen and passing the second pinhole aperture. Since, information about only a single specimen point is recorded, scanning must be done in the respective focal plane to obtain one full optical section. We have called the optical sections of the specimen as image slices.

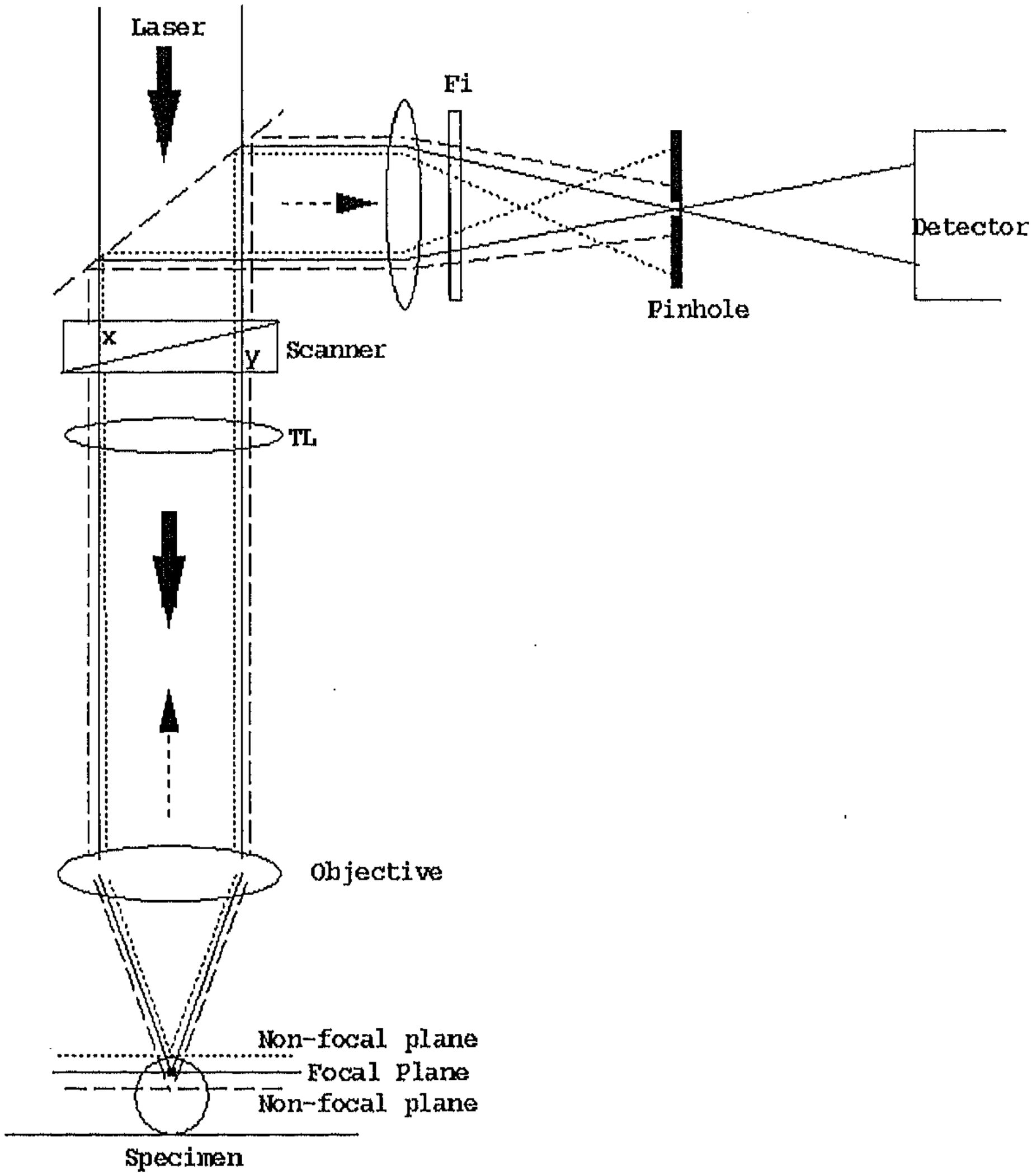

Fig. 2.2: Schematic diagram showing the working principle of confocal imaging

Scanning can be done either by moving specimen relative to the stationary beam of light or by moving the beam of light across a stationary specimen. These are known as stage scanning and beam scanning, respectively. Since only light from a thin specimen slice, centered on the focal plane is recorded by the photo-detector, there is no need to physically section the specimen. This optical sectioning capability is utilized for recording the 3D structure of a specimen through a repeated process of image recording,

while slightly re-focusing the microscope between successive images. Such optical sequential sectioning will produce a stack of 2D images, inherently in perfect register, from which the 3D morphology of a specimen can be evaluated.

The optical hardware of the Confocal Microscope includes mainly, the objective lens which influences the resolved details, contrast at which these details are present, the depth through the object from which useful information can be derived, and diameter of the useful field, etc.. The dichroic mirror, performs the function of filtering the reflected light and directing it towards the photo-detector. The success and failure of a particular microscope implementation in achieving true confocal function depend on the correct choice of the pinhole size and shape to approximate as closely as possible, the ideal point detector. The images of the source and the detector pinhole overlap in a confocal microscope. The position of the illuminating light spot in an image plane is also the position of the image of the light spot formed in the sample (Pawley, 1995).

The refractive system produces many kinds of aberrations that may affect the final image output. These aberrations include defocusing, spherical aberrations, coma, astigmatism, flatness of field, distortions due to non-linear magnification from center to edge of the field, longitudinal chromatic aberrations, chromatic magnification difference, reflecting objectives, etc..

Defocusing causes change in size and intensity distribution of the unit image point (voxel). Spherical aberration has the effect that paraxial rays are focussed differently from peripheral rays. Blurring of the image produces an asymmetrical intensity change. Chromatic aberrations or wavelength dependent aberrations are caused mainly by two factors. The refractive index of every optical glass varies with wavelength, a factor called dispersion; and the wavelength λ effects the size of the voxel. Longitudinal chromatic aberration is caused due to the result of changes in lens focal length Δf with changing wavelength λ. Because magnification is proportional to $\frac{1}{frequency}$, the magnification also change with λ, producing lateral chromatic aberrations. If the magnification of the object is different for different λ, sharp edges in the image will show blue or red fringes. In confocal scanning of fluorescent specimens, lateral chromatic aberrations can cause the excited light to return to a location nearer to, or farther from, the axis than the apparent location of the same source. This results in intensity loss at the pinhole and the subsequent image.

Cogswell et al. (1995), have studied the specimen illumination path in the confocal microscopy and its effect on image quality. The power fluctuations in the laser, the vibration in microscope due to cooling fans, intensity attenuation by polarizing filter and misalignment of the plane of polarization of the laser are some of the readily recognizable defects connected to laser source. Some of these defects can be rectified by adjusting microscope design parameters (in case of cooling fans) and carefully selecting monochromatic, polarized laser. For collecting multi-spectral images, multiple illumination frequencies may have to be used. In such a case, the spectral filters are utilized in the illumination path to isolate the specific λs from a multimode laser. In these cases the optical quality of the filter is critical.

Confocal scanning microscopes are particularly attractive by virtue of enhanced lateral resolution, purely coherent image formation (in reflection) and optical sectioning. The only difference between the basic structure of the confocal and the conventional scanning microscope is that the confocal arrangement uses a point detector rather than a large area one. All the considerable advantages of confocal microscopy derive from the small size of this detector. In the presence of a very large pinhole, the sectioning almost disappears. If I(Z) is the axial image intensity as a function of axial direction Z, then Fig. 2.3 shows the effect of increasing the pinhole size on axial image intensity. Thus the axial resolution can be improved by using very small sized pin holes (Pawley, 1995). The lateral resolution also deteriorates if finite sized detectors are used. In particular the imaging becomes partially coherent. As a result image interpretation and calculation become more difficult.

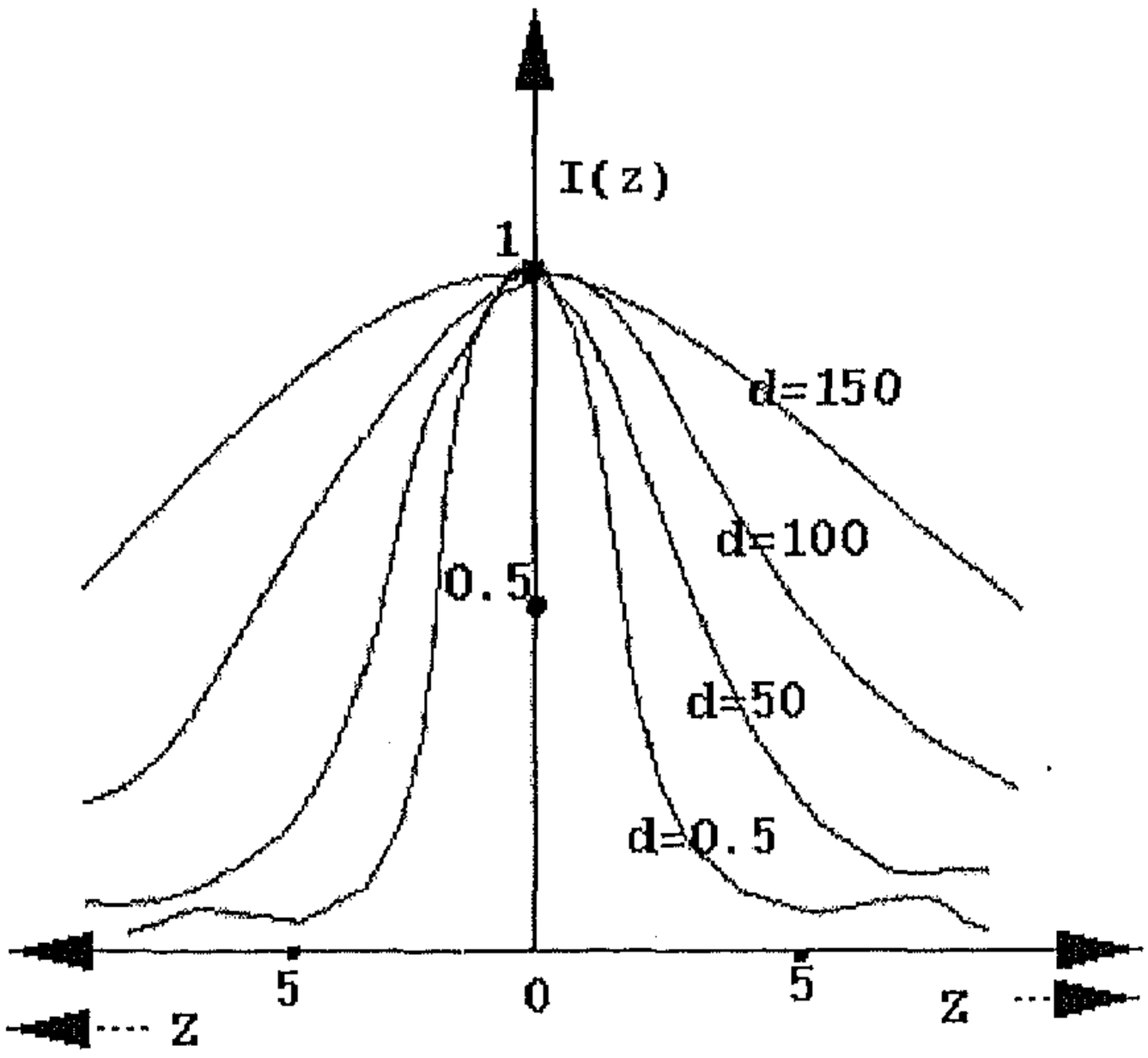

Fig. 2.3: Diagram showing the effect of increasing the pinhole size

The quantum efficiency, responsivity, spectral response, inherent noise, response time and linearity of the photo-detector used in the confocal microscope affect the resulting image. Internal detection with semiconductor devices is associated with two general classes of noise. The first one that can be measured without an applied bias voltage, arises from thermal motion of charge carriers within a material and is known as Johnson, Nyquist or thermal noise. The second category of noise source is only measurable in the presence of a bias voltage and is specific to the type of device and the variable measured in the photo-conversion process. In photo conductors, there also exists generation-recombination (g-r)

noise, which is due to fluctuation in the rates of thermal generation and recombination of charge carriers, leading to a fluctuation in the average carrier concentration. In diodes with an applied bias, shot noise is apparent. This noise is due to the quantal nature of the current carriers and results in a statistical variation in the amplitude of the measured current. The other form of noise, which is not strictly controllable by analytic treatment is, $\frac{1}{frequency}$ noise, so named because the power varies inversely with frequency. The ohmic leakage at the active leads along the insulating material of tube, the thermionic emissions, etc., add to the noise.

In the following section, we have presented the details about image acquisition process using confocal microscope. We have also briefly outlined the feature setup and the specimen preparation methods we have followed.

2.2 Specimen Preparation and Image Acquisition

The use of vital fluorescent dyes has allowed the microscopists to make inquiries about the activities of the cell's interior, both in vitro and in vivo. In addition, development of immuno-fluoroscence labeling has allowed researchers to correlate functional biochemical data with structural data. In order to obtain high contrast images, the immuno-fluorescent staining protocols have tended to flatten the specimens under study to reduce the effect of out of focus light on the final image. This tendency has pushed the biologists either to study thin cells or cells grown in conditions that are not optimal. Confocal microscope extends the utility of fluorescence-labeling techniques and with its ability to exclude the out of focus information, it permits the acquisition of 3D intensity data sets that can be viewed as 3-D images.

2.2.1 Influence of Specimen Properties on Imaging

The specimen volume between the recorded layer and the objective may influence the recorded image data, both geometrically and photometrically. This should be remembered especially when using these data quantitatively. It is obvious that light may be absorbed and scattered, resulting in images that will grow progressively darker as scanning proceeds deeper down into the specimen volume. Besides absorption and scattering, the specimen volume may also refract the light. This effect results in reduced light intensity, lower resolution and geometrical distortion. It has been observed that the optical sectioning performance can be seriously degraded and ghost images may occur due to such refraction effects in the specimen. Refraction will also influence the depth scale in the recorded volume. This is because there will be a difference between the vertical movement of the specimen stage and the movement of the focal plane within the specimen volume. This scale factor is given by the ratio of the refractive indices of the specimen and the medium above. Thus for a specimen having refractive index lower than that of the medium above the depth scale will be elongated. Otherwise, it will be compressed.

One of the effects of specimen induced aberrations is that the power density of the illuminating spot will progressively decrease as the depth within the specimen increases. This means that for applications such as quantitative fluorescence investigations, the irradiance at any point in the focused spot (and hence the amount of fluorescence excited) will diminish with depth. Similarly these same aberrations will ensure that a smaller than expected fraction of the fluorescence signal will be focused back to the detector pinhole. This effect, in addition to the loss in irradiance due to scattering and absorption by the specimen, etc., must be considered if quantitative fluorescence measurements are desired.

2.2.2 The Material

We have processed thick specimens of the prostate carcinoma. The specimen preparation, fixing and image acquisition has been done with the help of pathologists, physicians and physicists of Bio-Medical Image Analysis Division, Institute of Pathology, GSF, Munich, Germany. Routinely processed formalin-fixed and paraffin embedded tissue specimens from radical-prostatectomies of several patients with prostatic adenocarcinoma were used to acquire the images. Consecutive sections were made consisting of a 15µm thick section for Fluorescence in Situ Hybridization (FISH) with subsequent CLSM scoring. Also sections of 5µm thick are made for haemoxilin-eosin staining (H & E) for FISH. The 5µm thick section images were subsequently used to take the images under fluorescence microscopy for comparative study of FISH signals within the cell nucleus image of a thin (5µm) and thick (15µm) tissue specimen. Sections were mounted on slides and baked overnight at 37° C for better adherence.

For double hybridization experiments 30µm thick sections were prepared and stained with methylene blue. From these sections the corresponding tumor areas were selectively cut out with a fine scalpel under microscopic control. For desegregation of tumor nuclei the modified protocol of Alers (Alers et al., 1995) was used. Briefly after deparafination and rehydration, the samples were digested in a pronase E solution (0.05 % in phosphate buffered saline, PBS, pH 7.0) for 2 hours at 37° C , with vigorous vortexing every 15 minutes. The cell suspension was then centrifuged, washed twice in cold PBS before filtering through a nylon mesh (pore size 30µm) to remove any remaining tissue fragments. The cells were resuspended in a cold Carony's fixative (methanol/acetic acid = 3/1) and dropped on to clean slides.

Fluorescence In Situ Hybridization (FISH): For the purpose of marking the FISH signals, the specimen preparation is as follows. α-satellite DNA probes specific for the centromeric region of chromosome 7 and 12, respectively, were generated. The probes were biotin-(#7) and digoxigenin-(# 12) labeled by nick translation according to standard procedures. The specifics of the probes were checked on metaphase preparations from peripheral lympho cytes of healthy donor. The hybridization mixture consisted of carrier DNA (0.5 µg / µl herring sperm DNA), mastermix 2.1 (final concentration: 55 % formamide / 1xSSC, 10% dextran sulfate) and the labeled DNA probes. This mixture was denatured at 72° C for 5 minutes and chilled on ice till use.

For Fluorescence in situ Hybridization (FISH) of 15µm thick sections, the slightly modified Zitzelsberger protocol (Zitzelsberger et al, 1994) was used. The pre-treatment of sections with pronase E solution (0.05 % in PBS) was performed at 37°C for 20 to 40 minutes. This proteolytic pre-treatment step had to be optimized for each paraffin block. Those cases which did not exhibit strong signals throughout the section thickness even after intense proteolytic digestion were additionally treated by microwave with 750 watts for 2 minutes in a citrate buffer (pH 6.0). After the denaturation of the sections in 70% formamide (70% formamide / 2xSSC) at 72°C for 20 minutes, the sections were dehydrated in a series of 70%, 90% and 100% ice cold ethanol and dried. Denaturation of the slides containing desegregated nuclei was performed in 70% formamide at 72°C for 3 to 20 minutes, the 5µm paraffin sections were treated by Zitzelsberger protocol (Zitzelsberger, 1994). 30µl of the hybridization mixture were applied to each slide, covered by a glass coverslip and sealed with rubber cement. After overnight incubation at 37°C post-hybridization washing was performed at 43°C as described in Zitzelsberger protocol.

The biotin labeled centromere 7 probe was detected by streptavidin conjugates. Detection of the digoxigenin labeled probe of centromere 12 was performed by an anti-digoxigenin antibody (Boehringer, Mannheim) and repeated cycles of Cy-3 conjugated rat anti-mouse and mouse-anti-rat antibodies. After washing, the nuclei were counter-stained with propidium iodide (PI, Sigma) in single FISH experiment, with DAPI (4', 6-diamidino-2- phenylindole, Sigma) in double hybridization experiments, and subsequently mounted with an antifade solution (Johnson et al 1981).

2.2.3 Image Acquisition

Proper image acquisition is one of the important steps towards the success of this kind of project. Since no specimen or specimen preparation process is perfect, more care should be taken during image acquisition process to avoid the noise and to highlight the region of interest in the image. In the field of confocal microscopy, the effect of hardware noise and the presence of out-of-focus information are the direct results of image acquisition process. Careless image acquisition may result in specimen photodamage.

Set-up Features for Image Acquisition: Fluorescence images are scanned using a Confocal Laser Scanning Microscope (CLSM) Zeiss LSM 410. Essential setup features for the acquisition of FISH signals in tissue sections are as follows: Lens Zeiss PNF 100x, 1.3, zoom =2, realized by scanning unit). The scanned field of 62.5µm X 62.5µm is sampled to 256 X 256 pixels giving a pixel size of 0.25 μm^2 in x and y direction. Excitation laser lines are selected according to the fluorochromes used. For propidium iodide (PI) used as DNA counter stain and Fluorescein Iso-Thio-Cyanate (FITC) labeled signals both are excited by the Argon line 488*n*m . Lateral resolution of $\approx 0.5\mu m$ is obtained by the system. The lateral resolution is related to the wavelength of the excitation laser as $resel_{lat} = 0.8\lambda/2(NA)$ where NA is the numerical aperture which is 1.3 in the present case. The emission of FITC and PI fluorescent materails is measured simultaneously in two separate channels using a bandpass 515 - 565 *n*m for FITC and a lowpass LP 590 for the PI channel, respectively. The axial

distance selected between two subsequent confocal images depends on further evaluation strategy. If a spatial isotropic representation of the 3-D data is intended, the axial distance is identical to the lateral distance of the pixels, i.e. 0.25 μm. For a 16 m thick section this results in a sequence of 64 scanned images. If only the sampling theorem should be met, roughly a 0.5 μm distance is enough, noting that the confocal axial resolution of a lens with numerical aperture NA = 1.3 is given by $resel_{axi} = 1.4\lambda\eta/(NA)^2$ where η is the refractive index of the object. Axial resolution is approximately equal to $1\mu m$. The FITC emission is associated with the green channel and the PI emission with the red channel of a RGB color image. The image data are stored on disk in TIFF format.

2.3 Noise Reduction and Image Enhancement

Several quantitative distortions can be introduced into 3-D stacks of optical sections during data collection. Once the sources of errors are identified, some can be prevented by modifying the microscope setup, while others are to be corrected either at the time of data acquisition or afterwards.

Most of the errors that can be corrected by image processing are, low axial resolution, the uneven illumination, photobleaching effects, out of focus information or blur, various kinds of noise artifacts, etc.. Confocal microscope has an inherent property of minimizing the out-of-focus information in an image due to its unique pinhole point detector. The arrangement shown earlier in Fig. 2.2 stops the out-of-focus laser beams from reaching the photo-multiplier tube. This helps in doing away with computationally expensive deconvolution process.

2.3.1 Window Slicing

One of the important aspects before image enhancement, is to separate the background and foreground regions. Window slicing which is also known as amplitude thresholding converts all the pixels or voxels which are below a threshold T_s to the lowest gray value that is zero (indicating dark). The voxels having intensity value above the threshold is kept undisturbed. This gives us an image of uniform background separated from the foreground consisting of different gray levels.

Confocal image stack shows uneven variation in the illumination of the specimen. The last few image-slices normally show very low average image intensity due to various optical problems as well as the photobleaching. Threshold selection based on local histograms has an advantage that the adverse effect of variation in the image intensity on the threshold value is minimised. For images with distinct background it is possible to select the threshold from the gray level histogram using the mode method i. e., by choosing the gray level that corresponds to valley position in the histogram as threshold value. We have observed that the histogram of our image data sets exhibits unimodal property. Hence the valley may not be found explicitly in the histogram of the images. In such cases it is often possible to define a

good threshold at the *shoulder* of a histogram (Sahoo et al., 1988). Since both the valleys and the shoulders correspond to the concavity of the histogram, a threshold can be chosen by analyzing the concavity of the histogram (Rosenfeld and De la Torre, 1983). We have used the empirical formula,

$$\tau = (\mu \pm k\sigma)$$

where σ is the standard deviation of the gray value and k is a constant determined experimentally. Here, $\tau = (\mu + k\sigma)$, when the mode point of the histogram lies close to the minimum gray value in the image and $\tau = (\mu - k\sigma)$, when the mode point lies close to the maximum gray value in the image. This is diagramatically shown in Fig. 2.4. The above formula gives uniformly good results to the images we considered in our experiments. There are many other efficient methods to automatically select the threshold (Sahoo et al, 1988). As the method explained above was giving acceptable result on almost all the image data sets and is simple to implement, we have not used any other methods.

Fig. 2.4: Diagrammatic representation of threshold selection.

As the data sets have shown much variation in light intensity along axial as well as lateral directions, it is appropriate to use local thresholding. This reduces the influence of local variation in the light on the overall threshold value. For calculating the threshold value based on local histogram, the local window size was selected interactively. Minimum size of the window chosen is $s_1 \times s_2 \times 1$ where $s_1 \times s_2$ is the approximate size of the largest cell cluster among all optical sections. We have provided sliders in the Graphical User Interface (GUI) to set the approximate local window size by looking at the largest cell signature. The maximum size of the local window is limited to $256 \times 256 \times 1$ which is one optical section size in the data. Once the threshold is chosen all the voxels below the threshold are converted to lowest gray value i. e., zero (depicting black) and the voxels with gray value above the threshold are kept undisturbed. Fig. 2.5(b), shows the result of window slicing as a sequence of a few representative image slices of an image stack. The original image slices are shown in Fig. 2.5(a). Sometimes, window slicing results in creation of holes in the cells and small noisy island like object structures in the background. This is due to the presence of dense non cellular matters in the background and dark intra-cellular objects within the cell. We have developed a size and shape heuristic based filter to reduce this effect.

2.3.2 Size & Shape filter

The *size and shape heuristic* based filter removes all the isolated noisy objects and restore the proper gray level to the hole like structures in the image. The function of the filter can be briefly explained as follows. The size of all the isolated objects is calculated. If the size is below a pre-defined size threshold then such objects are considered as artifacts and its voxel intensity are changed to background intensity. Similarly, the holes are identified. If the holes are smaller than the pre-defined threshold, then the original gray values of the voxels belonging to the holes are restored. We have used shape feature in case of FISH signal segmentation which is explained in chapter 5. Fig. 2.5(c) shows the result of size filtering of the window sliced images. After window-slicing and size filtering of the image stack, the background noise is reduced and the background gray value becomes spatially uniform.

2.3.3 Correction of Intensity Attenuation

The uneven illumination along the depth of the specimen results in the spatial variation of light intensity in the image. This has to be rectified and the image intensity has to be evenly restored for further automatic analysis of the images. The reasons for the degradation of light intensity along the depth of the stack are discussed earlier. Besides these optical problems, the photobleaching of the specimen also contributes to the degradation of intensity. The photobleaching can be briefly explained as follows.

When fluorophores in a specimen are raised to the singlet excited state, it decays back to its ground state by emitting the photons generating fluorescent signal; alternatively, a transition to the triplet state with a molecular oxygen can generate a non-fluorescent molecule. This process, known as photobleaching, occurs with each exposure of excitation light.

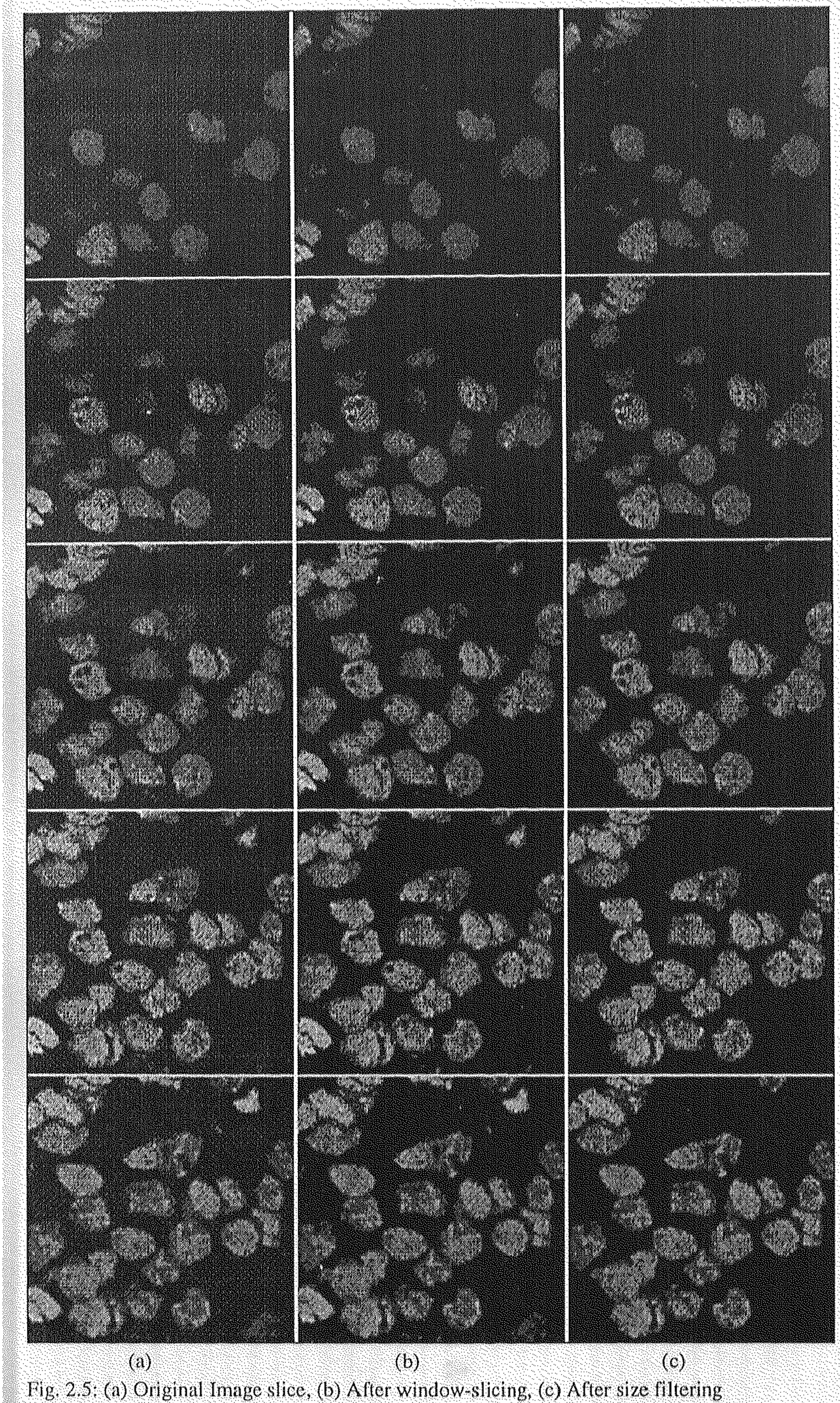

(a) (b) (c)

Fig. 2.5; (a) Original Image slice, (b) After window-slicing, (c) After size filtering

The repeated exposure needed to generate a 3-D data by optical sectioning will bleach most of fluorophores in the specimen. This causes a significant image intensity difference at the beginning and at the end of the stack of optical sections. Without restoring the image intensity level, subsequent operations such as segmentation and feature measurement do not give correct results. In most of the cases we ignore the last few image slices of the image stack due to low image intensity level. This results in under evaluation of the cell features and other malignancy related features such as Fluorescence in situ Hybridization signals. To avoid this, restoration of the image intensity is necessary.

Photobleaching can be modeled as a first order decay process and hence computationally corrected (Pawley, 1995). In confocal images, variation in image intensity is not just due to photobleaching. The problems with optical system as well as the opacity of the specimen also contribute to the process. When we plot the average image intensity of each image slice against depth of the stack, we have observed that the illumination degradation is not linear. It is not possible to define the variation of image intensity as a linear decay as is evident from Fig. 2.7 (a).

Aslund et al., (1995) have given a brief review of the methods to compensate for depth dependent light attenuation in images from confocal microscope. Rigaut et al (1992) have proposed a mathematical correction method based on log-logistic equation: $I_z = I_0 / \left\{1 + (z/Z)^{\xi}\right\}$ where I_z is the mean field intensity, I_0 is the theoretical value of I_z when $z \to 0$, the constant Z represents the value of z at which the detected fluorescence intensity $\left(I_z\right)$ is half that of I_0 and the constant ξ depends upon the shape of the curve of I_z against z. Parameter estimations were made using the linear form $log\left\{\left(I_0 - I_z\right)/I_z\right\} = \xi\, log(z) - \xi\, log(Z), \quad \forall \quad z \neq 0$ with $log\left\{\left(I_0 - I_z\right)/I_z\right\}$ against $log(z)$. The parameters were estimated by computer, iterating over the value of I_0 (above the highest observed value of I_z) until the highest linear regression correlation coefficient is found. Rigaut et al. (1992) have reported that very close fits of I_z against z are obtained by this method.

We have implemented a simple method of restoration of intensity of the foreground voxels by comparing it with the highest intensity image slice in the stack. Let I_i be the image slice having maximum average image intensity, i. e.,

$$I_i = max\left\{I_1, I_2, \ldots, I_n\right\}$$

where $I_1, I_2, \ldots, I_n$ are the intensities of 1, 2, ..., n th image slice in the stack. We consider this image slice i as the standard image slice and increase the average image intensity of remaining image slices in the stack to be on par with average intensity of image slice i.

Let the sensitivity α of a pixel with respect to its neighborhood is defined as the ratio of sum of the differences of pixel intensities in the neighborhood to the maximum of pixel intensities in the neighborhood, i. e.,

$$\alpha = \frac{\left(\sum_{p=1}^{N} \left(I - I_p \right) \right)}{max\left\{ I_p \right\}} \text{ for all } p \in W$$

where W is a 3×3 neighborhood and N is the total number of pixels in W. Simple restoration of the image intensity by increasing the mean intensity of the image slices results in decrease of α. An ideal algorithm should find the maximum light restoration with minimum loss of pixel sensitivity. This is an optimization problem and a trade off should be reached based on the application.

If we consider the average intensity of the whole image slice as an indicator of image intensity, one can find too much variation both in lateral directions and along the depth, which is independent of photobleaching and other optical phenomena. The first few image slices may have one or two cell signatures with a relatively high gray value while the middle and/or last image slices may have very few cell signatures as shown in Fig. 2.8(a). Thus increasing the average image intensity of the whole image slice increases the background intensity too, which is undesirable. The graph in Fig. 2.6, shows the average intensity of complete image slices plotted against depth. We have considered only those voxels that belong to a particular region of interest where the intensity compensation is necessary while avoiding the other regions such as background. The foreground (highlighted by locally high gray value or image intensity due to specific fluorescent material) of the image is considered as the region of interest in the present case. The variation of intensity along the depth in the background region is of little interest as we try to maintain the background at the lowest intensity in all the image slices of the stack. For this purpose the pixels belonging to the foreground are considered for enhancement.

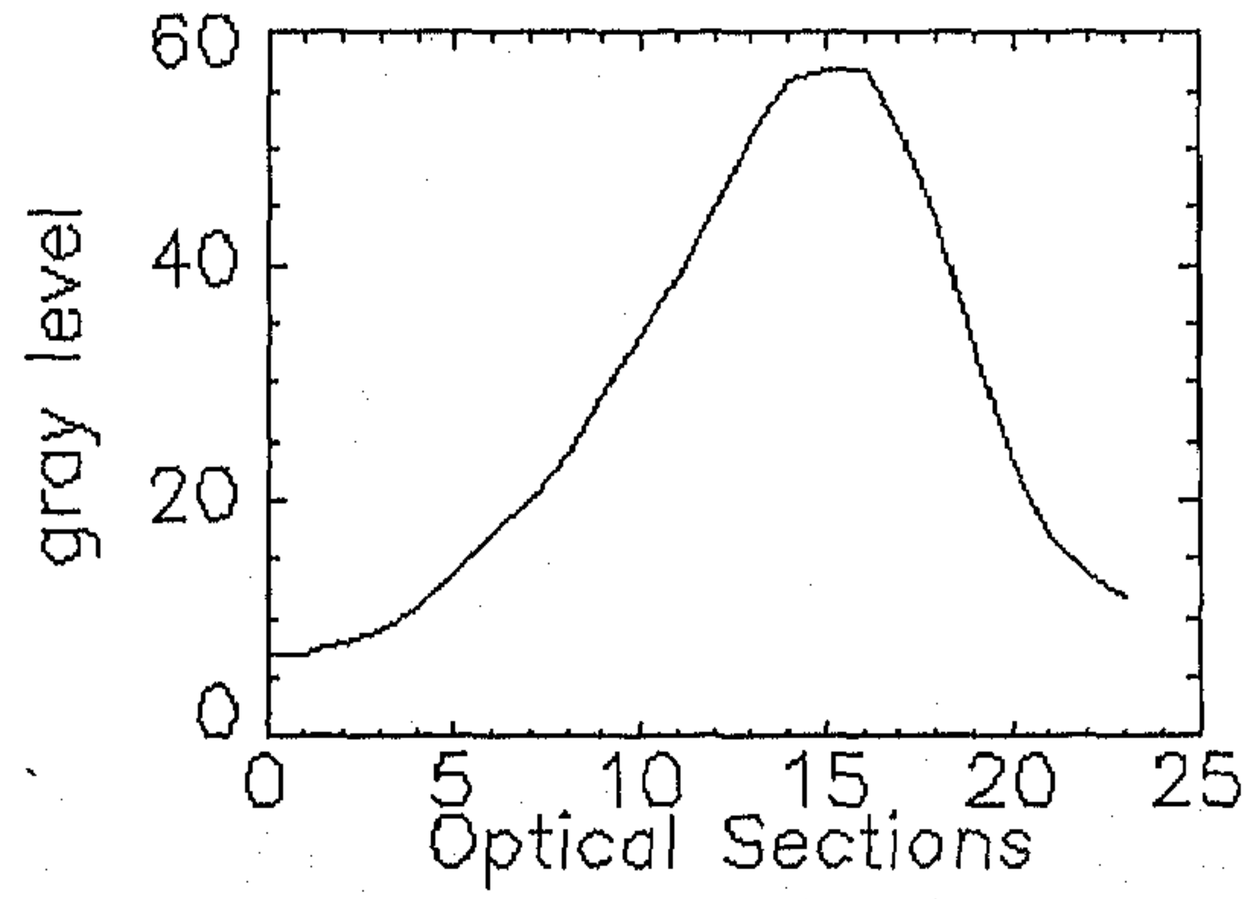

Fig. 2.6: Average image intensity against the depth of the image stack.

Direct Restoration: Let the mean intensities of the image slices 1, 2, ..., n, in the image stack be $\overline{I_1}, \overline{I_2}, \ldots, \overline{I_n}$. The variation in the average image intensity of the foreground pixels is plotted as shown in Fig. 2.7. The maximum average intensity of foreground of the image slices is considered as a reference image slice, i. e., if $\overline{I_i}$ is the average intensity of reference image slice, such that $\overline{I_i} \geq \overline{I_j}$ for all j, then, image slice i is considered as the reference image slice and $\overline{I_i}$ as the standard image intensity value.

The difference between the average intensity of image slices with the reference image slice is calculated. Let $\beta_k = \left|\overline{I_i} - \overline{I_k}\right|$, be the difference of average intensity of the foreground in k *th* image slice and the reference image slice i. Then for the k th image slice the gray level of each pixel of the foreground is enhanced by a factor $c\beta_k$ i.e., if $I(x, y, k)$ is the intensity of voxel at (x, y, k) then the enhanced intensity is given as $I(x, y, k) = I(x, y, k) + c\beta_k$ where c is an experimentally chosen constant. Ideally c should be 1. As stated earlier, this simple addition of the average value to the image intensity results in the loss of pixel sensitivity. A trade off optimizing the requirements of light intensity and loss of sensitivity is useful. This tradeoff is also imaging and application dependent. As the confocal microscopy images do not give clear details of the intra-cellular structures as well as our interest being limited to measure the quantitative features of cells and the tissue, we have ignored the pixel sensitivity issue.

Iterative Restoration: In this process every image slice is compared with the immediately next image slice in the stack. The difference of average intensity is calculated. If β_k is the difference of foreground image intensity of k th and $(k+1)$ th image slices, i.e. $\beta_k = \left|\overline{I_k} - \overline{I_{k+1}}\right|$, then the gray level of each pixel of the foreground of image slice k (if $\overline{I_k} < \overline{I_{(k+1)}}$) is increased by factor β_k and vice versa.

$$I(x, y, k) = I(x, y, k) + c \cdot \beta_k \quad ; \text{ if } \overline{I_k} < \overline{I_{k+1}}$$

$$I(x, y, k+1) = I(x, y, k+1) + c \cdot \beta_k \quad ; \text{ if } \overline{I_k} > \overline{I_{k+1}}$$

The process is carried out for all the image slices in the stack and is repeated till the average foreground image intensity of all the image slices is same. Practically, the iterative process is stopped when the difference between maximum intensity image slice and the minimum intensity image slice is less than a small threshold λ, i. e., the iterations are stopped if

$$\left|\max\left\{\overline{I_1}, \overline{I_2}, \ldots, \overline{I_n}\right\} - \min\left\{\overline{I_1}, \overline{I_2}, \ldots, \overline{I_n}\right\}\right| \leq \lambda$$

where λ is determined experimentally. Fig. 2.7, shows the graph of average image slice intensity against depth before and after intensity restoration. Fig. 2.8(a), shows the original image slices of a prostate tissue specimen. Fig. 2.8(b), shows the intensity restored image

slice. From this figure it is evident that enhancement of the foreground pixels to a maximum average intensity level reduces the effect of photobleaching as well as other optical problems.

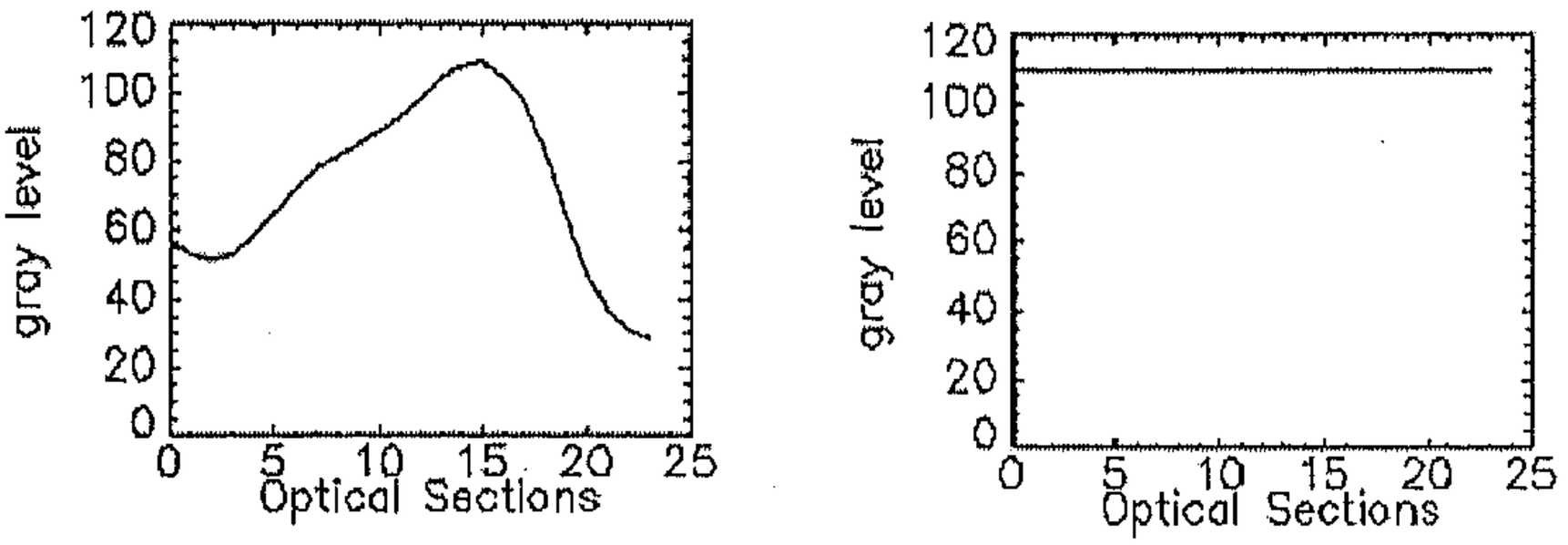

Fig. 2.7: Graph showing the average image intensity of the foreground against the depth for two specimen images. (a) Before Restoration (b) After Restoration

2.3.4 Morphological Opening and Closing

Morphological opening and closing of the 3-D image using a $3 \times 3 \times 3$ six connected structuring element results in removal of thin and frail connections between cells and also fills up the small holes in the foreground. The opening of image B by structuring element K is denoted by $B \circ K$ and defined by $B \circ K = (B \ominus K) \oplus K$. The closing of the image by sructuring element K is denoted by $B \bullet K = (B \oplus K) \ominus K$, where $\ominus$ is an erosion operator and $\oplus$ is a dilation operator.

Opening an image with the disc structuring element smooth the contour, breaks narrow isthmuses, and eliminates small island and sharp peaks or capes. Closing an image with a disc structuring element smooths the contours; fuses narrow breaks and long, thin gulfs; eliminates small holes; and fills gaps on the contours (Haralick and Shapiro, 1992). We have used a three dimensional $(3 \times 3 \times 3)$ six connected structuring element for opening and closing. The morphological operations has resulted in delinking of cells which are thinly connected, filling up of small holes as well as removal of isolated noisy voxels.

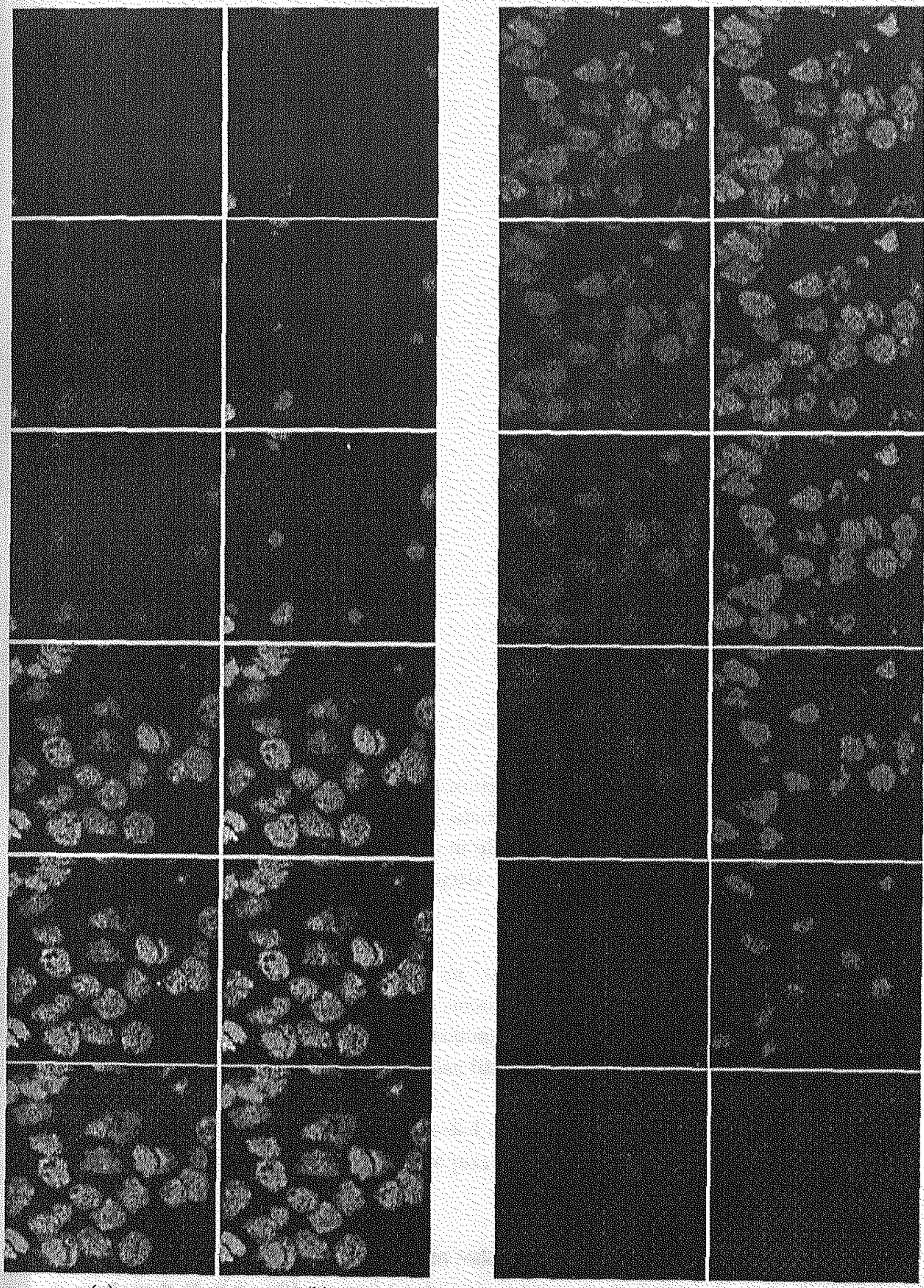

(a) (b) (a) (b)

Fig. 2.8: Image slices 1, 2, 3, 11,12, 13, 18, 19, 20, 21, 22, 23, of a stack of 24 image slices
(a) Before restoration (b) After restoration

2.3.5 Crispening

The next step in image enhancement is to crispen the cell surface. We have used the conventional process of adding a high pass signal to the image for this purpose. Let $u(x, y, z)$ is the input image and $g(x, y, z)$ is the gradient magnitude image, then the crispening process can be written as

$$v(x, y, z) = u(x, y, z) + \lambda \cdot g(x, y, z)$$

where $\lambda \geq 1$. We have used $\lambda = 1$ as the scale factor. Fig. 2.10(b) shows the result of surface crispening. Surface crispening process also enhances the noise intensity in the foreground. This is undesirable. One of the simple ways of reducing this is to subject the image stack to smoothing. The smoothing should be done in such a way that the edge sharpness of the desired objects is preserved while noisy interior is smoothed.

2.3.6 Smoothing

Roysam et al., (1995), have proposed unsupervised noise removal algorithms for 3-D confocal fluorescence microscopy. The main aim of the algorithms proposed by them is to limit any smoothing to the interiors of the object regions and hence avoid the blurring that is associated with the conventional methods. The method needs an initial input of underlying random process parameters. They have shown the result of their methods on neuron images. In case of histo-pathological images, the smoothing inside the object is necessary but the boundary of the object should be prevented from blurring due to smoothing.

The aim is to smooth the highly textural cell chromatin without causing any damage to the sharpness of the boundary features which is used for segmentation purpose. Also any human interaction is kept at minimum as our ultimate aim is to build a system which is more automatic and can be used by pathologists who do not have much training in image processing methods.

Simple spatial averaging blurs the cell boundary while smoothing. This is an undesirable effect. Symmetrical Gaussian smoothing blur the edges while smoothing, though the influence of far off voxels on the smoothing is reduced. To reduce the blurring effect on the edges, we have used directional Gaussian filtering.

A 5×5 Gaussian filter is sub-divided into six directional windows as shown in Fig. 2.9. The Gaussian convolved values of the pixels in each directional window is calculated as shown.

The maximum of the convolution values in all the directional windows gives the desired result. If $v(x, y; \theta)$ are calculated in several directions as,

$$v(x,y;\theta) = \frac{1}{N_\theta} \sum_{(m,n)\in W_\theta} \sum u(x,y) \cdot G(x-m, y-n)$$

where $G(x,y) = exp\left\{\frac{\left(x^2+y^2\right)}{2\sigma^2}\right\}$ is a Gaussian filter, N_θ is the total number of pixels present in the directional window W_θ as shown in Fig. 2.9.

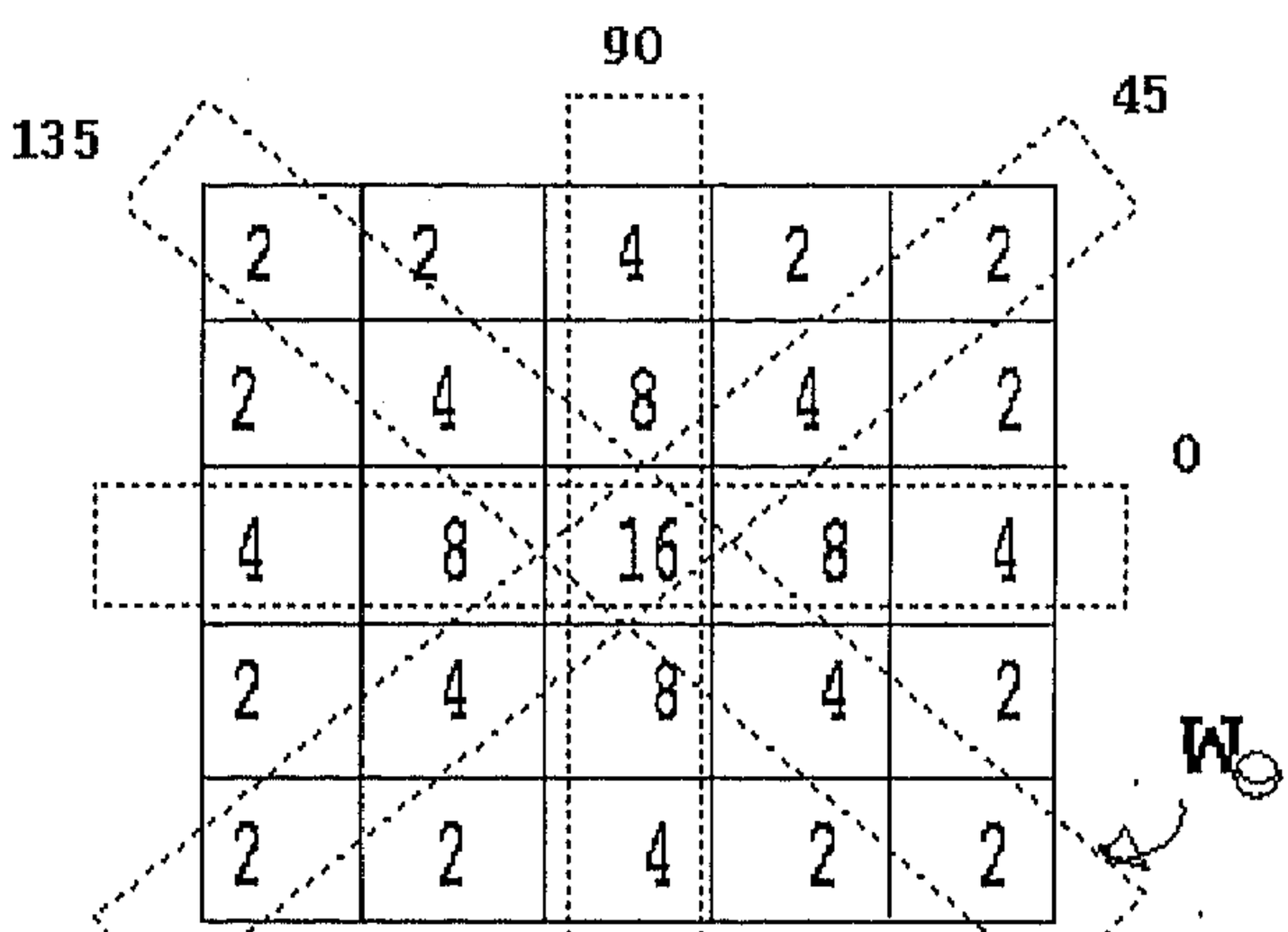

Fig. 2.9: Directional Gaussian weighted filter.

A direction θ^* is found such that $\left|u(x,y) - v\left(x,y;\theta^*\right)\right|$ is minimum. Then the output image

$$v(x,y) \Leftarrow v\left(x,y,\theta^*\right)$$

is the desired result. Directional Gaussian smoothing technique is applied seperately to all the image slices in the image stack.

Fig. 2.10(d) shows the result of directional Gaussian smoothing in comparison with a simple spatial averaging (Fig. 2.10(c)) to reduce the noisy peaks in the image while protecting the edges.

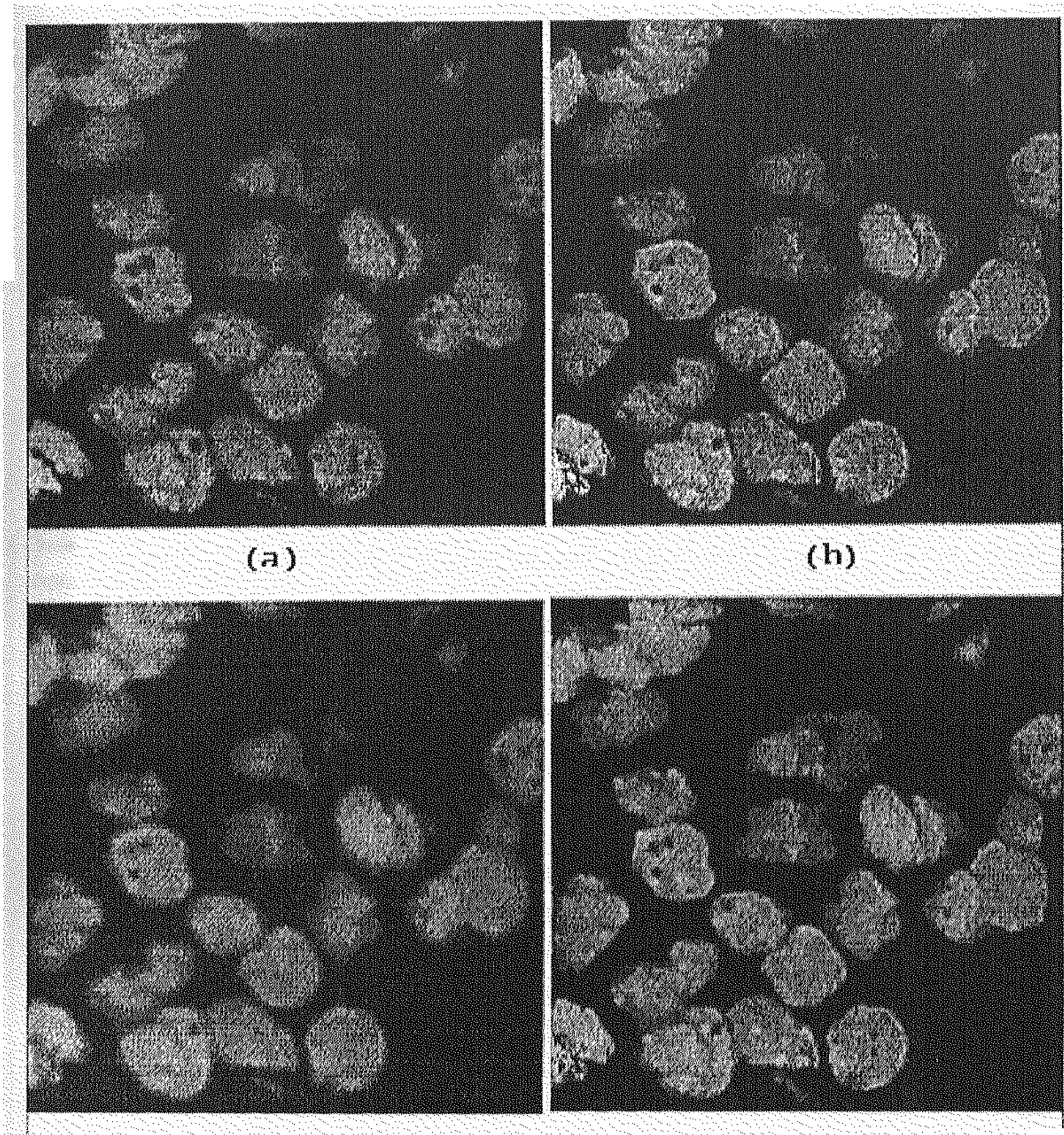

Fig. 2.10: Result of image enhancement steps shown on a representative image slice. (a) Intensity restored image slice (b) After crisping (c) Spatial avaeraging (d) Directional Gaussian smoothing

2.3.7 Enhancement of Axial Resolution

One of the important enhancement steps to be carried out is the improvement of axial resolution of the image stack. Poor resolution of the image stack leads to error in segmentation. Due to anisotropy in voxel lattice, the direct 3-D processing algorithms fail to properly make use of spatial neighborhood relations. To avoid these errors, and to enhance the qualitative and quantitative accuracy of visualization and analysis, a suitable interpolation process has to be used to increase the axial resolution of the stack. We have done this by virtually inserting the interpolated image slice in between the actual image slices in the stack.

Classical interpolation techniques fall into three categories : Contour based, intensity based and shape based interpolations.

Contour based interpolation (Boissonat, 1988) take a set of binary images containing cross sectional boundaries of the objects and generate a new set of interpolated binary sequence representing the surface of the objects. Since only the contours of the selected features are used in the interpolation process, critical intensity information would be lost. Intensity based interpolation takes the original voxel intensity values and generates a new set of interpolated voxel intensities. If there is a shape variation in the two source images, this method results in error. This is so because calculation of the interpolated value only takes a limited number of data points and produce wrong estimation when there is shape variation between two source images.

Shape based interpolation (Raya and Udupa, 1990) takes a set of binary images representing cross sections of objects segmented from the intensity-value data and performs morphological interpolation between shapes and contours. To avoid the errors due to contour based interpolation and intensity based interpolation, we have developed a method where the contours of the objects in the interpolated image slice is first obtained by logical operation over the source images and then using these contour pixels as the control points, the intensity of the pixels within the contour are calculated by morphing two source images. The process is explained below

Consider the two tone version of two neighboring image slices (source images) j and $(j+1)$ where the object is represented by gray level 1 and background by 0 as shown in Fig. 2.11. For creating a image slice in between j and $(j+1)$, we have to choose some control point in the interpolated image slice towards which the source images are distorted during morphing. It can be argued that if by some means we can get the overall boundary of the objects in the interpolated image slice, we can use these edge pixels as control points and fill the gray level within these boundary points using morphing or weighted averaging technique. The overall boundary of the objects in the interpolated image slice can be found by using simple logical operations as follows. The two tone version of the neighboring image slices j and $(j+1)$ are subject to pixel-to-pixel X-OR operation. The resulting image consists of the portion of the object which is common to the objects in both j and $(j+1)$ image slices. This is shown diagrammatically in Fig. 2.11. The medial axis of this image gives the boundary of the objects in the interpolated image slice.

If the objects in j and $(j+1)$ image slices are laterally shifted or there is a strong variation in shape of the objects between two source images then the resulting medial axis need not be continuous. To join the disconnected boundary, we have applied the following simple operation. The contours of the objects in the two source images are obtained over a two tone version of the source images j and $(j+1)$. The common portion of the boundary of the objects in j and $(j+1)$ image slices are obtained by pixel-to-pixel AND operation of the two boundary map of the source images. The result of the AND operation is added to the

medial axis of the interpolated image slice by logical OR operation. This results in linking the broken contour. The process is shown diagrammatically in Fig. 2.12. Fig. 2.13, shows the each interpolation step as applied to a pair of CLSM image slices.

To fill the intensity information within the boundary contour of interpolated image slice, the window-sliced version of source images j and $(j+1)$ are distorted towards the position of the contour based control points in the interpolated image slice. Then, the two deformed images are blended with simple weighted averaging to generate the gray value in interpolated image slice. Let $G_j = I_{j0}, I_{j1}, I_{j2}, \ldots, I_{jn}$ be the gray value of the object pixels in source image j and $G_{j+1} = I_{j0+1}, I_{j1+1}, I_{j2+1}, \ldots, I_{jn+1}$ are the gray value of the object pixels in source image $(j+1)$. Then, the gray value of corresponding object pixels in interpolated image slice is given as $\frac{w_1 G_1 + w_2 G_2}{2w}$ where w_1, w_2 and w are the constants which are calculated experimentally. In our experiment we have used all the weights as 1 that simplifies the method to simple averaging. For the pixels which fall outside the boundary contour in the interpolated image slice, the gray value is given as zero. Since most conspicuous features to human eyes in images occur at the places with higher gradient magnitudes, which are also where the contour or boundary point usually locates, using contours as control lines for morphing are very effective. Fig. 2.13(e) shows the result of interpolation by morphing between two images.

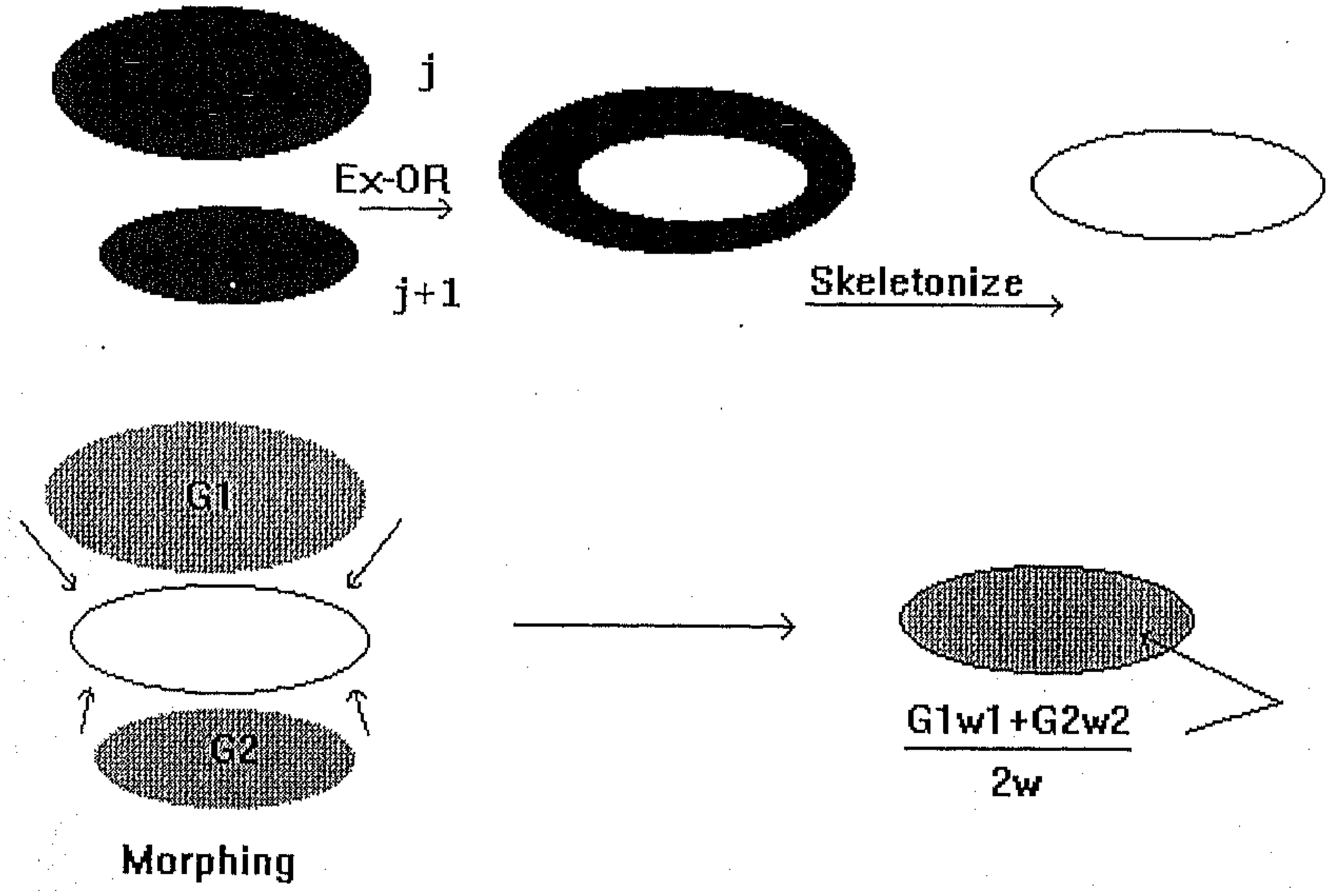

Fig. 2.11: Diagramatic representation of Interpolation by morphing

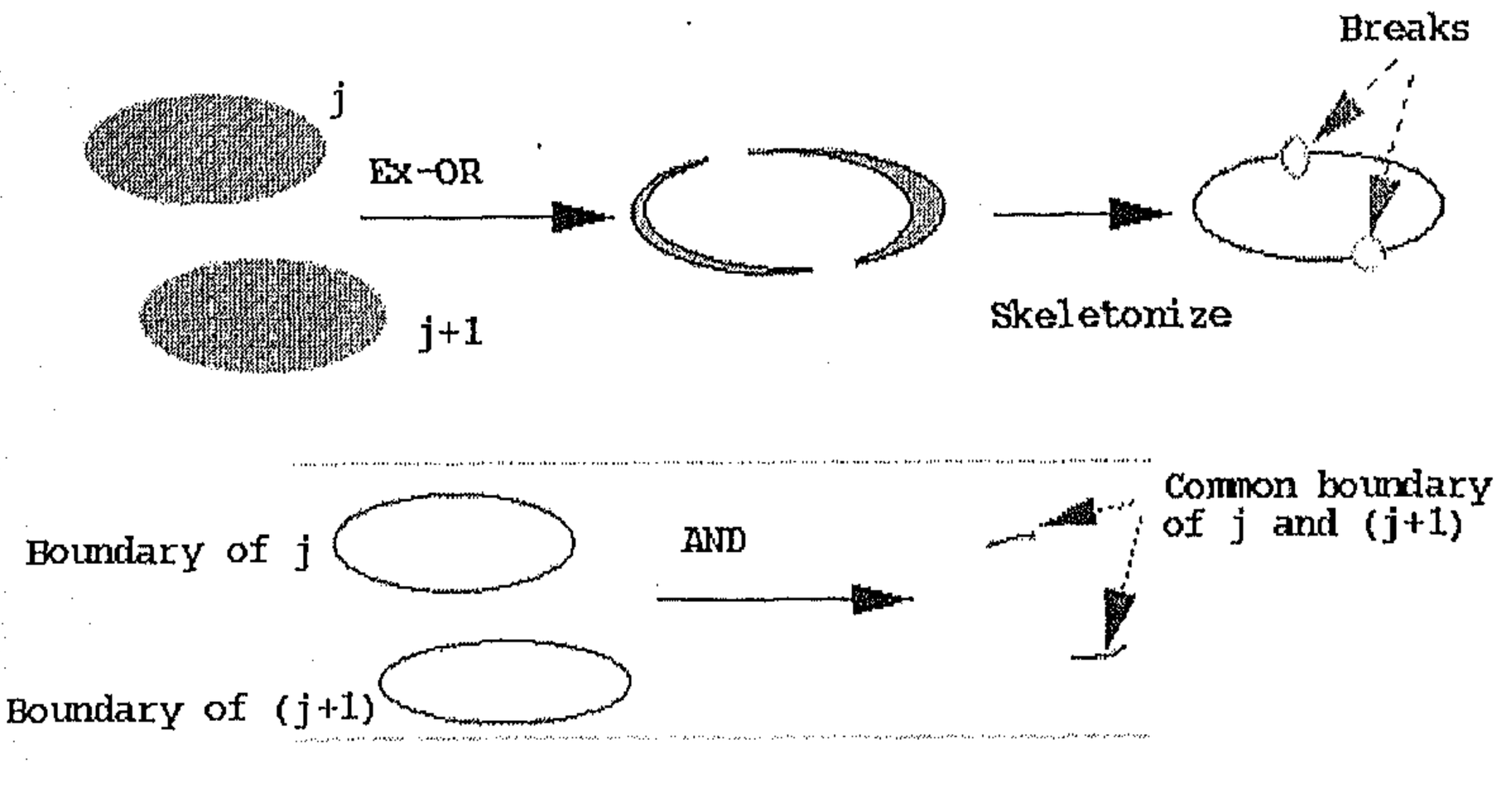

(b)

Fig. 2.12: Interpolation by morphing when the object shape in the source images are different or when they are laterally shifted.

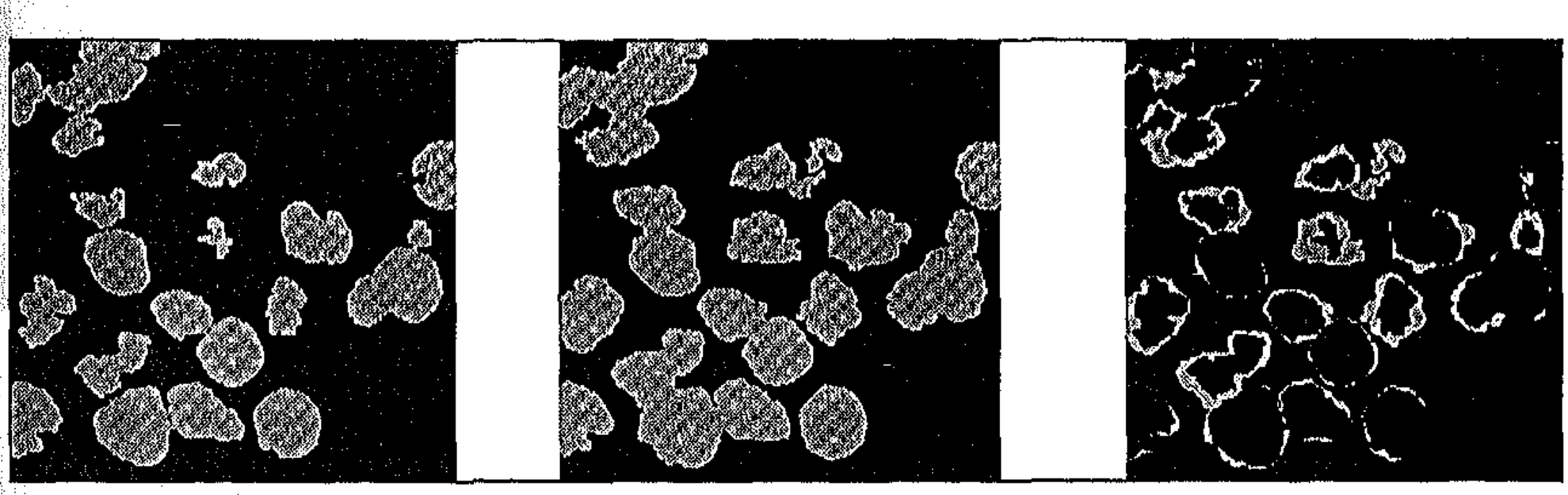

(a1) (a2) (a3)

Fig. 2.13(a): Two-tone version of the source image slices are subject to X-OR operation (a1) , (a2) Two-tone version of source image 1, source image 2, (a3) After X-OR operation

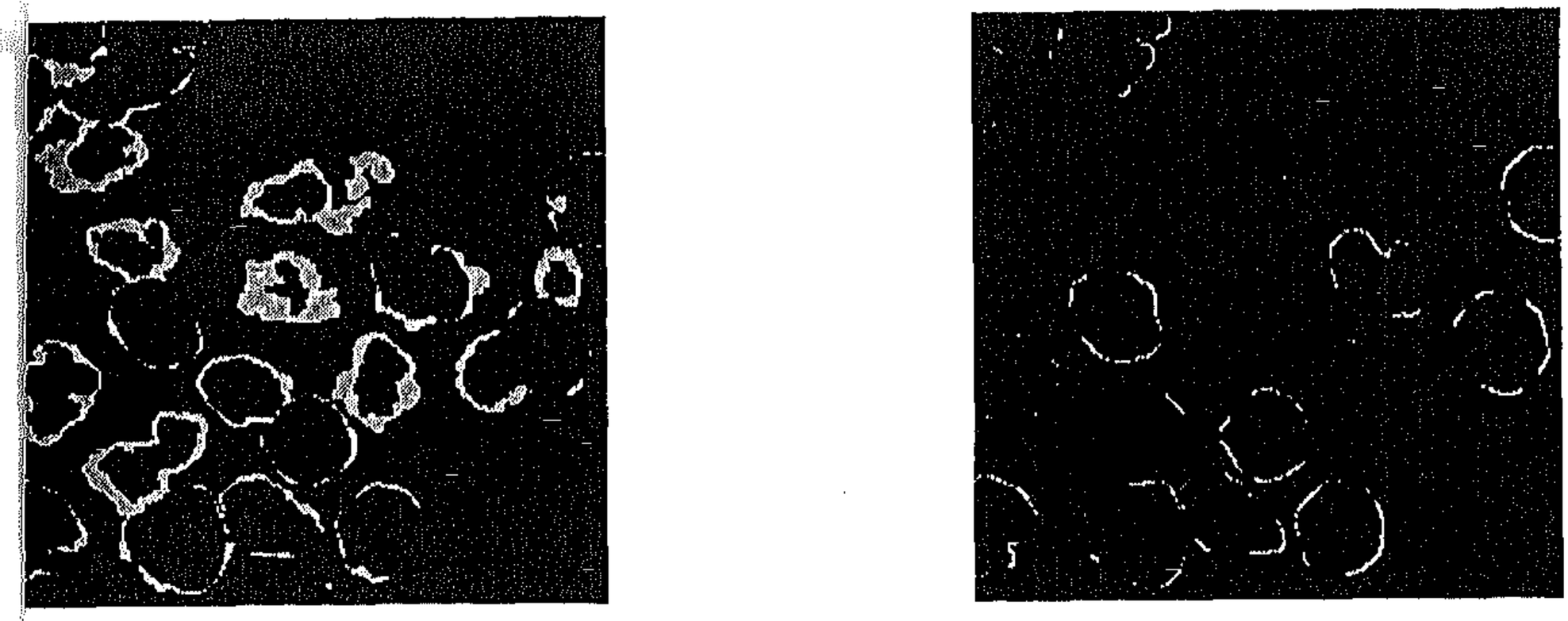

(b1) (b2)

Fig. 2.13(b): After skeletonization of the image in Fig. 2.13(a3)

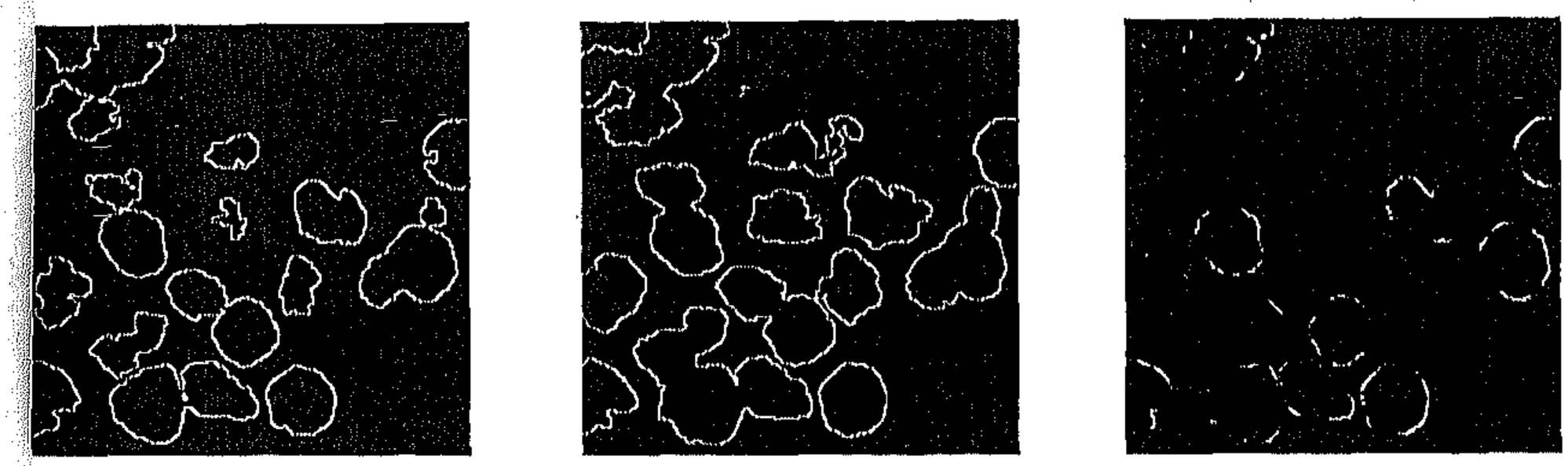

(c1) (c2) (c3)

Fig. 2.13(c) : Result of X-OR operation on the boundary of the source images
(c1), (c2): Boundary of source images, (c3) Result of ANDing (c1) and (c2)

(d1) (d2) (d3)

Fig. 2.13(d): Result of linking the broken contours , (d1): Same as Fig. 2.13(c1), (d2): Same as Fig. 2.13(c3), (d3): Complete contour in the interpolated image slice = (d1) X-OR (d2)

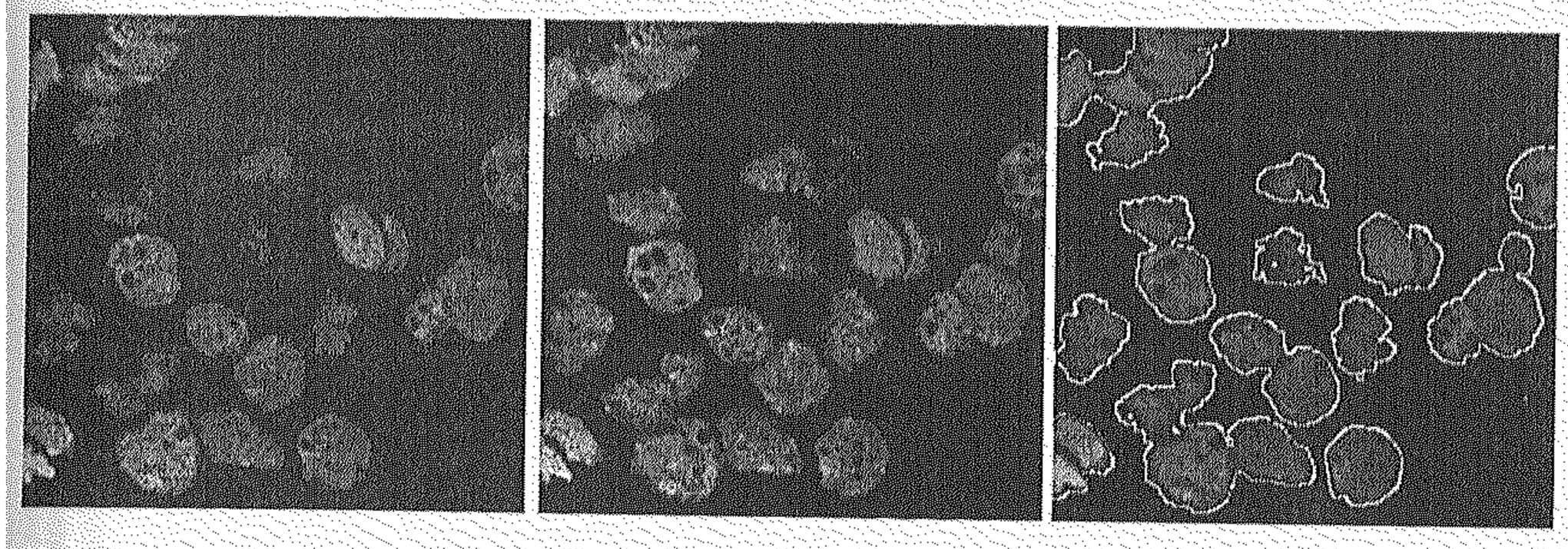

(e1) (e2) (e3)

Fig. 2.13(e): Two source images (e1) and (e2) , (e3) Result of morphing

Fig. 2.13: Result of each step in interpolation by morphing as applied to two representative image slices

2.4 Discussion

In this chapter we have discussed (a) the working principle of the CLSM (b) the reasons for degradation in image quality and (c) the effect of various optical and electronic components of the microscope system on the image quality. Though this is by no means a complete study, which is not the aim of this thesis, we believe that this study gives a necessary introduction to the confocal microscopy and the challenges ahead to build an image analysis system. The specimen preparation method and the image acquisition setup features are given briefly. Though we believe that the system should work on all 3-D histo-pathological images, we have not tested it on the images obtained under different setup features as well as by different specimen preparation methods. We have tried our best to make the system image independent. We have tested this by applying the same system to work on the quantitative analysis of filamentous bacteria in industrial sludge. The results obtained are encouraging.

Often the noise present in the image appears to be image dependent as it comes from specimen preparation faults, photo damage, faults in the image acquisition system while acquiring a particular data set, etc.. Major source of artifacts is the specimen preparation. It is true that there is nothing called ideal specimen. Preparing a specimen to acquire a stack of optical sections is a tedious task which requires scientific precision to preserve the cellularity and architecture of the tissue from falling apart.

Sometimes we may have to use many of the conventional image processing filters such as hybrid median, olympic, etc., to reduce the noise and properly smooth the image. Though the computer programs for doing these conventional filtering are made available in Graphical User Interface (GUI) we have built, they are kept as optional for use. We have also implemented some other noise reduction filters and enhancement methods which can be used if and when required. Processing steps such as window slicing, size & shape filters,

directional Gaussian, edge enhancement, reducing the attenuation along the depth and improving the axial resolution are done on all the image data sets. Chapter 5 explains some of the noise reduction methods used to segment and identify FISH signals in a signal channel of the multi-spectral image. In chapter 6 we have briefly discussed the influence of noise reduction and image enhancement steps over the measurement of pathologically important feature values.

Chapter 3
Edge Based Segmentation

3.1 Introduction

Segmentation is a key to the success of most of the image understanding systems. Many segmentation techniques exist in the literature but none can be applied satisfactorily on all real and synthetic images. If there is a single object with a distinct and uniform background, segmentation turns out to be trivial. In medical image analysis, segmentation is one of the most difficult problems.

There are two stages in segmenting the histo-pathological images. In the first stage, the region containing cells is segmented from the background. This gives the overall boundary of the objects of interest. In the second stage each individual cell is separated from the others, so that cell level features can be computed.

When the 3-D image is generated as a stack of 2-D image slices, we can segment the image stack by two approaches. One approach is to apply the 2-D algorithms on each image-slice and pool the results together. The other approach is a direct 3-D approach. The interactive techniques used commonly in 2-D processing are too tedious to be applicable to many 2-D image-slices, which constitutes each 3-D image. In images where the cells are well isolated and the background variation is less, segmentation can be achieved by thresholding and labeling (Kohler, 1981; Lee et al., 1990, Sahoo et al., 1988).

Existing image segmentation algorithms can be divided into two broad classes. The first class attempts to build regions in the image based on the similarities of some characteristics (or features) of the picture elements. The second class of algorithms locates those edges in the image, which correspond to object boundary or surface discontinuities based on pixel intensity gradient. In this chapter we mainly deal with edge based image segmentation.

Edges are one of the most important properties of objects in an image as they correspond to object boundaries or changes in surface orientation or material properties (Binford, 1981; Brady, 1982; Torre and Paggio, 1986). The edge based segmentation methods search for the gradient peaks featuring the cell surface. The search for these gradient peaks can be done using simple edge detectors such as Sobel operator (Sobel, 1970), Laplacian of a Gaussian (LoG) operator (Marr and Hilderth, 1980) or Canny operator (Canny, 1986), where no prior information is provided about the possible location of the surface of the objects. Every gradient peak within certain threshold is considered as a possible candidate for representing the surface of the cells. It is well known that the result of these edge detectors is a large number of edgels and a discontinuous cell boundary. Some of the edge operators also produce double edges in many cases. To obtain complete segmentation, several problems such as elimination of noisy edgels, reconstruction of the continuous boundary, elimination of double edges, etc., have to be solved. Heath et al., (1998), have done an elaborate qualitative

comparison of the edge detectors on some real life images. The quantitative comparison of these edge detectors can be found in Fram and Deutch (1975), Chaudhuri and Datta Majumdar (1993), etc.. There are, in fact, very few attempts to compare the performance of the edge detectors. We still evaluate the performance of the edge detectors by looking at the results (Jain and Binford, 1991).

The choice of a particular segmentation method depends on factors such as efficacy of the segmented results, how accurately features can be measured from the segmented results as well as the complexity involved in the design and implementation of algorithms (Garbay, 1986). In a study by Abmayer et al., (1980), it has been observed that over 40% of the free-lying cells have been rejected because of the discontinuous boundary of the cells detected by gradient operators. Bengtsson et al., (1979), and Nordin et al (1982), have described high-resolution segmentation of the cells based on the Fourier expansion of the cell contour and the associated problems. To some extent they also discuss the problem of cell overlap detection. A study on application of these edge detectors to mark the boundary of cells in histo-pathological images can be found in (Garbay , 1986, 1982; Chassery and Garbay, 1983). Some of the 3-D segmentation techniques for real life images are described in Acharya (1987). Many new boundary-finding algorithms based on either boundary/surface modeling or on some form of iterative refinement of the possible edges, have been published in the recent times. To name a few, boundary estimation by stochastic modeling (Cooper et. al., 1981), maximum likelihood edge estimation, segmentation and tracking of cell movement (Laymerie and Levine, 1993), multiscale edge detection (Ziou and Tabbone, 1993), multi-resolution image segmentation (Park et al., 1995), detection of cell boundary by snakes (Bamford and Lovell, 1998), etc.. With all these efforts, segmentation of cells in a tissue image is still a open problem. There is no single global segmentation algorithm, which can be used for segmenting cells in all types of histo-pathological images.

In this chapter, we have presented semi-automatic edge based segmentation methods to draw the boundary of the cells. These methods are (1) layered segmentation (2) active contour/surface model for cell segmentation. All the segmentation methods are applied on the noise reduced and feature enhanced images. Noise reduction and feature enhancement methods were explained in chapter 2. This chapter also includes a subjective evaluation of different edge based segmentation methods on various histo-pathological data sets. A quantitative study of different methods based on the accuracy in marking correct edges is also given in comparison with interactively marked cell surface.

3.2 Layered Segmentation Method

This is a semi-automatic segmentation technique. In this method, one of the image slices in the image stack is considered as a representative image. In this image, touching and overlapping cell boundary pixels are marked interactively while remaining part of the cell boundary is obtained by finding the pixels having atleast one background pixel in their neighborhood. Overall boundary of the cell cluster can also be obtained by applying any of the simple edge detectors on the window-sliced and enhanced image stack. The interactively traced portion of the cell boundary is considered as initial reference contour for finding the

overlapping and touching cell boundary in its neighboring image slices. Here we assume that the boundary of the same 3-D cell signature in the neighboring image slices is very close to each other. The assumption holds good due to the high resolution of the confocal images and the near isotropic voxel lattice obtained by interpolation.

3.2.1 Representative Image: Selection and Segmentation

One image slice from the middle of the enhanced image stack that represents maximum number of cell signatures in the image domain, is chosen as the representative image (RI). In case we are interested in segmenting only one cell from the cluster, an image slice where the cell signature is approximately maximum in size is chosen as the RI. Fig. 3.1(a), shows a representative image chosen from one of the data sets. The overall boundary of the cell cluster is marked by simply finding those voxels belonging to foreground which have at least one background voxel in its immediate eight neighborhood. Fig. 3.1(b), shows the overall boundary of the cell cluster thus marked in a representative image slice. The part of the cell boundary where the cells are touching each other or overlapping, is marked interactively using a mouse driven software. The segmented representative image forms the basis for the automatic segmentation of the cells in the remaining image slices of the image stack. Fig. 3.1(c), shows the representative image slice before and after interactive segmentation for an experimental data set. This representative image slice guides the marking of cell boundary in its neighboring image slices.

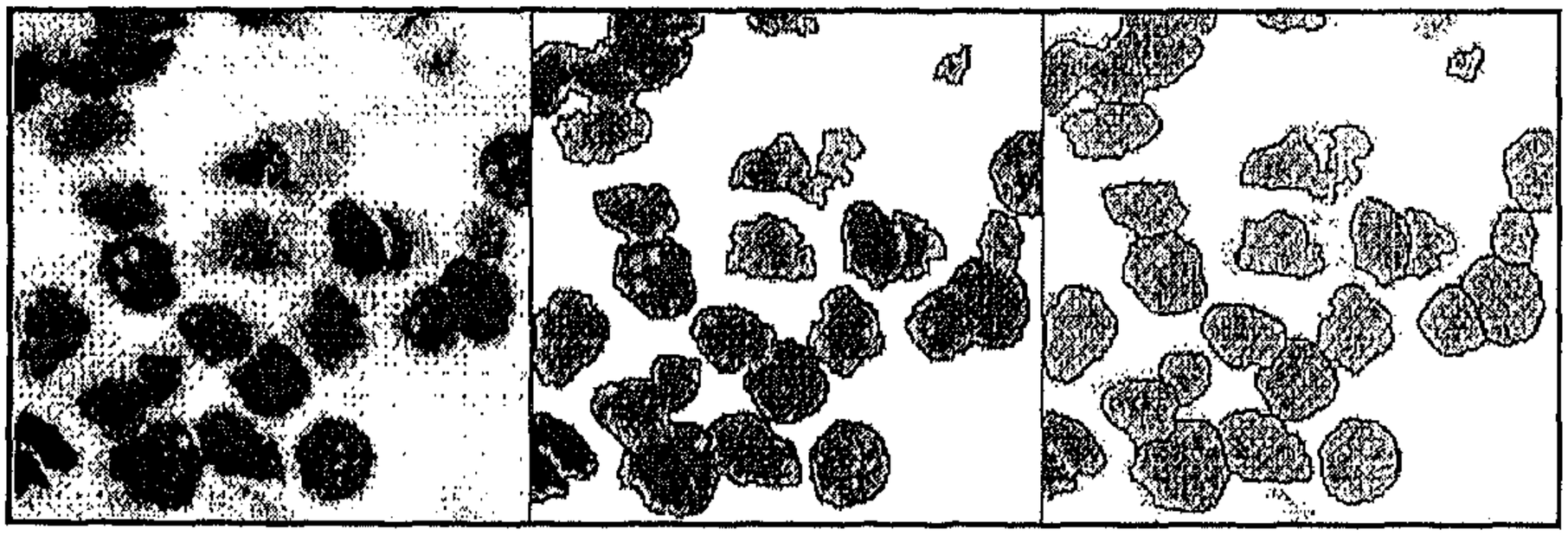

Fig. 3.1: Representative image segmentation (a) Original (b) before interactive segmentation (c) after complete marking of the boundary.

In the layered segmentation approach, we virtually superimpose the boundary of the previously segmented image slice to its neighboring image slice. This virtual boundary forms the initial boundary location of the cells in the current image slice. A small neighborhood of virtual boundary pixels along the normal vector of the initial locations is searched for finding the actual boundary pixel.

There are two methods for searching the pixels along its normal vector namely *Basic line search* and *Stratified line search* (Lai, 1996; Amini et. al., 1990). For each pixel in the

initial boundary v_i where, i= 0, 1, 2,...., basic search technique restricts the search in the region $\Theta = \bigcup_{i=1}^{n} \Theta_i$ where Θ_i contains voxels on the normal vector h_i,

$$\Theta_i = \left\{ v_i = \overline{v_i} + k \cdot h_i; \quad k = -\frac{(m-1)}{2},\ldots,-1,0,1,\ldots,+\frac{(m+1)}{2} \right\}$$

assuming that m is odd without the loss of generality. In our case we have used m = 1 i.e. the search region of each pixel in every stage considers only three pixels along the normal vector.

The computational complexity of an exhaustive search for n number of pixels in the neighborhood of size m will be $O(m^n)$. In the basic line search method, the search region is decomposed into n independent stages, where each stage considers only p neighboring points making the computational complexity to be $O(nm^p)$. In the basic line search we have adopted p=1 and hence the computational complexity of basic line search is $O(nm^3)$. When the cell shape deviates considerably, from one image slice to another, initialization by axial propagation will be poor, and search region defined by m may not encompass an actual edge pixel. Increasing m increases the computational complexity. In such cases, we have to increase the total search region and adopt stratified search technique to quickly arrive at near optimal position. The stratified search technique breaks the search region Θ_i into disjoint segments of length l, $\Theta_i = \bigcup_{j=1}^{\frac{m}{l}} \Theta_{ij}$ where,

$$\Theta_{ij} = \left\{ v_i = \overline{v_i} + (lj + k) \cdot h_i; \quad k = -\frac{(l-1)}{2},\ldots,-1,0,1,\ldots,+\frac{(l+1)}{2} \right\}$$

assuming l is odd. This results in the reduced computational complexity of $O(nm^3/l^2)$.

Once the small region containing the optimum edge pixel is found, then basic line search strategy can be applied to select the most appropriate edge pixel within the region. We have applied the stratified line search only if the actual edgel is not found within the small window defined along the normal vectors of the virtual edge location. The actual edge locations are believed to be characterized by a zero crossing in the second derivative and a high gradient value above certain threshold as its first derivative. The threshold is chosen experimentally.

3.2.2 Implementation

The implementation of the layered segmentation method can be described in few steps. In the first step, the boundary information from the i th image slice is virtually superposed on (i+1) th image slice. This is diagramatically shown in Fig. 3.2. Fig 3.2 (a), is the i th segmented image slice while Fig. 3.2(b) shows the $(i+1)$ th image slice. Fig. 3.2 (c) shows the virtual superposition of i th image slice on $(i+1)$ th image slice.

Let E_1 represent the set of edge pixels (edgels belonging to the overall boundary) of $(i+1)$ th image obtained by simple search of neighborhood for background voxel. Let the superposed boundary pixels be represented by the set E_2 .

In the second step, the neighborhood of pixels in E_2 is searched along the normal vector. If a pixel of E_1 is within a small neighborhood Θ (= 1 x 5) along the normal vector of E_2 then that pixel is removed from the set E_2. Let E_3 be the set of remaining pixels in E_2.

In the third step, the pixels of the set E_3 are considered as the initial edge pixel position for the boundary search in current image slice. The gradient magnitude of the pixels along the normal vector of the pixels of E_3, within the specified region Θ, is calculated. The pixel position whose second derivative corresponds to zero crossing and the first derivative shows a maximum local gradient magnitude and is above a pre-defined threshold, is considered as the actual boundary pixel. When all the neighborhoods Θ_i corresponding to the voxels of E_3 are treated, the processing of $(i+1)$ th image is complete. Processing of $(i-1)$ th image is done in a similar way.

Fig. 3.2(d) shows the portion of initial location the boundary pixels belonging to overlapped and/or touching portion of the cells. Fig. 3.2(e) shows the result of layered segmentation forming complete boundary of the cells in $(i+1)$ th image slice. The pixel level search technique at different directions is shown in Fig. 3.3. The arrows denote the direction of search which is along the normal vector of the initial pixel position (shown as dark pixels in Fig. 3.3) in a window. The boundaries of the newly segmented image slices are used to segment their neighboring image slices respectively. Fig. 3.4, shows the result of layered segmentation over a CLSM image stack. Fig. 3.4(a) are the original image slices, Fig. 3.4(b) are the results of overall edge detection and Fig. 3.4(c) is the result of layered segmentation.

When we move from one image slice to another, we may come across some new cells. If a new cell signature appears while processing, appearance of the new cell is suspected. If next two slices support the evidence then the appearance of a new cell is confirmed. Otherwise, the signature is rejected as an artifact. The boundary of such a new cell is automatically taken care of during the marking of overall boundary of the cell cluster.

The final boundary of the cell nuclei is overlaid on the original data set to isolate the cells. The resulting volumetric image is subject to 3-D component labeling. The 3-D component labeling is done as follows. The image slices are scanned slice by slice in a raster pattern. When an object voxel is found, a unique label is assigned to all the twenty-six connected voxels in the image stack within the boundary of the corresponding object. Scanning is continued from the position where it was previously stopped, till a voxel belonging to a new unlabeled cell is encountered. The whole process is continued till all the cells are labeled. This kind of component labeling can be successful only if the boundary of the cell signatures in each image slice when pooled together forms a closed surface around the

cell of interest. In the present case, since the axial resolution of the image stack is very high and the voxel lattice is made almost isotropic by interpolation, the boundary contour of the cells in each image slice when considered together, forms a continuous surface. Fig. 3.6(b) and Fig. 3.6(c), shows number of cells segmented and uniquely labeled before and after layered segmentation of the image stack. This result is shown on a different image data.

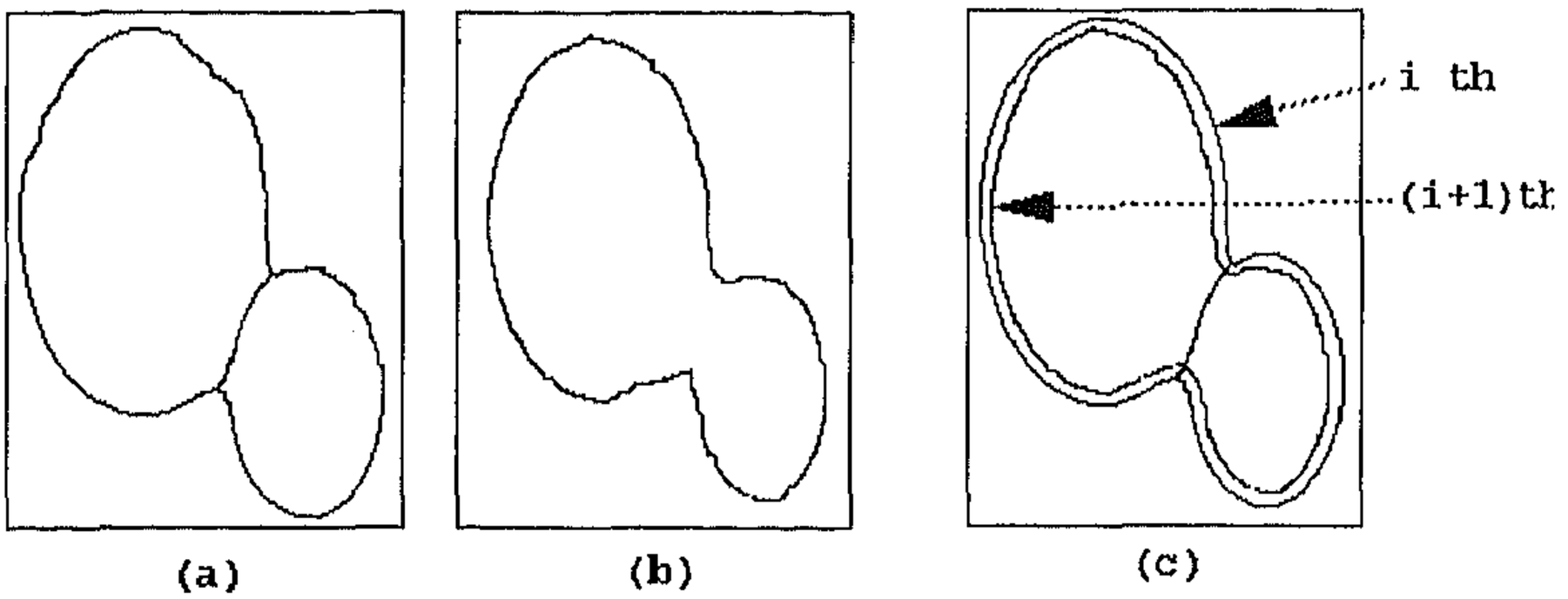

Fig. 3.2: Process of search in layered segmentation. (a) Segmented i th image slice with clearly marked boundary, (b) $(i+1)$ th image with overall boundary, (c) After super imposing the boundary of i th image on $(i+1)$ th image slice, (d) A small region around the initial location of the boundary where the cells touch or overlap, (e) After marking the proper boundary where the cells touch or overlap.

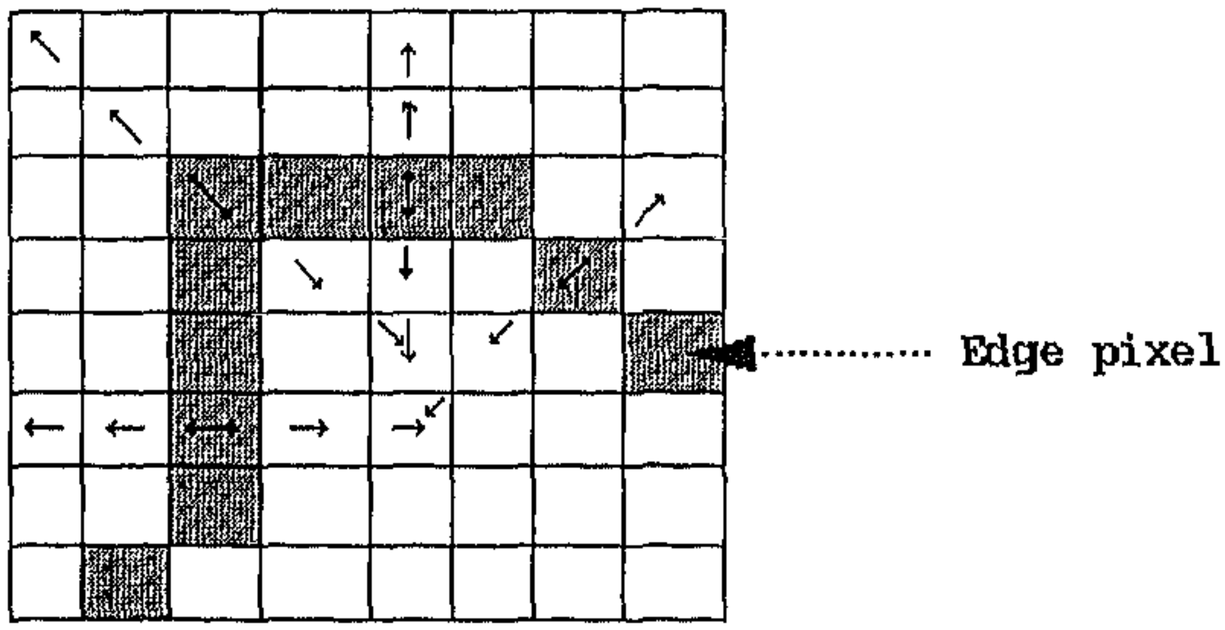

(f)

Fig. 3.3: Pixel level search

3.2.3 Deletion of Unwanted Cell Nucleus

The unwanted cells are those which are not completely represented in the image stack. Cells that appear at the border of the image stack are usually not complete i. e. truncated. To remove such cell nuclei, the first and last image slice in the image stack are first considered. If these image slices show any signature of the cell nuclei then the size of the signature is calculated. If this size is above a pre-defined size threshold, it shows a lateral truncation of the nuclei. The size threshold is chosen experimentally. In our case we have chosen size threshold as 625 voxels (25 × 25 pixel area). The cells having a signature bigger than 625 voxels in the first and/or last image slices, or in the first and/or last columns of all the image slices taken together, or first and/or last row of all the image slices taken together, is deleted from the segmented image volume. Also the cells which are of no interest to pathologist are deleted by clicking on such a cell and reading the corresponding label. The resulting image is subjected to 3-D re-labeling, and all the cells are labeled sequentially. Fig. 3.5(d) shows a result after deletion of the unwanted cell nuclei.

The boundary contour of the cells marked by this method may still be erroneous as the major part of it is decided by window-slicing followed by searching method and the search technique does not impose any smoothness or continuity criteria. The near blind marking of the high gradient pixel within the search region may result in unavoidable zigzag boundary as well as discontinuities. These errors have to be reduced using post-processing techniques such as smoothing and edge linking.

Layered segmentation is useful only when the cell shape do not deviate much from one image slice to another. In case of large deviation in the cell shape from one image slice to another or when the axial resolution of the image stack is poor or when there is a large lateral shift in the cell signature position in consecutive image slices, layered segmentation fails to give the good results. This is because the search region becomes too large resulting in more computational complexity.

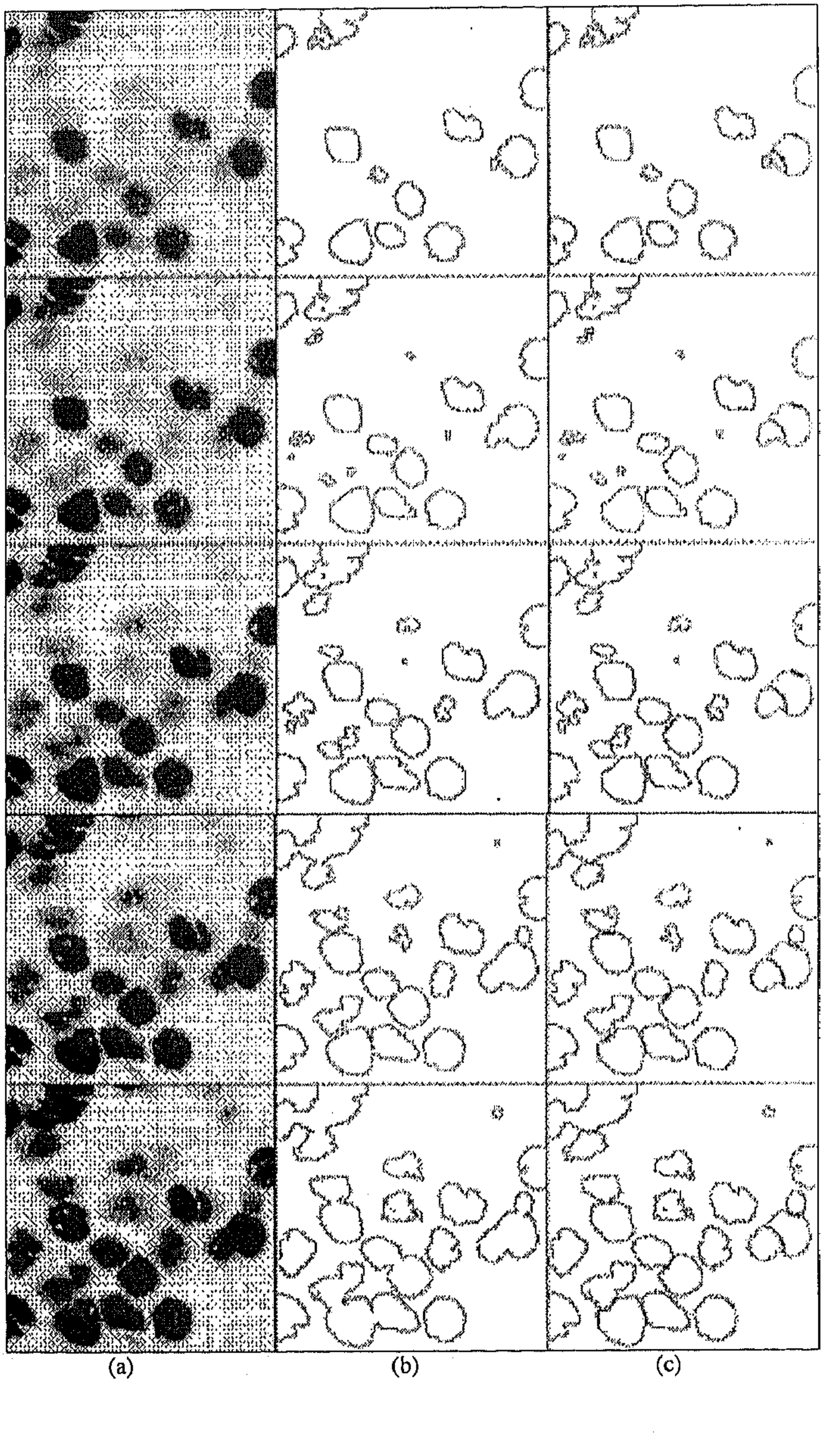

(a) (b) (c)

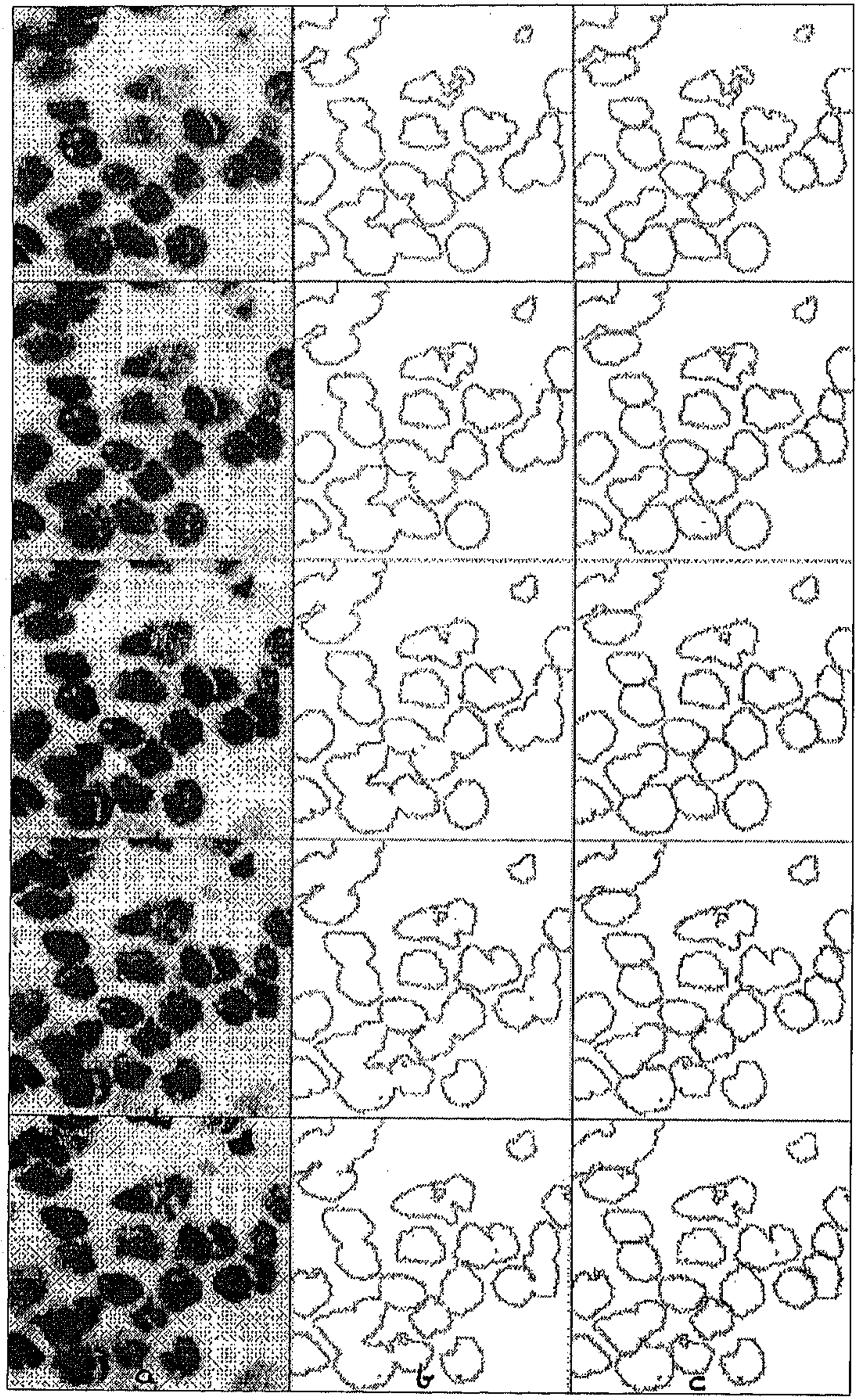

Fig. 3.4: Results of layered segmentation (a) Original image slices (b) Results of overall boundary marking by LoG operation (c) Result after layered segmentation.

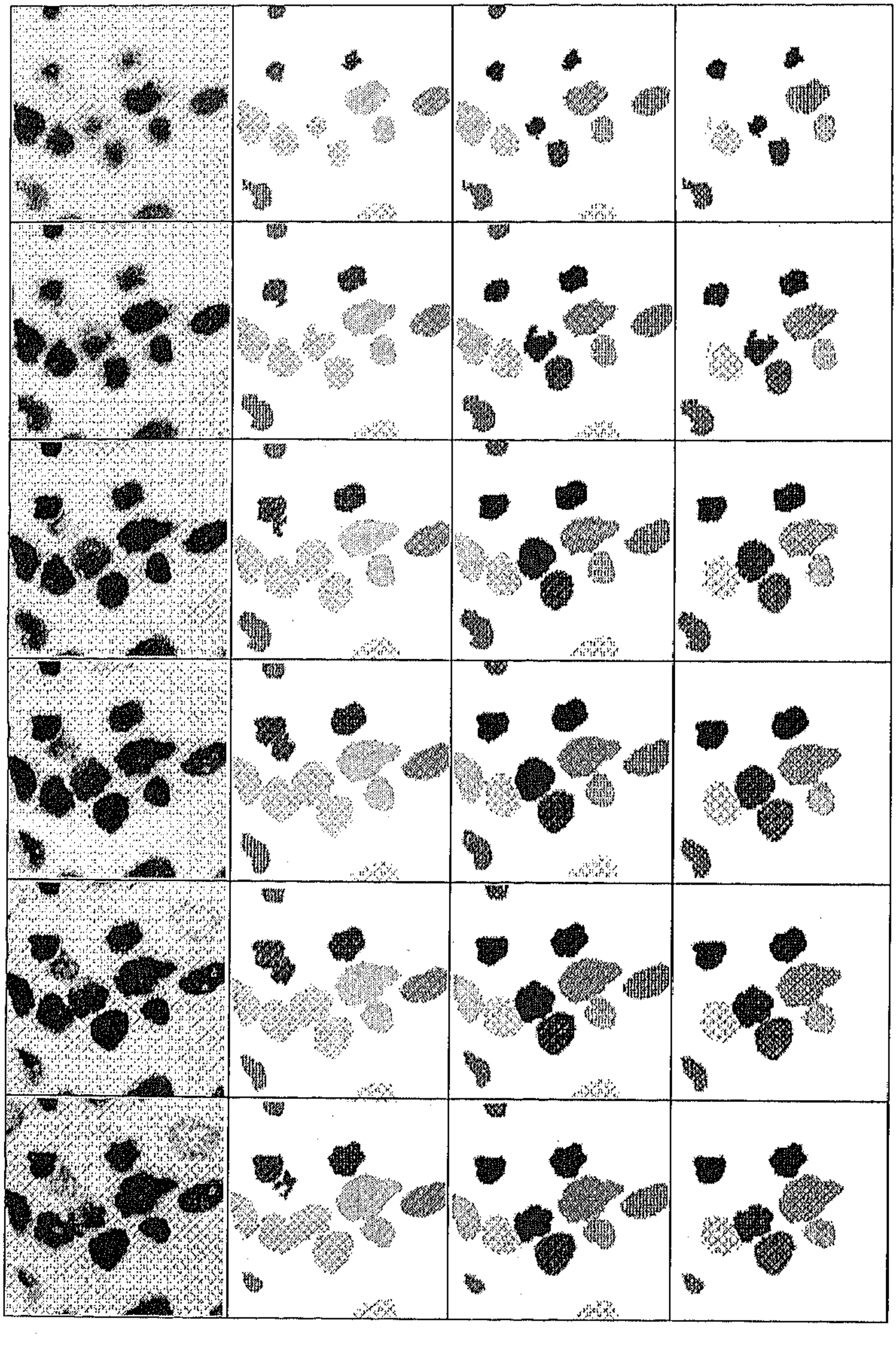

(a) (b) (c) (d)

Fig. 3.5: (a) Original Sequence of Image Slices (b) Result of LoG operation and labeling (c) After layered segmentation and labeling (d) After deletion of unwanted nuclei.

The layered segmentation technique is sensitive to noise as it blindly chooses the pixel lying within the search region and having satisfied the gradient threshold, as actual edge pixel. Often the resulting boundary between the touching and overlapping cells are zigzag in nature or may be discontinuous also. This needs post-processing steps such as edge linking and smoothing to get a proper segmentation results. But, for most of the data sets where the cells are thinly touching each other, the layered process gives an acceptable result. The segmentation obtained by layered process may not give accurate shape features as major part of the boundary is obtained by simple window-slicing and neighborhood finding process. The effect of layered segmentation process on the cell feature measurement is discussed in chapter 6.

Once we have the initial boundary contour that gives the possibility of actual cell surface being within the small region, application of active contour models can also be considered for marking the smooth and continuous cell boundary resulting in the segmentation of the cells. The advantage of the active contour models is that it maintains smoothness and continuity of the contour.

3.3 Segmentation by Active Models

An active model is a deformable curve or surface, which is composed of elastic materials. The deformation in the size and shape of the active model is forced by energy-minimization process. The internal forces due to elastic nature of the active surface or contour model impose smoothness and continuity during deformation while the external forces direct the deformation of the model towards the desired feature. In this approach, a contour or surface model is initialized near the surface of the cell either interactively or otherwise. Contours are used in 2-D plane-by-plane approach while the surface model is used in direct 3-D processing.

The internal energy of an active model consists of elastic energy (given by the first derivative of the active model's pixel location) and bending energy (second derivative of the active model's pixel location). The external energy consists of energy due to external forces derived from the image properties such as pixel intensity, gradient, distance value of the active model's pixel location, etc.. The contour/surface model deforms and moves under the influence of these energies and converge to the optimum cell surface where, the internal energy of the contour balances with the external energy i.e. the total potential energy associated with the model becomes minimum. The active models used in a 2-D approach is known as active contour models or snakes and in direct 3-D processing, it is known as active surfaces, or deformable models.

The active model approach was first introduced by Kass et al. (1988), as a regularization approach to the ill-posed edge detection problem. Several improvements and modifications were proposed to this basic approach in the subsequent years. Some of the notable works in this field can be seen in the papers by Cohen and Cohen (1993), Naster and Ayache (1993), Fua and Brechbuhler (1997), etc.. Application of the active contour models

for accurately marking the boundary of the isolated cells in the 2-D tissue images can be found in papers by Leymarie and Levine (1993), Bamford and Lovell (1998), etc..

Active models can be broadly classified into two types namely free-form and parametric. The free-form active models have no global structure of the template. The initialized model is constrained only by local continuity, smoothness constraints and external forces. The free-form active models can represent arbitrary shapes as long as the continuity and smoothness constraints are satisfied. The parametric model needs some information of the geometric shape, which can be encoded using a small number of parameters. The active model application discussed in this chapter is a free-form type.

There are two methods of using the active models to segment the cells in volumetric images. Active contour models or snakes can be used to mark the cell boundary in each image slice. This constitutes 2-D plane-by-plane approach. The resulting boundary of the cell signatures in each image slice can be used to construct the surface of the cells. In the direct 3-D approach, a geometric shape model that is similar to the shape of the cell, such as ellipsoid surface, is used as initial active model. The surface of the ellipsoid is made to deform under the influence of image forces and take the form of cell surface. We have designed and implemented both methods and compared the results.

3.3.1 Formulation of Active Model

An active model can be defined as an ordered set of n points called control points, $V = \left[v_1, v_2, \ldots, v_n\right]$ where each control point of the active model, v_i is defined over the finite grid (digital image) of size M X M X N: $v_i \in \mathbb{E} = \{(x, y, z)\}$, x, y = 1, 2,..., M and z = 1, 2,..., N (Lai, 1994). Fig. 3.7, shows the concept of spatial interval and the control points diagramatically.

Let $v(s,t)$ be the initial contour with parameters s (spatial interval) and t (time), defined on a given open interval Ω and T, respectively. We consider this active contour to be a function of the spatial co-ordinates x, y and z with the same parameterization: $v(s,t) = (\mathrm{x(s, t)}, \mathrm{y(s, t)}, \mathrm{z(s, t)}) : s \in \Omega,\ t \in T$. Then the total potential energy of the active model at any given time t can be written as,

$$E_{total}(v(s)) = \left(\frac{1}{2}\right)\int_{\Omega}\left\{E_{\mathrm{int}}(v(s)) + E_{ext}(v(s)) + E_{con}(v(s))\right\} ds$$

where E_{ext} is the energy due to the external forces derived from image data, E_{int} is the total internal energy of the active model and E_{con} is the force due to externally imposed constraints such as penalty terms, region based forces, etc. (Leymarie and Levine, 1993). In every iteration of optimization process, the control points move in such a way that the total

potential energy of the active model is minimized. The internal energy of the control points depends only on the location of control points while the external energy can be derived from the properties of the image pixel where the control points are located. Formulation of different energy terms is explained below.

Energy Formulation As mentioned earlier, the total potential energy of the active model can be written as

$$E_{total}(v(s)) = \left(\frac{1}{2}\right)\int_{\Omega}\left\{E_{\text{int}}(v(s)) + E_{ext}(v(s)) + E_{con}(v(s))\right\}\, ds$$

where E_{ext} is the energy due to the external forces derived from image data, E_{int} is the total internal energy of the active model and E_{con} is the force due to externally imposed constraints such as penalty terms, region based forces, etc..

An active model can be considered as composed of abstract elastic materials such as springs and rods. The springs make the active model to resist expanding while the rods make them resist to bending. As these properties depends solely on the location of the active model control points and not on any image properties, one can say that the elastic energy and the bending energy are the internal energy of the active model. The total elastic energy of the active model, i. e., sum of the elastic energy of each spring, can be calculated as the sum of squares of the distances between adjacent control points. In analogous terms, the elastic energy is given as the sum of the first derivative of the location of the control points defining the active model. Hence, the elastic energy between the equidistant control points i and $(i-1)$ is,

$$E_{elastic}(v_i(s)) = \omega_1(s)\cdot\left\|\left(\frac{\partial v_i(s)}{\partial s}\right)\right\|^2$$

$$= \omega_1(s)\cdot\left(\left(x_i - x_{i-1}\right)^2 + \left(y_i - y_{i-1}\right)^2 + \left(z_i - z_{i-1}\right)^2\right)$$

The weight $\omega_1(s)$ regulates the tension of the active model surface. This weight corresponds to the strength of the springs imagined to be connecting the control points. This formulation gives a simple elastic property that make the active model to shrink. The weight $\omega_1(s)$ can be calculated at the beginning of each iteration as it is a function of the distance between the control points. To simplify the process, we have set the value of $\omega_1(s)$ to a small constant usually much less than 1. Fig. 3.6 shows a schematic diagram of how elastic force acts on control points of an active model.

The other kind of material we have considered as constituting the active model along with the springs, is rods. This resists sharp bending of the active contour or surface model. The resistance to the bending can be considered as bending energy and hence, calculated by sum of the squared curvatures of the active contour or surface measured at the control points. In analogous terms the total bending energy of an active model can be defined as the integral

of the second derivative of the location of the control points over a closed contour or surface. Hence,

$$E_{bend}\left(v_i(s)\right) = \omega_2(s)\left\|\left(\frac{\partial^2 v_i(s)}{\partial s^2}\right)\right\|^2$$

$$= \omega_2(s)\cdot\left(\left(x_{i+1} - 2x_i + x_{i-1}\right)^2 + \left(y_{i+1} - 2y_i + y_{i-1}\right)^2 + \left(z_{i+1} - 2z_i + z_{i-1}\right)^2\right)$$

The weight $\omega_2(s)$ regulates the rigidity of the active model. The weight $\omega_2(s)$ can be calculated at the beginning of each iteration as the function of the curvature of the active model at each control point position. To keep the computation as simple as possible, we have set the value of $\omega_2(s)$ as a small constant usually much below 1.

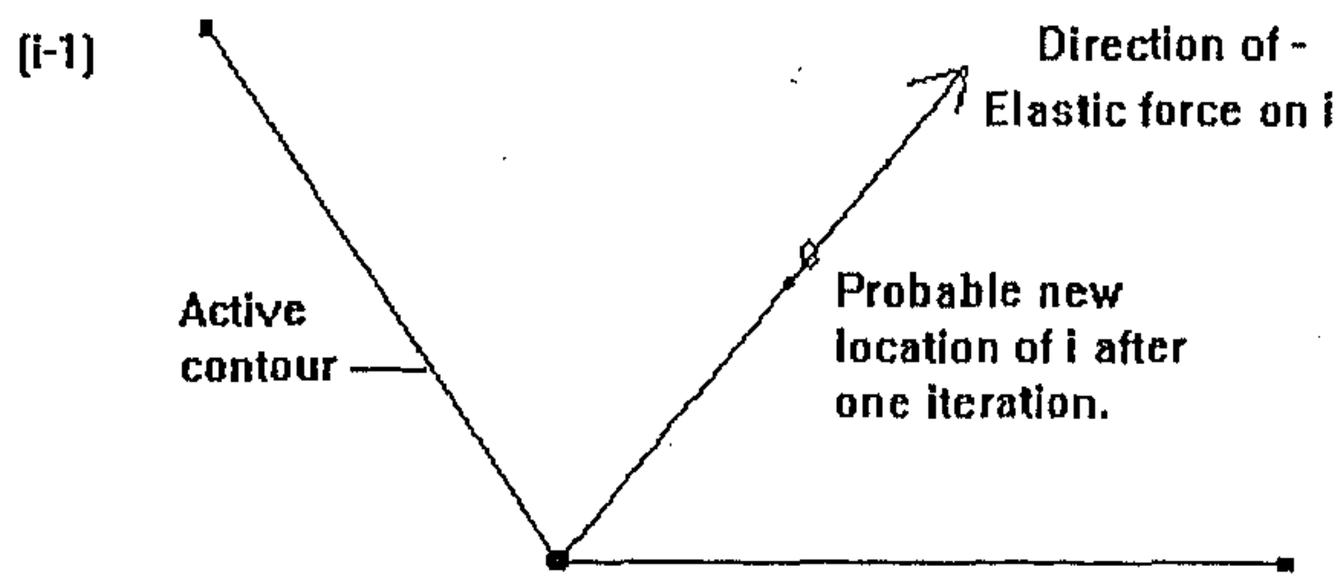

Fig. 3.6: Schematic diagram showing the control points of a partial active contour model and the action of elastic energy.

Thus the total internal energy of the active model can be formulated as,

$$E_{int}\left(v(s)\right) = \int_{\Omega}\left\{\omega_1(s)\left(\frac{\partial v(s)}{\partial s}\right)^2 + \omega_2(s)\left(\frac{\partial^2 v(s)}{\partial s^2}\right)^2\right\} ds$$

The external forces acting on the model during optimization can be derived from different image properties such as image intensity, image gradient, distance map, regional information and other externally imposed hard constraints. Generally, the pixel properties where the control points of the active model is located, gives rise to the external forces. The external forces guides the deformation of the active model towards a desired feature in the image. In the present application we are interested in marking the smooth and closed boundary or surface of the cells. Hence the predominant external force is derived from the gradient map of the image. The gradient vectors show a peak magnitude at the boundary or surface of the cells and are directing towards the surface. Though this is a desirable property

to guide the active model towards the optimum boundary or surface, the influence of gradient vector is limited to the immediate vicinity of the cell surface. This drastically reduces the capture range of the gradient force and the active model has to be initialized very close to the object surface. To avoid this, we have used the force derived from the distance map of the overall cell boundary. The active model that is not initialized very close to the cell surface, deforms under the distance force in the initial stages and moves close to the cell boundary where the gradient force dominates making the active contour to converge to the optimum location of the cell surface. Thus,

$$E_{ext} = k_1 \oint_{\Omega} D\left(v(s)\right) ds + k_2 \oint_{\Omega} g\left(v(s)\right) \cdot ds + E_{con}$$

where k_1 and k_2 are tuning constants for controlling the magnitude of the force, $D\left(v(s)\right)$ and $g\left(v(s)\right)$ are the energies due to distance and gradient maps.

We have calculated the distance and gradient force not directly from the pixels under the active model control points but by searching a small region along the normal vector of the control points. The minimum distance value or the gradient value within this region is considered as the external force due to the corresponding source.

For calculating the external forces, the search region (a pre-defined region along the normal vector of the control point) is divided into small sub-regions of size 1×3 voxels. The external energy is chosen as the sum of the minimum distance value and the minimum gradient value within the search region Θ_i, i. e.,

$$E_{ext}\left(\Theta_i\right) = \min_{j \in \Theta_i} E_{ext} = \min_{j \in \Theta_i} \left\{ d\left(v_{ij}(s)\right) + g\left(v_{ij}(s)\right) \right\} + E_{con}$$

where $d\left(v_{ij}(s)\right)$ and $g\left(v_{ij}(s)\right)$ are the distance and gradient value at ij, $j = \{-1,0,+1\}$ being the possible minimum energy locations of $v_i(s)$ within Θ_i.

Calculation of external energy directly from the underlying image pixel makes the active model more vulnerable to noise. The resulting external energy may be large enough to force the control points out of the image domain. Thus considering the minimum gradient value or distance value within a small region of the control point minimizes the effect of spurious local peak.

Constraints (E_{con}): The ability to apply constraint is essential for the accurate modeling of complex objects that obey known geometric and semantic constraints (Fua and Brechbuhler, 1997). Constraints are enforced with an intention of being able to track or fit corners, cusps and deep concavities when these were recognized in the image. One of the simple method of forcing the active model surface to the corners of the object is by introducing tangential discontinuities in the image. This is done as follows.

After the active model reaches a stable state, the contour or surface is examined for the regions where the contour or surface has bent significantly. Several breaks are introduced in such locations and the active model is allowed for further energy minimization. When the new stable state is reached, if any change in position and energy of the model has occurred, then the validity of creating a corner or the cusp at the chosen position is confirmed. The disadvantage of this method is that it needs an interpretation stage to locate the places where the active model has bent significantly. This has to be done after the active model has reached a stable state. An improvement for this is to mark the corners and deep concavities before optimization. Once the stable state of the active model is reached, the breaks are automatically introduced at those points, which fall on the normal vector of the marked corners and concavities. The energy minimization is further continued till a new stable state is reached.

Traditional ways to enforce such constraint is to add penalty terms to the model's energy function. In such cases, the optimizer, selectively ignores the other energy terms of the objective function and minimizes the energy due to constraints only. Given a set of r hard constraints (marked locations) $C(s) = \{c_1, c_2, c_3, \ldots, c_r\}$, the corresponding (nearest) control points are forced to seek the location of these constraints irrespective of the internal and external energy acting on it.

In the present application, the pixels of the corners, protrusions and concavities of the cell surface are marked interactively by clicking on such points after viewing the cells in a Graphical User Interface (GUI). Once the stable state is reached, the active model surface is checked for passing through the marked constraints. If a constraint is left outside the active model, then the corresponding control point of the active model (one that falls along the normal vector of the marked constraint) is pulled towards the marked constraint by using a constraint force or energy. Then the active model is again subject to minimization of energy and reach a new stable state. Fig. 3.12, shows few externally marked constraints over a two dimensional image to which the active model is forced to converge.

If E_{con} is the energy due to externally enforced constraints and there are N constraints for the active model to satisfy then E_{con} can be written as $E_{con} = \sum_{m=1}^{N} \rho_m \cdot C_m^2$ where ρ is a scaling constant which controls the externally enforced constraint energy. Extensive use of penalty terms would make the active model to neglect the image forces resulting in poor convergence. The cells in a histo-pathological images are more or less convex in shape. The presence of sharp corners and/or deep concavities are most of the times considered as artifacts and hence rectified in the pre-processing stage. Thus the necessity of using hard constraints or penalty terms arises only due to poor initialization of the active model

Another problem is due to uneven variation of external forces along the deformation path of the active model. This results in some control points of the active contour/surface skipping the respective global optima or many control points getting attracted to a nearby strong edge points causing clustering of the control points. This is an undesirable effect. To reduce the effect of noisy local optima, we have built a smooth and slowly varying potential surface based on distance and gradient maps. The active model control points navigate over this potential surface and reached the global optima. We have minimized the clustering of control points around a single local peak by limiting the movement of the control point in its tangential directions to a maximum of one voxel width on either side of the control point while allowing larger flexibility along the normal direction, i. e., by reducing the elasticity of the model.

Energy minimization is an iterative process where the total internal energy of the active model becomes equal to total external energy imposed on the model. When the total potential energy is minimum, we say the active model has reached its optimum shape and location. During each iteration the active model moves or deforms in such a way that the total potential energy associated with it decreases. Since the optimization process is an iterative process, one of the important aspects is to formulate a terminating criterion for the iterative energy minimization. If $E_{area}(v(s))$ is the length of the active contour (surface area) of the active model at any instant t, then we stop the iterations when,

$$\left|E_{area}(v(s,t)) - E_{area}(v(s,t-1))\right| \leq \lambda$$

where λ is determined experimentally and $E_{area}(v(s))$ is given as,

$$E_{area}(v(s,t)) = \oint_{\Omega} v(s,t)ds\,.$$

This kind of criteria for termination is known as steady state criteria. Leymarie and Levine (1993) have used a steady support criteria where they terminate the optimization when they reached the minimum field potential rather than minimum length or surface area of the active model.

3.3.2 Potential Surfaces

Active models deform towards optimal shape under image derived forces. The movement of the active model control points can be considered as the navigation on a potential (energy) surface due to different external forces. A potential surface is a topographic representation of the different energy maps such as gradient map and distance map. The necessity of the smooth and evenly varying potential surfaces arises due to the high noise sensitivity of the active models as well as to maintain the even movement of the control points. A local noisy intensity peak or a gradient peak would make the active model to shrink around noisy pixels or may drive the corresponding control point out of the image domain. A

smooth, noise-less and slowly varying potential field is thus necessary for the proper optimization of the active model.

Another problem is the capture range of the gradient potential due to which, use of gradient force alone is not sufficient to force the convergence. The gradient vectors pointing towards the edges generally have large magnitude only in the immediate vicinity of the cell surface. The remaining region being homogenous would fail to exert any gradient force on the initial model located not so close to the optimal positions. We have built a gradient potential surface with a higher capture range as follows.

The gradient map or the edge map of the enhanced and window-sliced image stack is normally considered as a potential surface due to gradient energy. The extension of the gradient field can be done by successively diffusing the edge map by smoothing and scaling. This considerably increases the capture range of the gradient potential.

Fig. 3.7(b) shows a gradient potential surface obtained by diffusion and scaling of the edge map. Still, the capture range may not be large enough to attract the far off control points. One such example is when we initialize an approximate ellipsoid surface as an active surface model for a deformed cell. The best possible solution in such cases is to introduce a varying potential field in the homogeneous region where the gradient potential does not exist. This can be done by introducing the distance potential (Cohen and Cohen, 1993), in addition to extending the gradient vector field as far as possible by diffusion process.

A distance map can act as a distance potential surface to bring the active model to near optimal locations. We have generated a 3-D distance map based on the path generated distance transforms proposed by Borgefors (1996). Here we briefly explained this method. The overall surface of the cell clusters is marked as explained in section 3.1. The voxels belonging to the surface of the cells are set a distance value zero and all other voxels in the image are set to some large number (ideally infinity). The distance map is computed using two raster scans over the initial image.

In the first raster scan, starting one voxel from the border, a new distance value is computed for each voxel. Compute the sums of the values of the already visited neighbors and the corresponding local distances. The local distances are calculated as follows. The neighboring voxels sharing the face is said to have a local distance of 3, voxels sharing edges are given local distance value of 4 while the voxels sharing corners are given local distance value 5. These weights give the best approximation of the Euclidean distance values. In a twenty-six neighborhood, there are thirteen already visited voxels for each central voxel. Thus the new distance value for the voxel will be the minimum of the 13 sums. This scan computes the distances from the left-up-top.

In the second scan the scan direction is reversed. Again, for each voxel the sum of the already visited neighbor distance values and the local distances are computed. The only difference is that now the central voxel itself must be included, adding a local distance zero. Thus the new, final, value is the minimum of 14 values. The second scan computes the

distances from right-down-bottom. A similar method can be used for calculating the distance map in two dimensions with a suitable weights for local distances.

Fig 3.7 (a), shows a sequence of image slices of the distance based potential surface generated by the above method. Thus an active model placed at the far off location will be well within the capture range of the total potential field. The active model encounters greater gradient force when it moves close to the actual surface of the cell.

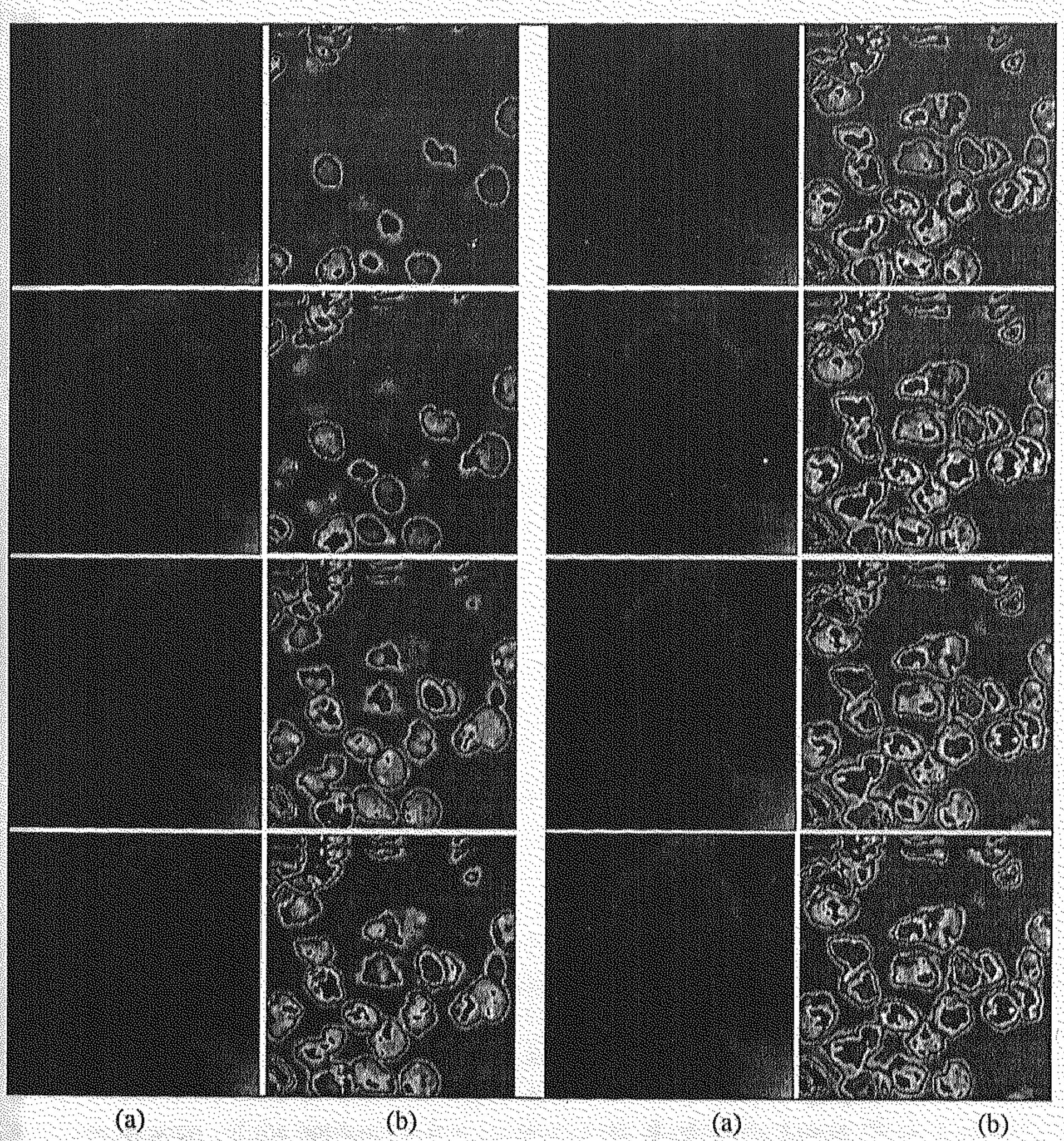

Fig. 3.7: Distance and gradient potential surface of a 3-D image data shown as a sequence of image slices. (a) Distance based potential surface (due to inability of the printer to print more than 16 gray levels, the image appears total dark) (b) Gradient potential surface

3.3.3 Initialization and Optimization of Active Models

The robustness of the segmentation based on active models depends, in general, on the relative difference of position and topology of the initial model with respect to data. A close initialization with correct topology guaranties a proper segmentation. Furthermore the closeness of the initial model greatly influences the time of computation needed for the recovery. Theoretically speaking, active models can be automatically initialized using methods such as Hough transforms (Lai, 1996), binarization (Delingette, 1998), partially interactive methods along with edge operators, etc.. But Hough transforms are computationally complex and need not give proper result in a noisy multi-dimensional images. Binarization technique may not give an enclosing boundary around the cell of interest when the cells are touching or overlapping on each other. Several methods are proposed to avoid the errors due to poor initialization. They are multi-resolution method (Leroy et al., 1998), pressure forces (Tek and Kimia, 1995) and distance potentials (Cohen and Cohen, 1993). The basic idea in all these methods is to increase the capture range of the external forces and guide the model towards the object surface. Use of pressure forces (Cohen, 1991), directional attraction, requires a prior knowledge of whether to shrink or expand during optimization. Use of gradient vector flow (Xu and Prince, 1998) when the objects are closely arranged may not give proper results as the extension of the gradient field results in overlapping of the potential fields due to different objects.

For a 3-D image in the form of a stack of 2-D image slices, initialization of the active model can be done in two ways. One method is a 2-D plane-by-plane approach where an interactive initialization is done in one image slice or a direct 3-D processing where a deformable surface is automatically initialized by interactively adjusting the surface model parameters.

Plane-by-Plane Approach

In this approach a contour is interactively initialized around the cell(s) of interest in one image slice. The optimum active contour of this image slice is used as initial contour model in the neighboring image slices. The process is continued till the cell boundary is marked in all the image slices where the cell signature is present. Initialization of the cell boundary can also be done like partial interactive marking of the boundary of the cells in layered segmentation process explained in section 3.2.1.

When the change in cell shape from one image slice to another is too large and abrupt and/or if the axial resolution of the image stack is poor, the proposed automatic axial propagation of the optimum active contour to the neighboring image slices results in poor initialization. The introduction of additional image slices by interpolation based on morphing smooth the abrupt deviation in cell shape to a major extent. This helps in automatic initialization of active contour by propagating optimum contour from previously processed image slice.

As stated earlier, hard constraints are used to force the corresponding control points of the active model to the desired cell concavities or protrusions. The hard constraints are marked interactively. In our experiments we have rarely used these hard constraints as the increase in capture range of the external forces was good enough to drive the poorly initialized active model to small concavities and protrusions in the cell boundary

The optimum cell boundary of i th image is then axially propagated to its neighboring image slices as an initial contour. Thus the optimum contour of i th image slice acts as an initial active contour in $(i+1)$ th and $(i-1)$ th image slices. The process is continued till all the image slices in which the cell signature is present, are processed. Fig. 3.8 and Fig. 3.9, shows some result of active contour optimization over a different CLSM image data. Results are shown as a sequence of image slices.

When we propagate the optimum contour model along the axial direction, we come across few interesting situations such as, (a) A cell of interest may divide into two separate cells, (b) Two touching cells around which the contour is initialized separating each other, may drift apart (c) A separate cell may come in contact with the cell of interest.

Another interesting situation is, as we are dealing with a 3-D object, which may be simply connected in 3-D but the same can not be said for simple conceitedness in 2-D. Here we have discussed, how the active contour model behaves in this kind of situations and what modifications have to be made to the process of energy minimization to avoid poor optimization.

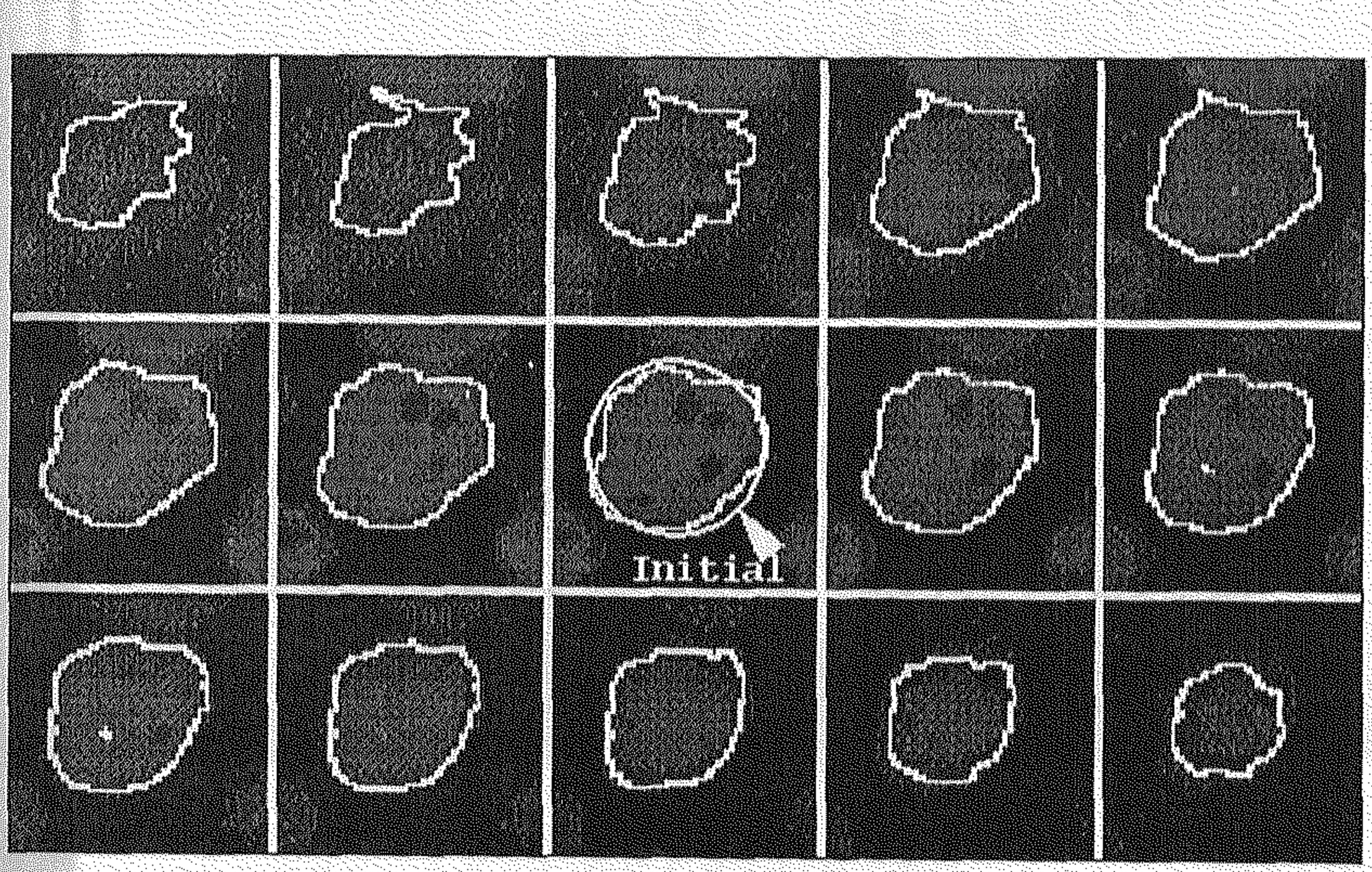

Fig. 3.8: Result of active contour optimization over a single cell image shown as a gallery of optical sections.

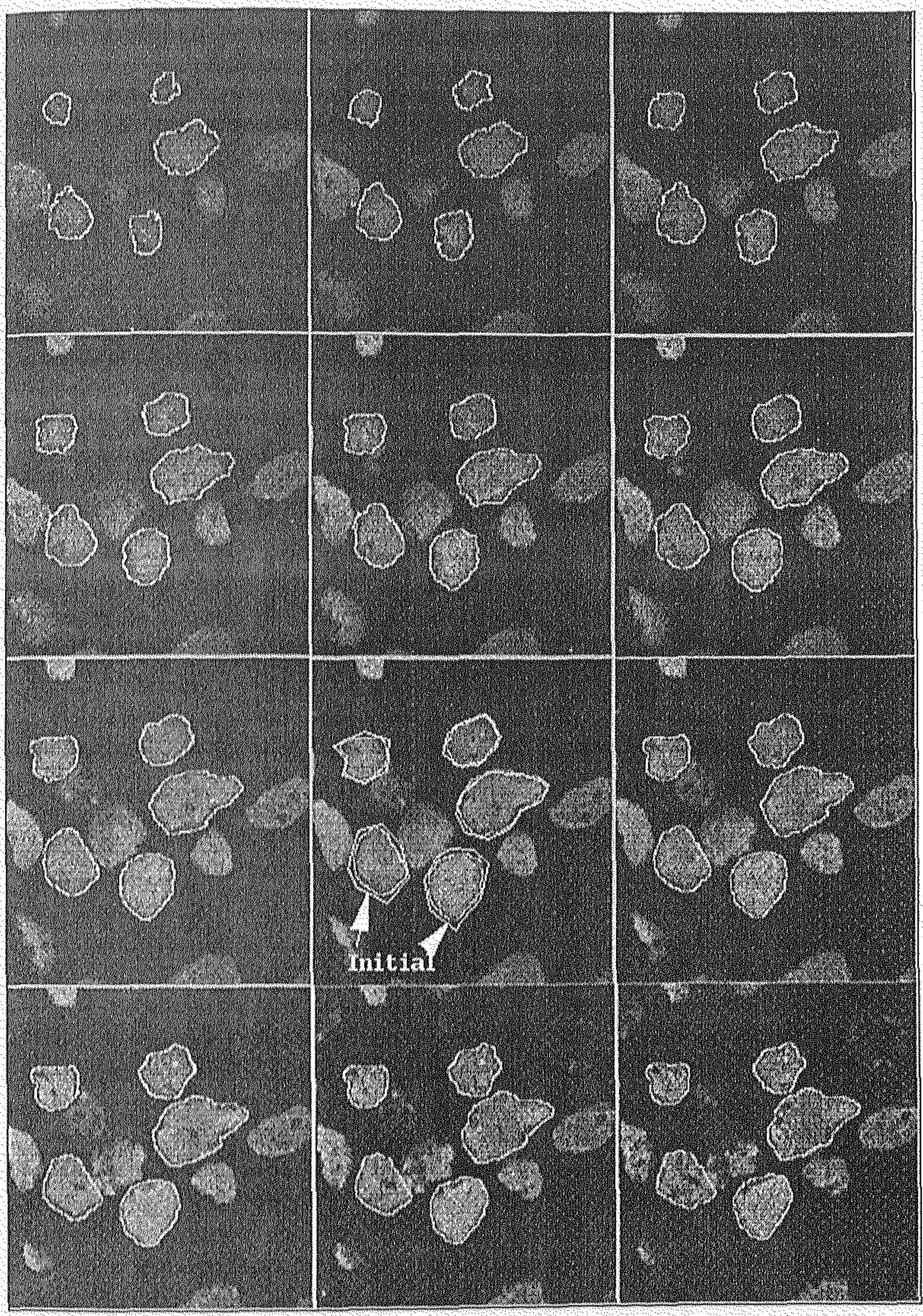

Fig. 3.9: Result of optimization of a ACM to segment a individual cells among the cluster of cells

Some Interesting cases: When we propagate the optimum active contour from one image slice to another, we may come across situations where the cell may separate into two distinct cells due to cell division. When the cell separates into two entities, either the whole active contour may be stretched to cover both the signatures or a part of the active contour may get attracted by a strong boundary feature of a separating cell. Both the situations are undesirable. The simplest option is to interactively reinitialize the active contour when the single cell separates into two distinct signatures. This increases the interactiveness of the method. We have tackled this problem as follows.

The cells are segmented and labeled separately in each image slice by thresholding and component labeling. During the automatic initialization of the active contour, the contour is made as a function of that cell which it encloses maximally. This is done by virtually filling the closed active contour region and testing which cell has a major share of the area signature of the closed contour model. Cells other than the cell of interest, are considered as virtually non-existing. This forces the active model to converge onto the cell of interest.

When a different cell touches the cell of interest as we move along the depth of the image stack, the active contour is unaffected by it and continues to converge based on the energy derived from the local potential surface as if the other cell is not existing. This is because, the influence of other cells is minimized by using the regional information obtained from the labeled image volume.

The next situation is when two touching cell separates. The initial contour separating the two cells is shown in Fig. 3.10(a). When the cells separate, the control points of the active contour, which was common to both the cells, get attracted to the cell having strong boundary feature. Since the gradient magnitude characterizing the cell boundary is highly uneven, the common control points get unevenly distributed around the cells as shown in Fig. 3.10(b). This introduces some discontinuity in the contour around the cells. The broken contours can be connected either by linear interpolation or by any other contour linking techniques. The resulting continuous contours are then subject to energy minimization process.

An object which is simple connected in 3-D may not be simple connected in 2-D, This is true when we represent a non-convex 3-D cell in a stack of 2-D images. The result is, same cell may be represented by two signatures when we trace along the depth of the specimen or two signatures may merge as they all belong to the same 3-D object. In the first case, the problem is not so acute as the image enhancement and the potential surface construction would automatically solve the problem. Before the cell signature becomes two distinct parts, gradual concavity forms at the breaking point of the cell. Since the formation of a concavity is gradual and smooth, the active contour convergence will not be affected adversely. When the concavity deepens and subsequently becomes two signatures of the same cell, the control points of the single active model get redistributed around two distinct signatures. This is shown diagramatically in Fig. 3.11.

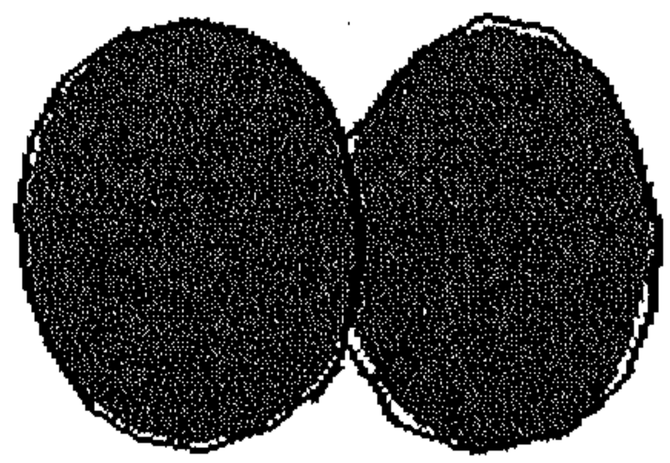

Fig. 3.10: Diagrammatic representation of optimization when two distinct touching cells separate (a) Two touching cells with initialized contour separating them (b) When the touching cells separate, control points get redistributed (c) after connecting broken contour and optimization

The axial resolution of the image stack is enhanced to an extent that any large and abrupt deviation in the cell shape is smoothed. Since optimization of active contour model is also done in these interpolated image slices, the contour initialization will be in realistic locations when we propagate from one slice to another.

In the second type of problem where two separate cell signatures may be a part of the same 3-D cell the problem becomes complex. The separately initialized contours around distinct cell signatures do not allow the merger of the contours when the signatures are merged. This is because the gradient magnitude variation within the cell cytoplasm is high enough to indicate some false boundary.

In the number of specimen images tested, we have not come across this type problem of simple connectedness. The solution may be to initialize the contour where the cell is

represented by a single signature. We have observed that the problem of simple conceitedness of a 3-D cell seldom appears. This may be because, the cell shape is approximately convex.

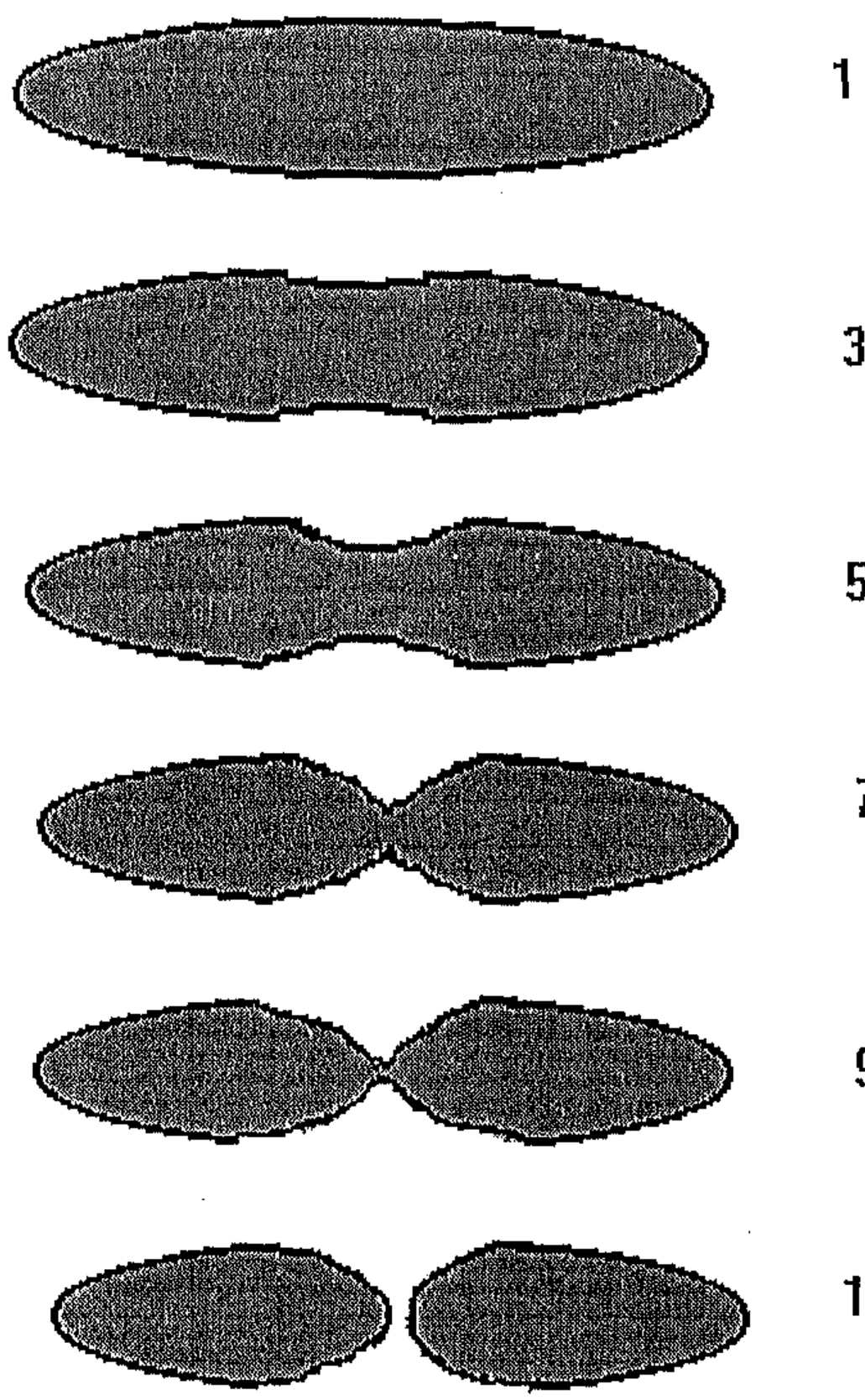

Fig. 3.11: Diagrammatic representation of propagation and optimization of active contour of a simple connected 3-D cell that is not simple connected in 2-D. The numbers besides the cells give the position of the image slice in the stack.

Another interesting case is the presence of sharp corner are deep and narrow concavities as discussed earlier. We have to use interactively marked hard constraints to force the active contour to converge to such points. The application of hard constraints is explained earlier. The corresponding control points of the active contour model is forced to neglect all the smoothness and continuity criteria and converge to the marked constraints. The broken contour is linked by linear interpolation and the energy minimization is continued till a new stable state is reached. Fig. 3.12, shows the application of interactively marked constraints for forcing the ill-initialized contour to the global optima.

To segment large number of cells in a volumetric data set, we can make use of multiple active contour models. The problem is again due to the strong boundary features of the neighboring cells. We have reduced this effect by using the regional information as explained earlier. Fig. 3.13 shows the result of application of multiple active contours on a close cluster of cells.

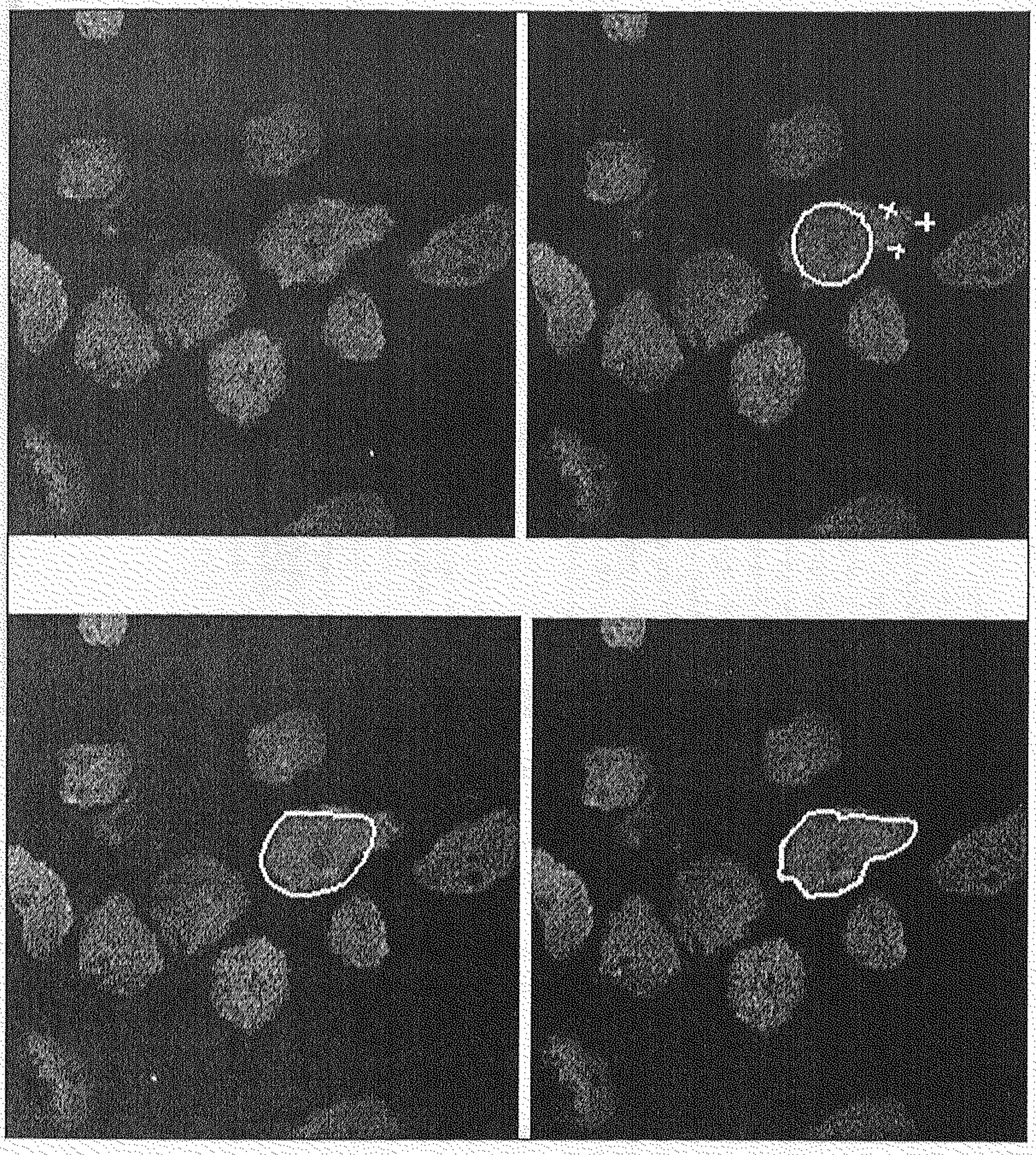

Fig. 3.12: Showing forceful convergence to externally marked constraints
(a) Original image slice (c) Constraints are interactively marked (c) Forceful convergence to marked constraints (d) Convergence of the contour when the constraints are absent..

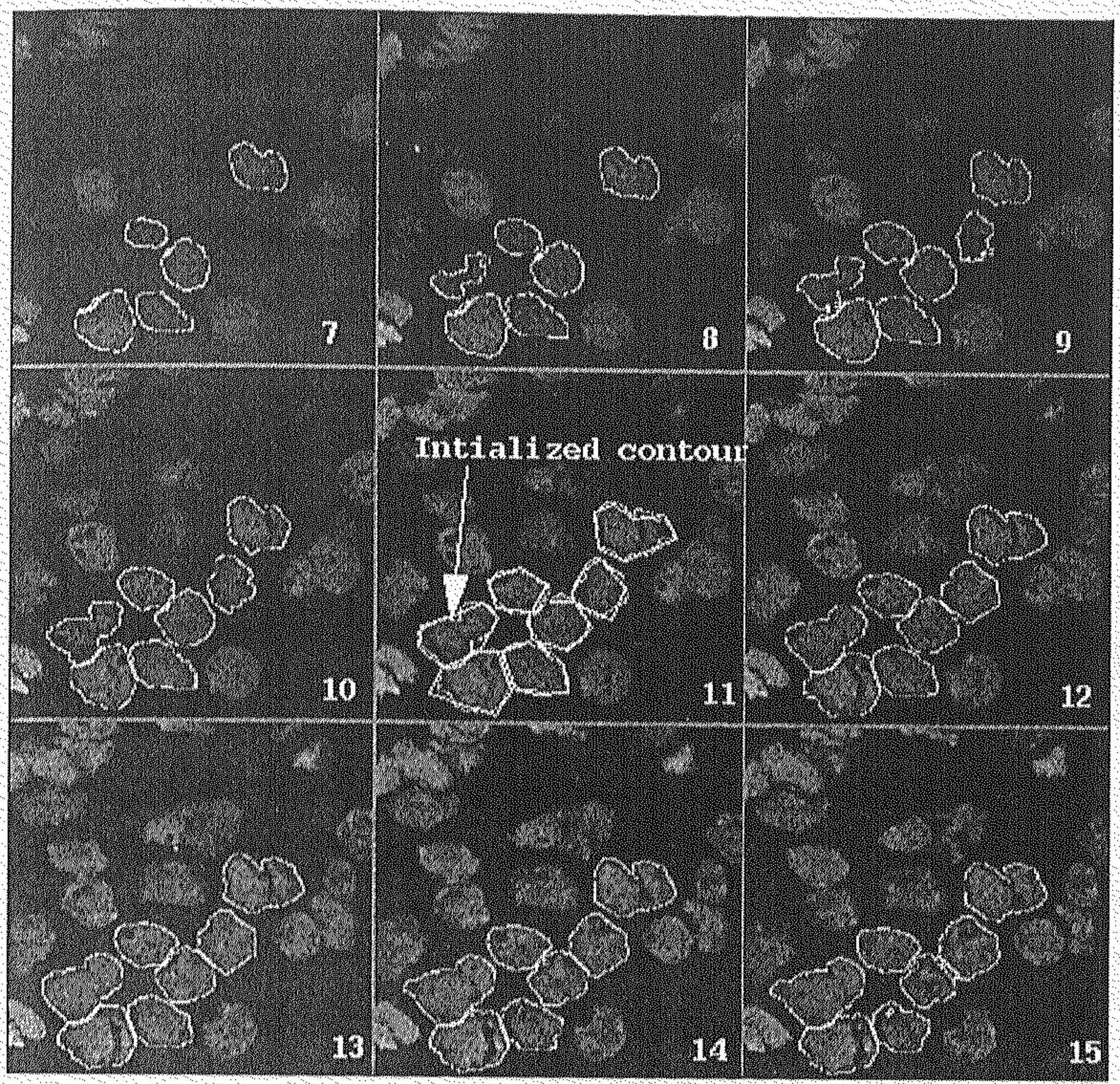

Fig. 3.13: Result of application of multiple active contour models

Open Contour Models : We can also use the open contour models along with the overall cell cluster boundary, to mark the closed boundary of the touching cells. The open contour model is initialized on the particular part of the cell boundary where the cells are touching or overlapping each other such that the open contour along with the overall boundary of the cell cluster forms a continuous closed contour. This is similar to the marking of boundary in the representative image slice in case of layered segmentation approach explained in section 3.2.1.

In an open contour method the position of the contour ends should be fixed. Since we join the open contour to the overall boundary drawn by low level method, we consider these joining points as the fixed points of the open contour for optimization purpose. Only the open active contour model between the fixed points is subject to optimization process. The optimum boundary thus marked is virtually superposed on the neighboring image slice as in layered segmentation. The part of this virtual boundary, which has no counterpart in the pre-defined neighboring region along the normal vector, forms the initial open contour for the

neighboring image slice. The end points are roughly fixed to the nearest overall boundary pixel before optimization

Fig. 3.14, shows the result of application of open contour models for segmentation of CLSM tissue images. Open contour method is very much comparable to the layered segmentation method proposed in this chapter. Only difference being that we use energy minimization for optimization in case of open active contour models while a blind search is done to find actual edgel in case of layered segmentation.

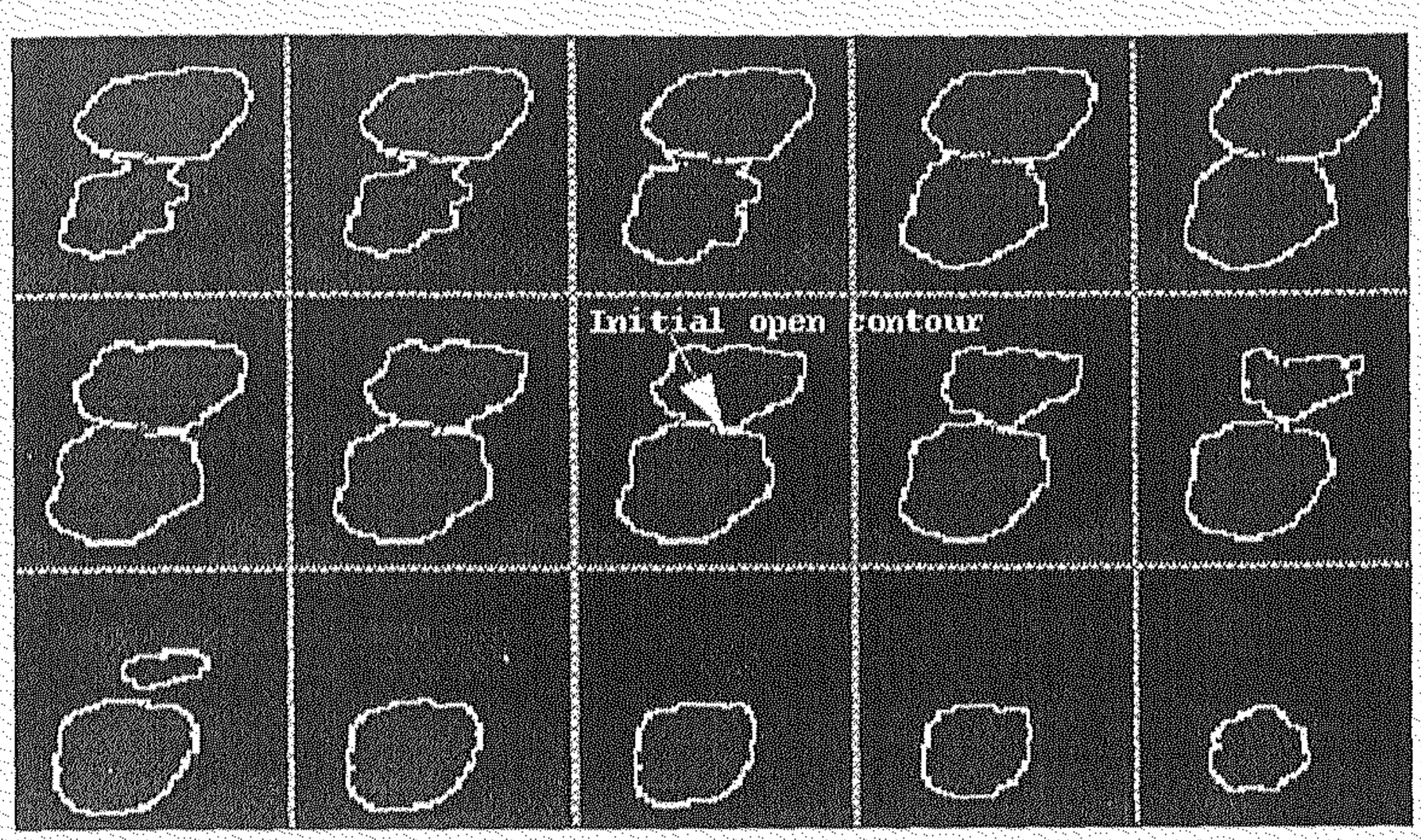

Fig. 3.14: Results showing the application of open contour models along with the overall boundary of the cell cluster obtained by simple searching.

Direct 3-D Approach

Direct 3-D processing of the volumetric images can be more efficient as it is more robust to noise (vander Voort, 1989) and optimally uses the spatial neighborhood relation. Several problems we face in the 2-D plane-by-plane approach such as problems due to simple connected 3-D objects, etc., can be avoided in direct 3-D approach. Problem of forcing the active surface to converge to the concavities is more difficult here as the concavities can occur more abruptly than progressively like in case of 2-D approach.

In this approach, a 3-D geometric surface model is initialized around the cell of interest. The voxels belonging to the surface of the initial models are subject to energy minimization process leading to new set of voxels converging towards the actual cell surface.

In case of 3-D histo-pathological images, interactive initialization of a geometrical shape is a difficult task as it involves initializing the surface in each image slice and construct an enclosing surface later. Automatic initialization is also a non-trivial problem. This is because the cells can have irregular shapes and irregular spatial orientations. We have used a partially interactive method as it helps in initializing the geometric surface as an active model

around the cell boundary. In case of active surfaces (direct 3-D approach), if the objects to be segmented are more or less similar in shape and size, it is computationally inexpensive to use the surface of a simple geometric model as the initial reference. We have designed a graphical user interface (GUI) using which a cell is selected by clicking at the approximate center and an ellipsoid surface is automatically constructed around the cell. The lateral radii of the ellipsoid can be interactively adjusted while axial radius is automatically calculated. Initialization process is briefly explained below.

If (x, y, z) is the center of the ellipsoid then the surface coordinates of the ellipsoid are given by $x = a\cos\theta\sin\phi$; $y = b\sin\theta\sin\phi$; $z = c\cos\theta$ where a,b and c are respective radius in x, y and z directions, θ and ϕ represents the cubicle angles.

Since the image is displayed in XY, YZ and XZ planes simultaneously as shown in Fig. 3.15, it is easy to locate the approximate center of the cell and the number of image slices the cell is occupying. If N_s is the total number of image slices the cell is occupying, then $\frac{N_s}{2}$ can be considered approximately as the axial radius 'c' of the deformable ellipsoid. Normally images are acquired in such a way that the whole cell nucleus is present within the first and last image slice. So one can approximately assume the axial radius 'c' to be half of the height of the image stack. For providing the lateral radii 'a' and 'b' we have designed an elliptic cursor as shown in Fig. 3.16, whose lateral radii and the angle of orientation can be varied with the help of mouse driven software.

It is extremely difficult to calculate the spatial orientation of the cell nuclei before segmenting them. This is because two touching cell nuclei can have totally different spatial orientations when compared to the orientations of the individual cell nucleus.

The spatial orientation of the ellipsoid model can be interactively adjusted using the GUI and the mouse buttons, where the angle of orientation is read in with the help of elliptic cursor. If i, j, k and i', j', k', are the unit vectors in old coordinates x, y, z and new coordinates x', y', z' respectively, then the relation of the old and new coordinate system is given by,

$$x' = x_c + \{x\cos(i',i) + y\cos(i',j) + z\cos(i',k)\}$$
$$y' = y_c + \{x\cos(j',i) + y\cos(j',i) + z\cos(j',k)\}$$
$$z' = z_c + \{x\cos(k',i) + y\cos(k',i) + z\cos(k',k)\}$$

where (i',i) is the angle between the vectors i' and i, i. e., between new and old axis of abscissas, (j',i) is the angle between new axis of ordinates and old axis of abscissas and so forth. $OXYZ$ is the old system of coordinates and $O'X'Y'Z'$ are the new system of coordinates. For simplifying the initialization, we keep the angle between OZ and OZ' as

same i. e., we rotate the ellipsoid around OZ hence $(i',k),(j',k),(k',i),(k',j)$ is 90^o and (k',k) is 0^o.

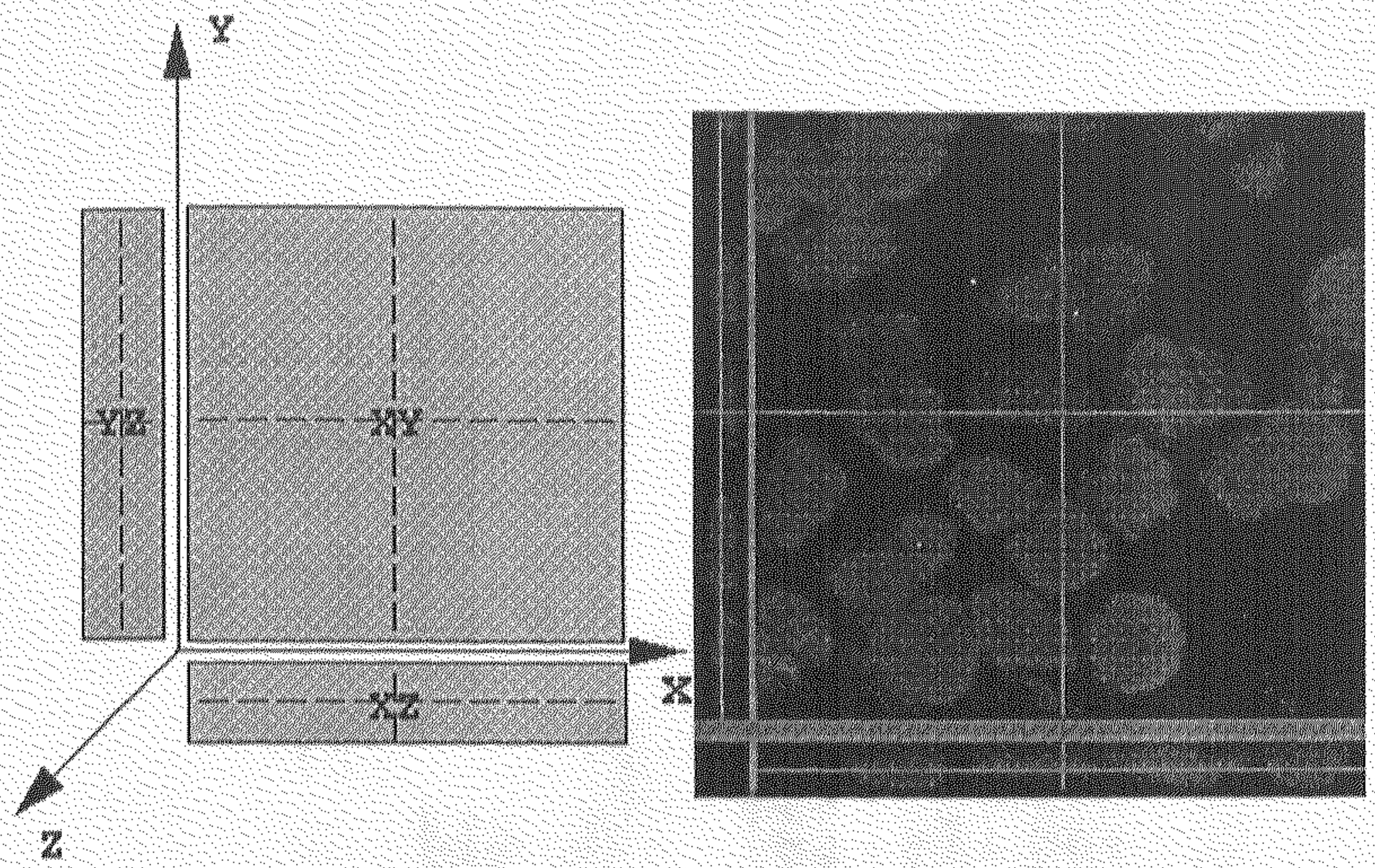

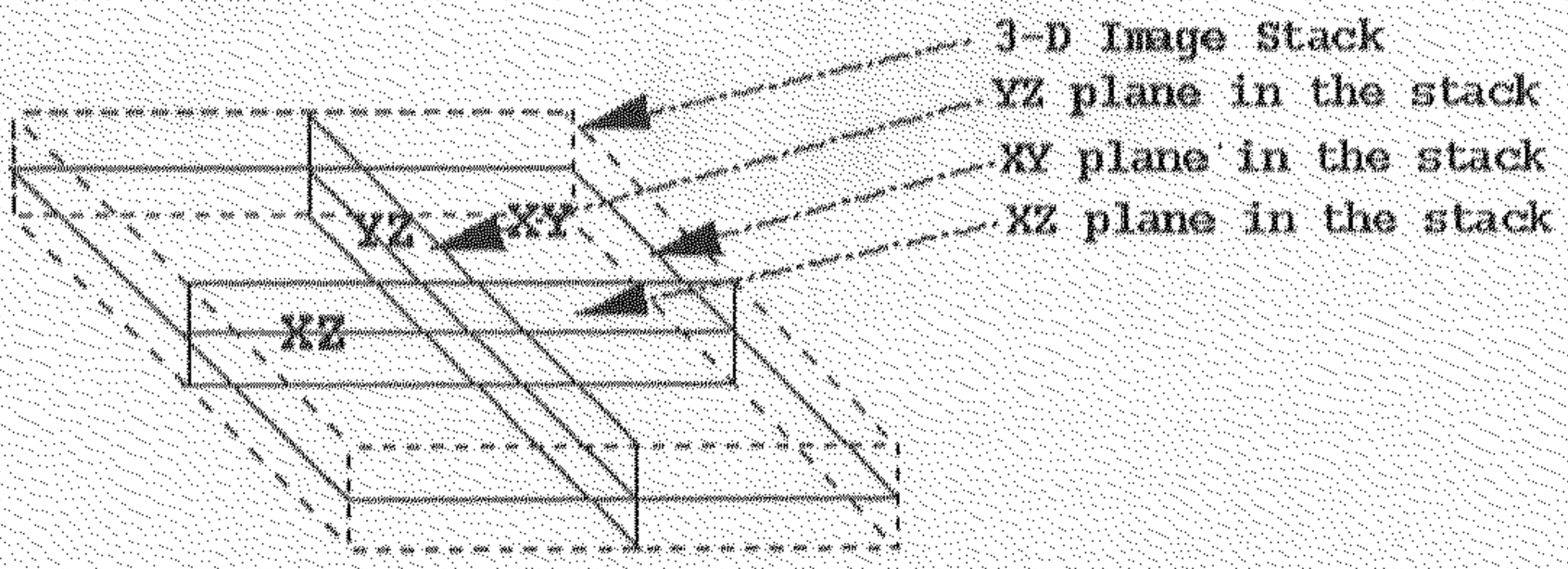

Fig. 3.15: Schematic diagram of the display of the image data in GUI.

This simplifies the co-ordinate transformations to,

$$x' = x_c + \{x\cos(i',i) + y\cos(i',j)\}$$
$$y' = y_c + \{x\cos(j',i) + y\cos(j',j)\}$$
$$z' = z_c$$

If $(i',i) = \psi$ i. e., the angle of rotation of the ellipsoid with respect to OX is ψ, then

$$x' = x_c + \{a\cos\theta\sin\phi\cos\psi + b\sin\theta\sin\phi\sin\psi\}$$
$$y' = y_c - \{a\cos\theta\sin\phi\cos\psi + b\sin\theta\sin\phi\sin\psi\}$$
$$z' = z_c + c\cos\theta$$

Such an initialized ellipse is shown in Fig. 3.17(a).

It is true that for a highly deformed cell, part of the ellipsoidal surface may get initialized far from the cell surface. In such cases one has to use hard constraints to force the convergence if the initial model lies outside the capture range of both gradient and distance potential.

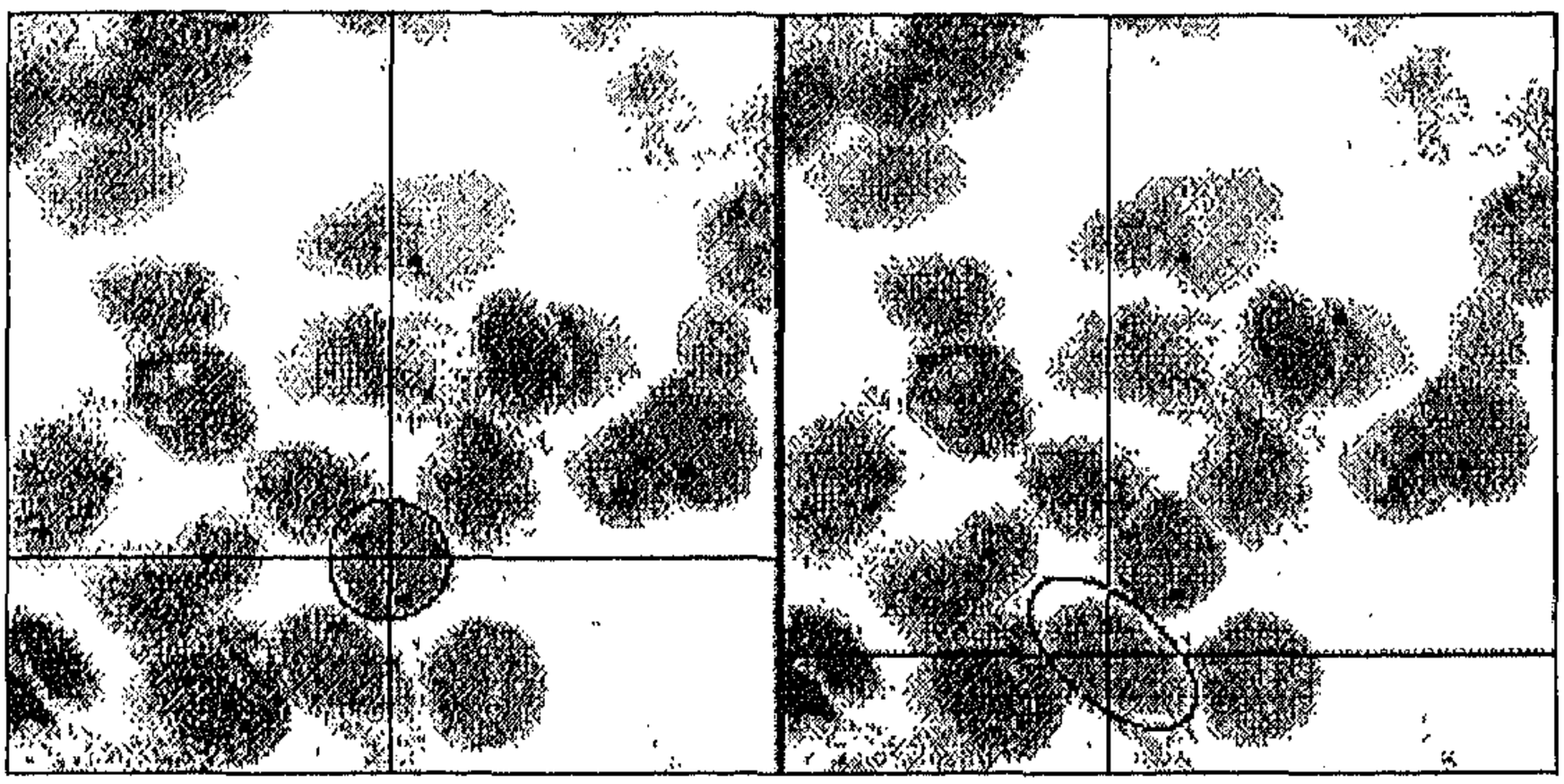

Fig. 3.16: Cursors for initializing active surface (a) Circular cursor (b) Elliptic cursor

All the voxels of the surface are considered as control points of the active surface for the purpose of optimization. Though this slows down the optimization, the resulting surface will be more smooth and have better volume enclosing properties. As direct 3-D approach uses the spatial neighborhood relation optimally, it is more robust to some of the local noisy artifacts. Fig. 3.17(b) shows the result of active surface optimization.

One of the major problems we face with the direct 3-D processing is that the initialization of the model very close to the optimum locations can not be guaranteed. This makes the model to be sensitive to the neighboring cells having strong surface features. To minimize the influence of other cells, we have used the region based information from the thresholded and labeled image. Only the forces due to the corresponding cell are made to influence the active surface by virtually deleting the other cells from the image domain while constructing the potential surface.

Another problem is with the volume enclosing property of the active surfaces. In 2-D approach, area enclosing is simple and a continuous curve surves the purpose. In 3-D, volume enclosing by the optimized model is not so simple. In confocal image analysis, we have an

advantage that the axial resolution of the image stack is so high (unlike in macro-images such as MRI) that we can consider that the surface constructed by the boundary of the object in each image slice is good enough to enclose the cell volume. Another argument is that we have improved upon the already good axial resolution using interpolation technique and hence for all the practicable purposes, we can consider that the optimized active surface completely encloses the cell volume.

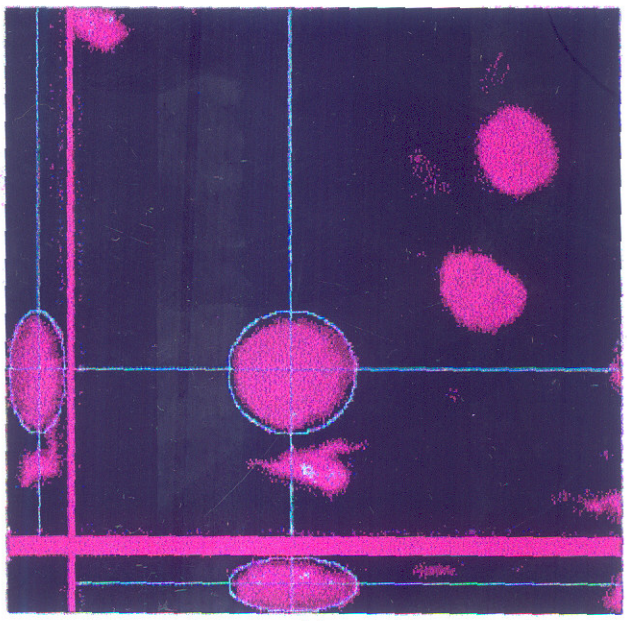

(a)

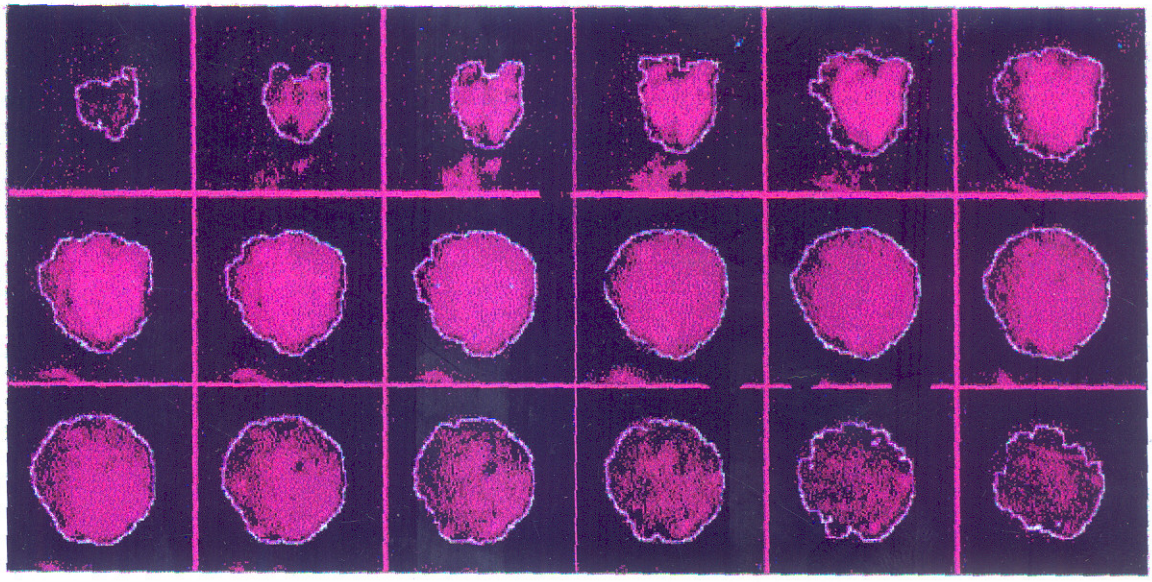

(b)

Fig. 3.17: Result of application of active surface for segmentation of a cell. (a)Initialized ellipsoid shown as ellipses around the cell (b) After optimization

Considering all the voxels in the optimum active contours or the surface as the members of the enclosing volume, we have fitted a pseudo-surface around the cell, using the software available with IDL (Research Inc. USA) interpreter language. When we are more interested in segmenting selected few cells for quick measurement such as DNA content, shape features, chromosome density, etc., direct 3-D processing is more efficient as it is quicker than 2-D plane-by-plane approach. Fig. 3.17, shows the result of direct 3-D processing as a sequence of image slices. Fig. 3.18, shows the pseudo 3-D view constructed from the surface generated by active surface optimization

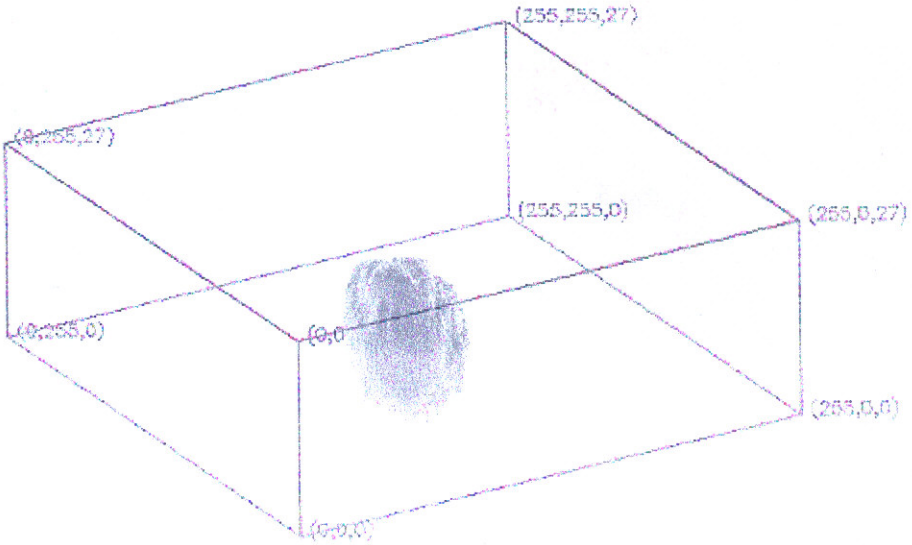

Fig. 3.18: A 3-D pseudo view of the cell shown in Fig. 3.20, after surface reconstruction.

Fig. 3.19, shows the application of the direct 3-D processing approach on another data sets. This data set is similar to the one shown for layered segmentation process and active contour model. This helps in subjective comparison of the results due to different segmentation methods presented in this chapter.

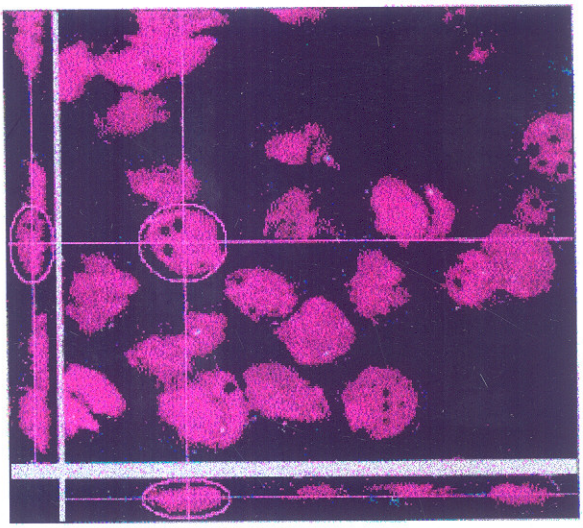

(a)

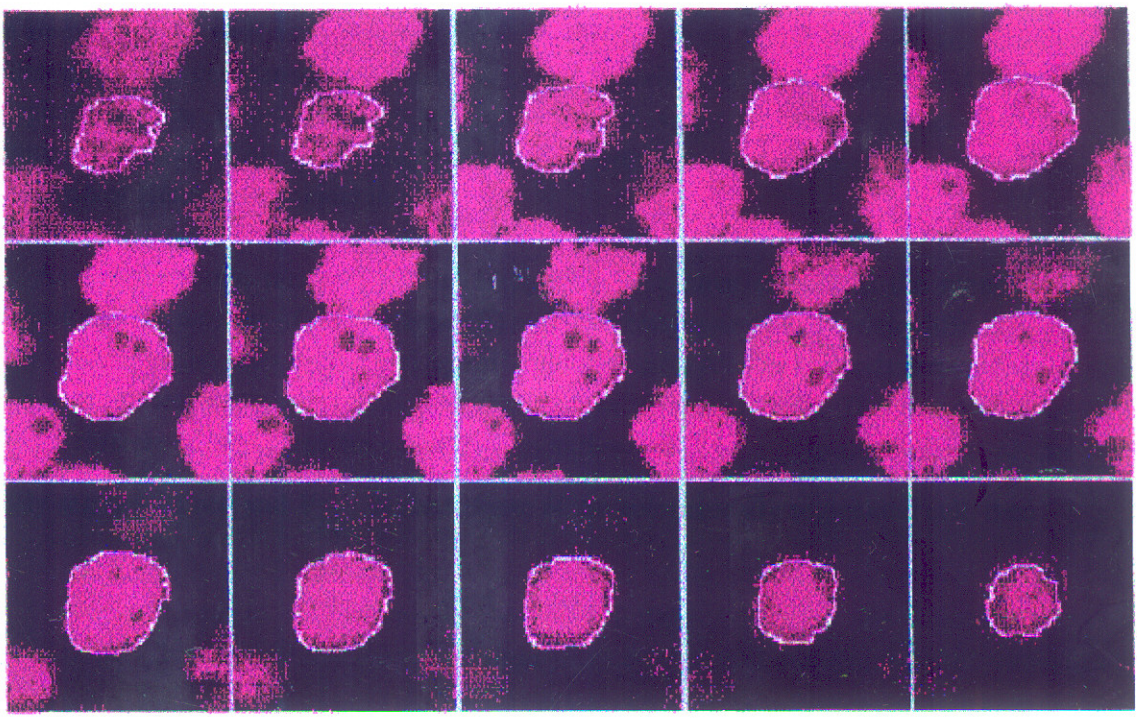

(b)

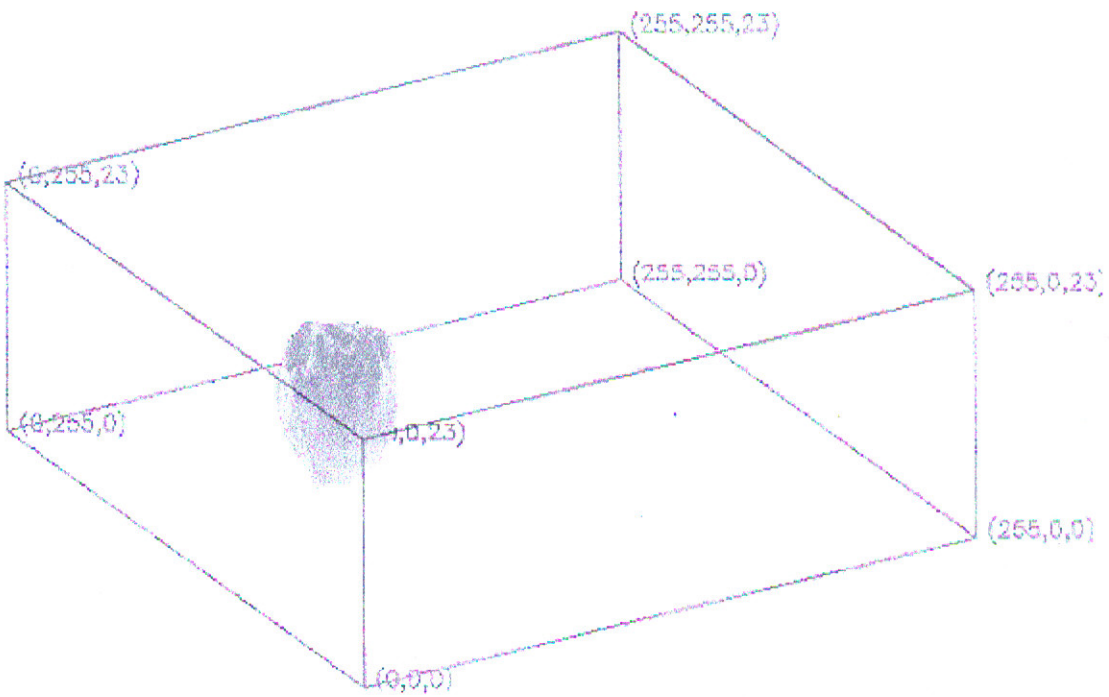

(c)

Fig3.19: Result of optimization of active surface model on a different image (a) Initialization (b) Result of optimization shown as a gallery of image slices (c) Surface rendered view of the segmented cell.

3.4 Comparative Study

After presenting three edge-based segmentation techniques, we need to compare them among themselves as well as with other edge operators such as Sobel operator and Canny edge detector. The comparison is based on some criteria and as applied to 3-D histo-pathological images. Here we have presented a brief study on subjective as well as quantitative evaluation of these edge based segmentation techniques with respect to segmentation of Histo-pathological images.

As a quantitative measure for the comparison, we have calculated the number of discontinuities (D), number of noisy edgels (E) and the percentage of symmetric difference in the total volume of the cells segmented by different methods. All the methods are compared with a manual segmentation, which is considered as a ground truth. The percentage of symmetric difference (%S) can be calculated as follows. If V_{man} is the volume of the manually segmented cell and V_{aut} is the volume of the automatically segmented cell, then

$$\%S = \frac{|V_{man} - V_{aut}|}{V_{man}} \text{ X } 100$$

Table 3.1, gives some of the results due to quantitative comparison of boundary or surface marking due to Sobel, Canny, Layered-segmentation, active contour models and active surface models. Results are given on two representative specimens. The comparison may vary drastically as the cells in different histo-pathological data may show different complexity in its architecture and other properties. While calculating the percentage of symmetric difference of the results due to Sobel and Canny, the discontinuous edges are linked manually and the noisy edgels are removed by size filtering the thresholded edge map. All the methods are applied on a noise reduced, window-sliced and enhanced images.

Sp. No.1	Sobel operator			Canny operator			Layered segmentation			Active Contour Model			Active Surface Model		
Cell No.	D	E	%S	D	E	%S	D	E	%S	D	E	%S	D	E	%S
1	13	136	9	8	118	7	0	0	7	0	0	3	0	0	5
2	9	128	11	7	93	9	0	0	8	0	0	5	0	0	5
3	8	95	8	5	65	8	0	0	8	0	0	6	0	0	7
4	5	78	4	5	61	5	0	0	7	0	0	4	0	0	5
5	11	103	7	10	82	5	0	0	5	0	0	4	0	0	4

Sp. No.2	Sobel operator			Canny operator			Layered segmentation			Active Contour Model			Active Surface Model		
Cell No.	D	E	%S	D	E	%S	D	E	%S	D	E	%S	D	E	%S
1	7	76	13	8	68	10	0	0	9	0	0	6	0	0	6
2	11	28	11	13	33	9	0	0	7	0	0	4	0	0	5
3	6	65	17	6	48	14	0	0	12	0	0	7	0	0	9
4	5	118	14	7	104	11	0	0	10	0	0	10	0	0	13
5	10	113	9	2	82	10	0	0	10	0	0	5	0	0	7

Table 3.1: Quantitative comparison of the performance of different edge based methods for 3-D cell segmentation.

Edge-detectors such as Sobel, Canny, etc., are simple to implement. When the cells in image are isolated and the image intensity difference between the foreground and background is considerable, these edge detectors provide acceptable results without the need for interactive boundary linking, etc.. But, these methods fail to mark the closed boundary when the cells are clustered together. The reasons for this is discussed earlier.

The layered segmentation method needs an interactive initialization of the touching and overlapping cell boundary in one image slice of the stack. Though the remaining process of boundary marking is done automatically, the accuracy of the boundary marking in the subsequent image slices depends on many factors. These include the level of noise content in the image, width of the search region, etc.. Another problem is the boundary pixel marking is a low-level process and is independent of the other boundary pixel positions. This can bring the unnecessary zigzagness to the boundary of the cells where they touch one another and introduce discontinuities. Some times the result of layered segmentation needs simple post-processing tasks such as linking and smoothing to obtain continuous contour.

On the other hand, the active contour models, uses a high level technique of energy optimization to mark the boundary. The continuity of the contour exists due to the smoothness constraint imposed by the elastic and bending energy terms in the contour optimization process. This smoothness gives more precise shape features and the accurate marking of the boundary at where the cells touch or overlap on each other. Though, active contours are also noise sensitive, our method of restricting the tangential movement of the contour pixels, reduces the effect of clustering and shrinking around a noisy pixel.

The main disadvantage with the active contour model is the need of interactive initialization. Initialization has to be done very close to the actual cell boundary. Results from simple thresholding and labeling methods may be needed to reduce the adverse effect of nearby cells having strong boundary features. Use of active models for segmentation of multiple number of cells in a large volume data is a computationally complex and time consuming process. Some of the disadvantages of this method is offset by the advantages such as accuracy in segmentation resulting in better feature measurement, etc..

The computational complexity of the layered segmentation is of the order of $O(nm^3)$ where n is the number of pixels in the virtual boundary, m defines the size of the search region along the normal vector as explained earlier. This is considering we use basic line search strategy for searching. When we use stratified search, the complexity reduces to $O(nm^3/l^2)$ where l is the number of stages the search region along the normal vector is divided. The active models are more computation intensive as it involves building smooth potential surfaces such as distance and gradient maps, calculation of internal forces, etc..

On an SGI-Indy, 200MHz machine, for a data set of 9Mbytes (256 X 256 X 24) having 12 cells in a touching or overlapping conditions, the computation time for different edge based segmentation methods are given in table 3.5.

Sl. No.	Sobel Operator	Canny Detector	Layered Segmentation	Active contour Models (snakes)	Active surfaces (3D processing)
1	4 Secs +M	6 Secs +M	33 Secs	36 Secs	28 Secs

Table 3.5: Time taken by different edge-based segmentation methods for segmenting selected cells in a representative image stack, +M indicates additional time required for manual correction of the results.

Layered segmentation, active contour and surface models require additional time for proper initialization of the model and more the number of cells in the image, more computation time is required.

Chapter 4
Region Based Segmentation

4.1 Introduction

Region based techniques stem from the fact that the voxels belonging to same region shows many similar properties. Most simple and primitive region based technique is thresholding the image based on local histogram of the voxel intensity and then labeling the isolated regions by connected component labeling algorithm (Udupa, 1990; Thurfjell, 1992). When the objects are well isolated, thresholding and labeling process may give acceptable results. But, real life images rarely show uniform gray-level within the object and in the background. Moreover, histogram based thresholding does not exploit the fact that the points from the same object are generally, spatially close due to the surface coherence (Jain et al., 1995)

In histo-pathological images the cells are clustered together and the boundary between them is not clear. Techniques such as split and merge algorithm (Jain et al., 1995), simple region growing (Zucker, 1976), multiple thresholding (Kohler, 1981), etc., do not yield acceptable results due to the fine textured nature of the cell chromatin and the presence of dense intra-cellular matters. Thus, region growing based on some kind of adaptive similarity measure of the voxel properties have to be incorporated to determine the membership of a particular voxel to its corresponding region. There are several region based segmentation techniques. To name a few, seeded region growing (Adams and Bischoff, 1994), successive erosion and dilation or successive pealing and thickening (Russ, 1995), watershed algorithms (Beucher and Meyer, 1993; Vincent and Soille, 1991; Malpica et al., 1997), etc..

In this chapter we have presented region based techniques for the segmentation of volumetric histo-pathological images. We have suitably modified and/or extended the conventional region based segmentation techniques so that they produce acceptable segmentation of the tissue images. The methods presented are 1) Constrained seeded volume growing, 2) Successive pealing and thickening, 3) Three-dimensional watershed with rule based merging technique to reduce the over segmentation. Results of all the three methods are compared subjectively as well as quantitatively. We have also presented an integrated technique which involves both edge-based and region based algorithms. This is shown to be reducing the human interaction with the segmentation process as well as giving acceptable accuracy of segmentation.

Segmentation of 3-D histo-pathological images can be considered as good iff the results show following properties. 1) Complete and detailed isolation of the clustered cells, 2) Minimum over-segmentation and under-segmentation of the cells, 3) Each visually perceivable 3-D cell region has been given a unique label, 4) The segmentation process should be less interactive and the results should be comparable to manually segmented results, 5) The process should be fast and efficient considering the large size of the volumetric

data sets. We have redesigned the region growing algorithms keeping in mind, the above mentioned requirements for the image to be considered as well segmented.

4.2 Constrained Seeded Volume Growing

This method is based on the well-established region growing techniques for similar gray values inside the object region. A region is defined as a connected set of voxels verifying some homogeneity criterion (Chasseray and Garbay, 1984). Similarity of different properties of the voxels belonging to the same cell holds the key to the success of this algorithm. The voxel properties include, intensity, gradient magnitude, global and local morphological criteria, etc.. In most of the earlier experiments (Garbay, 1986; Chasery and Garbay, 1984) the region growing techniques were tested successfully on the simple 2-D images where a single cell is present in the image or segmentation of single cell in a tissue is of interest. In such cases the segmentation becomes relatively less complex. Most of the results shown were on the blood or bone marrow cells where cells can be generally fit into some kind of convexity criteria. As mentioned earlier, we have done experiments on prostate carcinoma images of different patients which are at different carcinomic grades. We found that it is very difficult to constrain the seeded volume growing to simultaneously separate many cells in a tissue, using convexity criteria.

In case of complex 3-D images of a tissue specimen, where several cells are compactly arranged, and the separation between the touching objects is not characterized by high and uniform gradient peaks, more morphological constraints such as size and shape constraints are to be used to obtain optimum results. In many cases interactive correction and use of some heuristic methods besides controlled volume growing is necessary for the complete isolation of the cells. In this method we have implemented the similarity measures based on voxel intensity and intensity gradient magnitude. These similarity measures are made adaptive to the small local variations in the sense that the method of region growing is more robust to the presence of fine textured chromatin and other intra-cellular matters.

4.2.1 Seed Marking

Seeds can be marked interactively by clicking the mouse over cell(s) of interest and considering a small group of connected voxels around the selected voxel to calculate the seed properties. Seeds can also be chosen randomly all over the image. Number of seeds chosen in random methods must be high enough so that all the cells to be segmented will have at least one seed in it. We have used a more reliable and algorithmic approach for automatic seed marking. The method of seed marking is briefly mentioned below.

1. A $3\times3\times3$ six connected structuring element K with unit magnitude is defined.
2. Erode the two tone version of the noise filtered and enhanced image volume by K
3. Measure the size of each eroded individual object in the image. If the object size is below a pre-defined size-threshold (in the present experiment, we have used 80

$\left(\approx 3^5\right)$ voxels size as a threshold), mark that object as *seed* and no further erosion of such seed is done.

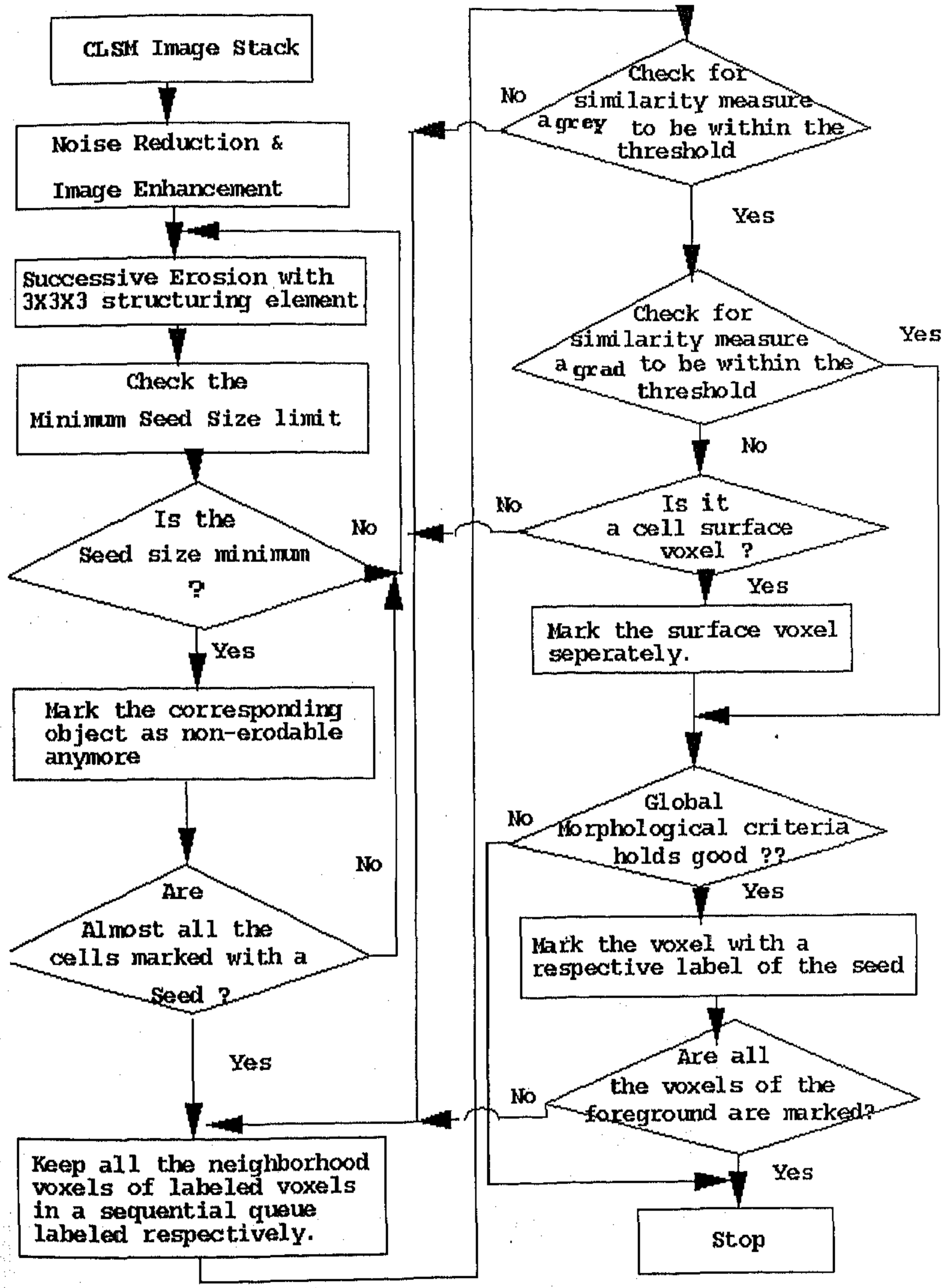

Fig. 4. 1: Flow diagram of the Seeded Volume Growing technique

The similarity measure calculated on the basis of single or a very few seed voxels may lead to wrong results in case of noisy images. This is because the seed point may fall on a noisy voxel resulting in erroneous seed properties. To avoid this we have set a minimum seed size consisting of few ($\approx 3^5$) connected voxels. When a few iterations of erosion assigns a unique seed to every cell, eroding further is not needed. Hence we have incorporated a criterion that after the first three successive erosions, number of individual objects in the image are counted for every alternate iteration. If the number of objects does not change then the algorithm should understand that all the cells are given a unique seed and stop further erosion, i.e., if $n(t)$ is the number of marked seed points at time t after first three iterations of erosion, then the erosion can be stopped if $|n(t)-n(t-2)|=0$. Fig. 4.2(c), shows the marked seeds (white regions) inside the cells. For many data sets where the cells are thinly connected, seed marking by successive erosion results in large seeds representing every individual cells. This results in a better similarity measure to start with. Careful control on the region growing process should thus provide adequate segmentation results provided that intensity/texture variation in the image domain is smooth.

When a single cell is needed to be segmented from a cluster of cells, an approximate center of the cell is selected by clicking such voxel in the image and considering a group or a small region of voxels around the selected pixel as the seed region to start with.

4.2.2 Volume Growing

Once the seeds are properly marked, then they are grown into their neighborhood voxels based on some similarity conditions. This is done by marking the neighborhood voxel as belonging to the cell region represented by the particular seed, if its gray-level properties match with the similarity measure calculated for the corresponding seed region. For a voxel to be considered as belonging to the cell of interest, the following properties should hold good.

1. Voxel gray value should be within the similarity measure threshold limits.
2. Voxel gradient magnitude should be within the pre-defined limits.
4. Global morphological condition such as size, compactness, elongation, etc., should be satisfied.

Similarity measure based on voxel gray value: The general assumption we made is that the voxels belonging to the same cell are approximately similar in their gray level. This may not be true in case of histo-pathological images. hence a data driven adaptive gray level range is used to measure the similarity between a neighborhood voxel and the seed region. If α_{gray} is the gray intensity similarity measure, then $\alpha_{gray}=\left|\mu-u_q\right|$ where u represents the image voxel, $\mu=\frac{1}{n}\left(\sum_{i=1}^{n} u_i\right)$ is the mean gray value of the marked region, n is the number of voxels in the already marked region and u_q is the voxel belonging to the neighborhood of the marked regions which are placed in an ordered queue for testing the similarity. In

case of highly texture images, the similarity measure needs to be normalized as follows.

$$\alpha_{gray} = \frac{\left|\mu - u_q\right|}{\sigma}$$

where σ is the standard deviation of the gray level of the marked regions. The standard deviation of the gray values is given by $\sigma = \frac{1}{n-1}\left(\sum_{i=1}^{n}\left|\left(u_i - \mu\right)^2\right|\right)^{\frac{1}{2}}$.

A threshold range is defined such that if $(\mu - \kappa \cdot \sigma) \le \alpha_{gray} \le (\mu + \kappa \cdot \sigma)$ where κ is an experimentally determined constant, is true, then the voxel satisfies the first and a major condition.

Similarity measure based on the gradient magnitude: This measure helps in marking the cell surface there by stopping the seed growth beyond the cell surface in to neighboring cells. The gradient similarity measure is defined as

$$\alpha_{grad} = \left|\left(\frac{1}{n}\sum_{i=1}^{n}\left|\nabla u_i\right|\right) - \left(\left|\nabla u_q\right|\right)\right|$$

where $|\nabla u|$ gives the gradient magnitude of the voxel intensity. A threshold range $\left(\mu_{grad} \pm \kappa\right)$ is considered for testing the voxel. Here, $\mu_{grad} = \left(\frac{1}{n}\sum_{i=1}^{n}\left|\nabla u_i\right|\right)$. If the voxel gradient magnitude exceeds this range then such voxel is considered as possible candidate to represent the surface of the cells. Presence of intra-cellular matters and fine textured nature of the cell chromatin adversely affects the assumption of uniform gradient magnitude within the cell. This can be rectified to a certain extent by adopting the normalized similarity measure similar to the one explained regarding α_{gray} or by locally smoothing the image before calculating the gradient magnitude.

Implementation: The seeds are first labeled using a 3-D component labeling algorithms as explained in chapter 2. The voxels belonging to immediate spatial neighbors (six connected) of each seed and is not already marked is put in a corresponding queue structure. If $s_1, s_2, s_3, \ldots, s_n$ are the seeds and $q_1, q_2, q_3, \ldots, q_n$ are the corresponding queues for each seed, then queues contain those unmarked voxels which have at least one of their six-connected spatial neighbor as already marked voxel or seed voxel. We have observed that use of six-connected neighborhood instead of eighteen or twenty-six connected neighborhoods for region growing gives more control over the process of region growing but it also slows down the region growing process. Depending on the application a trade-off in this regard should be achieved. For each voxel in the queue, the intensity and gradient similarity is calculated and if they are within the threshold range they are added to the corresponding marked region. If the voxels are not similar then they are checked for being a

noisy voxel or not. This is done by checking for its isolation property. If it is an isolated voxel or a part of small group of isolated connected voxels, showing a dissimilar intensity and/or gradient, it is considered as a noisy voxel within the region of interest and added into the marked region otherwise it is discarded. To some extent this process takes care of fine textural nature of cell cytoplasm. The similarity measures are not updated when the noisy voxel is added to the seed region after checking its isolation.

When the gradient magnitude of the voxel shows high gradient magnitude and falls outside the similarity range, we mark it as surface voxel. After every iteration the morphological criteria for size and shape of the marked regions is calculated. We have used size V, elongation $e = \left(\frac{R_{max}}{R_{min}} \right)$ and the shape factor $\gamma = \frac{A^3}{36\Pi\left(V^2\right)}$ of the marked region as the morphological constraints on the volume growing. If any of the conditions $\left|V(t)-V(t-1)\right| \rangle K_V$ or $\left|e(t)-e(t-1)\right| \rangle K_e$ or $\left|\gamma(t)-\gamma(t-1)\right| \rangle K_\gamma$, are true where K_V, K_e and K_γ are the experimentally determined constants, then the growing of that particular seed is stopped. The constants showing the morphological threshold are experimentally determined for few training data sets and an average of the values is fixed as corresponding morphological thresholds.

Once the volume growing process is over, the resulting image is subject to math-morphological opening as explained in chapter 2. This cuts of the thin and frail connections between different cell regions. Cells which are touching each other and not separated by smooth surface marked by surface voxels are merged. The resulting segmented cells may have holes caused due to dense intra cellular matters which differ in intensity similarity criteria. Such holes are filled using size & shape heuristics as explained in chapter 2. The process of volume growing is stopped when there are no more foreground are voxels left in the foreground or when the morphological criteria fails to hold good.

Use of normalized similarity measure considerably slows down the process of volume growing and should be avoided whenever is possible. Similar problem exists in updating the threshold range for voxel similarity after every iteration. One can simply opt for $(\mu \pm \kappa)$ as the threshold range or can design other data driven threshold values to speedup the process. Another method to speedup the process is to upgrade the similarity measure only when confronted with a voxel which is showing dissimilarity in its properties. Even after upgrading the similarity measure, if the voxel gray-level lies beyond the threshold range then such voxels are not marked as belonging to the cell region. We have used the later method in our implementation. In the present case, since the data sets have undergone rigorous noise reduction and edge preserving smoothing, we have not found much difference in the quality of the results, with or without using σ while defining the threshold range.

(a) (b) (c) (d)

(Contd.)

the marked seeds inside each cell. Fig. 4.2(d), is the result of volume growing. It should be noted that when the cells are not convex, successive erosion technique presented here may result in more than one seed per cell. Thus post-processing and interactive corrections are sometime necessary for complete isolation of touching or overlapping cells.

4.3 Successive Pealing and Controlled Thickening Method

This is one of the simple region growing methods which yield acceptable results in many cases. This is useful in automatically cutting off the touching and overlapping cells. This is also known as erosion-dilation technique (Russ, 1995). Fig. 4.3, shows diagrammatically, the complete process of successive pealing and thickening. We have explained the segmentation of cells in a 3-D image by successive pealing and thickening technique in few steps.

In the first step, the image is converted into two-tone by changing the gray value of the foreground voxels to one in a window-sliced and enhanced image volume. Then the foreground of the two-tone image is subject to a pealing process. Pealing is an iterative process of removing the voxels of the foreground which are having at least one background voxel in its immediate neighborhood. The process continues till a unique signature is obtained for each cell present in the foreground. Care should be taken that no cell signature completely disappears from the spatial image domain. Otherwise, it results in unrecoverable loss of information. To avoid the loss of information, we have set the minimum size of the object that can be subject to further pealing as approximately equal to 100 voxels. This is similar to the process of seed marking. The size threshold is enforced by calculating the size of the objects for every iteration of pealing process. To speedup the whole process, the size threshold is enforced only after first few iterations of pealing. Successive pealing can also be stopped if every cell of interest gets a unique signature within few iterations. Fig. 4.4(b) shows few representative image slices of an image stack after successive pealing. The white regions marked inside each cell are the regions obtained by successive pealing of the volumetric image.

In the second step, the cell signatures are subject to controlled thickening. The thickening process is converting voxels of the background into foreground if the background voxel contains at least one foreground voxel as its immediate neighbor. The thickening is done under the constraint that no two thickened signatures would touch or overlap on each other. The number of iterations for thickening process should be greater than the number of iterations done during pealing. Fig. 4.4(c) shows few representative image slices of an image stack after controlled thickening. In the third step, the thickened image is subject to one-to-one logical AND operation with the two-tone version of the original image volume. This marks the bifurcation between the cells in the cluster. The process is shown diagrammatically in Fig. 4.3.

In the fourth step, the 3-D component labeling algorithm is applied and all the isolated cells in the image are uniquely labeled. After labeling the segmentation process is said to be complete.

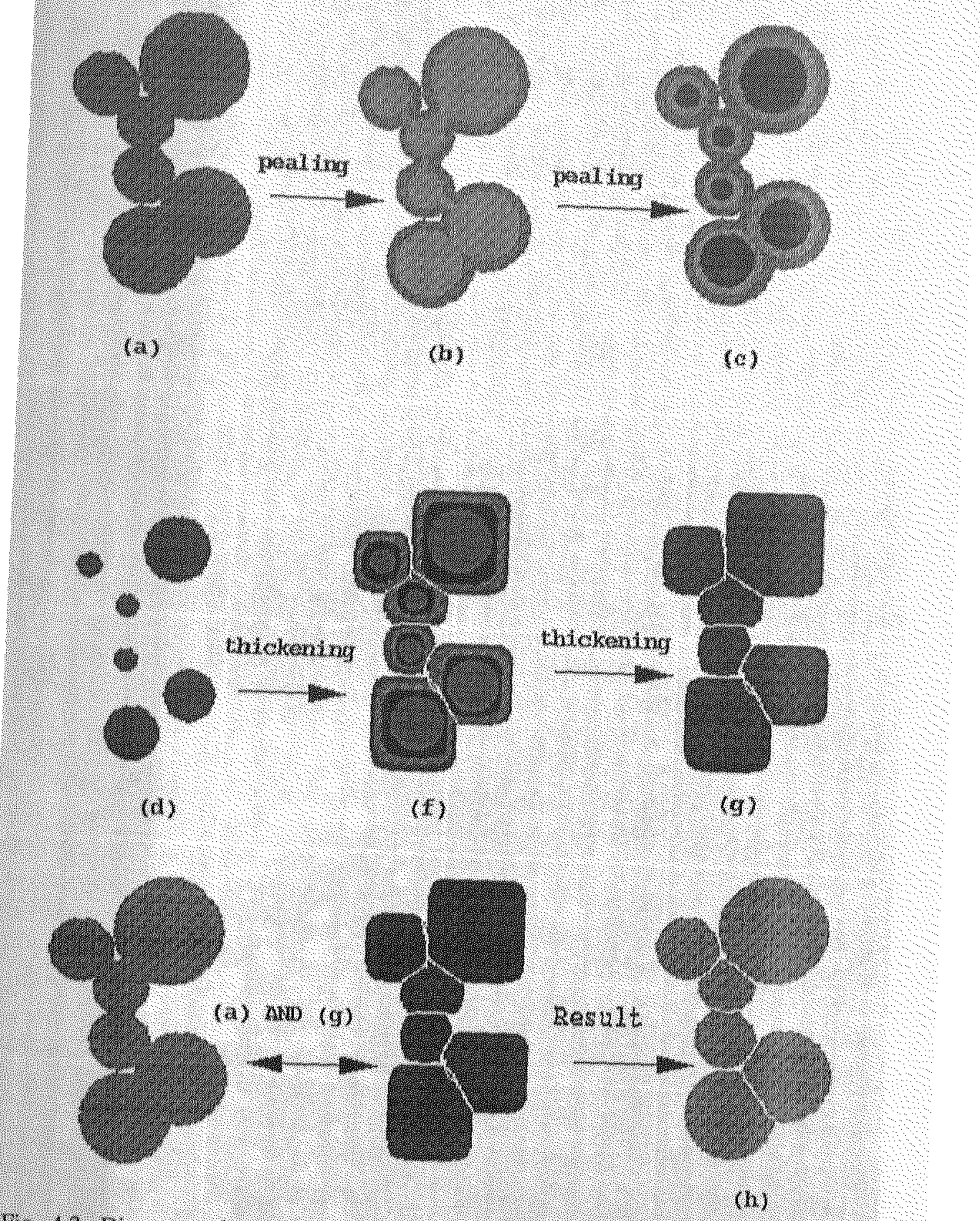

Fig. 4.3: Diagrammatic representation of Successive Pealing and Constrained thickening process for segmenting the cells in a cluster.

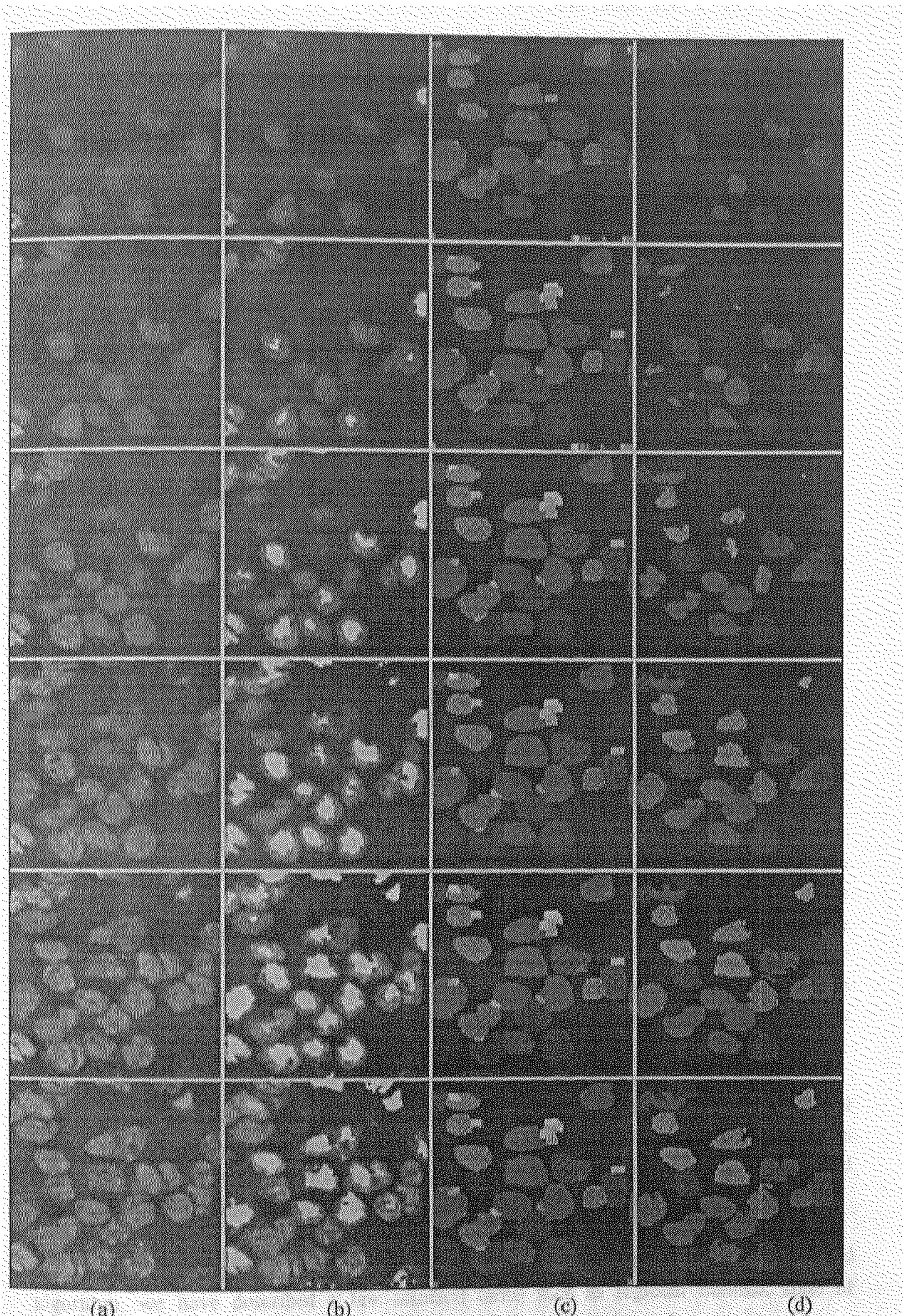

(a) (b) (c) (d)

Fig. 4.3 Result of successive pealing and constrained thickening shown over a sequence of image slices (a) Original image slices (b) After successive pealing (shown as white portion) (c) After controlled thickening (d) Segmentation results

Fig. 4.4(d) shows the result of this method over a CLSM image data set as a sequence of image slices. Fig. 4.10(c) also shows the result of same method on a different data set in comparison with the results of other region based segmentation methods. Only few representative image slices of an image stack is shown. The main disadvantage of this method is that the separation of cells does not consider the presence of local gradient peaks or any other cell boundary or surface features. This can lead to grave errors in calculating the shape and features of the cells. During pealing is a same cell gets two signatures, it invariably results in over-segmentation.

Another method of volume growing is based on defining the zone of influence of each seed of the individual cells on the basis of distance measure. Then the seeds are grown into all the voxels in its zone of influence. The zone of influence of each seed is separated by what is generally known as watershed lines. We have extended the classical 2-D watershed method to 3-D. We have improved the results of watershed algorithm by using a rule based merge technique to reduce over segmentation of the cells resulting in tiny objects.

4.4 Three-dimensional Watershed

Segmentation based on the use of watershed lines to separate the regions has been originally developed in the framework of mathematical morphology (Beucher, 1992; Beucher and Meyer, 1993). When we map the gray-scale image as a topographic surface, the topography can be compared to watersheds. The gray level of each voxel stands for the elevations of the corresponding watershed surface. Though mapping of gray levels as a topographical relief in three-dimensional image is more complex to understand, the algorithm is a simple extension of two-dimensional watershed to 3-D. Also, to separate the regions based on the gray level topography asks for either slowly varying gray level or uniform gray level within the object region.

Watershed algorithm can be described as an iterative region growing process like the earlier two described methods. Briefly, regional minima for each cell in the tissue image are marked first. A zone of influence (ZOI) of each regional minima is marked by calculating the geodesic distance of each voxel from the nearest regional minimum in the foreground of the image. The region grows only within the ZOI of each regional minimum. The skeleton formed while calculating the ZOI which are known as SKIZ surface separate different zones in the image domain.

Watershed algorithms were extensively used for segmentation of histo-pathological images though almost all the work done was on 2-D images. Some of the important works in this regard are of Beucher (1992), Beucher and Meyer (1992), Vincent (1993), Lockett and Herman (1994), Najman and Schmitt (1996), Malpica et al., (1997), etc..

Before going to implementation details and the improvement of the watershed algorithm, we have described a few standard terms such as regional minima, zone of influence, SKIZ, watershed, etc., concerning 3-D objects to be segmented.

The *regional minima* R_i of a 3-D object is defined as a connected group of voxels at the approximate center of the object characterized by the following property. If the shortest distance of this group of connected voxels from the object boundary is d_i, then it is not possible to traverse to another region of distance longer than d_i without traversing through the voxels of distance value shorter than d_i. In simple words, a regional minimum is a group of voxels or a single voxel, belonging to the object and has a maximum distance value from the nearest background voxel than other voxels in the object. Fig. 4.5, shows the concept of regional minima concerning a 3D object.

The *geodesic distance* d_i of a voxel i from the regional minima R_i of a 3-D object in a spatial image domain is the length of a shortest existing path which is included in F and linking voxel i and regional minimum R_i of the object. Fig. 4.5, presents the concept of geodesic distance.

The *zone of influence* (ZOI) of a regional minima R_i consists of all those voxels whose geodesic distance d_i from the regional minima R_i is smaller than their geodesic distance to all other regional minima $R_{j \neq i}$ where $j=1, 2,....,N$, N being the total number of regional minima in the image volume. Fig. 4.6 shows the concept of zone of influence diagramatically. The zone of influence of each cell marker (regional minima) approximately covers the voxels belonging to the respective cells. Analogous to the watershed terms, ZOI can be called as catchment basins.

Most simple way to find the regional minimum is to threshold the distance map such that each cell gets at least one regional marker. For defining the accurate zone of influence of each regional marker, Euclidean distance of all the voxels from the nearest regional marker should be calculated. Calculation of accurate euclidean distance for each foreground voxel from the nearest regional minima is computationally expensive. A very close-approximation to Euclidean map can be used to define the zone of influence of the each regional marker. We have used path generated distance transforms (PGDT) as proposed by the Borgefors (1996) for finding the zone of influence. The algorithm was briefly explained in chapter 3, section 3.3.2.

The *skeleton by zone of influence* (SKIZ) is defined as the surface consisting of those voxels in the foreground which do not fall into ZOI of any particular regional minima R_i where $i=1, 2,....,N$. Voxels of SKIZ surface would have the same geodesic distance from more than one regional marker. This SKIZ surface forms the *watershed lines* separating the zone of influence of different regional minima.

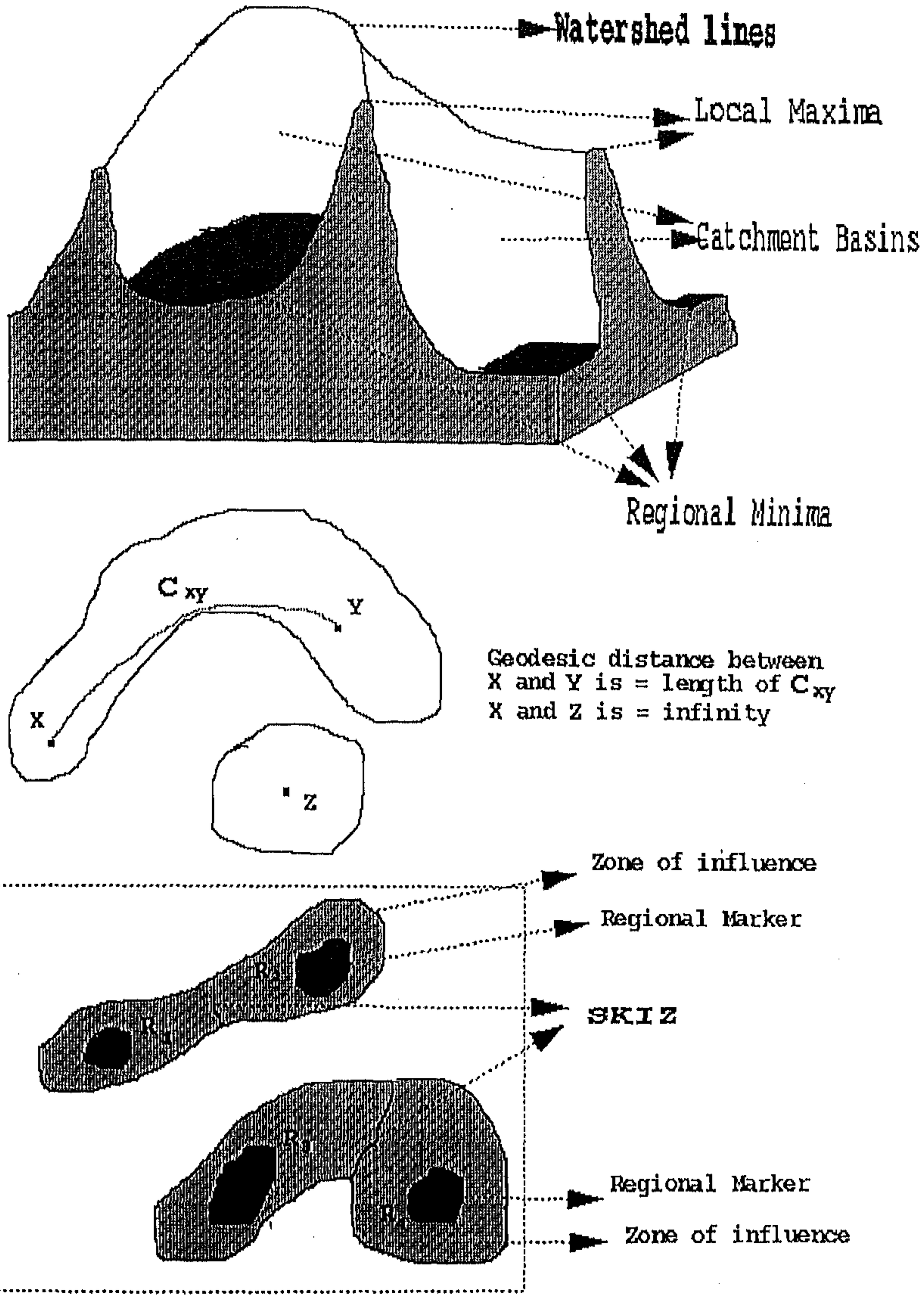

Fig. 4.5: Schematic diagram showing regional minima or markers and the concept of geodesic distance.

Implementation:

We have implemented the method of region growing in watershed based on the work by Vincent and Soille (1991), and Beucher and Meyer (1993), and extended the method with few modifications to encompass the 3-D objects. They have implemented the method in the framework of mathematically morphology. We have used conventional image analysis tools to arrive at the similar results. Here we assume that the image voxels are stored in a simple array and direct access to any of the voxels of the image volume is possible.

Enhanced and window-sliced image stack is converted to two-tone image by changing all the foreground voxel values to 1 and background is kept same i. e., zero. This two-tone volumetric image is used to calculate the geodesic distance map. As stated earlier we have used path generated distance transforms (PGDT) (Borgefors, 1996) for calculating the geodesic distance map. The distance map is then suitably thresholded such that at least a part of each cell region is changed due to thresholding. These regions in the thresholded map is superposed on the distance map as regional markers. Thresholding a distance map at suitable level such that every cell gets a regional marker, can be easily done if all the cell nuclei in the image volume are of approximately same size. Unfortunately that is not the case with the data sets we are working on. This asks for setting the distance threshold value for every new data set to be segmented. One way to circumvent this is to find the marker by successive erosion method which is explained for marking the seeds in controlled seeded volume growing method. Superpose these seed markers as regional minima. Each minimum is labeled using 3-D component labeling algorithm as explained in chapter 3.

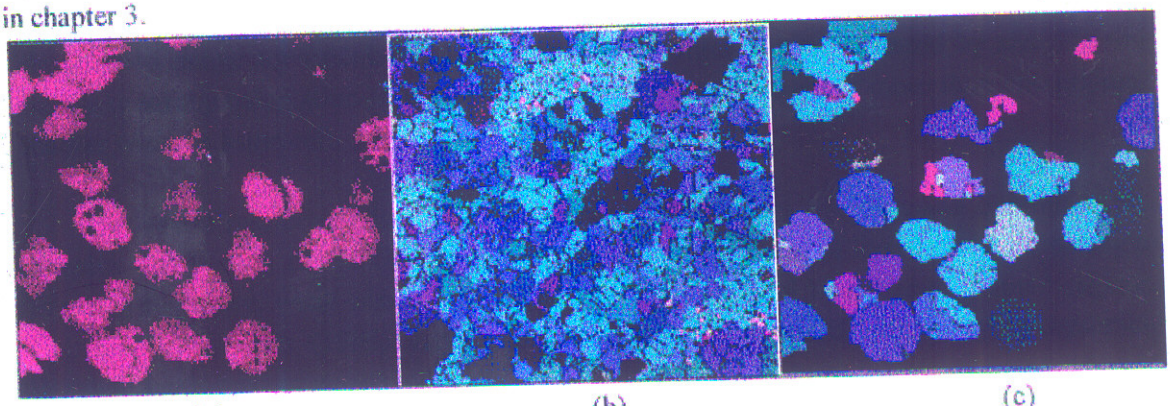

(a) (b) (c)

Fig. 4.6: (a) Original image slice (b) Result of 3-D watershed on un-enhanced image which considers gradient topography for marking the zone of influence (c) Classical 3-D watershed on enhanced image which considers the 3-D distance map for marking the ZOI.

As stated earlier, PGDT technique (Borgefors, 1996) is used for calculating the geodesic distance map. The inverse distance map serves as the map defining the zone of influence of each regional minima. The regional markers are then superimposed on this distance map. Each regional marker is then grown into its immediate neighborhood based on certain condition. The regional minima i is grown into its neighborhood voxel v_j iff the value of -

the v_i in the distance map is lower than the value of regional marker in the distance map. In other words, if v_i is at higher level than the regional marker in ZOI then, the regional marker is grown into voxel v_i .

The process of region growing stops when all the neighborhood voxels of the regional marker have a distance value higher than the voxels belonging to the regional marker or when no more voxels in the neighborhood are left whose level in the ZOI is higher than the regional minima.

4.4.1 Automatic Merging of the Over Segmented Cells

In histo-pathological images, inside of the nuclei is a texture chromatin and the outside is a cytoplasm which is also textured. The texture variation is so dominant that it makes it difficult to discriminate between the contour lines of the cell and the chromatin texture patterns. If we construct the watershed lines directly from such a textured image, it results in a severe over-segmentation as shown in Fig. 4.6(b).

The over-segmentation of the cells by the direct construction of the watershed lines in the image domain, is due to the fact that every regional minimum becomes the center of a catchment basin, i. e. every regional minimum is considered as belonging to a unique cell and it's ZOI is calculated. Even if we use the enhanced and window sliced image for the application of watershed algorithm, some over-segmentation persists as is evident from Fig. 4.6(c). when we automatically choose the regional marker by thresholding the distance map, there is every possibility that same cell may get more than one regional minimum. Successive erosion also results in more than one marker seed per cell. The holes which appear inside the thresholded image for calculating the distance map which are not restored by size filtering results in wrong calculation of the distance map and hence results in more than one regional marker within a same cell.

Several researchers have tried to address this problem (Najman and Schmitt, 1996; Beucher and Meyer, 1993). One possible method is to make use of hysterisis thresholding to suppress the noisy, weak contours, representing the watershed lines between small regions. Najman and Schmitt (1996), have listed various reasons for ill suitability of hysterisis thresholding in case of watershed. They are

1. Hysterisis thresholding is suitable for edges and it produces non-closed contours while watershed contours are already closed contours which are obtained as a complimentary to the set of regions,

2. Hysterisis thresholding on watershed segmentation produces barbs, etc..

Some of the proposed method to overcome the over segmentation problem is the geodesic reconstruction (Beucher; 1990), the hierarchical segmentation (Beucher and Meyer, 1993), hierarchical segmentation using dynamics of contour (Najman and Schmitt, 1996),

etc.. We have proposed an extension to 3-D watershed technique which identifies the over-segmented objects based on simple size & shape features and merge them with their parent cell. Instead of finding one marker for each object at the initial stages, which is a highly complex to make it automatic, we allow the watershed to build on the enhanced image volume. After getting the first stage of segmented results, we identify the over-segmented objects and merge them with the parental objects. Merging takes place under some size, shape and connectivity conditions.

Let N be the total number of segmented objects due to the application of 3-D watershed segmentation method. It means, there were N regional markers separated by a watershed surfaces. Let T_{size} be the size threshold, i. e. a cell should have a minimum size of T_{size}. All the tiny fragments of the cells whose sizes are below T_{size} are considered as noisy and are merged with corresponding parent cell. We assign fragment '*a*' to a parent cell '*A*', if, the following conditions hold good.

1. '*A*' and '*a*' should be touching neighbors
2. If '*a*' is sharing its boundary with more than one large cell fragment, then the length of the boundary it shares with '*A*' should be larger than the length of the boundary it shares with any other touching large object.

If these conditions are satisfied then the fragment '*a*' is merged with the parent cell '*A*'. To reduce the possible errors due to group of tiny fragments being sandwich between two large objects, we merge those fragments first which are touching neighbors to large objects. Also, after merging one fragment to a large object, the same large object is considered only after all the other large objects are checked for merging possible single fragment. In case, when fragment '*a*' does not have any large touching neighbor but has many small fragments as its neighbors, then there is a possibility that a single cell might have been over-segmented to such a level that there is no fragment of size above threshold T_{size} belonging to that cell. In such cases, all the tiny fragments which are touching each other and not connected to a larger object, are merged to form a single object. If this merged object is above the threshold T_{size} then it is considered as a cell otherwise it is discarded as a noise artifact.

Fig. 4.7, shows the result of automatic merging of the small objects in the over segmented image volume. There can be still many cases where large individual cells are found to be segmented into two or three different objects. This may be due to the fact that such artifacts do not fall into the size threshold chosen by trial and error methods.

This merging based on heuristic method gives better result than the result obtained by hysterisis thresholding. Table. 4.1 gives the comparative result of segmentation by classical 3-D watershed with suppression of over segmentation by selective marker techniques (Beucher and Meyer, 1993) and by rule based merging method presented in this chapter.

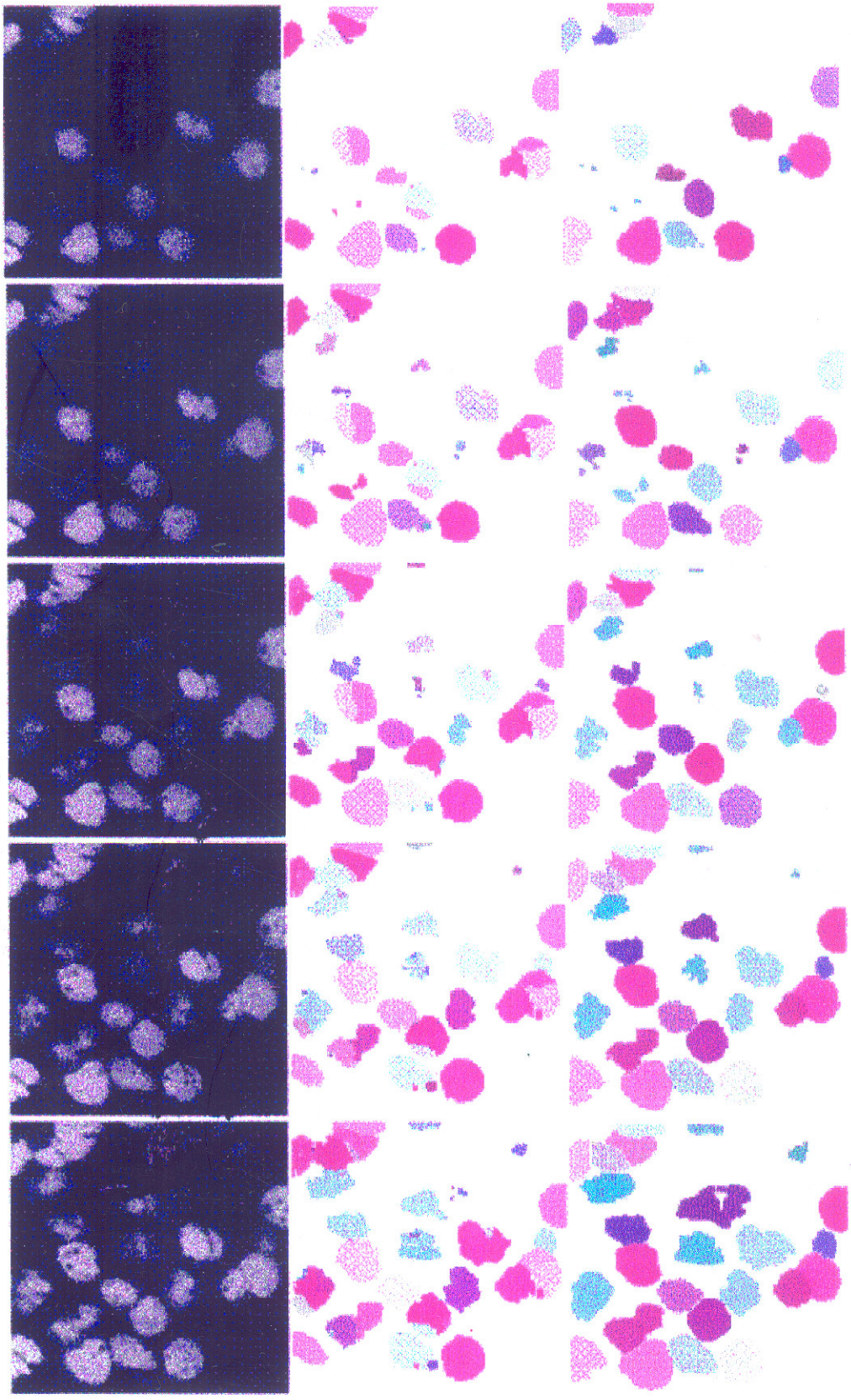

(a) (b) (c) (contd.)

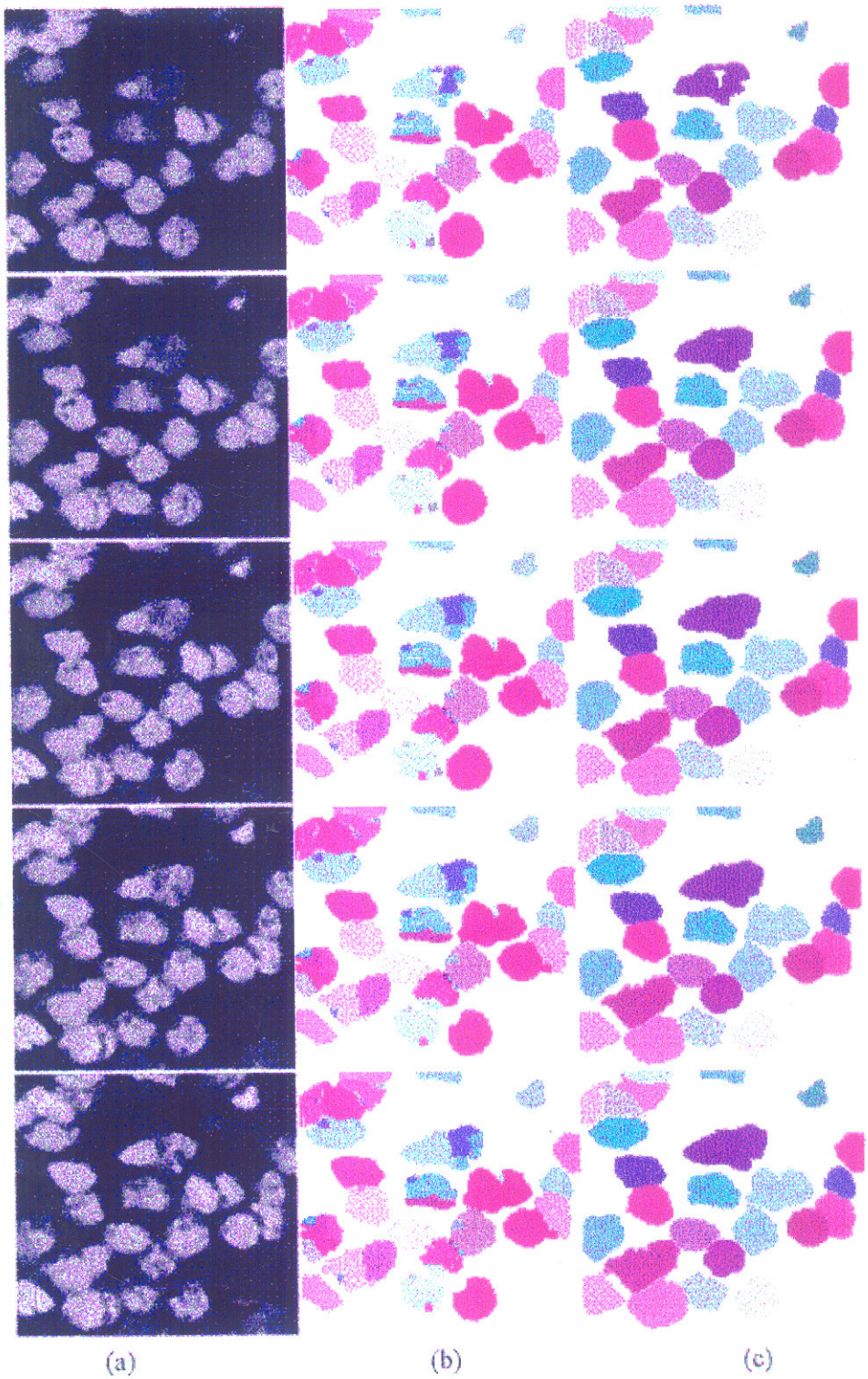

Fig. 4.7: Result of modified watershed algorithm on volumetric tissue images (a) Original image slice (b) After classical 3-D watershed on enhanced image stack (c) After automatic merging of the tiny fragments.

Sl. No.	Actual number of cells present	Number of cells by simple 3-D watershed	Number of cells by selective marker technique	Number of cells by rule-based merging technique
01	23	42	24	24
02	31	56	31	32
03	18	29	23	21
04	42	67	47	38
05	26	38	29	26
06	12	19	12	12
07	05	05	05	05
08	31	49	34	33
09	28	43	31	31
10	37	56	42	40
11	11	11	12	13
12	12	12	12	12
13	16	21	18	17
14	28	44	30	31
15	07	09	07	08
		%error=53%	%error=9%	%error=2%

Table. 4.1: Comparison of different methods to reduce the over-segmentation

4.5 Comparative study

In this section we have compared the performance of region based segmentation techniques. A subjective as well as quantitative comparison of these methods is also presented. The comparison is done in the context of the segmentation of volumetric histo-pathological images.

In the seeded region growing, the marked region gets extended to the neighborhood voxels based on the voxel similarity conditions constrained by global and local morphological criteria. In a highly textured image volume, the seeded region growing fails to produce the proper segmentation due to large dissimilarities in the voxel properties. The low and uneven gradient magnitude characterizing the surface of the cells makes it difficult to mark the surface voxels and hence in most of the cases, smooth surface will not appear between touching and overlapping cells. The normalization of the similarity measure to reduce the effect of noisy peaks in the voxel intensity, results in slowing down the process. An extensive pre-processing is needed to smooth out the fine texture and influence of noisy

voxels on the volume growing. In the same time the edges which constitutes the cell boundary should be enhanced so that a smooth surface can be marked during region growing.

In malignant tumor tissue specimen images, the cells can not be put under strict convexity and shape constraints. This makes it difficult to define the global morphological criteria and/or to aggregate the voxels to fit the cell under some convexity assumption. More often seeded volume growing causes the under segmentation due to over growth of the seed of one cell into the touching and/or overlapping neighboring cell. A stringent similarity measure to check this over growth would fail the region growing due to textural nature of the cell cytoplasm as well as other intra-cellular matters. Also, when the surface separating the two touching cells is not detected properly, the marked regions are merged causing the under-segmentation. In a highly textured cell, the growth may be too slow and stop before marking the complete cell volume. Since many voxels fall outside the similarity measures, they may left unmarked even after the process of volume growing is completed. This is also one of the reasons for under segmentation.

The main advantages of the seeded volume growing method is that it is simple to understand and easy to implement. With a reasonable amount of pre-processing, seeded volume growing technique produces acceptable results. This method can also be used to define a small region around the contour of the marked regions where an advanced techniques such as active contour models or active surfaces can be used to precisely locate the cell surface. When the shape of the cells are more or less similar and there are very few cells clustered together, this technique gives efficient segmentation.

The successive pealing and thickening method is also very simple and effective. When the precision of the segmentation is not important as in finding the cell density, testing the clustering property of the cells, etc., this technique can be used for segmentation. It is simple and an effective means to isolate the touching and overlapping cells in a tissue image. One of the problems in this technique is, a cell may erode to more than one fragment while successive pealing is done. Each fragment is then treated as a separate object while thickening. This results in over segmentation. The automatic merge heuristics may not work in this case as the objects in the segmented image may have similar size. A disadvantage of this method is that the segmentation of the touching and overlapping cells is not along the gradient variation but is guided by dilation of the seeds. This results in a wrong marking of boundary where cells touch one another. In case the image containing cells which differ predominantly in their size and shape characters, the segmented image, may not reflect the variation of shape and size of the cells as in original image. Moreover, the precision of the segmentation is limited by the local thresholding done on the original intensity image. In both seeded volume growing and successive pealing technique, labeling the isolated object after every iteration of erosion to avoid loss of information due to complete erosion is a time consuming process considering the number of objects to be isolated and the size of the data set.

In the three dimensional watershed algorithm, the regional minima gets extended to the neighborhood voxels based on the geodesic distance value of the neighborhood voxel or its level in the zone of influence of each regional marker. Each cell should have only one

regional minima/marker to avoid the splitting of a single cell into different object regions causing the over segmentation of the image volume. Sometimes an interactive correction of the segmentation results is necessary. 3-D watershed technique with a rule based merging is relatively complex process and the precision of the result is very much dependent on proper selection of regional markers and the marking of zone of influence of each regional minima. Here also the accuracy is limited by the local thresholding done to calculate the geodesic distance map.

Table 4.2 gives the comparative results based on ability to mark correct number of cells by each region based method. Table 4.3 shows the comparative results of seeded volume growing technique, successive pealing-thickening and 3-D watershed with merging with respect to the ability to give the precision in measuring the features such as percentage of symmetric difference in total volume and 3D shape factor. The relative difference in volume can be calculated as follows. If V_{man} and V_{auto} are the volume of the manual segmented and automatically segmented cells respectively. Then,

$$Diff. = \frac{V_{man} - V_{auto}}{V_{man}} \times 100\% .$$

Sp. No.	Manual Segmentation	Controlled (seeded) Volume Growing	Successive Pealing and Thickening	3D Watershed with heuristic merging
1	23	21	23	24
2	31	26	35	32
3	18	18	18	21
4	42	33	48	38
5	26	25	31	26
6	12	12	12	12
7	5	5	5	5
8	31	27	30	33
9	28	21	37	31
10	37	33	41	40
11	11	11	11	13

Table 4.2: Comparative results of number of cells uniquely labeled by different region based segmentation methods.

Sp. No.1	Manual Segmentation		Controlled (seeded) Volume Growing		Successive Pealing and Thickening		3D Watershed with heuristic merging	
Cell No.	Relative differenc.	Shape factor	Relative differenc.	Shape factor	Relative differenc.	Shape factor	Relative differenc.	Shape factor
1	0%	0.656	+5%	0.638	+7%	0.791	+4%	0.645
2	0%	0.621	-2%	0.577	+3%	0.633	-2%	0.593
3	0%	0.857	-6%	0.839	+4%	0.932	-5%	0.902
4	0%	0.633	+6%	0.629	+7%	0.519	+3%	0.647
5	0%	0.757	+4%	0.739	+4%	0.780	+5%	0.785

Sp. No. 2	Manual Segmentation		Controlled (seeded) Volume Growing		Successive Pealing and Thickening		3D Watershed with heuristic merging	
Cell No.	Symm. differ.	Shape factor	Symm. differ.	Shape factor	Symm. differ.	Shape factor	Symm. differ.	Shape factor
1	0%	0.581	+7%	0.570	+7%	0.463	+5%	0.563
2	0%	1.221	+5%	1.416	+5%	0.971	+3%	1.201
3	0%	0.587	+3%	0.52	+5%	0.633	+3%	0.614
4	0%	0.633	-4%	0.642	+6%	0.656	-4%	0.455
5	0%	0.589	-6%	0.552	+3%	0.598	-5%	0.575
6	0%	0.460	+1%	0.453	+7%	0.476	-2%	0.483

Sp. No. 3	Manual Segmentation		Controlled (seeded) Volume Growing		Successive Pealing and Thickening		3D Watershed with heuristic merging	
Cell No.	Symm. differ.	Shape factor	Symm. differ.	Shape factor	Symm. differ.	Shape factor	Symm. differ.	Shape factor
1	0%	0.988	+3%	1.134	+5%	1.247	+4%	1.122
2	0%	0.831	-8%	0.756	+3%	0.873	-3%	0.783
3	0%	0.569	-3%	0.578	+6%	0.591	-1%	0.591
4	0%	0.683	+4%	0.605	+5%	0.671	+2%	0.675

Table. 4.3: Comparative study of different region based segmentation method corresponding to their ability in measuring simple features. Results are shown on few selected cells of three representative image data.

4.6 An Integrated Approach for Segmentation

It is generally known that combining different methods of segmentation gives good result. This general principle of integrating different methods is well accepted in computer vision. Grinekar (1980), was the first published work, where an integration of the different methods was used. In this work, edge detection was done in the specified region around the borders of the segmented region obtained by region based techniques. In the approach by Anderson et al. (1987), it was assumed that number of regions was approximately known and this information was used to estimate the parameters of an edge detection process. The result of the edge detection was then used to initialize and assist a region growing process. But in many of these works, the results are shown either on the artificial images or on the real images where objects are well isolated. When ever an attempt was made on a complex real life image, the results were found to be poor.

In the integrated approach for segmentation by Pavlidis and Liow (1990), a split and merge algorithm is first used with the parameters that results in over-segmented image. Then region boundaries are eliminated or modified on the basis of criteria such as integration of

contrast, variation of the image contrast along the boundary, etc.. The approach was not a toggling approach in the sense that either boundary based or region based techniques were used first and the algorithm would not revert to a similar technique for refining the results. For obtaining better results, enhancement of the intermediately results and filtering of the noisy edgels has to be done before approaching the next stage of a hierarchical approach. As per our knowledge, integrated approaches for segmentation of cells is not done earlier and the result of integrated approaches on a real life 3-D images has not been tested.

We have designed an integrated approach based on the methods and results obtained by applying different edge and region based techniques explained in chapter 3 and 4. It is basically a refinement process where edges and regions of the cells of interest are refined automatically in an hierarchical approach. We have not only integrated different segmentation techniques but also used image enhancement and filtering of the noisy objects, etc., in the integration. This has given a vastly improved results as noise and unwanted edgels are reduced in the intermediary stages. Heuristic region merging techniques are also incorporated to reduce the over-segmentation of the object in the intermediary stages. Additionally, we have used edge-based and region based techniques more than once in a whole process till we get a satisfactory result. The proposed approach is completely automatic and found to give acceptable results even on complicated image data sets. Fig 4.9, shows the block diagram of the steps involved in integrated approach.

In the proposed approach we perform the integration of region based techniques and the edge based techniques by toggling between the different techniques till the complete and precise segmentation is obtained. The whole approach is divided into two stages. They are,

1. Coarse Segmentation,
2. Refinement.

In the coarse segmentation step, different low-level segmentation techniques are integrated to segment the cells in a cluster and to obtain an approximate closed contour as a boundary of each cell. This stage involves noise reduction, boundary enhancement, merging to reduce the over-segmentation, etc., in addition to the integration of edge detectors, seeded region growing or watershed techniques. Some times, based on the visual evaluation as well as the computational time required to get the coarse segmentation, we have used successive pealing and thickening method instead of seeded region growing and watershed techniques to isolate the regions belonging to different cells.

In the refinement step, the boundary of the isolated region is refined by the process of energy minimization as explained in chapter 3. Once the boundary or the surface of the cells are fine-tuned to give the precise segmentation of the cells in a cluster, the cells are labeled using 3-D component labeling algorithm and feature extraction process is started. We have explained the integrated approach in few steps without going into much details of each segmentation techniques as most of them are explained in detail in chapter 3 and chapter 4.

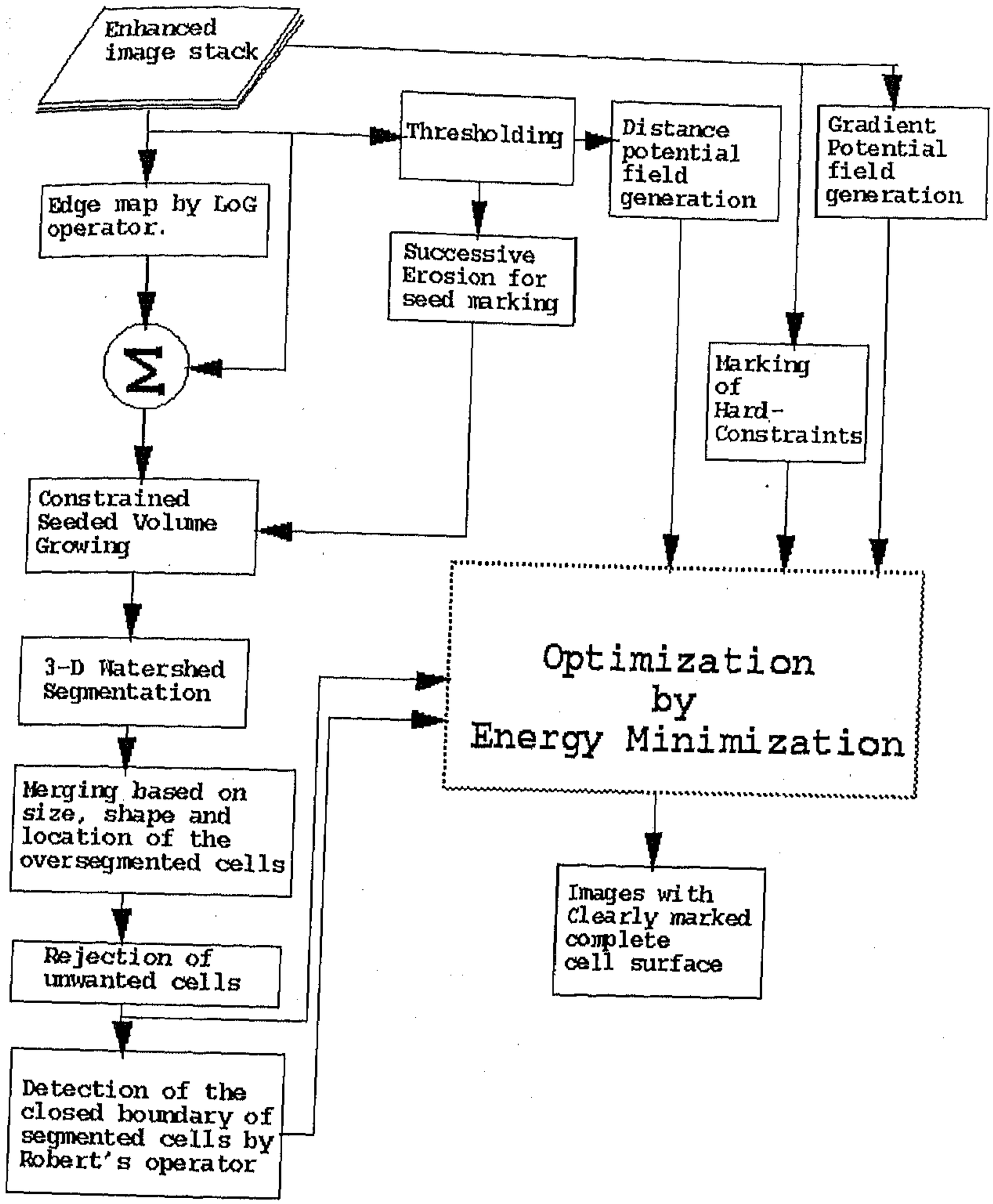

Fig. 4.8: Block diagram of the integrated approach for segmentation

4.6.1 Coarse Segmentation

In the first step, all the enhancement and noise reduction techniques such as intensity restoration, directional smoothing, interpolation, etc., which are explained in chapter 2, are applied on the image stack. The edge detection based on simple edge detectors such as Roberts or Prewitt edge operator is first applied on enhanced image stack. The resulting edge

map is then suitably thresholded and size filtered so that much of the noisy edgels are removed. This edge map is then used to enforce the boundary around the cells. Let f_{en} be the boundary enhanced image stack. A two tone version of the image stack is obtained by converting all the foreground voxels to white i. e., gray value 1. The background voxels are already made zero during window-slicing operation of the image enhancement process.

The second step is an important stage in coarse segmentation. Depending on the complexity of the image one or more region isolation techniques explained earlier in this chapter has to be used. If the number of cells in the image is relatively less and all the cells are having more-or-less regular shape, then seeded volume growing can be a best starting point. Here, the two-tone version of the image stack is subject to successive erosion to mark the possible seed points which are unique for each existing cell in the image.

The seeds are grown by marking the neighborhood voxels as belonging to the cell region if the voxel satisfies the intensity and gradient similarity properties as explained earlier in section 4.2. We have done away with the morphological criteria as the coarse segmentation stage is not expected to give precise segmentation any way. The enhanced boundary of the cell stops the growth of the seed beyond the respective cell boundary in most of the cases. Due to very low and uneven gradient magnitude at the places where cells touch each other or overlap, two separate regions may get merged as the surface voxels may not be strong enough to be separately marked while the seeds are grown. Also when the successive erosion to mark the seed is stopped automatically, two seeds of close cells may still be spatially connected thus clubbing the two cells under a same region. In such cases, the seeded region growing can be followed by 3-D watershed technique. Since the geodesic distance map generated with the help of a segmented result from the seeded volume growing, is better than the one calculated from a simple thresholded image, the accuracy of the result of watershed will be close to the ideal segmentation. In case the seeded volume growing gives necessary isolation of the cells of interest, the third step of the coarse segmentation is simply skipped. To lessen the human interaction in decision taking, we go through the third step if the image contains large number compactly arranged cells.

In the third step, the result of the seeded region growing technique is subject to further segmentation based on an extended watershed algorithm. A path generated distance map of the boundary of the segmented regions is generated (Borgefors, 1996). The inverse distance map is considered as a geodesic surface defining the zone of influence. The groups of connected voxels having a distance value below a pre-defined threshold are considered as regional minima. Then a classical watershed algorithm is applied as explained earlier in section 4.4.

The over-segmentation is reduced by recognizing the over-segmented objects and tiny fragments of the objects by size and other connectivity properties. They are merged to the parent cell under specific criteria defined to find the belongingness of the fragments to a particular cell. These criteria are explained in section 4.4.1. The result is further subject to 3-D cell re-labeling before selecting the cells of interest.

In the fourth step, the unwanted cells in the image are rejected by clicking on those cells and deleting the voxels of corresponding label. Generally we keep all the cells which are fully represented in the image volume as cells of interest. Those cell which are truncated are automatically detected by checking the cell signature size in the first and last XY, YZ and XZ planes of the image stack. If the signature of the cells in these planes are above a pre-defined threshold, such a cell is considered as truncated and hence are left out of the further processing steps. We have used a signature size of 625 voxels as a threshold to consider cell truncation. This marks the region of interest in the 3-D image with the voxels of each cell region is approximately separated or labeled. This step ends the first stage of coarse segmentation. Fig. 4.9(b) shows the final result of coarse segmentation.

In some cases, application of either seeded volume growing or watershed algorithm results in unacceptable coarse segmentation. Fig 4.10(b) shows one such example. In such cases we have used successive pealing-thickening algorithm to isolate the touching and overlapping cell regions. The reason why we don't use the successive pealing and thickening algorithm on all data sets is, it is time consuming and in the complicated images of varying cell features, the region isolation is found to be largely lacking in precision.

4.6.2 Refinement

Once the approximate region of the cell is marked, it is easier to search for the location of the cell surface in a small region around the boundary of the isolated regions found by coarse segmentation. We have done the refinement process using active model optimization technique.

The boundary or the surface of the cell regions in a coarse segmented image is obtained by simple search operation. A foreground voxel is marked as a boundary voxel if at least one of its immediate twenty-six connected neighbors is background voxel or is belonging to different region in the foreground. The closed boundary or surface of the cell regions thus obtained is considered as initial active model for fine tuning the boundary location to the required precision. Fig 4.9(c), shows the boundary/surface of the cell region thus obtained and initialized as a initial active model around the respective cells.

From the coarse segmentation results we can define a small region in which the actual boundary of the cells fall. This is done by using erosion, dilation operators. The isolated regions as obtained by the coarse segmentation is separately dilated using a $3\times3\times3$, twenty-six connected structuring element. Similarly, an eroded version of the coarse segmentation result, is also obtained. The two-tone versions of the dilated and eroded images are subject to one-to-one X-OR operation. The resulting image defines a small region around the boundary of the cell region in a coarse segmented image. The active models are then made to deform and converge to the appropriate location within this region.

The total potential energy of the initial surface or boundary model is subject to minimization. The external energy is calculated from the diffused gradient field of the original image. Here we have not used any distance potential as the initial surface model is very close

to the true locations and the capture range of the diffused gradient field is extended to all the voxels in the defined region by smoothing and scaling process as explained in section 3.3.2.

The initial model surface being very close to the actual surface of the cell even where the surface concavities and protrusions exist, hard constraints or penalty terms need not be used. The region based information obtained from the coarse segmentation stage is used to deal with the problem of closely located cells having strong boundary features. The problem of simple connectedness or the cell division, etc., does not arise as the initial boundary or surface of the cell is available at each image slice of the stack.

The result of the active model optimization is considered as indicating the precise boundary or surface of the cell. Fig. 4.9(d) shows the result of active model optimization. The boundary or surface obtained by the active model optimization is superposed on the original image stack to isolate the touching and overlapping cells. The resulting image is again subject to 3-D component labeling. In case application of a 2-D approach for active model optimization, the resulting contours are subject to 2-D contour interpolation and the surface of the cell is reconstructed from the contours (Boissonat, 1988).

Fig. 4.9 and Fig. 4.10, shows the result of integrated approach for automatic segmentation of the cells in a three-dimensional tissue image. Results are shown as a sequence of image slices. Only few image slices are shown as it is enough to prove the merit of integrated approach. In Fig 4.9, seeded region growing and three-dimensional watershed with automatic merging is used for coarse segmentation of the cell regions while in Fig. 4.10, successive pealing and thickening algorithm is used. Fig. 4.10, also shows how 3-D watershed with merging techniques may still produce erroneous segmentation for some type of data sets.

By subjective evaluation of the results, one can easily conclude that the integrated approach gives best results. The major advantage of the integrated approach is not only the precision with which the cell surface is marked but also complete minimization of the human interaction in the segmentation process. We have not come across any such methods in the multi-dimensional histo-pathological image analysis. It may not be proper to use the integrated approach always. Integrated approach takes more time compared to any of the individual approaches. Based on the need of precision and for what purpose the tissue image is being segmented, one has to choose the proper method of segmentation.

4.7 Discussion

Region based segmentation methods are simple and easier to implement. Compared to simple edge detectors, region growing methods are more efficient in the sense that no complex processes are needed to reduce the error in segmentation. The region based methods are useful to measure the features such as size, eccentricity etc., of a cell of interest. Another advantage of region based methods is that they give us a choice to choose the cells of interest for segmentation. The region based segmentation methods presented in this chapter can be-

said as self-contained processes in the sense that no human interaction is needed during the segmentation.

The seeded region growing method is more similar to the watershed process of region growing. There are several other region based methods such as split and merge techniques, multilevel thresholding, etc., which, follow slightly different techniques for segmentation.

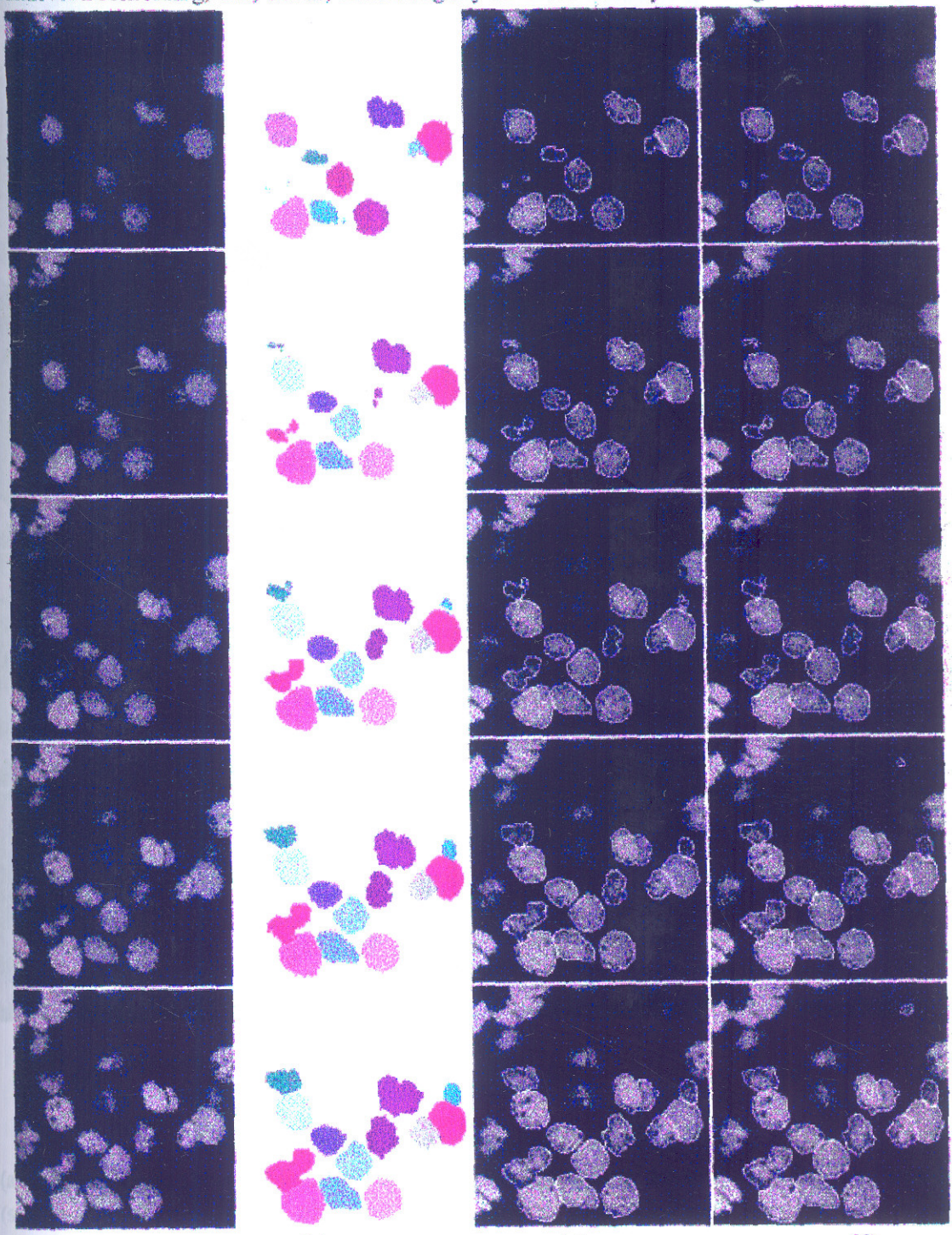

(a) (b) (c) (d)

(Contd.)

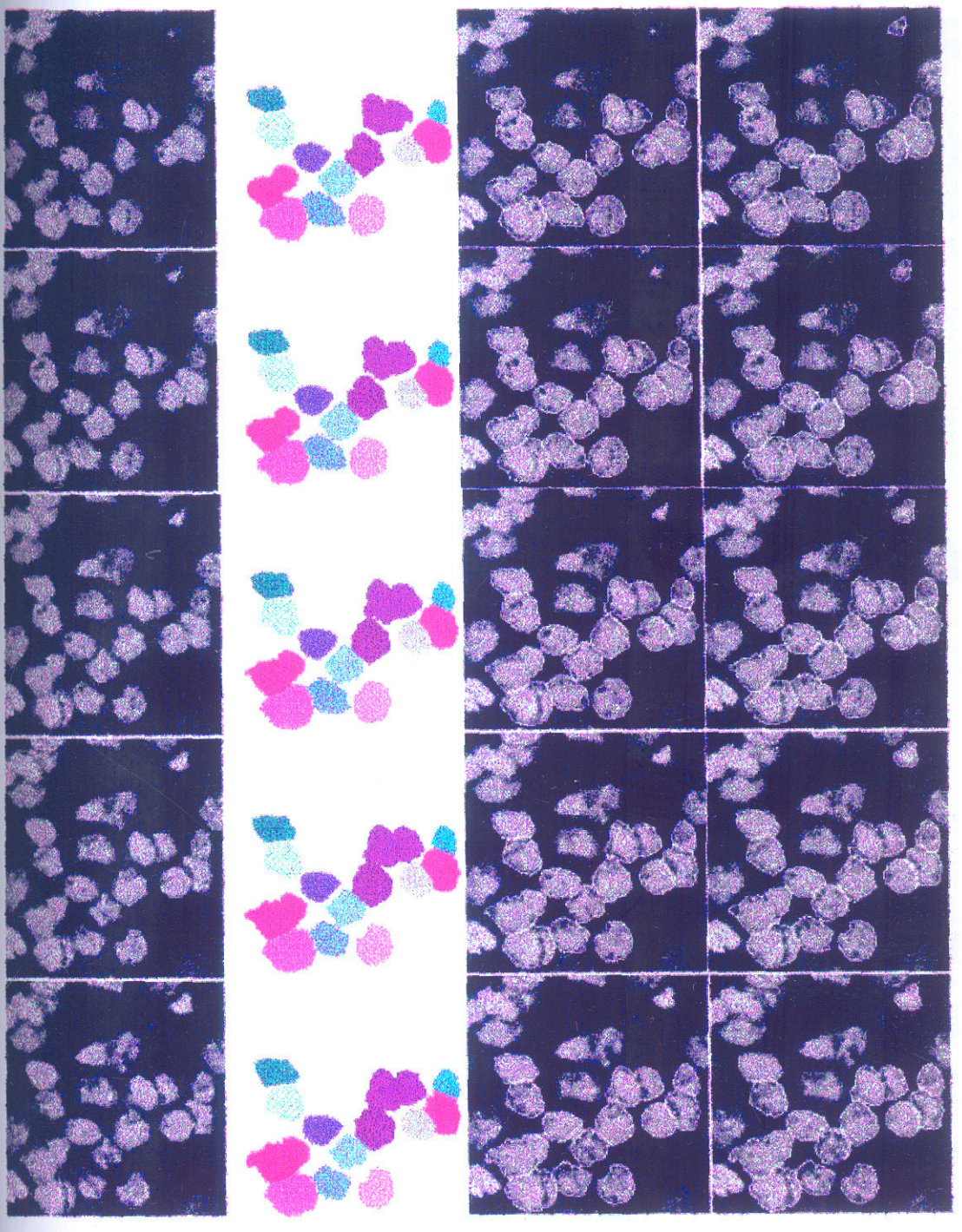

Fig. 4.9: Comparative result of cell surface marking

(a) Original Image slices (b) Result of coarse segmentation after deleting the cells of no interest. (seeded region growing and classical 3-D watershed with rule-based merging is used) (c) Initialized surface model around the cells of interest (d) Result of energy-minimization.

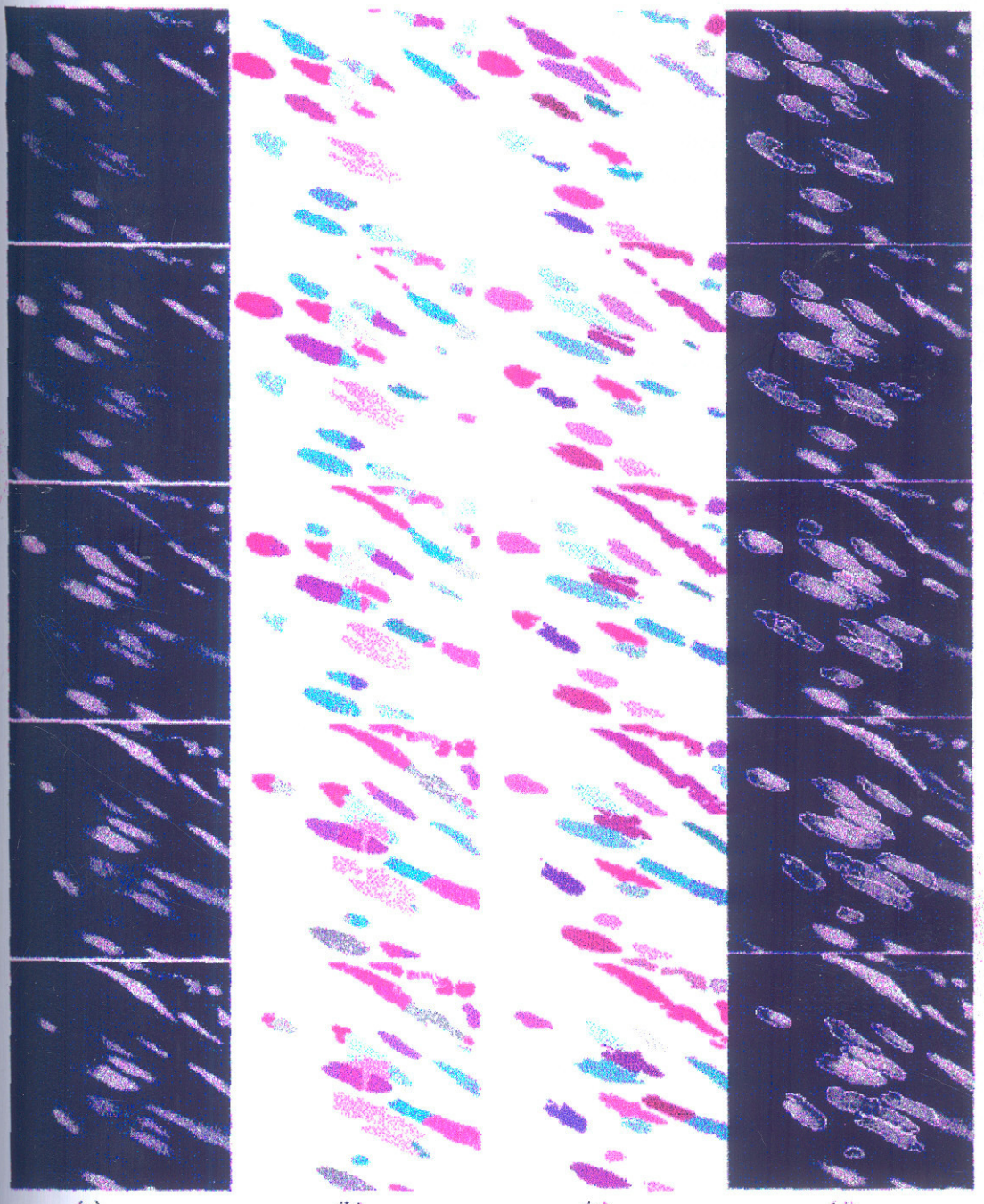

Fig. 4.10: Comparative result of cell surface marking
(a) Original Image slices (b) After 3-D watershed and merging (c) After successive pealing and thickening (d) Result of energy minimization to obtain precise segmentation.

The choice of similarity criteria, the noise present in the images, the fine textural nature of the cell cytoplasm, etc., upsets the results of segmentation in case of region based techniques. The result of region based segmentation may not be very accurate.

It is evident from the results and discussion of the integrated approach that the combination of the edge and region based techniques can provide the best possible segmentation with minimum human interaction. One reason may be that the initial coarse segmentation defines a smaller region in the image domain where we can search for high gradient peaks to form the closed boundary or surface of the cells. This reduces the use of complex mechanisms to remove the noisy edgels which results when edge-detector is used to mark the surface of the cells. The integrated approach has to be further improved to speed up the process. The ambiguity in selecting the proper technique for coarse segmentation can also be reduced by some kind of heuristic decision making based on the total size of the foreground. This may give an approximate idea about the cell density and hence the ratio of the foreground to background size can be used as deciding factor for the proper choice of the coarse segmentation technique. Though we have not implemented this, this is one of the ideas we are proposing for our future work. Also the quantitative evaluation of the results obtained by integrated approach has to be compared with other methods to ascertain its accuracy.

Chapter 5
Quantitative Evaluation of FISH Signals

5.1 Introduction

Malignancy related feature evaluation is useful in the prognosis of the carcinomic patient. Fluorescence in Situ Hybridization (FISH) signal count per cell nuclei is one of the important and useful malignancy features (Zitzelsberger et al., 1994). In molecular pathology, FISH signal counting along with morphological grading, staging and tumor size can be used as an important prognostic tool. FISH, using centromere-specific DNA probes allow the detection of numerical chromosome aberrations in the interphase nucleus and are generally referred to as 'interphase cytogenetics' (Hopman et al 1991).

FISH has made it possible to stain selectively various DNA sequences in interphase cell nuclei (Netten et al, 1996). The DNA sequences may be chosen to detect specific abnormalities or to facilitate the process of identification and quantification of numerical and structural chromosomal abnormalities. The number of FISH components indicates the gain (trisomy) or loss (monosomy) of certain base-sequences in deoxyribonucleic acid (DNA). Several researchers have shown the reliability of this technique for an evaluation of numerical chromosome aberrations (Alers et al., 1995, Herrington et al., 1995). To enable a correlation of FISH analysis and histo-morphological pattern, the FISH evaluation procedure was modified for its application on routine paraffin-embedded tissue sections (Dhingra et al., 1994)

From the currently available knowledge on the interphase analysis of paraffin-embedded tissue section from prostatic carcinoma, gain and loss in chromosome #7, #8, #10, #17, X, Y, are found to be associated with malignancy potential (Alers et al., 1995, Zitzelsberger et al., 1994). A large variation in the FISH count was shown to be associated with high histological grading (Baretton et al., 1994) and an advanced stage of disease (Henke et al., 1994). The quantitative evaluation of the loss or gain in DNA is useful in qualitative diagnostic pathology. Studies (Johnson and de Nogueira, 1981; Babu et al., 1990) have shown that trisomy of chromosome #7 is found in malignant and non-malignant tumors of lung, kidney, brain, as well as in prostate. Zitzelsbergar et al., (1994), have shown that the trisomy of chromosome #7 may be used as prognostic factor because of correlation with the development of lymph node metastasis and with grade of differentiation. Therefore, for improved diagnostic and prognostic values, quantitative evaluation of FISH signal is useful.

One of the disadvantages in evaluation of the FISH signals based on the conventional microscopy images is the considerable number of nuclei sliced during the sectioning and/or thin specimen preparation. Such truncated nuclei do not represent the complete chromatin of the cell nuclei. This causes the under-estimation of the chromosome copy number (Hopman et al., 1991) and incorrect evaluation of the variation in FISH signal count. A correlation between an average signal count from routine sections and corresponding touch preparations

containing predominantly complete nuclei has been demonstrated by Dhingra et al., (1994), and Hopman et al., (1992). To guarantee a reproducible, unbiased signal count per nucleus and realistic feature values, whole nucleus should be inspected and analyzed in three dimensions (Dhingra et al., 1994 ; Aubele et al., 1996). To estimate the distribution of FISH signals per cell, a large number of cells have to be analyzed, especially when the frequency of aberrant cells is low.

Visual counting of the FISH signal in the 3-D stack of images is a tedious, fatiguing and time consuming task. One has to display a gallery of all the 2-D images to facilitate the counting process. If the tissue architecture shows large density of cells, then the amount of work gets proportionally increased. This is because, a gallery of images of a box around each cell of interest should be displayed for clear presentation. Fig. 5.1 shows the gallery of a portion of the image depicting a particular cell that can be used for visual counting of the FISH signals in a particular 3D cell. Still, erroneous counting is possible since the visual correlation of the same signal in different slices is difficult. Additionally, identification and segmentation of the overlapping FISH signals are not trivial tasks. Automation of FISH signal counting is a difficult problem. It involves segmentation of the 3-D tissue image to mark the corresponding cell region in the FISH signal channel, assigning the FISH signal membership, segmentation of the signal and automatic counting of the same. The algorithms for automatic FISH signal counting must be accurate. The number of false negatives must be as low as possible. On the other-hand, the algorithm must be fast and efficient. The goal of quantitative FISH evaluation is to measure precisely, the pathological alterations i. e., gain or loss of a particular chromosome in the cell nuclei. In the image volume FISH signals appear like tiny objects consisting of high intensity voxels extending to several image slices and is located entirely within the cell nucleus. Fig. 5.2(a) shows the surface rendered display of the FISH signals while Fig. 5.2(b) shows one of the image slices of the FISH signal channel.

5.2 Evaluation of FISH Signals

For a normal cell, the cell nucleus shows two FISH signals in chromosome #7 and any variation in this number can be attributed to abnormal pathological status.

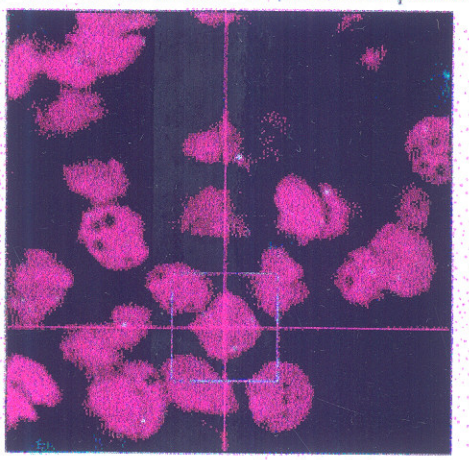

(a)

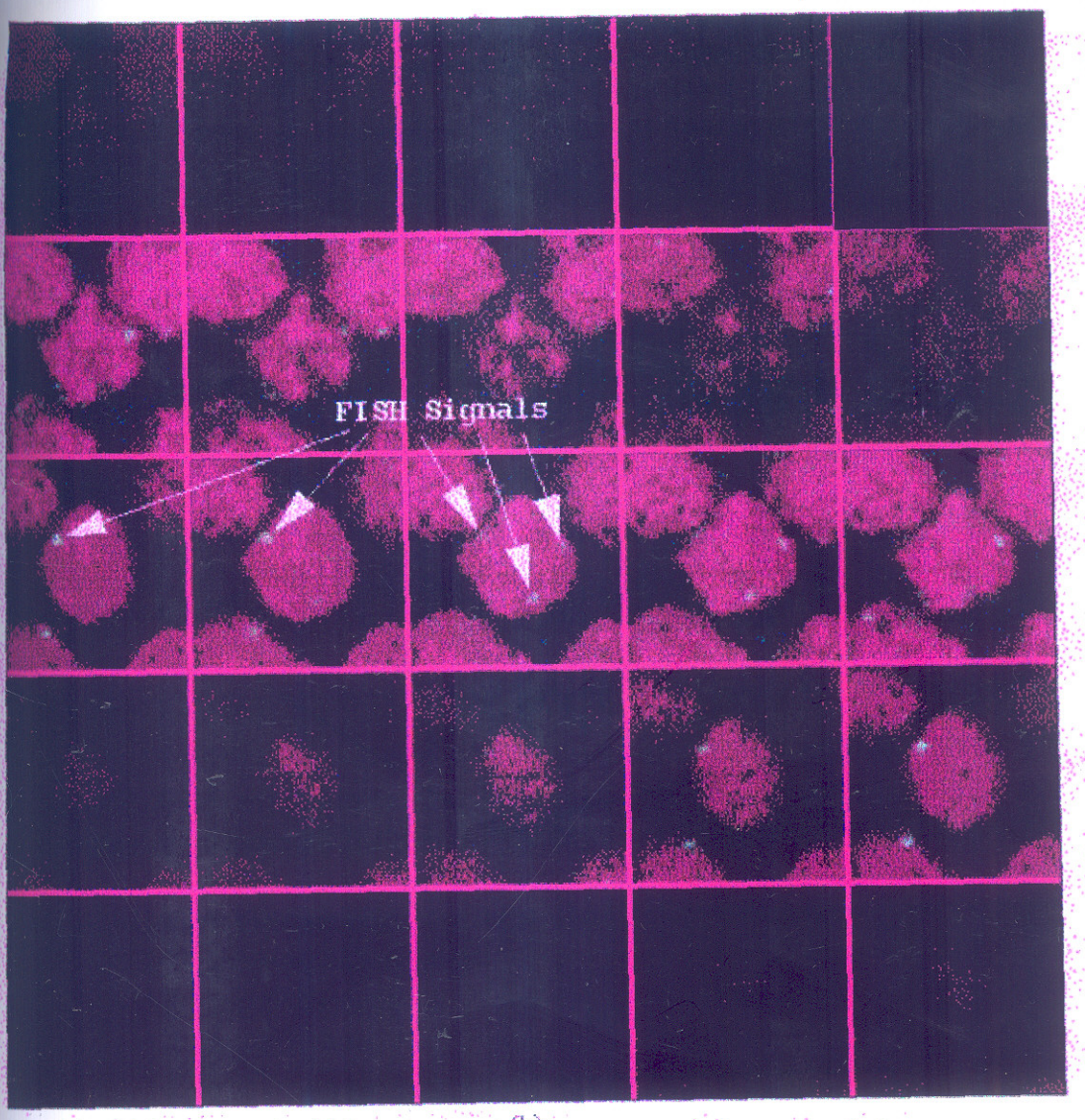

(b)

Figure 5.1: Image display for visual (manual) counting of FISH signals in a cell
(a) Selection of a cell of interest by drawing a box around it.
(b) A cell of interest is displayed as a gallery of images for visual FISH signal counting.

But, to count the FISH signals, they should be distinguished from noise and associated with a particular nucleus. Visual counting of the FISH signal is difficult, time consuming and cumbersome process as explained earlier. We have developed a simple method for automatic segmentation and counting of the FISH signal. Before attempting any automatic methods based on heuristics or otherwise, let us define the morphological properties and parameters of a FISH signal. A fluorescence signal is a spatial spot with parameters like size, shape, intensity, etc., within some range. The parameters of each signal can be obtained in two steps namely detection and estimation. In case of overlapping signals, it is quite difficult to distinguish them if the intensity peaks of the two overlapped signals are very close to each other. We have incorporated a charecterization of the overlapped signals by fitting a Gaussian --

models to the intensity profile of the overlapped signal. The features signal under each Gaussian profile is separately estimated to decide the validity of the signal.

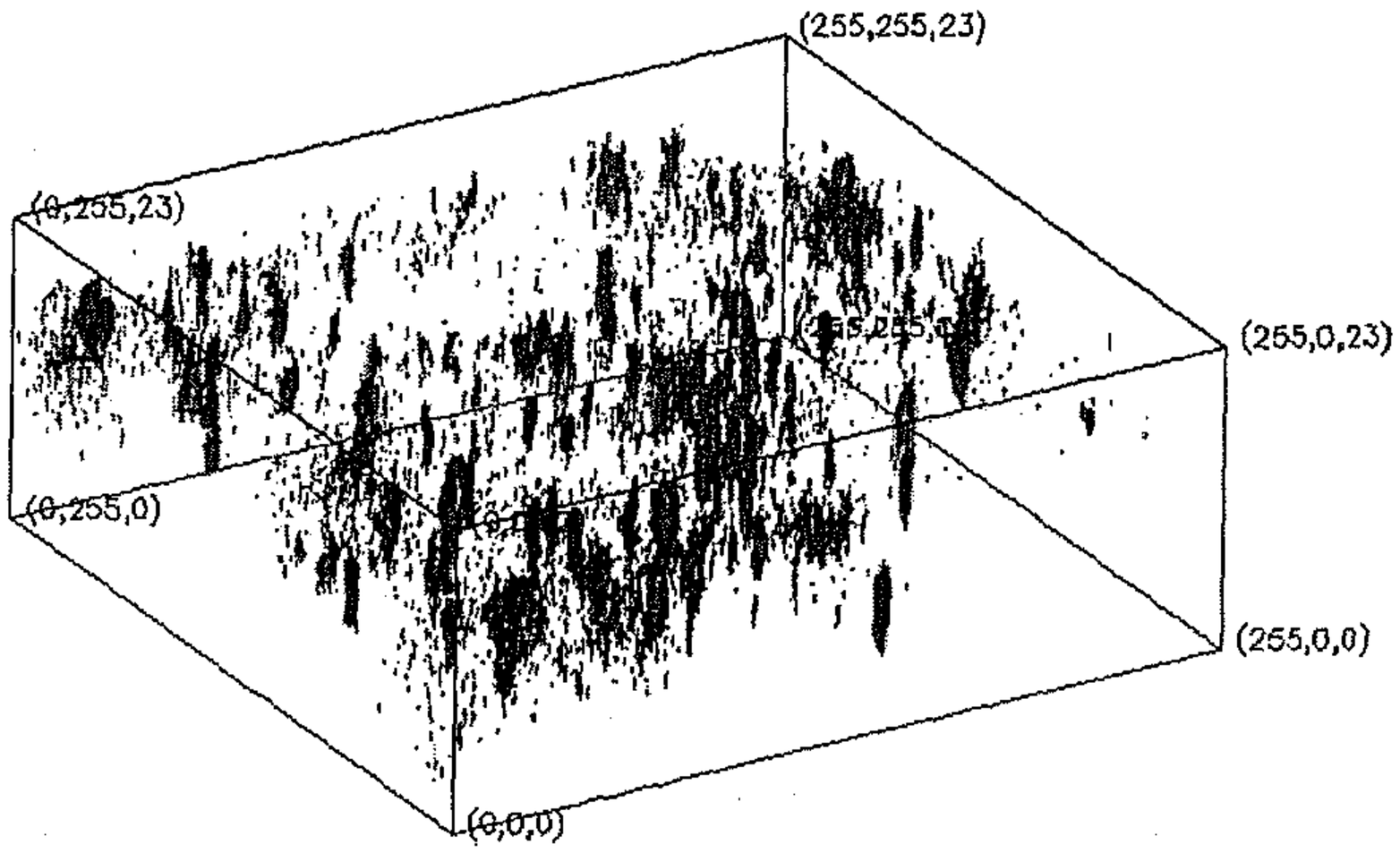

(a)

(b)

Figure 5.2: FISH Signal Channel (a) Surface rendered display of FISH signal channel (b) Middle optical section of the FISH signal channel of the volumetric image

The simplest algorithm for detecting FISH signals is to use its distinguishing property from the background. The usual approach is to suppress noise by filtering the image and to enhance the signal by a suitable method. Then the features of the signals are estimated for detecting the actual FISH signal from the artifacts. The region of interest for counting the FISH signals is only within the cell nuclei. Hence all the image elements which fall outside the cell region are discarded. For this purpose the segmented and labeled tissue image is virtually superposed on the signal channel by one to one mapping. Thus the non-cellular regions, regions belong to truncated cells, highly deformed cells, etc., are cleaned out.

In this chapter, we have described various features of the FISH signal and their importance in segmenting the signal from the noise artifact. We have also presented the possible reasons for error in identifying the proper FISH signals and suitable solutions to them are discussed. A comparative study of manual counting of the FISH signals and the automatic counting is also presented.

5.2.1 Possible Errors in Signal Identification

The FISH signal channel usually is corrupted by hardware noise or error in specimen fixation. This is evident from Fig. 5.1 and Fig. 5.2(b). Some of the errors caused due to noise or other means in the FISH signal channel are,

1. Split FISH signals
2. Overlapping FISH signals
3. Missed FISH signals
4. False FISH signals
5. Out of focus FISH signals
6. Debris
7. Loss of FISH signal due to over segmentation
8. Increased FISH signal count due to improper segmentation
9. Error in defining the FISH signal
10. Error due to ambiguity about FISH signal located near the boundary
11. Error due to FISH signal located on the overlapped or touching portion of the cell nuclei

.*Split FISH signal* error occurs when we count two signals when there is only one. This error occurs when the signal lies on the common boundary of the touching cells and counted as a FISH signal in both the cells. This error is avoided as follows. If the signal intensity peak and at least 40% of the FISH signature is in one cell then the signal is counted as belonging to that particular cell. The signature size threshold is set experimentally. When a large signal is disconnected due to poor axial resolution, similar error results.

Overlapping FISH signals error results in under-estimation of the signal density per cell nucleus. This error may occur due to overlapping signals in the specimen itself or when the signal channel is smoothed and thresholded during detection phase. If the FISH signals are located close to one another then they may join together during smoothing. If the resolution of

the image stack is poor it may also cause two closely located FISH signals one below the other to be counted as only one. Characterization of the overlapping signals is a difficult problem. If the overlapping signals show two distinct intensity peaks in the intensity profile, then it is possible to match the signal model to each intensity peak and decide whether two signals are really overlapping. In section 5.4 'Detection and Counting of Fish Signals', we have explained the method to detect overlapping FISH signals.

Missed FISH signal error is due to poor segmentation of the cells in the tissue, causing only partial cell chromatin being identified as the cell, while the rest being is considered as background. Due to uneven illumination of the specimen and attenuation of light intensity due to depth, some portion of the cell may not be recognized during thresholding. Any signal present in those parts is deleted in signal channel too, as we do not consider the image elements outside the cell region. Also, the attenuation of the light intensity and the photobleaching of the fluorescent labeled specimen may cause the deletion of some signals at the depth of the specimen. Wrong feature calculation of the signals during segmentation and identification process may also cause the missed FISH signal error.

False FISH signal error is one of the main causes for erroneous signal count. Noise, artifacts due to improper dye application, specimen damage, etc., get prominently reflected in the FISH signal channel. Sometimes, it is not even possible to visually distinguish them from the real FISH signal. Proper specimen preparation, noise reduction, selection of right features, etc., can reduce the error due to false FISH signal.

Out-of-focus FISH signal error is caused due to the presence of out of focus information in the FISH signal channel or due to out of focus cells in which FISH signals can be hardly seen. Since the confocal imaging reduces the out-of-focus information considerably, this error is less predominant. In case of wide-field microscopy and other imaging techniques, the blurred FISH signal may not satisfy the criteria set for identifying the FISH signal causing errors. This error can be reduced by deblurring the image using Wiener filter or other methods (Roysam et al, 1995; Roysam et al, 1992).

Debris due to ill usage of fluorescent materials in the specimen, presence of air bubbles in the specimen, etc., is reflected in the image causing errors in FISH signal counting. Most of the debris can be removed by simple size filtering and proper featuring of the signals.

· *Over-segmentation of the tissue* causes major error in the evaluation of FISH signals. If the same object is divided into several objects with different labels, it causes under estimation of FISH signal count per cell nucleus. Similarly, under-segmentation where more than one cell is given the same label, causes under evaluation of FISH signals. Any error in marking the cell boundary causes error in FISH count when the signal lies very close to the boundary. If the signal lies on the touching or overlapped cell boundary, an ambiguity arises about the membership of the FISH signal. As we have mentioned earlier, the signals lying on the common boundary of the cells can be assigned to a particular cell by checking the location intensity peak in the signal profile and the size of the signal signature in each of the cells.

Wrong selection of FISH signal features causes major error. FISH signal channel is contaminated by various types of noise. No noise reduction technique completely removes the artifacts without affecting the signal considerably. Hence it is very important to distinguish the FISH signals from the noise artifacts, based on proper features. Wrong selection of features results in either counting the group of noisy voxels as FISH signals, or rejecting a weak FISH signal as a noisy artifact.

5.2.2 Feature Selection for FISH Signals

One can choose various image features of the FISH signals to identify them and segment them from the noise artifacts. As there is no definite shape, size or orientation as well as location of the signal within the cell nuclei, one has to undertake a supervised feature selection on a large number of data sets before finalizing the list of FISH signal features. We have undertaken the visual identification and interactive segmentation of the FISH signals over one hundred image data sets of thick prostate tissue specimen. This is done with the help of a molecular pathologist. With this manual analysis, we have selected some main features and range of their values which can be used to identify signals in testing data sets. Some of the FISH signal features thus identified are,

1. Volume of the FISH Signal V.
2. Relative volume defined as the ratio of the size of the FISH signal to the average size of all the FISH signals identified within the corresponding cell nucleus R.
3. Average intensity of the FISH signal I_{avg}.
4. Relative intensity defined as the ratio of the average intensity of the FISH signal and the average intensity of all the FISH signals within the corresponding cell nucleus I_r.
5. Total fluorescent intensity I_{tot}.
6. Location of the FISH signal s.
7. Shape (three-dimensional) of the FISH signal Υ.
8. Local background gray level B.

Thus the parameter vector can be written as $P = \left[V, R, I_{avg}, I_r, I_{tot}, s, \gamma, B \right]^T$. For a set of data the FISH signals are first visually identified with the help of a pathologist. The parameters defining these FISH signals are then calculated to find lower and upper limits for these features. Thresholds for the features such as relative size and relative intensity are also set experimentally. Based on the experimental results on the test data sets we have defined the range and the average value for all the parameters in vector P.

Before measuring the features of the signals, the noise associated with the channel should be reduced and the signals have to be enhanced to distinguish them from the background. We have used hybrid median filter, Gaussian smoothing and point finders such as top-hat filters to reduce the noise and enhance the FISH signals. Size and shape heuristics along with the other features mentioned above are then used to identify and segment the FISH signals.

5.3 Noise Reduction and Signal Enhancement

The noise removal in the signal channel needs careful handling of the methodologies since the difference between the noise feature value and the signal feature value is too low. Many heuristics and standard noise reduction methods are used to filter out the artifacts.

Median Filtering: In the first step, we have used a two-dimensional median filter on each image slice. A simple median filter replaces the input pixel by the median of the pixels contained in a small window around the pixel. We have used a 3×3 window W for this purpose. If $v(x,y)$ is the filtered pixel value then $v(x,y)=median\{u(x-m,y-n)\}$ over $(m,n)\in W$. This filter removes isolated pixels and the binary noise in the signal channel. We have not used three-dimensional median filtering since larger window increases the computation load. Also, isolated single pixels are very well removed in 2-D filtering itself. Fig. 5.3(b), shows a representative image slice of a typical FISH signal channel, before and after median filtering.

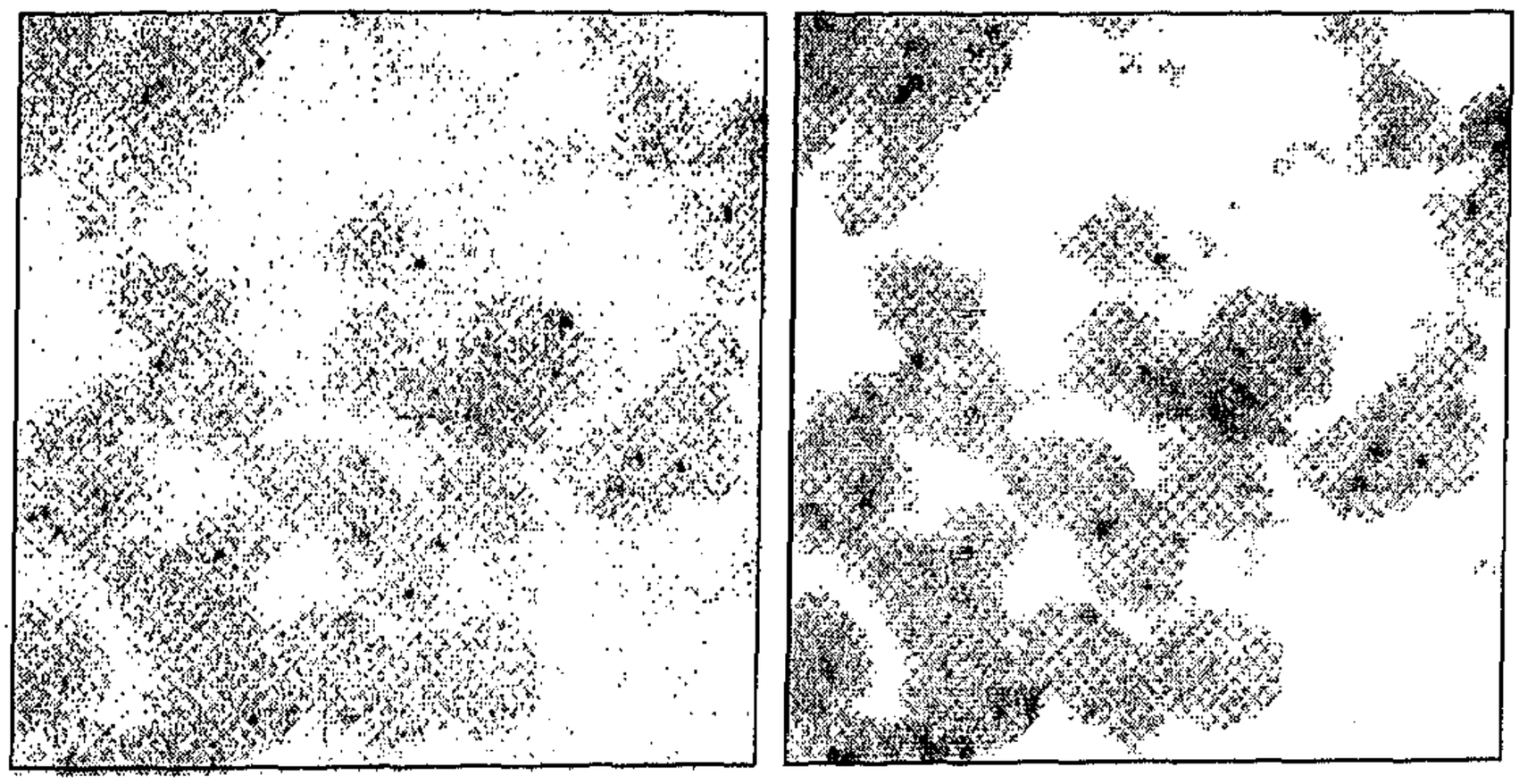

Fig. 5.3: Result of median filtering on a signal channel (a) original image slice (b) Median filtered image slice

Gaussian Smoothing: The next step is smoothing. FISH signals are the localized features. Simple spatial averaging, not only blur the signal but also increases the chances of connecting two closely located signals. Since Gaussian smoothing does not give much importance to far away voxels, the distortion of FISH signals will be minimum by Gaussian filtering. The 3-D Gaussian function is given as $G[i,j,k]=e^{\{-(i^2+j^2+k^2)/(2\sigma^2)\}}$. The degree of smoothing is characterized by σ. We have used a symmetrical Gaussian filter with $\sigma^2=2$. Because of Gaussian smoothing, weak noisy signals and isolated voxels are smoothed out. Fig. 5.6(c) shows a representative image slice of the FISH signal channel after Gaussian smoothing.

There will be some degree of blurring of FISH signal due to smoothing. The Top-hat filtering is used to enhance smooth FISH signal by comparing it with a local background gray value. We have extended the two-dimensional top-hat filter to third dimension. This is

done since the FISH signals are essentially three dimensional in nature. The three dimensional top-hat filtering technique is explained below.

Top-hat Filtering: The ideal top-hat filter is basically a point finder. It consists of a flat disc that rests on a surface and a central crown of smaller diameter. This filter is centered on each pixel in the image, with the brim resting on the surface as shown in Fig. 5.4. Any signal that `sticks up' through the crown of the hat is considered to be FISH signal and is brightened up to higher level. The size of the central crown is defined by the smaller of the two neighborhood regions as shown in the Fig. 5.5. The larger region represents the local background which the point of interest must exceed in brightness.

The top-hat method finds the maximum brightness in the larger surrounding region and subtracts that from the brightest point in the interior region. If the difference exceeds some arbitrary threshold which is the height of the crown of the top-hat filter, then that point in central crown is considered as signal.

The 3D top-hat filter consists of $C_1 \times C_2 \times C_3$ core voxels in a cube of size $W_1 \times W_2 \times W_3$ window where $W_i > C_i$ for all $i = 1,2,3$. Fig. 5.5, shows diagrammatically the 3D top-hat filter we have used with $W_1 = W_2 = W_3 = 5$ and $C_1 = C_2 = C_3 = 3$. This filter is centered on each voxel in the image. The top-hat method finds the maximum brightness in the larger surrounding region and subtracts that from the brightest point in the interior core region. If the difference exceeds some pre-defined threshold, then that point in central crown is considered as FISH signal and is enhanced. The threshold is chosen as $(\mu + k)$ where μ is the average gray value of the window $W_1 \times W_2 \times W_3$ and k is an experimentally determined constant. Fig. 5.6(d), shows a single representative image slice of the FISH signal channel after top-hat filtering.

Size & Shape Filtering: When there is a cluster of noisy voxels with relatively high intensity, smoothing and thresholding may result in making the noisy cluster into a connected component. This can cause error in automatic counting of FISH signal. Also, the air bubbles and improper use of fluorescent materials are reflected as relatively large objects in FISH signal channel. Such noises and artifacts are removed by size and shape heuristics.

· We have defined a size and shape filter to remove this kind of artifacts. The maximum and minimum size of the FISH signal is defined. The objects which do not fall within the size criteria are considered as noise artifacts and removed. The maximum size range is kept as three times the average size of the signal, so that overlapped signals are not rejected before being analyzed. Though FISH signals do not have any definite shape, it is observed that these signals are also three dimensional in nature. Hence, only those signals which are within the pre-defined size range and occupy at least two consecutive slices in the image stack is considered as valid signal. Fig. 5.6(e) shows the effect of noise filtering using size and shape filtering.

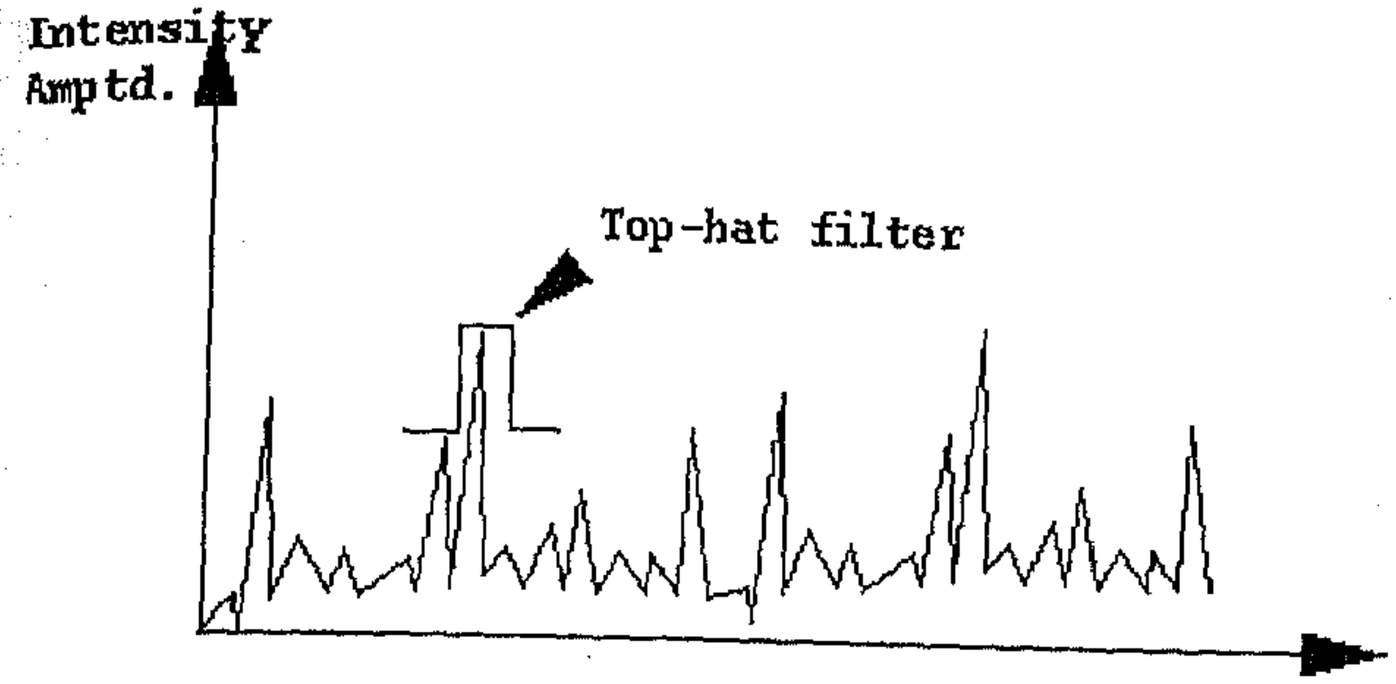

Fig. 5.4: Simple example of top-hat operation on one dimensional sequence of signals.

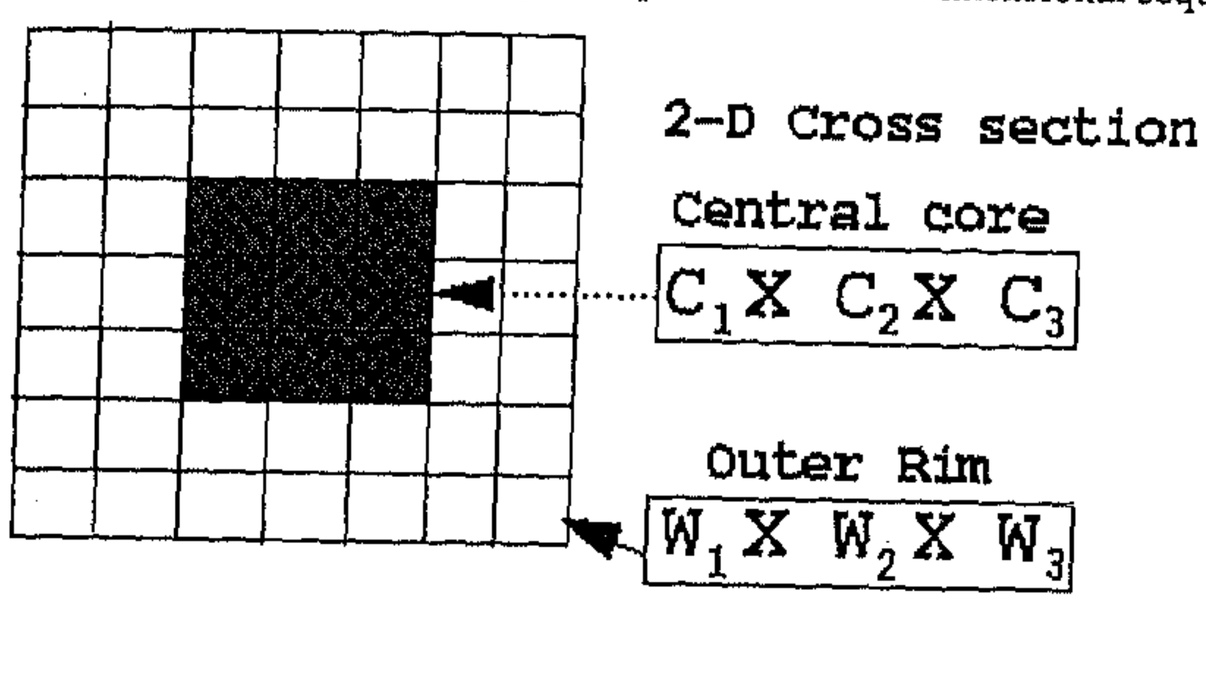

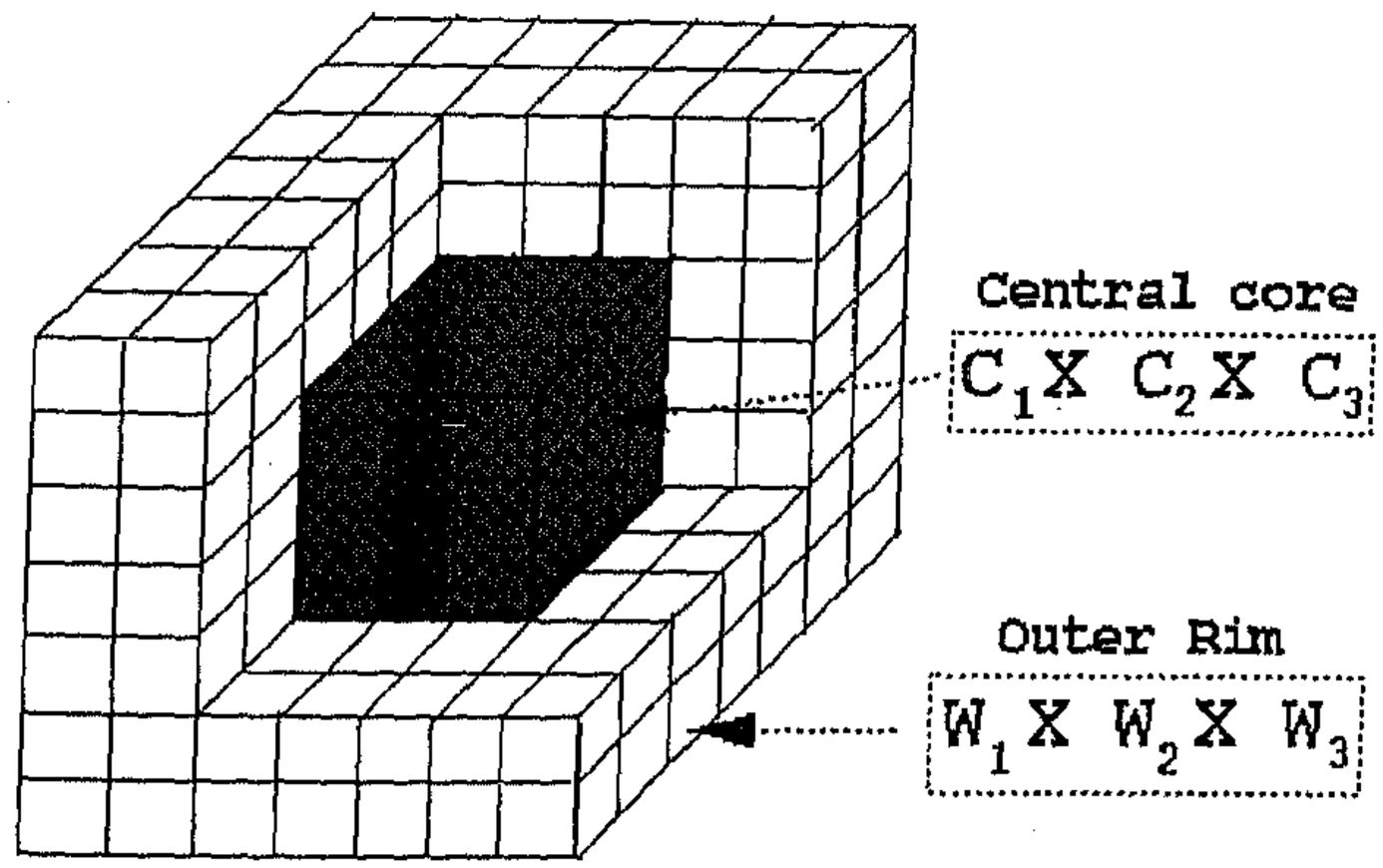

Fig. 5.5: A three dimensional top-hat filter. In the top is the 2-D cross-section of the 3-D filter.

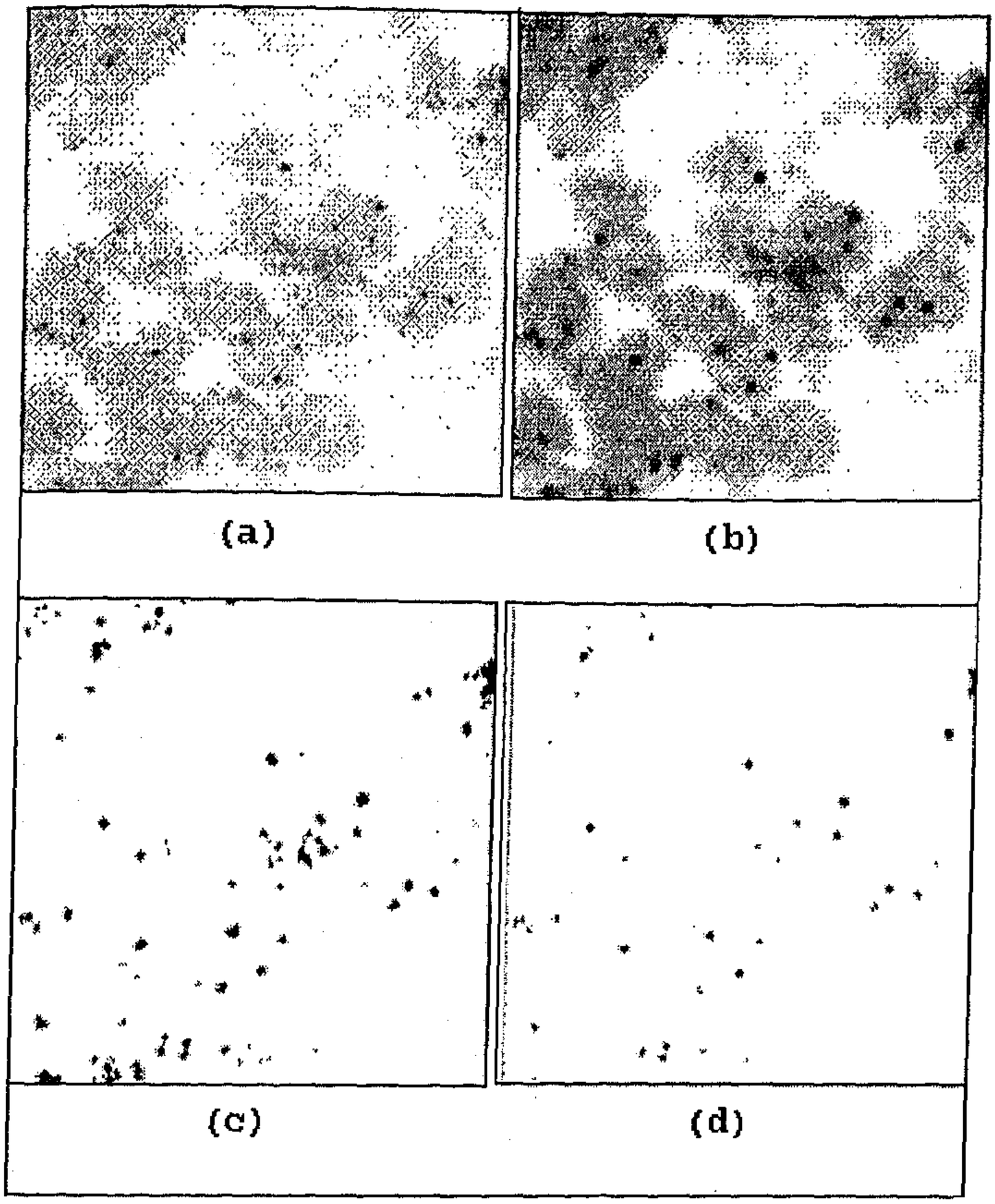

Fig. 5.6: Result of different steps of noise reduction shown over a single representative image. (a) Original image slice of a signal channel (b) After Gaussian smoothing (c) After top-hat filtering (d) After size & shape filtering.

5.4 Detection and Counting of Signals

A reasonable method to detect FISH signals and to determine their parameters should have the following properties.

-- The method should be translation, scaling and rotation invariant.
-- The method should be able to detect the range of parameters of the signal.

-- The accuracy by which the parameters are determined must be as accurate as the level of noise permits. Thus, the method should degrade smoothly as the level of noise monotonically increases.

-- For further analysis, the method should yield a measure of certainty for each signal by describing how well it resembles a ideal FISH signal.

-- The method should require a minimal number of user-defined parameters. Also, it should be as generally applicable as possible and be efficient in computer time and memory.

A simple algorithm for detecting the signals which satisfies the above mentioned conditions, is to threshold the image at appropriate level and characterize the signal by using its property to distinguish it from background. All the image elements which exceeds a particular threshold are examined for whether they satisfy the range of feature values present in the feature vector P.

Let $W = \left[w_s, w_R, w_{Iavg}, w_{Ir}, w_{Itot}, w_s, w_\gamma, w_B \right]$ be the weights assigned to different features of the FISH signal described in section 5.2.2. If $P = \left[V, R, I_{avg}, I_r, I_{tot}, s, \gamma, B \right]^T$ is the feature vector defining the FISH signal, and the vector defining the decision taken based on each feature is $d(P) = \left[d(S), d(R), d\left(I_{avg} \right), d\left(I_r \right), d\left(I_{tot} \right), d(s), d(\gamma), d(B) \right]^T$ then, an object in the image space is considered as FISH signal if the weighted combination of the decisions taken over individual features, is above a pre-defined threshold. The elements in the decision vector takes the value 0 or 1. If the value of the corresponding feature is within a predefind range, the $d(.)$ takes a value 1 otherwise 0. All the threshold are chosen experimentally. For this purpose, the FISH signals are first identified manually in more than 25 data sets which are considered as design sets. Features of each FISH signal is estimated and the range of the feature value from the minimum found in design set to maximum value found, is considered as threshold range.

Let us represent the wighted decision vector as ,

$$F_i = W \times d(P)$$

to be the feature vector of the possible FISH signal under inspection.

If F is weighted feature vector of a ideal FISH signal, then the match error between the ideal FISH signal and the signal under inspection can be defined as

$$e_i = \left(F - F_i \right)^2$$

If this error is below an experimentally defined threshold, then the signal is considered as authentic and counted. If the error is above the threshold, then the image element may be a overlapped FISH signal or is a noise artifact due to debris, etc.. All the thresholds are calculated by finding the features of FISH signals in training data sets.

Automatic detection of the overlapped signals is done by inspecting and characterizing the intensity profile as well as macro-feature of such signals. The signals which do not confirm to the matching error is subject to second stage of analysis. Here, the signal is tested for overlapping error. If the size of the signal is below the lower threshold of the size feature range, such signals are discarded as artifacts. If it is above the maximum size of the size feature range and its intensity features such as I_{avg}, I_{tot}, I_r are also above the average feature range, then overlapping of two or more FISH signals is suspected. We have used a Gaussian model fitting technique to resolve the overlapped signals and to finde the parameters of the feature vector of such signals (Noordmans and Smeulders, 1998).

First, the image element is searched for multiple intensity peaks. If the multiple intensity peaks of approximately identical magnitude are present, then a local Gaussian model of the signal is extracted for each intensity peak. Fig 5.7, shows the process of fitting the Gaussian model to each intensity peak present in the intensity profile of the overlapped signal. The amplitude of the Gaussian model is equivalent to the intensity peak in the profile. The spread of the local Gaussian model of the intensity profile is defined by $\frac{\sigma}{N}$ where σ is the standard deviation of the intensity of voxels of the whole image element and N is the number of intensity peaks present in the image element.

Fig. 5.7, is a diagrammatic representation of the intensity profile of a two overlapping signals and a noise artifact. The magnitude of the intensity peak I_n of the n th peak is calculated from the profile plot. The local Gaussian spread σ_n of the n th intensity peak is calculated as explained earlier. Then Gaussian model of n th peak can be given as,

$$G_n = I_n \cdot exp\left\{\frac{x^2 + y^2 + z^2}{\sigma_n^2}\right\}.$$

The feature vector of each local Gaussian fitted profile is checked for the validity of the model to be a FISH signal. The weighted decision vector of each locally fitted Gaussian model is compared with ideal feature vector F. The overlapped object is considered as constituting as many signals for which the match error is below threshold.

.The 3-D component labeling based on simple region growing is used to count the detected FISH signals within a specified region. The signal channel of the multi-spectral, volumetric image is scanned from top left in a raster pattern. Whenever a voxel of a FISH signal is found, all the voxels connected to it are given a unique label. The scanning is continued from the point where it was left till another voxel which is not already labeled but belongs to the signal is found. In this way a complete image is scanned and all the voxels belonging to a signal are given a unique label. The result of labeling the FISH signals also gives the number of FISH signals in the cell nucleus. The process is repeated for all the cells and the FISH signals per cell nucleus are documented for further analysis.

If U_m is m th image data set of a tissue specimen containing N nuclei, and if there are j FISH signals in the i th nuclei then it is documented as $U_m(i) = j$ where i = 1,2,...., N. For normal nuclei j = 2.

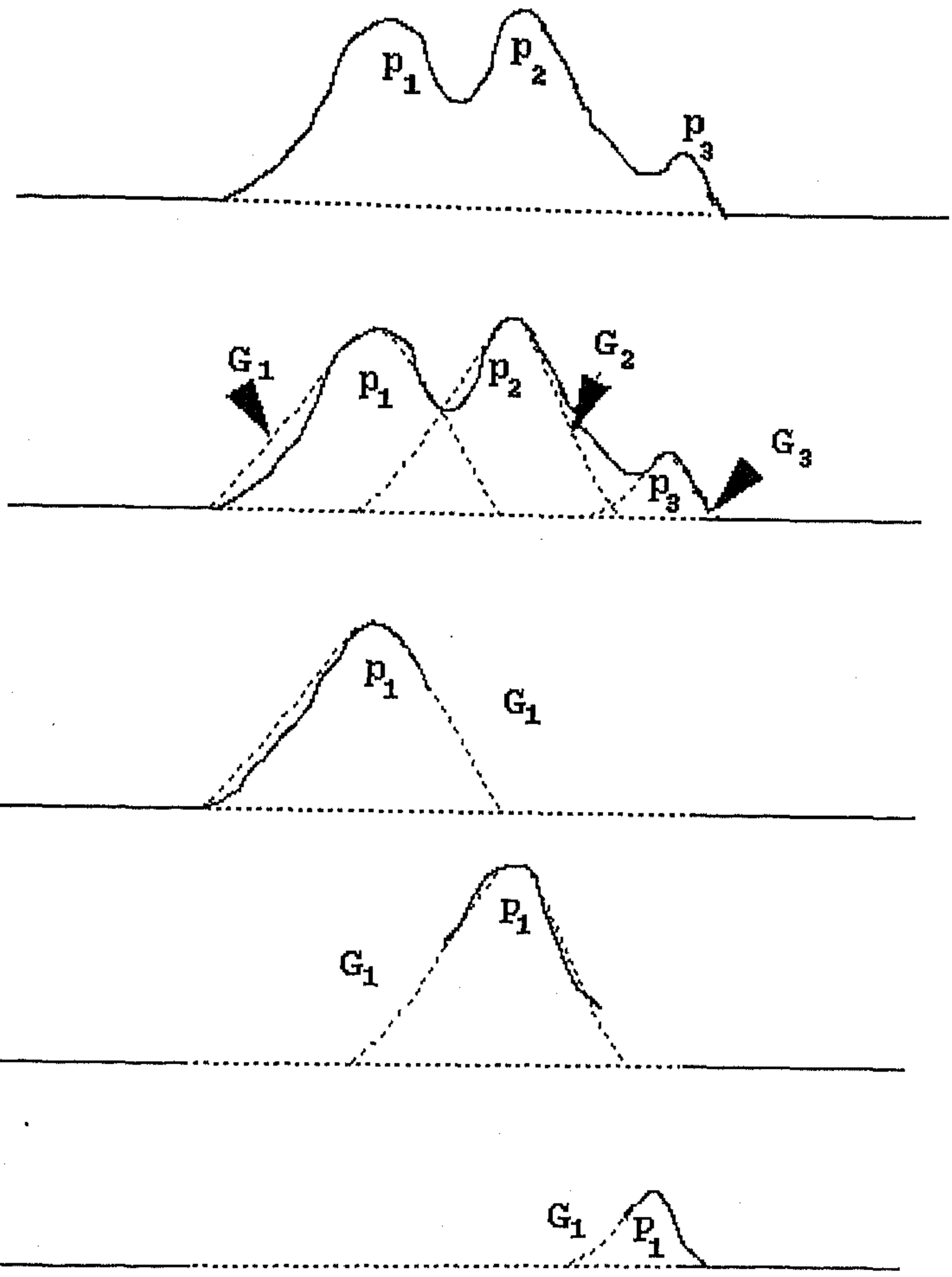

Fig. 5.7: Characterizing procedure for overlapping FISH signals. The intensity peaks are shown in dark continuous curve while the fitted Gaussian models for each peak is shown as a dotted curve. The last three images show separated profile of the overlapped signals. G_1, G_2, G_3, are the Gaussian models of intensity peaks P_1, P_2, P_3.

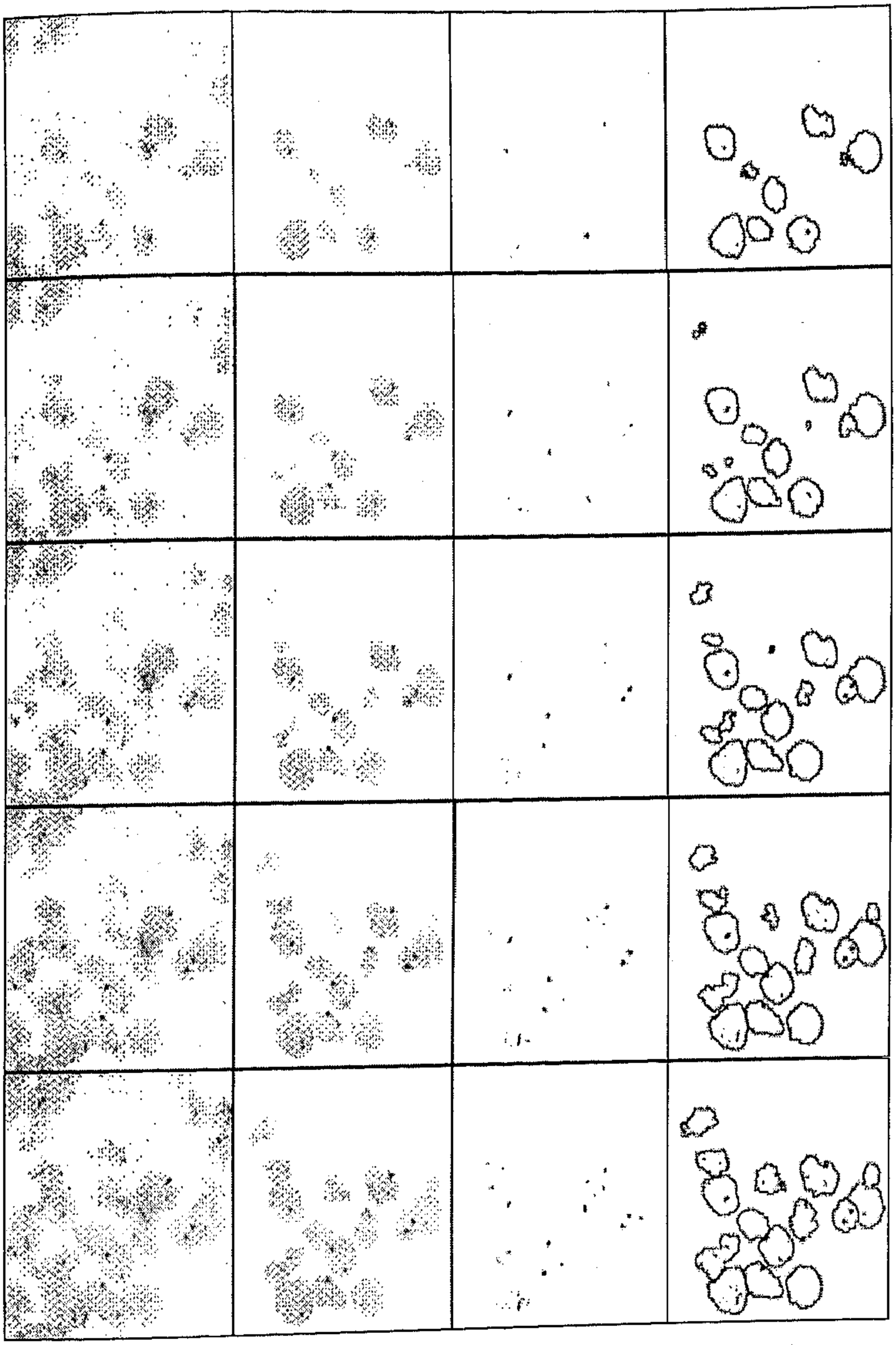

(a) (b) (c) (d)

(contd.)

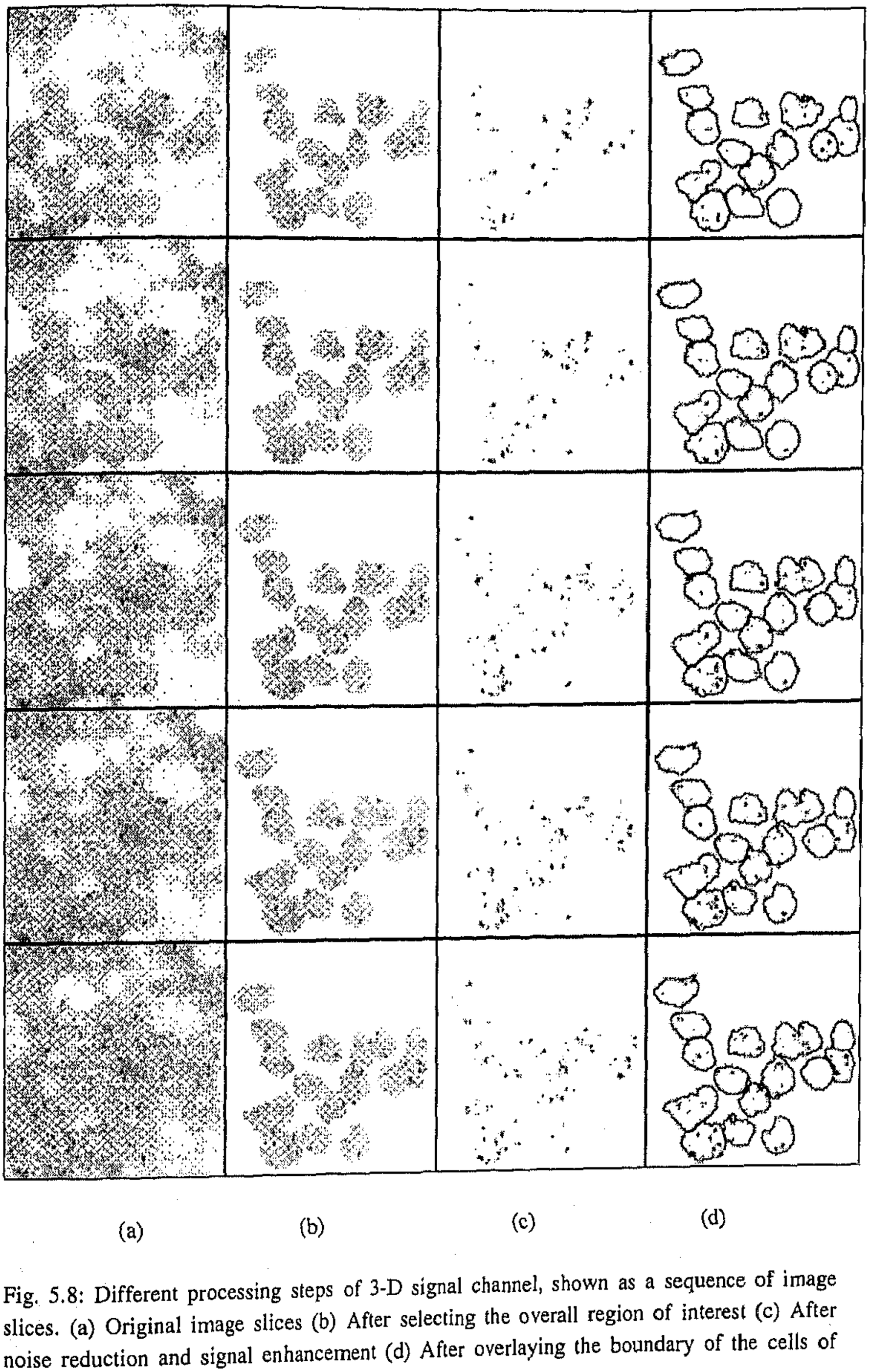

(a) (b) (c) (d)

Fig. 5.8: Different processing steps of 3-D signal channel, shown as a sequence of image slices. (a) Original image slices (b) After selecting the overall region of interest (c) After noise reduction and signal enhancement (d) After overlaying the boundary of the cells of interest.

5.5 Comparative Study

Tissue Segmentation for FISH Signal Count:

Segmentation of the tissue cells has a definite influence on the outcome of FISH signal count. Accurate evaluation of the FISH signal depends on how precisely we are able to mark the cell boundary. Segmentation methods such as thresholding and labeling do not isolate the cells completely. Even if they do so, the accuracy of segmentation depends upon how well the threshold is chosen. At lower threshold values, a noisy artifact which falls outside the cell boundary may also get to consider FISH signals as belonging to the cell. Moreover, at lower threshold cell, clusters do not separate into individual cells and hence, any attempt to count the FISH signals per cell fails. At higher threshold, only bright part of the cells remain in the foreground thus projecting wrong FISH signal count. Similar problem persists when the we try to mark the surface of the cell using simple edge detectors.

Segmentation methods based on Active contours or Active Volumes for marking the complete surface of the cells results in better accuracy in the subsequent evaluation of the FISH signals. But, these methods need interactive initialization and are computationally expensive. When the FISH signals have to be counted in a large number of data sets, with many cells of varying size and shape, application of active model process becomes very time consuming.

Use of region based tissue segmentation techniques very useful in FISH signal evaluation. They provide reasonably good segmentation of the tissue into isolated cells. Though the methods like constrained volumetric region growing (explained in chapter 4) may not isolate the cell clusters completely, it can be corrected with a minimum interaction unlike other edge based segmentation methods. Methods like 3-D watershed with automatic merging also gives good result. The FISH signal count error in such cases may occur when the signals are located near the cell boundary or on the surface where the cells touch or overlap on one another. Integrated approach for cell segmentation can be used for accurate marking of the cell boundary in the signal channel. Though the process is time consuming, it has the advantages of all the segmentation techniques and the human interaction is minimum.

In general, the difference of error in FISH count, based on each cell segmentation by active models, watershed or integrated approach is found to be minimum.. In cases where FISH signal falls very close to the cell surface and/or near the touching boundary of the two cells, confirming the cell membership of the FISH signal is difficult. Segmentation methods which accurately mark the cell surface such as active models or integrated approach might be necessary in such cases. Since the signals in all the cells are not of interest and counting is done only in the cells which are of interest to pathology, use of active models or integrated approach is a better option.

Here we have presented a comparative study of the usefulness and the accuracy of different cell segmentation methods presented in this thesis with respect to FISH signal

evaluation. Results based on different methods is compared with manual FISH evaluation. The percentage error has been listed. The percentage error can be defined as,

$$\%\ \ error = \frac{\rho_{man} - \rho_{auto}}{\rho_{man}} \times 100$$

where ρ_{man} and ρ_{auto} are the manual FISH signal count and automatic FISH signal count.

Table 5.1 lists the FISH signal count on five data sets spanning 22 segmented cells, based on different three-dimensional segmentation methods applied to the tissue image. The percentage error in signal count for each segmentation method on each data set is also given.

Sp. No.	Cell No.	3D Evaluation				
		Manual Count	Edge-based Segmentation		Region Based Segmentation	
			LoG Operater	active contour model	Volume growing	3D water - shed
1	1	3	5	3	3	3
	2	2	2	2	2	2
	3	3	4	3	2	2
	4	4	4	4	4	4
error		0%	25 %	0 %	8 %	8%
2	1	2	2	2	2	2
	2	2	5	2	2	2
	3	3	4	3	3	3
	4	1	3	1	1	1
	5	2	2	2	2	2
	6	4	4	4	4	3
error		0%	42 %	0 %	0 %	7%
3	1	5	4	4	4	4
	2	2	2	1	2	2
	3	3	2	3	2	2
	4	3	2	3	2	2
error		0%	25 %	15 %	25%	25%
4	1	2	2	2	2	2
	2	2	4	2	2	2
	3	2	2	2	2	2
error		0%	32%	0 %	0 %	0%
5	1	1	0	1	1	1
	2	2	2	2	2	2
	3	2	2	2	2	2
	4	1	0	2	2	2
	5	2	2	2	2	2
error		0%	25%	12%	12 %	12%

Table 5.1: Comparative analysis of influence of different tissue segmentation techniques on FISH signal evaluation. Result on representative five data sets is shown.

Fish signal count on over one hundred data sets spanning more than four hundred cells has shown that the integrated approach and active model based segmentation gives more precise results. The watershed technique with automatic merging also shows better precision in signal counting. Table 5.2 gives the percentage error for different methods over more than 100 data sets

sl.no.	Segmentation techniques	Percentage error
1	Sobel edge detector	38 %
2	LoG edge operator	36 %
3	Canny edge operator	28 %
4	Layered Segmentation	13 %
5	Active contour models	6 %
6	Active surface models	9 %
7	Seeded Volume Growing	16 %
8	Successive pealing-thickening	8 %
9	3-D watershed	23 %
10	3-D watershed with merging	11 %
11	Integrated approach	6 %

Tabel 5.2: Comparison based on the percentage of error in FISH signal count based on different tissue segmentation techniques.

Visual and Automatic Counting of FISH Signals:

As mentioned earlier, one has to undertake the experiment on a large number of data sets for reliable result. In such cases, the visual counting method is highly time consuming and fatiguing. Moreover, visual counting is not always reproducible. To confirm the usefulness of automatic counting of FISH signals, we have compared the visual counting results over 100 data sets with the automatic counting. Cells which are out of focus and are not of interest to pathologist are rejected. Also, the cells which are at the border of the image are rejected since the completeness of such cell nuclei can not be ascertained.

The visual counting is done by a pathologist and we consider it as a gold standard for all comparative study purposes. The visual counting has taken more than a week (including rest hours) while the automatic counting of the FISH signals in all the selected cells is completed within a period of less than three hours including loading image data sets and manually indicating the cells of interest.

Table 5.2 shows the result of manual counting and automatic counting. We have used an integrated approach of segmentation of the cells for automatically marking the region of interest in the signal channel. The accuracy of the result obtained by automatic detection and counting of the FISH signals was approximately 94%. From these results, we can conclude that the automatic counting is at par with the visual counting and the percentage of error is -

well within the acceptable level. Automatic counting is more advantageous as it is fast and reproducible and it will help the pathologists to work on more important tasks.

Sp. No.	No. of cells	Visual Count	Automatic Count
1	5	13	13
2	4	10	9
3	9	23	21
4	13	31	31
5	6	17	17
6	3	8	8
7	11	28	25
8	9	23	25
9	8	17	19
10	14	33	33
11	6	15	15
12	10	21	20
13	13	13	13
14	18	18	15
15	26	26	25
16	9	9	9
			error = 5 %

Table 5. 3: Comparative analysis of manual and automatic count

2D and 3D Evaluation of FISH signals:

As discussed earlier, the 2D image may not represent the complete cell nuclei due to truncation of the cells. This results in underestimation of the FISH signal count. To substantiate this we have undertaken a study of FISH signal count in 2D image and 3D image of a same material. Both the images are obtained using CLSM. 15μm and 5μm thick tissue specimens are used to obtain 3D and 2D images respectively. Table 5.3 shows some results of FISH signal count due to 2D and 3D image evaluation.

In 2D image evaluation done by pathologists for more than four hundred cells spanning over one hundred data sets, trisomy (presence of three signals) of chromosome-7 was found in only 30% of the data sets while polysomy (presence of more than three signals) was found in 33% of the cases. The monosomy (presence of only one signal) was found in 28% of the data sets studied. Two FISH signals in cell is found in at least one cell of almost all the data sets. There were also few cases where no FISH signals were detected in some cells.

In comparison, the 3-D evaluation has shown trisomy is present in approximately 90% of the cases and polysomy in more than 70% cases. Monosomy was found in only 65% of the cases. In no cell, we found zero FISH signals. Two FISH signals are found in many cells of different data sets. This shows that FISH signals can be more precisely detected and

counted by 3D evaluation of the images of thick tissue specimen. This also shows that the 2D evaluation for FISH signals results in remarkable underestimation of the chromosome copy number and thus, limited for interpretation.

The results obtained by automatic evaluation of the 2-D and 3-D images approximately concurs with the earlier comparison results between 2-D and 3-D evaluation done manually on the same data sets by the pathologists (Aubele, 1996). Table 5.4 gives a representative example of comparison between 2-D and 3-D evaluation.

Sp. No.	Cell No.	2-D Evaluation	3-D Evaluation
1	1	2	2
	2	2	2
	3	1	2
	4	2	3
2	1	2	3
	2	2	3
	3	1	2
	4	1	2
3	1	2	2
	2	3	3
	3	1	2
	4	2	2
	5	1	2
	6	2	4
4	1	2	3
	2	2	4
	3	2	2
	4	2	2
5	1	1	3
	2	1	3
	3	2	2
	4	1	2
	5	1	2
	6	1	1
6	1	2	2
	2	2	2
	3	2	2
	4	1	2
	5	2	2
	6	1	1
	7	2	3
		error = 29 %	

Table 5.4: Comparative analysis of 2-D and 3-D evaluation of the FISH signals in selected cells of a few data sets.

5.6 Discussion

We have considered nearly two hundred image data sets from 14 different patients for the experiments. Twenty-five data sets are used to design the ideal FISH features. The range of feature values and the proper weights for each features is defined for these data sets. This is

done manually with the help of a molecular pathologist. The remaining data sets are used as test sets and the experiments are done on these sets to determine the practical validity of the segmentation and counting method. We have obtained 95% accuracy in automatic counting of the FISH signals.

The FISH signals per nuclei are first visually counted and documented. The results obtained by using different segmentation methods and counting are compared with the visual counting. Table 5.3 shows the results of visual counting and automatic counting of the FISH signals on several representative image data sets. It is found that the results of automatic counting are at par with the visual counting. Errors are some time observed if the FISH signal is too weak and is rejected as noise and/or a strong noise cluster being accounted as a signal. The percentage of error is well within the acceptable level. Another important factor we have discussed is the influence of different segmentation technique on FISH signal counting. If the signal is well within the cell nuclei, all the segmentation methods would provide an acceptable result. If the signal lies very close to the cell boundary or falls on the boundary voxels, then, more precise segmentation with some prior knowledge about the cell boundary location is necessary. This is also proved by the high accuracy rate in FISH counting using the active model method for segmentation of the cells. If automation is the only factor to be achieved then the integrated approach for segmentation would provide the best possible result.

With all these cares taken, errors can still occur. The main reason is due to the problems associated with specimen preparation. Though, analytically, the methods developed are correct, it has to be fine tuned by testing on more number of data sets.

Chapter 6
Feature Selection and Extraction

6.1 Introduction

Proper feature selection is a key to the success of automatic histo-pathological image analysis. In a medical diagnosis or prognosis system, the features have to be selected in consultation with the experts in the medical field. Algorithms have to be developed for precise quantification of these features. These algorithms have to be tested on several data-sets before considering it as a valid feature for automatic analysis. It is difficult to design algorithms for precise quantification of tissue features such as architecture of the tissue, spread of malignancy, etc.. Many heuristic and empirical methods have to be used. Architecture of the tissue, cell arrangement pattern, etc., have to be measured in comparison to healthy tissue. Instead of measuring the precise quantitative value of features like architecture, it should be ranked on the basis of its similarity with normal tissue architecture.

There are simple cytological features which can give enough and reliable results for diagnosis in many cases. In the earlier works on histo-pathological images by Choi (1996) and Nordin (1989), list of features based on contours, textures and regions are given. More number of features need not give better classification result. Instead, sometimes they may increase the complexity of classification process and decision making. To increase the accuracy of classification, it is better to make use of several small feature sets in a multi-stage classification process.

It has been experimentally observed that a two-dimensional analysis of what is essentially a 3-D object, may not give accurate evaluation of the features in tissue specimen. In a two-dimensional image, the feature measurement may not depict the true feature values. This is due to the sliced cell nuclei, use of thin and flat specimens, etc.. It is difficult to perceive the spatial architecture of the tissue using a two-dimensional image analysis. It has been shown earlier in chapter 5 that the features like chromosome density within the cell nuclei can only be measured accurately by evaluation of the three dimensional images.

In this chapter we have discussed the criteria for selection of best features. Feature extraction or measurement algorithms for various geometrical, shape, moment, histogram-based features concerning 3-D histo-pathological images is discussed. A llist of important cytological features is also discussed. In addition we have presented a study on influence of image enhancement techniques as well as segmentation techniques on the feature values and feature extraction methods. We have given less importance to textural features as our data sets show magnified tissue images where the cells are big enough to test for cytological features. Texture features in the form of histogram features, cell density, inter-nuclear distance, etc., are discussed in detail.

6.2 Feature Selection

Selection of a few and effective features is an important task as it results in reduction of complexities arising due to too many features. An effective and meaningful feature can be defined as the one which increases the difference between neighboring class averages and decreases the variance within the class. Here class stands for the rank indicating the extent to which the particular disease has deteriorated. Though this is a major criteria to select the features for a particular classification purpose, there are many other conditions that govern quick and efficient extraction of the features. Some of these criteria for selecting the features from the histo-pathological images are listed below.

1. Ability to clearly differentiate subclasses of the same disease: This is one of the major criteria. The feature should be able to increase the difference between neighboring class averages and decrease the variation within the class. The class indicates the different grades of the same pathological disorder.

2. Ability to quickly extract the feature value: In a process involving large, multi-dimensional and multi-spectral data sets, feature extraction becomes slow and computationally complex process. A good feature should be the one which is simple to understand and compute as well as, can be quickly measured using automatic methods.

3. Dependency of the feature value on segmentation: It is desirable to have features which are more robust to the small errors in segmentation. It has been observed that many features that are important for the pathological classification such as shape, etc., are sensitive to the errors in segmentation. A study on the same is presented at the end of this chapter in section 6.7.

4. Ambiguity in quantifying the feature: Features such as tissue architecture is difficult to quantify. This is because, they exhibit different structure for tissues from different organs. Even the tissue sections from the same organ also show variation in the tissue architecture. The heuristic quantification may lead to a kind of ambiguity as these measurements are done in comparison to the architecture of the healthy tissue while there happens to be no proper definition of the architecture of the healthy tissue. Lesser the ambiguity, better and easier the quantification of the feature.

5. Possibility of finding the similar feature in all the data sets: This is an important criterion. The feature should exist in all the specimens of same class. If the feature is found to be not existing in some image data this indicates different class of the disease.

6. Simplicity: The feature should be simple to understand and extract from the complex, multi-dimensional images.

7. Need for 3-D analysis: Lesser the need for the multi-dimensional analysis, easier the feature extraction process. Most of the features need at least three-dimensional analysis for measuring them accurately.

8. Concurrence with pathologists' views: This is one of the most important criteria. Most of the features can be calculated by simple manipulation of the image properties. In case of histo-pathological images, it is the pathologist who knows better about the importance of the feature. So all the features selected should concur with the pathologists' view of its importance in deciding the particular sub-class of a disease.

These criteria are made to carry different weights based on the importance of the feature for a particular problem. In almost all the cases, the feature measurement depends on the image acquisition set up. A same specimen whose images are acquired under different setup conditions may give different feature values. Thus it is very important to maintain same standards while dealing with a particular disease. Additionally, the features should be normalized based on image acquisition conditions before comparing them to the images which are acquired in different conditions.

Following are some of the essential setup features which should be kept same while dealing with a particular problem. 1. Microscope Settings, 2. Voxel size, 3. Lateral & Axial resolution, 4. Laser Wavelength, 5. Size of the specimen to be scanned, 6. Scan pattern and Datum position, 7. Control Settings, 8. Specimen image enhancement criteria, 9. Cell segmentation rules and parameters, 10. Feature extraction methods, 11. Specimen rejection criteria.

6. 3 Feature Extraction

There are two approaches of featuring the cells in a tissue specimen image (Rodenacker, 1987). Based on feature extraction methods, these can be broadly classified as unsupervised approach and supervised approach. The first method is due to the knowledge of the image analyst, while the latter is based on the subjective evaluation experience of the pathologist. The supervised approach which is essential in medical image analysis, needs a thorough interaction between the image analyst and the medical expert. The common terminologies for the evaluation and description of cell and tissue properties can be defined by combining the knowledge of the image analyst and the medical expert.

Visual inspection and subjective evaluation of the histological specimens mainly deals with histological features rather than the cell features. One of the main disadvantages of considering only the histological features are the complexity and the heuristics involved in the quantification. Most of the times, the histological features are measured in comparison with the ideal tissue features. There will be lot of inconsistency in such cases as it is difficult to define the ideal tissue characteristics. In cases such as prostate tumor grading, it is not possible to accurately measure the amount of abnormality in the glandular structures of the tissue. To measure breakdown in the architecture and glandular arrangement of the cells in the tissue, more magnified images are needed. The data sets we have used are highly magnified tissue images clearly showing cells and their glandular arrangement. Hence many of the features we have measured are based on individual segmented cells. We have given more importance to measure the cytological features rather than histological ones. One of the

reasons is that the cytological features can be more accurately quantified provided a segmented image data while histological evaluation depends more on the experience of the pathologist.

Most of the measurement procedures for 3-D image can be directly generalized from the 2-D image measurement techniques. In three-dimensions, voxels can touch on a face, edge or a corner. It is more difficult to locate the internal holes in the objects. Properties such as orientation of the object in 3-D space takes two angles for representation. Some features such as skeleton of an object is harder to uniquely quantify in 3-D space. The practical difficulties of working with three dimensional image arrays are considerable. The size of the array and the time of computing is significant. Some consolation is obtained from the fact that the optical sections of the confocal microscope images are not widely separated. In some cases, we have calculated the features in each image slice separately and took the average feature value as a representative feature. This is done for measurement of only few features where the algorithm implementation is quite difficult in 3-D and the error in approximation is low. We have mentioned this if and when we adopted this method.

Generally stating, the feature set can be classified as shape features, texture features, spatial features, transform features and moment based features. These features are inter-linked in the sense that same features can be found under several different classes of the features. The spatial features include histogram features and amplitude features. The shape features include regenerative features such as boundaries or surface area, regions, moments, etc., and measurement features include volume, surface area, moment based features, etc.. The features which indicate the sub-classes of pathological disorders, mainly include shape features and histogram based features of individual cells and their relative variation. The other important features include variation in the tissue architecture, cell spread pattern, variation in dominant direction, etc..

Cell shape can be expressed in many ways. Combination of different radii, size, surface area, etc., can give a useful shape value for every different object. Following are some of the parameters that defines the shape in terms of directly measurable object features.

Size: Size of the cells is determined by total number of voxels present in the cell. Total number of voxels multiplied by the voxel size (=0.25 μm^2x0.5μm) give the total size of the cell. This can also be calculated as the zero order moment of the volumetric object. The actual size of the cell in a tissue specimen can be found out by dividing the total size of the cell by a magnification factor of the microscope. The importance of the cell size arises from the fact that it quantifies the nuclear DNA content of the cell. The size feature is also called as 'mass' of the cell when it is expressed as a number of voxels. Most of the tumors show large variation in the cell size that can be used to sub-classify the tumor into different pathological sub-classes.

Surface Area: Surface area of a 3-D cell can be approximated as the number of voxels belonging to the cell and is having at least one background voxel or the voxel belonging to other cells in its immediate spatial neighborhood. The two-dimensional counterpart of the surface area is perimeter.

Shape Factor: This feature is also known as *form factor* of a cell. It is defined as the ratio of surface area of the cell to volume of the cell. If A is the surface area of the cell and V is the volume of the cell then the shape factor γ is defined as $\gamma = \frac{A^3}{64 \cdot \pi \cdot V^2}$. For a perfect spherical shape, $\gamma = 1$. The two-dimensional counterpart is $\gamma = \frac{P^2}{4 \cdot \pi \cdot A}$ where P is the perimeter or the length of the boundary.

Eccentricity: It is also known as *aspect ratio* of the cell. If R_{max} is the maximum distance between cell centroid and cell surface while R_{min} is the minimum distance, then the ratio $\frac{R_{max}}{R_{min}}$ gives the eccentricity or the aspect ratio of the cell. Some times this feature is also referred as elongation. Fig. 6.1 diagramatically shows the eccentricity measure of an irregularly shaped cell. Sometimes, this is also measured as the ratio of the length of the major axis to the length of the minor axis of a best fit ellipsoid.

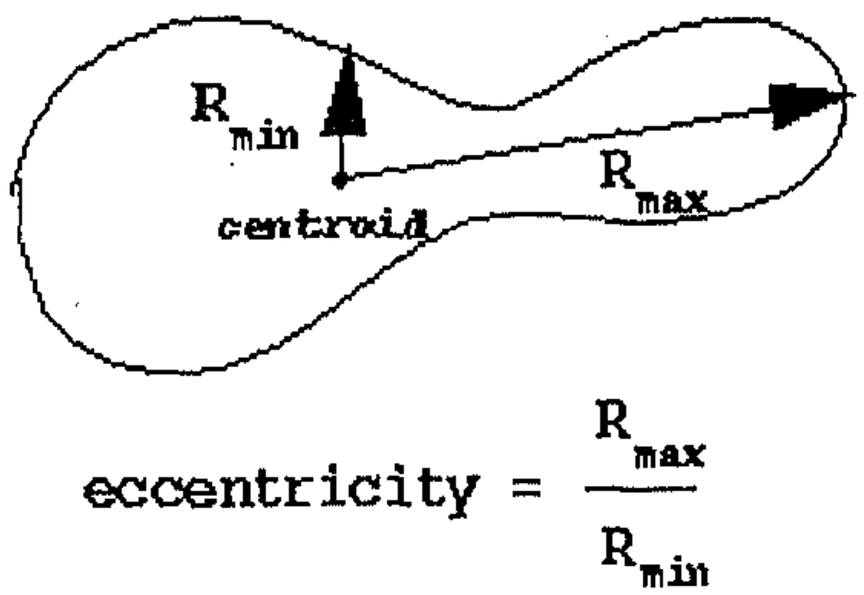

Fig. 6.1: Diagrammatic representation of eccentricity measure

Best-fit Ellipsoid: This is also generally called as image ellipsoid or image ellipse for 2-D objects. The best-fit ellipsoid is a constant intensity ellipsoid with the same mass and the second order moments of the cell of interest. Simply stating, any ellipsoid which satisfies the following conditions can be a best fit ellipsoid.

1. Total size of the ellipsoid and the total size of the cell is same.
2. The ellipsoid has a constant gray value equal to the average gray level of the cell
3. The center of the ellipsoid and the centroid of the cell is same
4. The spatial orientation of the major axis of the ellipsoid is same as the spatial orientation of the cell.

Roundness: Roundness of the cell is defined as the ratio of total surface area of the cell to the maximum diameter of the cell i. e., $\omega = \frac{A}{D}$ where D is the maximum diameter of the cell.

Convexity: Convexity is defined as the ratio between the surface area of a convex bounding body constructed around the cell and the surface area of the cell, i. e., $\frac{Convex\ Surafce}{Surface}$

We have used a simple method of constructing a polygonal convex hull around the cell and considering the surface area of this polygon as the convex surface. The method is explained below. In 3-D space, it is n-planar polygonal surface around the cell. This approximately defines the minimum area of a convex shape that will cover the original object (Russ, 1995). Fig. 6.2 shows diagramatically, the construction of a polygon around an approximate cell shape.

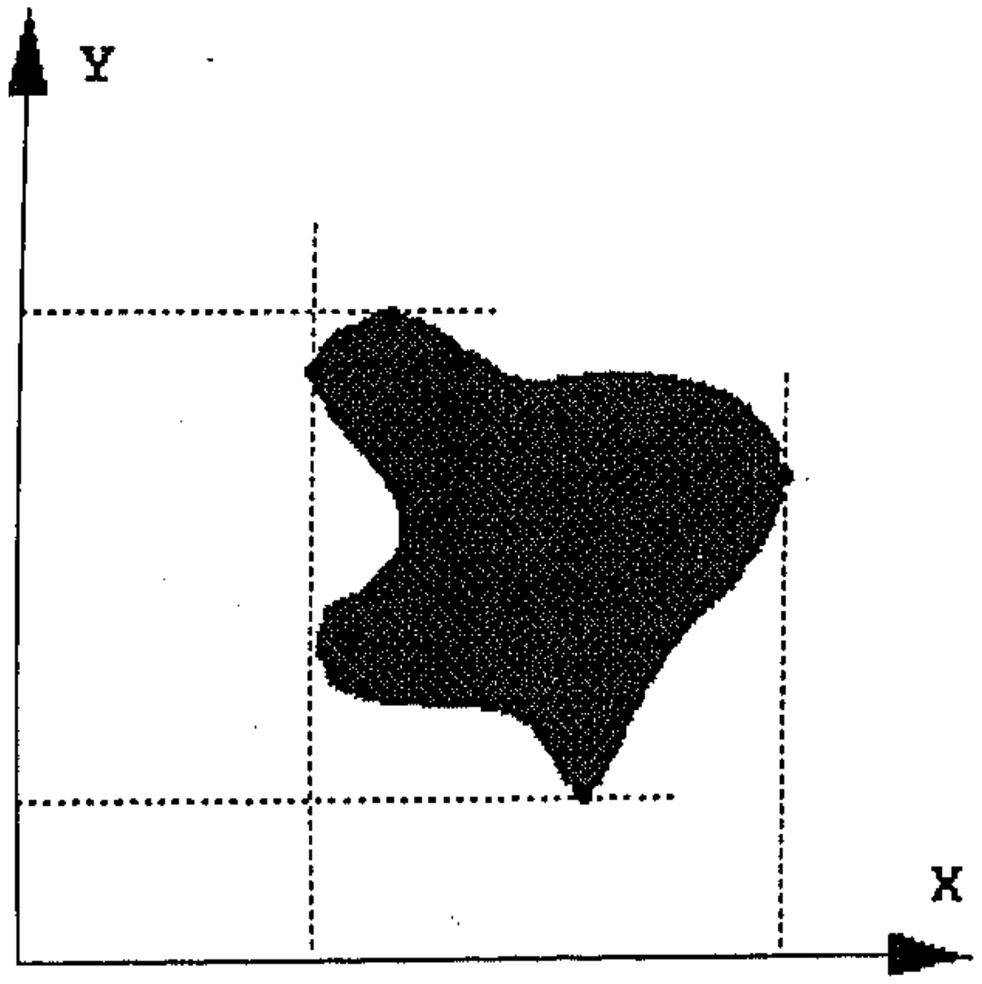

(a)

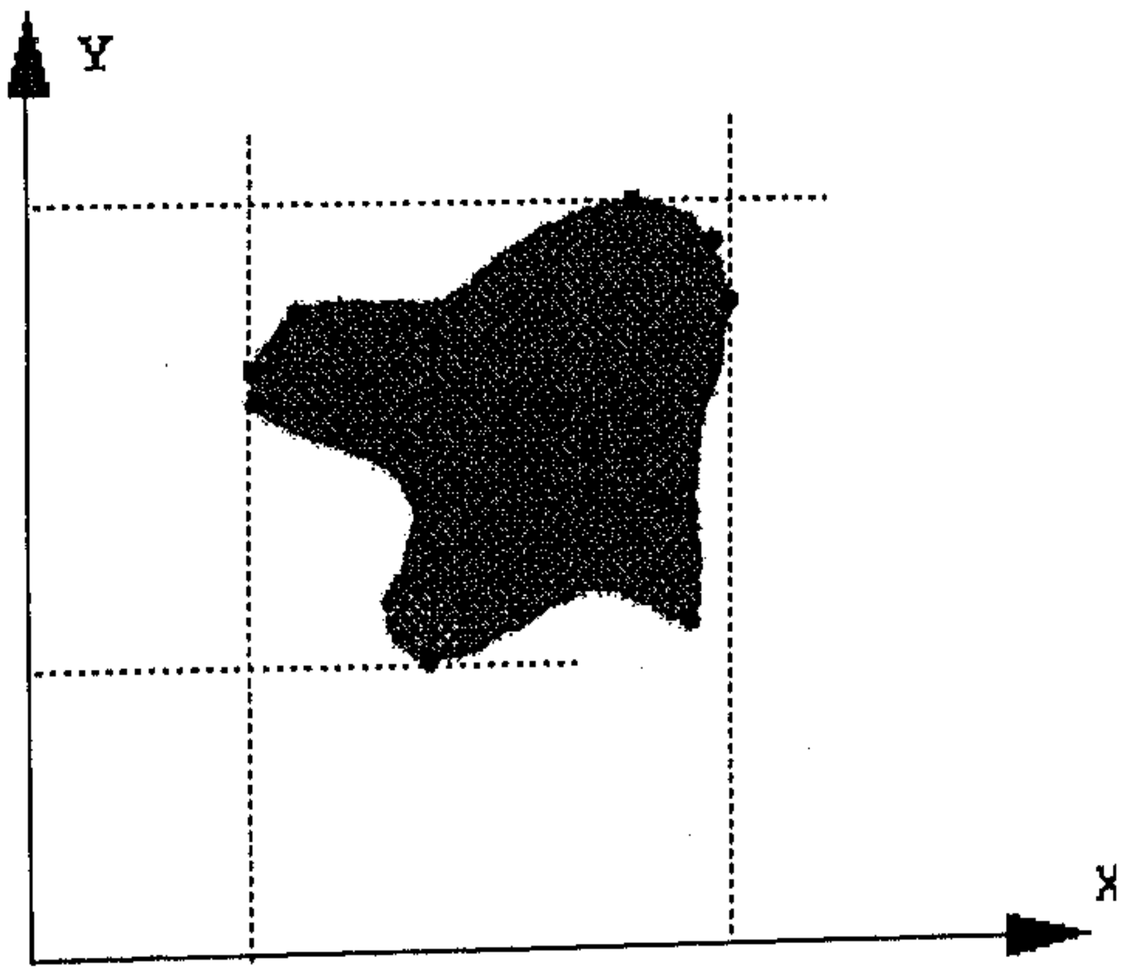

(b)

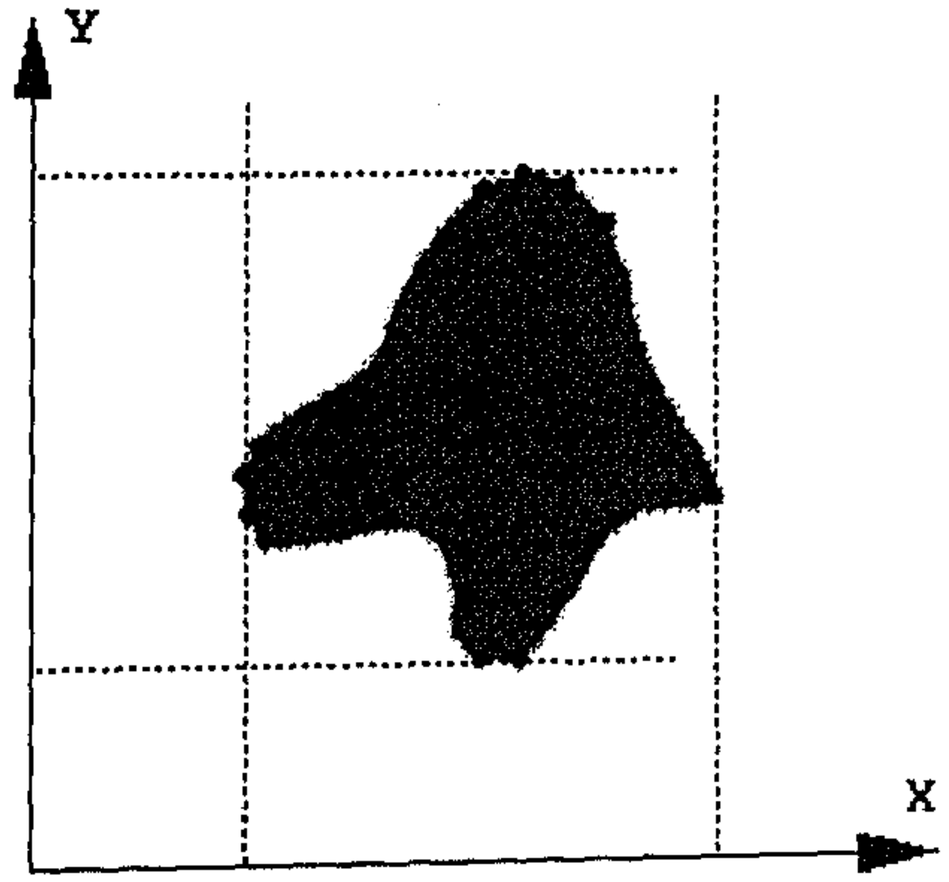

(c)

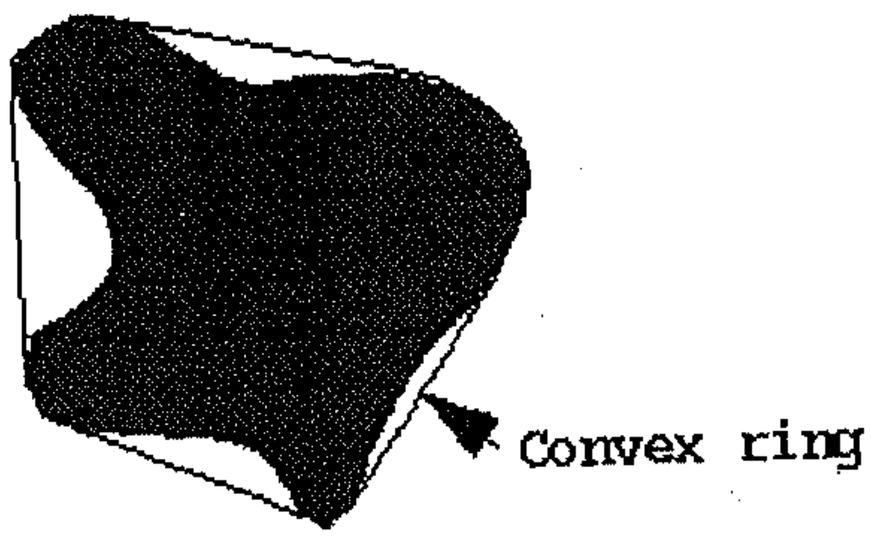

(d)

Fig. 6.2: Construction of N sided isolated polygon around a cell shown in 2-D (a) Locating extreme co-ordinates at 0° rotation, (b) Locating extreme co-ordinates after 45° rotation, (c) Locating co-ordinates after 90° rotation of the object (d) Convex ring constructed by joining all the extreme points found at different angle of rotations.

The boundary pixels are sorted to find the smallest and the largest coordinates. Then the co-ordinate axes are rotated to obtain another set of smallest and largest coordinates. For the purpose of constructing an n-sided convex string, a set consisting of n smallest and largest co-ordinates is needed. In our experiment we have used 8 directions of 22.5° difference (180°/8 = 22.5° step). This has resulted in a polygon of 16 corners and sides, approximately forming the convex string around the cell of interest.

This gives a two-dimensional convex hull. The extension to 3-D is straight forward. The extreme coordinates are marked at different combinations of Φ and Θ which represents a spatial angle. These marked extreme coordinates can be considered as node points. Polygonal surfaces can be constructed by properly joining the node points or by methods using voronoi diagrams. The total area of the polygonal surfaces can be considered as the convex surface. The volume enclosed by the polygonal surfaces is considered as the

convex volume of the 3-D cell. As the image stack representing the data has a very high axial resolution, it is possible to construct the polygon around the cell of interest in each image slice and taking the convex volume as the sum of the convex area of the object in each image slice. The error is minimized by using the image stack with isotropic voxel lattice obtained by mathematical interpolation. Similarly the convex surface area of the 3-D objects can also be calculated.

Solidity: is the ratio of convex volume of the cell to the actual cell volume, i. e. $\frac{Convex\ Volume}{Volume}$. The convex volume is measured as the volume bound by the convex surface constructed by n-sided polygon as explained above.

Compactness: Compactness is another way of defining the relation between the volume of the cell and the R_{max}. The compactness ς can be mathematically expressed as $\varsigma = \frac{\sqrt[3]{\left(\frac{6}{\pi}\right)V}}{2R_{max}}$. The compactness of a symmetrical sphere is 1.

All these features defined above gives useful shape values of the cells. the relative variation in the shape of the cells in a tissue specimen can thus be calculated and attributed to different sub-classes of the disease.

Other than shape features, one of the most important factor that can guide the sub-classification is the set of histological features. These include orientation or directionality of the cells in the tissue, most dominant direction, number of neighbors, cell density, clustering, inter nuclear distances, disruption of tissue architecture, etc.. Many of these features can not be quantified precisely and heuristics have to be developed for the purpose. The measured values are compared with the histological features of the healthy tissue architecture and subsequently ranked. In the following we have explained some of these features and methods to measure them in 3-D images.

Spatial Orientation of the Cells: This is one of the important features as it indicates the different subclasses of a pathological disorder in many types of tissues. For many organs in the body, the healthy tissue consists of the cells having same spatial orientation or directionality. In tumors, the cells lose their directionality and start swimming around aimlessly as the grade of the tumor increases.

In a three-dimensional image, the spatial orientation is represented by two angles. There are many ways to determine the orientation. This includes, the orientation of the longest dimension in the feature (Feret's diameter), orientation of the major axis of a best fit ellipsoid, etc.. Orientation defined by all the voxels in the image is often a better method because, it is less influenced by the presence or absence of a single or group of voxels around the periphery of the cell. We have extended the 2-D orientation formulation given in Russ (1995) for finding the orientation of the objects in 3-D space. Here orientation of a cell is calculated

based on its moment axis. The moment axis of a feature is the axis which best fits all of the voxels in the sense that the sum of the squared distances of the individual voxels from the moment axis is minimum. The orientation of the moment axis gives the orientation of cells in 3-D space.

Let the following be the set of co-ordinate summations derived from image features. We are not weighing the coordinates with their intensity values. Instead each voxel votes equally. This avoids the erroneous influence of dense intra-cellular matters, textured chromatin, etc., on the directionality of the cell. If there are n-number of image slices in the image stack and $\left(x_i, y_i, z_i\right)$ are the co-ordinates of the voxels belonging to the object, then let,

$$S_x = \sum_{j=1}^{n} x_{ij} \; ; \; S_y = \sum_{j=1}^{n} y_{ij} \; ; \; S_z = \Sigma z_i \; ; \; S_{xx} = \sum_{j=1}^{n} x_{ij}^2 \; ; \; S_{yy} = \sum_{j=1}^{n} y_{ij}^2 \; ;$$

$$S_{zz} = \sum_{j=1}^{n} z_{ij}^2 \; ; S_{xy} = \sum_{j=1}^{n} x_{ij} y_{ij} \; ; \; S_{xz} = \sum_{j=1}^{n} x_{ij} z_{ij}$$

Then the net moment about the X , Y and Z axes can be calculated by using the above summations as,

$$M_x = S_{xx} - \frac{S_x^2}{Volume} \quad ; \quad M_y = S_{yy} - \frac{S_y^2}{Volume} \quad ; \quad M_z = S_{zz} - \frac{S_z^2}{Volume}$$

$$M_{xy} = S_{xy} - \frac{S_x S_y}{Volume} \quad ; \quad M_{xz} = S_{xz} - \frac{S_x S_z}{Volume} \quad ;$$

Then the angle of minimum moment with respect to XY plane and XZ plane respectively can be calculated as

$$\Theta = tan^{-1}\left\{\frac{M_{xx} - M_{yy} + \sqrt{\left(M_{xx} - M_{yy}\right)^2 + 4M_{xy}^2}}{2M_{xy}}\right\}$$

$$\Phi = tan^{-1}\left\{\frac{M_{xx} - M_{zz} + \sqrt{\left(M_{xx} - M_{zz}\right)^2 + 4M_{xz}^2}}{2M_{xz}}\right\}$$

More details about the calculation of 3-D orientation can be found in Russ, (1995), Sadjadi and Hall, (1980), etc..

Most Dominant Direction: The spatial angles defining the directionality of the cells are calculated as explained above. Most dominant direction is that direction in which maximum number of cells are oriented. The spatial angles are divided into n sub-groups of equal arc length. This approximates the possible spatial direction to ${}^{n}C_{n}$ combinations of Θ *and* Φ. The central angles of each sub-group are considered as the direction of that sub group. Number of cells having orientation in the same range of each directional subgroup is calculated and the group direction having maximum number of cells is considered as most dominant direction. Let the total number of cells belonging to the most dominant direction be ρ_d and the number of cells having orientation other than the dominant direction be ρ_o. Then the disruption in directionality of the cells can be defined as $\frac{\rho_o}{\rho_d}$. This ratio will be zero when all the cells have the same direction.

Number of Neighbors: In many cases, the variation in the number of neighbors each cell pocess can give an indication on the spatial arrangement of cells in the specimen image. For finding the neighbors, a definition of the neighborhood that is consistent to all the specimen image data is necessary. A neighbor can be defined as a touching cell or an overlapping cell or all the cells in the cluster or all the cells within a specified distance from the cell surface, etc.. We have defined a spatial volume around each cell based on the cell centroid and its maximum radius R_{max}. A spherical volumetric space within the image domain with the cell centroid as its center and $2 \cdot R_{max}$ as its radius is considered as the spatial neighborhood of each cell. All the cells having their signature in this domain are considered as neighbors.

Inter-Nuclear Distance: This is one of the more precise measurement which is useful in quantification of a tissue architecture. We have calculated all the inter-nuclear distances as distances between cell centroids. Some of the features derived from the inter-nuclear distances are

1 Mean distance between cells: The nearest neighbor distance or the nearest cell centroid distance for all the cells in the image domain is calculated. The average of the nearest neighbor distances gives the average distance between the cells. This feature is helpful in quantification of the cell distribution in the image space.

2 Minimum Inter-Nuclear Distance: Distance between two nearest cells centroids within the image domain.

3 Variation in Inter-nuclear Distance: The distance of each cell from the nearest neighboring cell is calculated. The deviation in the nearest distance values is useful in empirical measurement of the cell distribution in the image.

Cell Density: Cell density indicates the number of cells present in the image. This is proportional to the number of cells in the tissue specimen under test. Lower cell density may indicate that the cells are spread out and are not exhibiting close cluster properties.

Calculation of the cell density as a number of cells within the complete image domain may lead to erroneous conclusions. In the image data sets, it has been visually observed that the cells can be clustered at some corner of the image and this gives lower cell density in overall image space. This may be due to the glandular arrangement of the cells with a narrow lumen in the prostate tissue as well as peculiarities of image acquisition and specimen preparation. We have divided the image space into a few sub-spaces and the cell density in each sub-space is calculated. We have divided the image space into five sub-spaces i.e., central and four corner spaces of size $150 \times 150 \times N_s$ which are overlapping on each other. N_s is the number of images in the image stack. If it is found that any part or the combination of neighboring partitions of the image space is exhibiting high cell density, then the cells are clustered at those places and only those part of the image space is used to calculate the cell density. This can also indicate the presence of outliers i. e., floating independent cells in a compact tissue.

Cell density in each part where cell signatures are present, is calculated and can be correlated with the different stages of the pathological disorder. This is a highly heuristic feature extraction method which worked well for many data sets.

Cell Distribution Pattern: The cell distribution pattern is an important feature for studying the spread of the malignancy in carcinomic disorders. If the cells are isolated and floating in the tissue, often this indicates higher grades of carcinoma. Precise quantification of the cell distribution pattern is a difficult task. An approximate quantitative idea about the cell distribution pattern can be obtained by studying the cell cluster properties, inter nuclear distances, cell density, etc..

Variation from the Ideal Tissue Architecture: This is one of the most important features. During visual categorization of the tumor specimens, pathologists look at the specimen through a microscope and visually compare the architecture of the tissue under investigation with the architecture of the healthy tissue. The amount of variation or disruption in the tissue architecture is then used to sub-classify the pathological disorder or to find the grade of abnormality. This is a qualitative approach. It depends on the experience of the pathologist in distinguishing different grades based on variation in tissue architecture. The result may not be reproducible and it varies from one pathologist to another. We have tried to quantify this feature based on heuristic methods. This feature is measured as the linear combination of different histological features. They are 1. Number of neighbors, 2. Cell cluster density, 3. Inter nuclear distance and 4. The connecting line pattern. Large number of neighbors to the cells indicates more number of cells within a limited space and hence the close arrangement of cell nuclei. Number of cell cluster and the cells per cluster also gives similar idea about the tissue architecture confined to image space. Inter-nuclear distance is also an important factor. A weighted combination of these normalized feature values can be used to define a macro-feature such as disruption in the tissue architecture.

In the following, we have described a method to rank the disruption in the glandular arrangement of the cells in a prostate tissue specimen images as an example. This is a heuristic approach but the result is found to be very supportive.

In a secretion gland tissue such as prostate, etc., cells are arranged in a ring like arrangement with a central hallow lumen. This is called glandular structure or acinus structure. A disruption in the glandular architecture may indicate a pathological disorder. The amount of disruption can be used to sub-classify the disease. We have developed a heuristic connecting line pattern method to quantify or rank the disruption in glandular architecture.

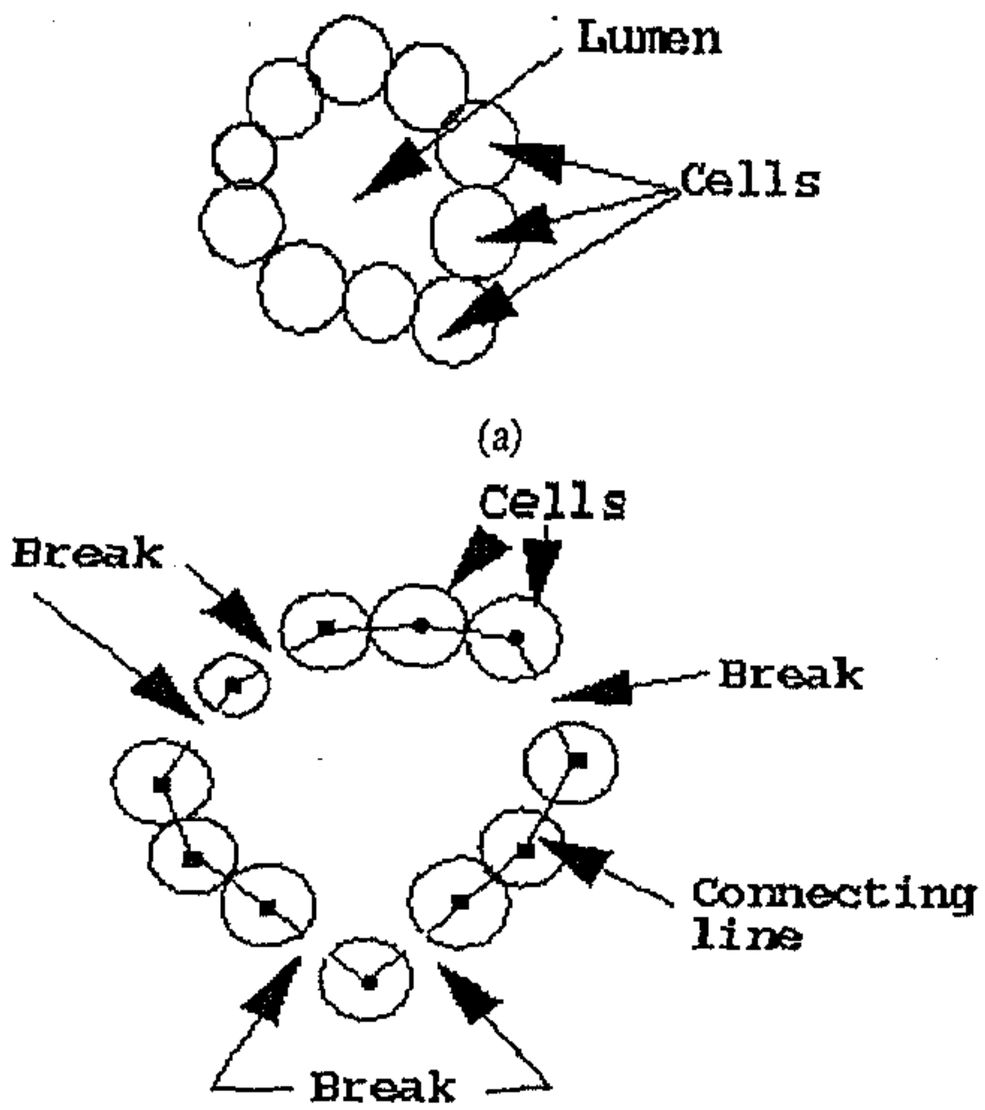

Fig. 6.3: Diagrammatic representation for quantifying the ring like architecture of prostate tissue glands. (a) A complete glandular arrangement of the cells (b) Break in the glandular arrangement of the cells.

A virtual line is drawn passing through the centroid of all the cells in a cluster. The criss-crossing of the lines is avoided by connecting the cells to another nearest cell centroid of the same cluster which is not connected to any other cell centroid. If this line does not pass through the background region, then the cells can be considered as touching and closely arranged. More the number of times it passes through the background, more the breaks in ring like arrangement of the cells. Thus number of times the line crosses the cell boundary into the background region can be related to the breaks in the ring like structure. It is possible that the line may pass through the background even while connecting to the centroid of the touching cell. Hence a break is considered only when the length of the connecting line passing through the background is more than a pre-defined threshold. The threshold can be a data driven one like the radius of the smallest cell, etc.. We have fixed this value as the average of R_{min} of

the cells in the cluster. This value for each cell was calculated while measuring the eccentricity of the cells. A schematic diagram of this feature indicating number of cross over to the background region by a connecting line is shown in Fig. 6.4, for different grades of the prostate cancer.

Table 6.1 gives some quantitative study in this regard and comparative view point of a pathologist ranking the gland disruption in a prostate tumor tissue. When only this measure is considered, the method is less useful. If considered along with other features such as inter-cellular distance, number of neighbors for each cell, etc., the comparison improves considerably. Nearly 75% correct ranking of the disruption in glandular structure can be obtained. It should be noted that the experiments are done on the image having a clear view of the glandular arrangement of the cells. In a low magnified images, this may not be possible.

Sp. No.	Pathologists ranking	Ranking by heuristic algorithm	
		Only breaks in the connecting line are considered.	Additional features like cell density and variation in inter-nuclear distance is considered
1	4	4	4
2	4	3	3
3	3	3	3
4	5	4	5
5	3	3	3
6	3	3	3
7	5	4	4
8	4	3	4
9	2	2	2
10	2	3	2
11	1	2	2
12	2	3	2
13	2	3	2
14	2	3	2
15	3	4	3
16	3	4	4
17	4	4	4
18	3	3	3
19	4	3	3
20	5	4	5

Table 6.1: Comparative study of disruption in acini.

Rank 1: perfectly acinous, Rank 2: Small variation, Rank 3: Began to break, Rank 4: Floating cells, Rank 5: No acinous structure

Another useful set of features includes the various measurements made on the gray level of the voxels belonging to the objects. This type of features can be broadly brought under the heading histogram features. Different histogram features which may be important to analyze the various grades and stages of the disease are explained below.

Histogram Features: These features are based on the histogram of a region of interest in the image domain. Histogram features can be best defined based on the gray level probability (Jain, 1995). Let u be the random variable representing a gray level in a given region of the image. Then the gray level probability $p_u(x)$ is defined as

$$p_u(x) = Prob[u = x] \approx \frac{No.of\ voxels\ with\ gray\ x}{Total\ No.of\ Voxels\ in\ the\ image}, \qquad x = 0,1,\ldots,255$$

Mean Gray value of the Cell: This gives the average intensity of the voxels belonging to the cell of interest. This can be calculated as $\bar{\mu} = \sum_{x=0}^{255} x \cdot p_u(x)$. This feature can be used to find out the variation in the average intensity of the cells and thus relate the darker or lighter cells to some stage of the pathological disorder.

Variance of the Gray Value of Voxels of the Cell: Variance and standard deviation of the image intensity within the cell can also be an important feature in some cases. The variance can be calculated as $\sigma^2 = \sum_{x=0}^{255} (x - \bar{\mu})^2 \cdot p_u(x)$; while the standard deviation is $= \sigma$.

Mean Absolute Deviation of the Gray level: This is one more feature representing the variation of the voxel intensity from the mean voxel intensity of the object. This can be calculated as $\frac{1}{N} \sum_{i=0}^{N-1} |x_i - \bar{\mu}|$ or $\sum_{x=0}^{255} |x_i - \bar{\mu}| \cdot p_u(x)$; where N is the total number of voxels in the image.

$$Skewness = \sum_{x=0}^{255} (x - \bar{\mu})^3 \cdot p_u(x) \ ; \ Kurtosis = \left(\sum_{x=0}^{255} (x - \bar{\mu})^4 \cdot p_u(x) \right) - 3$$ and

$Mode = x$; if, $p_u(x) = max(Prob[u = x])$, gives the other histogram features. The importance of these features depends on the maintenance of similar standards for image acquisition and specimen preparation. Many tissues and cells are known to show wide variation in their histogram features during different levels of pathological disorder.

Amplitude Features: of an image region include the average gray value of the region of interest, standard deviation and mean absolute deviations of the gray values in that region.

Cell cluster properties: Some times the shape and histogram properties of the cluster of cells taken together give a useful information about the tissue specimen. Some of the cluster properties are variation of the inter cluster distance, mean volume of the clusters, mean gray value of the clusters, number of cells in the clusters to cluster size ratio, variation in cluster volume, variation in cluster gray value, etc..

Texture Features: Features based on image texture plays an important role in most of the applications dealing with sub-classification of the pathological images. The fundamental texture measurement features are derived from the gray level co-occurrence matrix of the image. The gray level co-occurrence matrix $P(x, y, z)$ captures the spatial distribution of the gray levels in the image space (Jain et al, 1995). Some of the features which can be measured based on the gray level co-occurrence matrix are entropy, contrast, etc..

1 Entropy: $= \sum\sum\sum P(x, y, z) \cdot log(P(x, y, z))$
$x\ y\ z$

2 Contrast: $\sum\sum (x-y)^2 \cdot P(x, y)$; Contrast along the lateral direction

$\sum\sum (x-z)^2 \cdot P(x, z)$; Contrast along the axial XZ direction

Another texture function that can be used to measure the periodicity of the texture as well as a measure of the scale of texture primitives, is the auto-correlation function (Jain et al, 1995). Choi (1996), has used various textural features derived from co-occurrence matrix. These include, vertical. horizontal, minor diagonal and major diagonal sums of the co-occurrence matrix. From this matrix, features such as directional probability distributions, the mean of vertical, mean of horizontal, variance of vertical, variance of horizontal etc., were calculated. They have also measured angular second moment, difference moment, inverse difference moment, diagonal moments, product moments, etc.. Also given are many information measures such as directional entropy, total entropy, local homogeneity, etc..

The image data we are using, are highly magnified and the specimen area covered under the microscope is so small that the calculation of texture features based on gray level co-occurrence matrix, auto-correlation function, etc., are found be of less useful in sub-classification of the magnified 3D tissue structures. The features which can be measured using gray level co-occurrence matrix, such as, energy, contrast, homogeneity and auto-correlation are useful in cases of low magnified images where the cells appear approximately as a point in the micro-textured histological image.

The features described in the above section includes single cell features, relative cell features and complete tissue features. It has been observed that the single cell features and the relative cell features which can be clubbed under the name cytological features can be computed precisely from the segmented image. The same is not true with the histological features as many heuristics and ambiguous methods have to be used for quantifying histological features. The methods which are prescribed for histological or tissue features have to be studied on various types of data and should be statistically validated as a feature of importance for quantitative studies.

6.4 Importance of Cytological Features

Traditionally, histologic features such as the variation in tissue architecture compared to that of healthy tissue, is used to grade disorders such as prostate cancer. In recent times many researchers have tried to show that inspection of the cytological features by fine needle biopsy is good enough for grading the diseases like prostate carcinoma (Benson, 1988), (Mostofi, 1976), (Esposti, 1971). To assist the diagnosis and prognosis of a well differentiated cancer, Kline and Kannan (1985) have developed major and minor criteria for the cytological interpretation of well differentiated prostate cancer. They have defined five major and five minor criteria based on which a reliable grading of prostate cancer tumor can be done.

1. **Cellularity:** Similarity of the cells to the ideal healthy cell in its content, shape and other morphological features.
2. **Nuclear irregularity:** Relative irregularity in shape, size, etc., of the cell nuclei.
3. **Anisonucleosis:** This feature mainly deals with the variation in the size of the individual cells. The term anisonucleosis means the inequality in the size of the cell nuclei.
4. **Macronucleoli:** Nucleosis is a part of the cell nucleus in which ribo-nucleo protein is produced. Enlargement of nucleolus is a feature common to cells of tumors of different types.

The minor criteria for cytological diagnosis of prostate cancer are

1. **Polarity loss:** Loss of polarity can be measured by finding the orientation of the different cells in the tissue specimen. The extent to which the loss of polarity occurs can be directly correlated to the grade of the prostate cancer.
2. **Crowding:** Clustering of the cells in a tissue.
3. **Piling:** This also is related to clustering property where the cells are overlapping or piling one over the other.
4. **Microacini:** A single unit of the secretion gland such as prostate is called acinus if it has a rounded shape and a narrow lumen. Micro-acinus is the one where the tissue is characterized by small acini.
5. **Cell enlargement:** In a tumor, typically cells enlarge in size compared to healthy tissue. Appearance of enlarged cells can thus be related to a grade of prostate cancer tumor.

Other cytological features include variation in the individual cell shape, histogram features, connectedness, etc.. Each feature can be given a weight based on experimentally found importance of the feature and the pathologists view point. It has been observed that the variation in these features can be easily recorded and used for grading the carcinoma of the prostate. Similarly many other studies on fine needle biopsy of several pathological disorders have shown that in most of the cases the cytological features are good enough to differentiate the different stages of a pathological disorder. We have given more importance to the extraction of cell features in our work. In the next chapter we have shown how simple

cytological features are good enough for the sub-classification of the prostate cancer tissue specimen into different grades.

6.5 Influence of Segmentation Over Feature Values

In this section, we briefly investigate how the object feature measurement is influenced by the technique used for image segmentation and its parameter settings. To some extent, explains why we need more than one type of segmentation technique to segment the cells in a tissue before extracting their feature values. Young (1988), has pointed out that "The ability to derive accurate measures of image properties is profoundly affected by a number of issues". Quality of image segmentation is one such issue. The quality of image segmentation is determined by the overall efficiency of the segmentation techniques. We have used segmentation procedures such as local thresholding, simple edge detectors, active models, region based techniques as well as integrated approaches explained in chapter 3 and chapter 4 for cell and tissue feature measurements. For measuring the features like cell density or inter-nuclear distances, we don't need accurate segmentation of the cells but we need only the cells to get isolated by the segmentation process. In such cases, seeded volume growing, layered segmentation or pealing and thickening process can do a good job. Thus, depending on the feature we are interested in measuring, we have to choose a proper segmentation technique. We have selected few important features of the cells and tissue for checking the influence of different segmentation techniques on its measurement. These features are 1) Size, 2) Surface Area, 3) Shape Factor, 4) Eccentricity, 5) Convexity, 6) Spatial Orientation. The definition and the importance of these features are already discussed in section 6.3.

The next task is to define a measurement judging criteria. In an image understanding system, a goodness of object feature measurements can be assessed by their accuracy. Let the accuracy of the automatically measured feature be called as Measurement Accuracy (MA) and the Relative Measurement Accuracy (RMA) of a feature f is denoted as $(RMA)_f$. Then,

$$(RMA)_f = \frac{|A_f - M_f|}{A_f} \times 100\%$$

where A_f is the actual feature value whose measurement is based on the manually segmented cell and M_f is the measured feature value based on automatic and semi-automatic segmentation methods. The $(RMA)_f$ represents the disparity between the feature measurement based on different segmentation methods when compared to the manually segmented object feature measurement. The interactive segmentation done with the help of pathologist is taken as a gold standard for all comparative study.

Graphs 1-6 shown in Fig. 6.5, give the experimental results about the influence of different segmentation techniques on feature measurement. The X-axis of the graph represents various segmentation techniques incorporated in the image understanding system and the Y-axis gives the value of $(RMA)_f$. The X-axis numbers 1, 2, 3...., 11, represents simple local thresholding, sobel operator, LoG operator, canny operator, layered segmentation, active

contour models, active surface model, controlled seeded volume growing, successive pealing and constrained thickening, 3-D watershed with automatic merging and integrated approach for segmentation respectively.

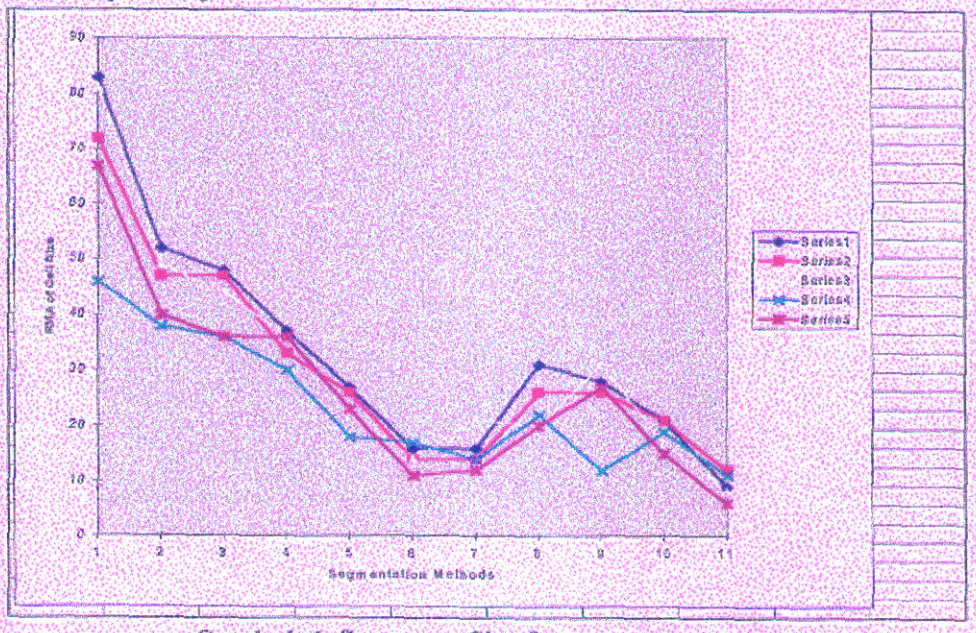

Graph. 1: Influence on Size feature measurement.

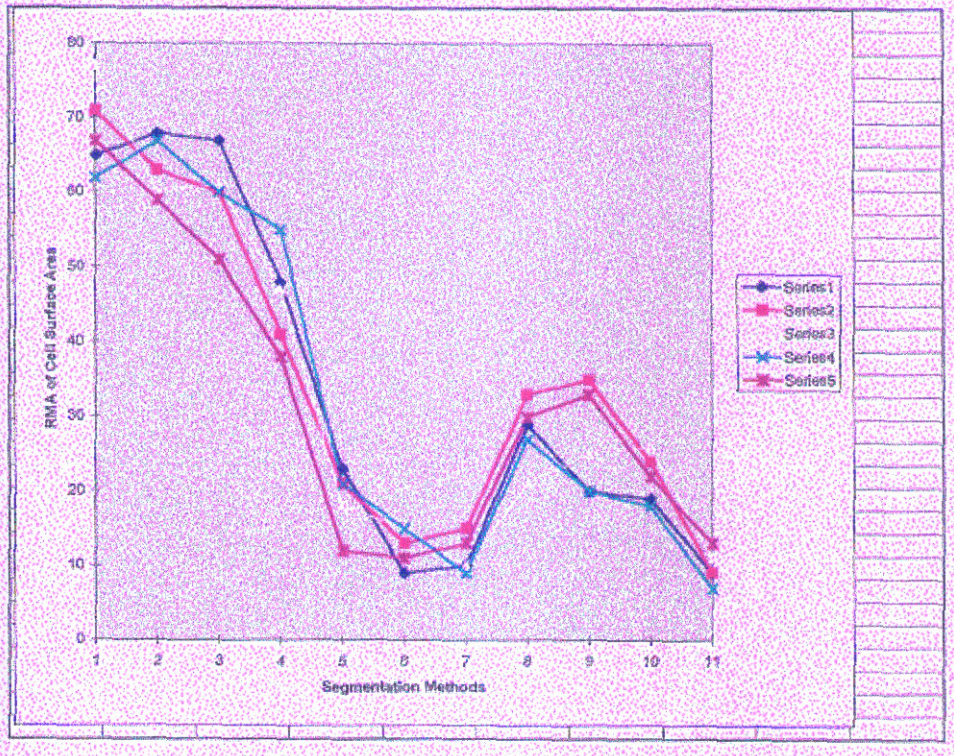

Graph. 2: Influence on surface area measurement.

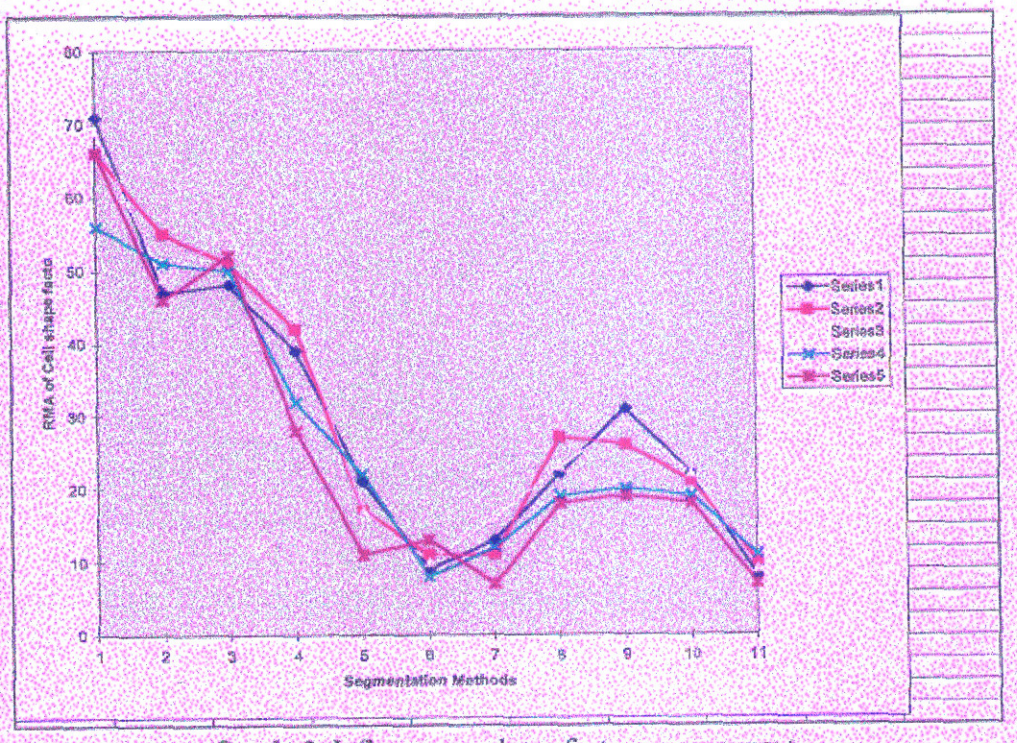

Graph. 3: Influence on shape-factor measurement.

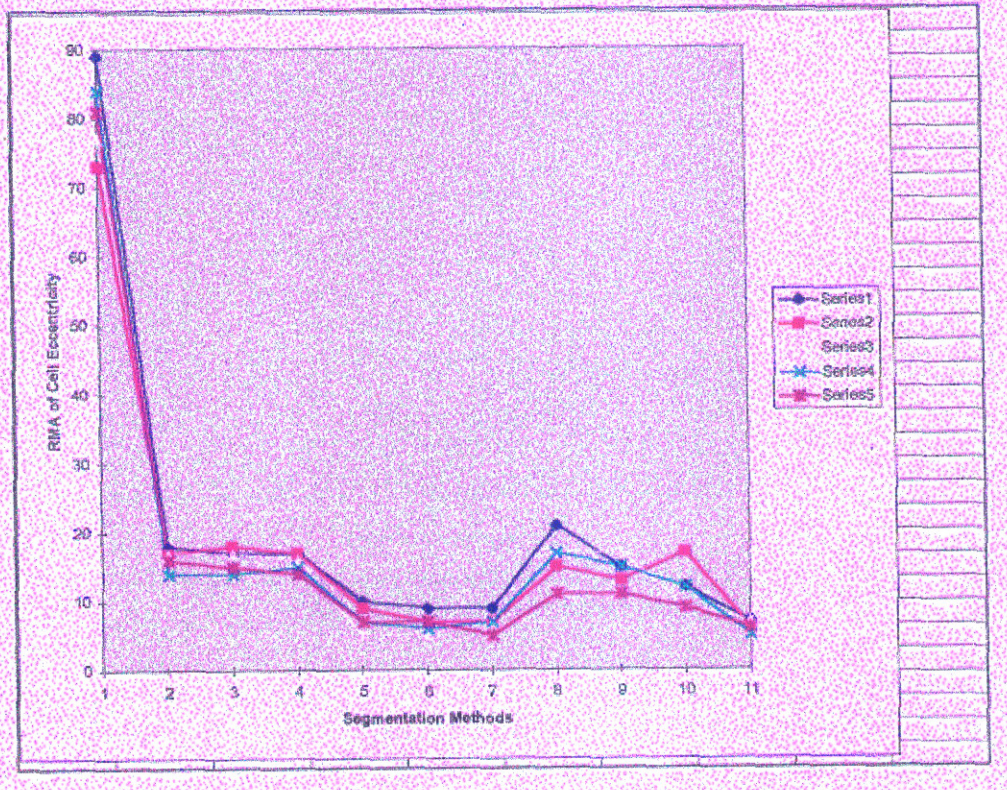

Graph. 4: Influence on eccentricity measurement.

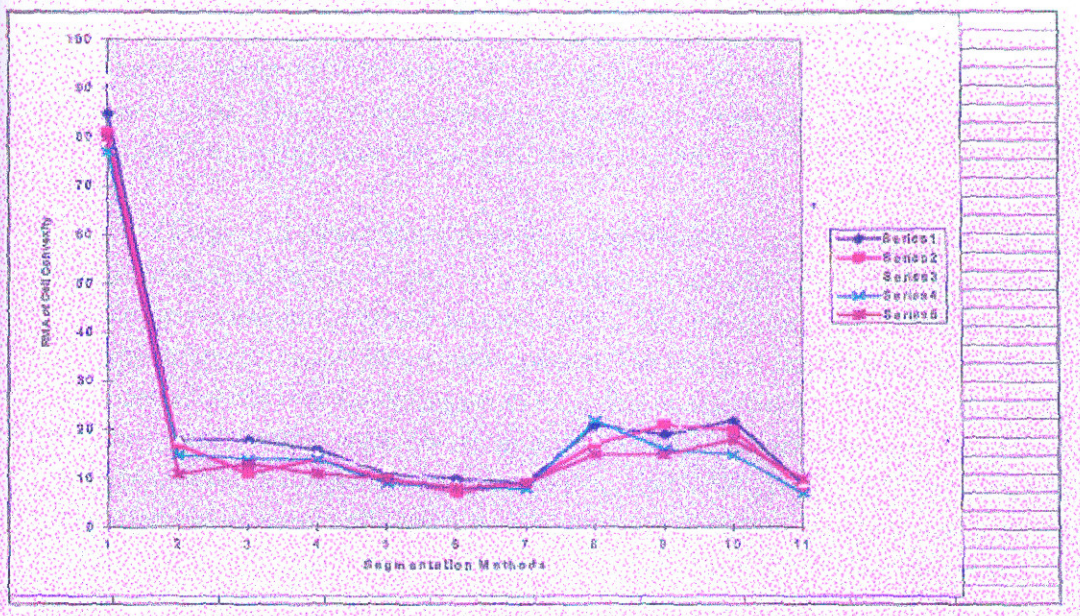

Graph. 5: Influence on Convexity measurement.

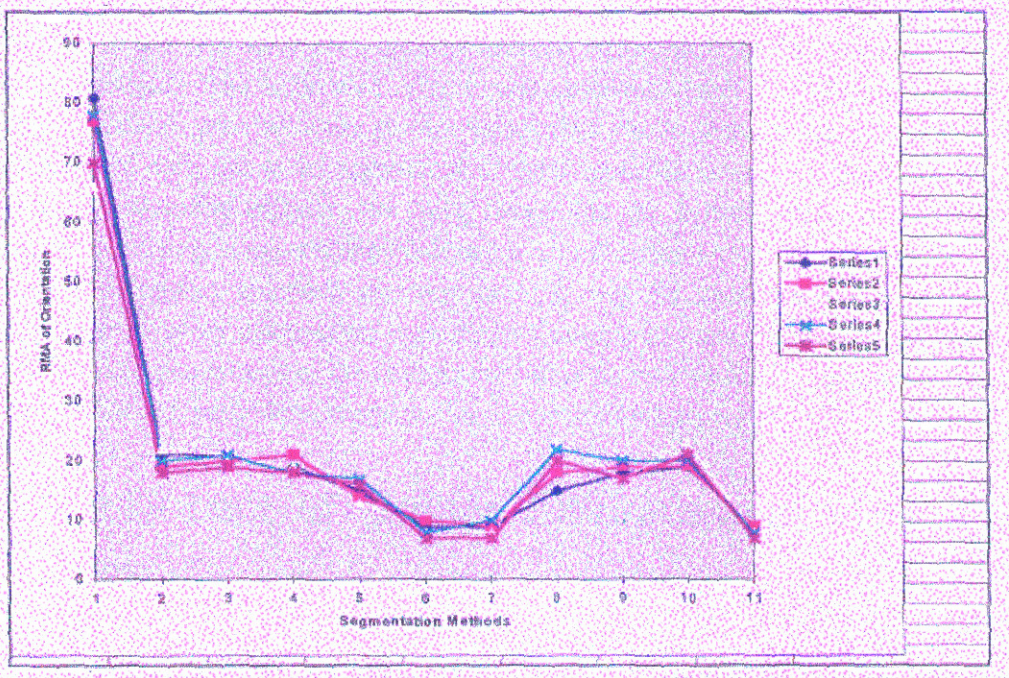

Graph. 6: Influence on directionality.

Fig. 6.5: Graphs showing the influence of different segmentation methods on measurement of different features. Series 1, Series 2, ..., Series 5, represents five different specimens. The X-axis numbers 1, 2, 3...., 11, represents simple local thresholding, sobel operator, LoG operator, canny operator, layered segmentation, active contour models, active surface model, controlled seeded volume growing, successive pealing and constrained thickening, 3-D watershed with automatic merging and integrated approach for segmentation respectively.

The graphs show that simple thresholding fails to isolate the cells in a tissue section images resulting in a large error in measured features. It is obvious as the cells are arranged in a compact cluster and the variation of intensity at the touching or overlapping boundary portions is less. The local edge operators produce reasonably good results but are plagued by detection of too many noisy edgels and broken contour.

Graphs 1-6 shows the influence of segmentation methods on size of the cells. The thresholding methods do not give accurate segmentation and hence large error can be found in feature measurement for almost all the features. The remaining segmentation methods shows varying influence on the feature measurement. Generally, it can be concluded that the simple edge detectors also results in large error in feature measurement. In some cases, region based methods have shown larger errors compared to active model approach for segmenting the cells of interest. As expected, the integrated approach has given a better accuracy for feature measurement in almost all the cases. The increase in computation and the time required to complete the process of segmentation are the main hurdles in using the integrated approach in all the cases for segmentation.

In cases where the cells are touching each other by frail connections, edge detectors along with some post-processing would give acceptable results and the feature values measured has less error compared to features measured from the images segmented using other methods. The high-level edge based techniques such as active contour models and active surfaces provide better feature values. But much of the advantage is lost when large number of cells are to be segmented as these methods are more interactive in nature and sensitive to noise artifacts. We have found that the features measured from the images segmented using integrated approach has given minimum error. Though this prompts to make use of integrated approach in every case, it may be disadvantageous as the integrated approach involves many other approaches resulting in slow processing. Depending on the image and arrangement of the cells in the image as well as the features to be measured, one has to choose from several segmentation methods for obtaining good measurement.

6.6 Influence of Image Enhancement Over Feature Values

Noise reduction and image enhancement are integral parts of an image understanding system. Image enhancement is normally done prior to the image segmentation. Conventionally, image enhancement is supposed to have better and correcting effect on image feature measurement. The image enhancement is influenced by the performance factor of noise reduction, smoothing filters and their ability to keep the feature values intact. Sometime measurements done on the enhanced image feature may give wrong feature values. For example, the value of the size of the cell (in number of voxels) measured on a resolution enhanced image is much more than the actual size measured over original image stack. This shows that though many of the enhancement tasks are needed for better segmentation of the cells in the image, their effect has to be taken care off while measuring the feature values.

We have chosen the noise reduction and enhancement methods explained in chapter 2 for studying the effect of image enhancement on feature measurement. The features which are much affected by the image enhancement, are histogram features and textural features. Image enhancement has an indirect influence on all measurements as the precision of segmentation process depends on the noise reduction and feature enhancement of the images. Shape features are also tested for studying the effect of image enhancement on feature values. The error in image measurement with and without enhancement is calculated as follows.

Let O_f be the measured feature value on the original image stack and E_f be the feature value measured from the enhanced image stack. Then relative measurement accuracy $(RMA)_f$ is defined as,

$$(RMA)_f = \frac{|O_f - E_f|}{O_f} \times 100\%$$

We have measured size, histogram features such as mean gray value, variance of the gray value of the cells in the image and compared them with the results obtained from the original unprocessed image stack. Graphs 1-3 shown in Fig. 6.6, shows the RMA in measured values of the features before and after image enhancement for different segmentation techniques.

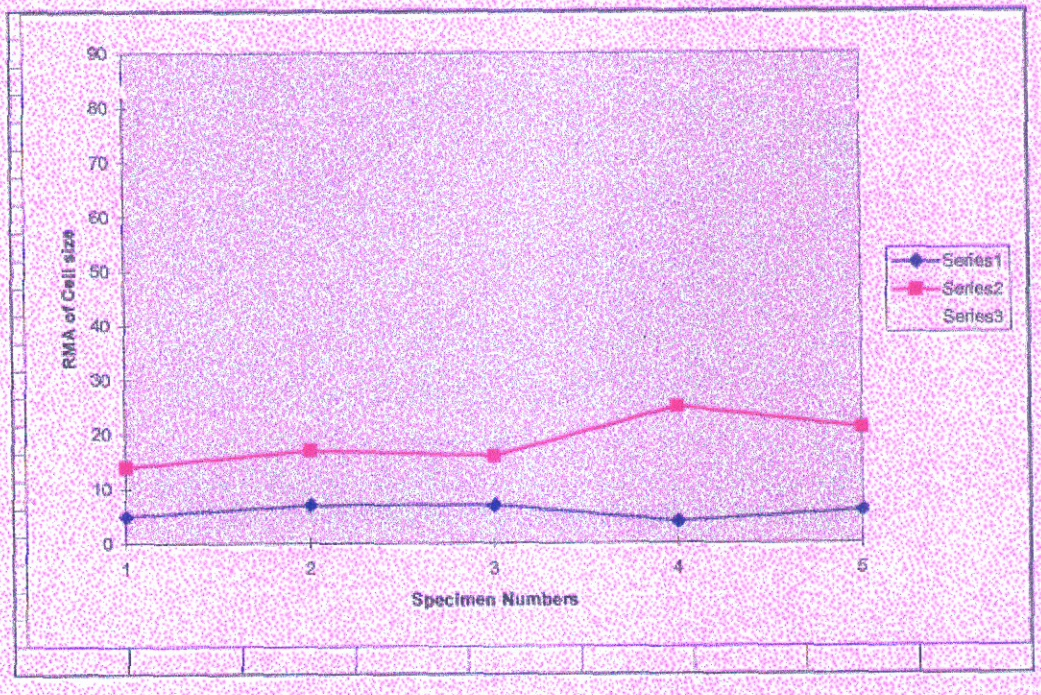

Graph. 1: Influence on Size of the cells

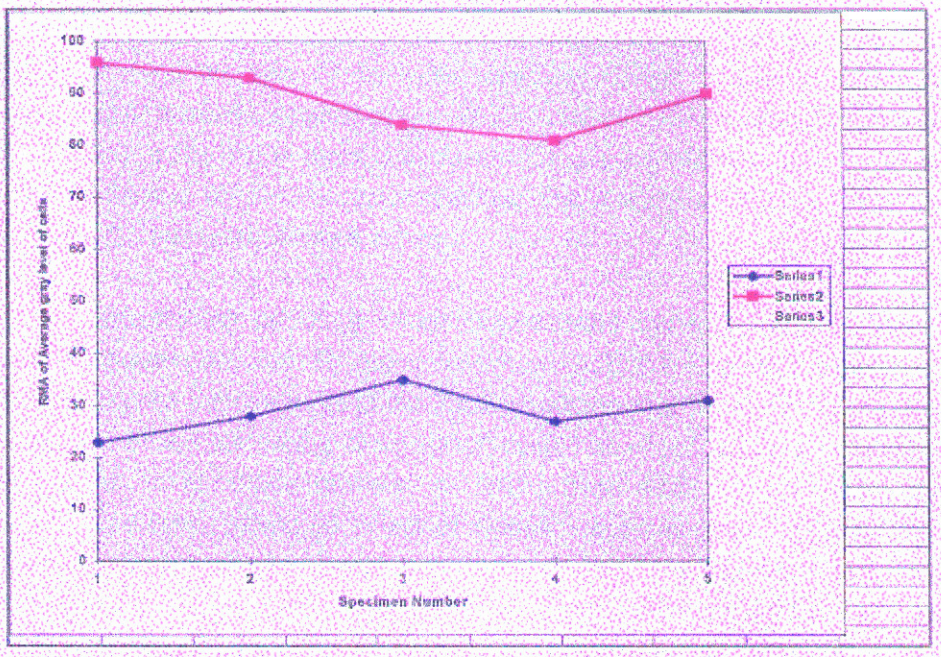

Graph. 2: Influence on Average gray value of the cell voxels.

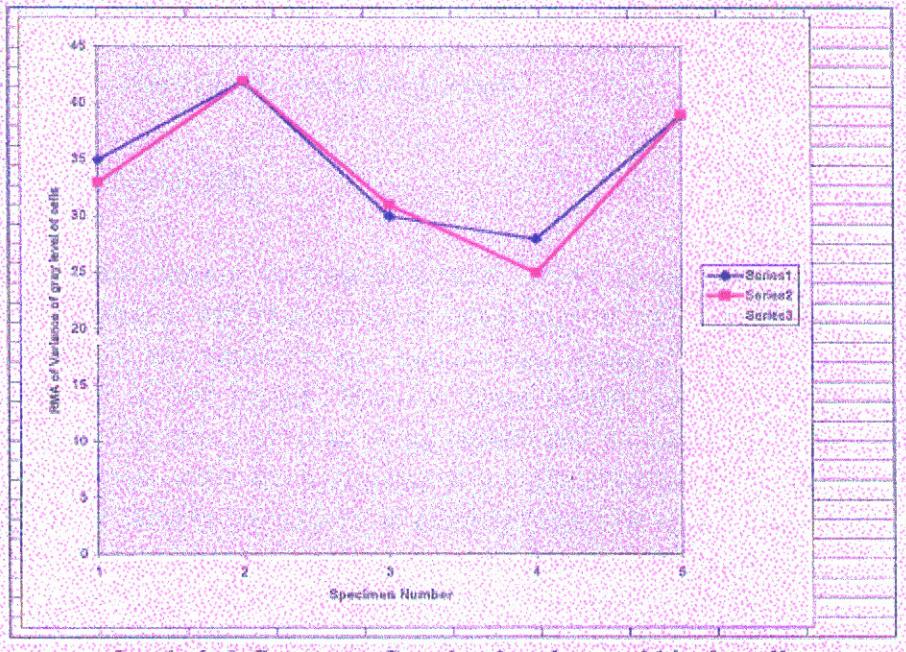

Graph. 3: Influence on Gray level variance within the cells

Fig. 6.6: Graphs showing the influence of different enhancement methods on measurement of different features. Series 1, Series 2, Series 3, represents three different image enhancement methods namely image crispening and directional Gaussian smoothed, after restoration of light intensity along the depth and after increasing the axial resolution to near isotropic voxel lattice respectively. The axis numbers 1, 2, 3, 4, 5, represents five different specimens on which experiments are conducted.

Graph 1 shows that the influence of image enhancement and noise reduction on size of the cell is quite less but the influence of improving axial resolution by interpolation has almost doubled the size of the cells measured. Graph 2 shows the influence of image enhancement methods on average gray level of the cell voxels while Graph 3 shows the effect on variance of the image voxel gray levels. Crispening and smoothing is found to be having greater influence on the histogram features. The restoration of light in the image stack also increases the histogram feature values.

Theoretically speaking, image enhancement and noise removal should improve the feature measurements too. Graphs shown above in Fig. 6.6, gives somewhat contrary results. One can say the improvement in the feature measurement by image enhancement depends on the feature we are measuring. If we calculate the size of the cell before enhancement and after making the voxel lattice isotropic, we find a large difference and hence the graphs have shown large error compared to actual feature values measured from manually segmented image. Similarly smoothed image may give a different histogram features when compared to the features in the original image. One way to reduce this ambiguity is to use the enhanced and noise reduced image for the purpose of accurate segmentation and then the segmented images are mapped to the original image volume for the feature measurement. We have used this method though this requires more computer memory. Thus, the features measured are rid of the ambiguities due to enhancement and noise removal. In case of large images, the storage requirements may become a practical problem.

6.7 Discussion

In this chapter we have introduced various image derived features which can be directly related to different grades or sub-classes of pathological disorder. We have not introduced any new feature in particular but have discussed the conventional image features with respect to 3-D images. Many of these features are difficult to measure visually. Moreover, subjective evaluation of the features and its values can differ from one medical expert to another and within a same expert on the basis of his experience. In a 3-D space some of the visual features are difficult to quantify accurately within a reasonable time. Features such as spatial orientation belongs to this category. The approximation of the feature measurement has to be done in consultation with the medical expert as to what level this particular feature is useful in deciding the prognosis and diagnosis factors of the patient.

Based on the kind of image, one can derive many other important features such as textures, etc., which have had a proven influence on automatic sub-classification. In the present case, the images obtained are highly magnified and the specimen area covered under the microscope is so small that the calculation of texture features based on gray level co-occurrence matrix, auto-correlation function, etc., are found to be less useful in sub-classification. The features which can be measured using gray level co-occurrence matrix, such as, energy, contrast and homogeneity are useful in cases of low magnified images where the cells appear almost as a point in the micro-textured histological image.

Some of the methods are implemented in 2-D and an average feature value considering all the image slices where the cell signature is present is used as an approximation of true 3-D value. This is done because of the simplicity and easy implementation for the respective features. We have also presented a brief study of the effect of image enhancement, noise reduction methods on the feature values. The study of the effect of segmentation on different feature measurement gives an insight about why we need more than one segmentation method. The ability to quantify and measure the cytological and histological features are a significant achievement in itself. Though the medical experts are not very much familiar with the use of numerical values to decide on the class or sub-class of a disease, it can be said that in a near future, this will become a necessity.

Chapter 7
Grading of Prostate Carcinoma and GUI

7.1 Introduction

Automatic classification of the tissue specimens based on the image analysis is useful in quick and efficient prognosis as well as diagnosis of the patient. The main advantage of computer assisted automatic classification is its reproducibility. While a single pathologist may be consistent as to where the line dividing the classes are to be drawn in a continuous diagnostic or prognostic scale, consistency across the pathologists may not be ensured. Pathologists, who are trained to classify the cancer tumors by visual inspection of the tissue samples, combine their understanding of the physiological processes and the ability to diagnose based on experience. This is a qualitative approach. This approach is reasonably accurate for differentiating between different diseases. But the same can not be guaranteed in sub-classifying or in differentiating different pathological grades of the same disease. While the eye does a good job in making qualitative determinations, it is less effective at the precise quantification of the tissue characters. To assign different grades to the cancer tumor based on intrinsically quantitative variation, computer assisted measurement of feature values is more useful. There exist a few attempts to automate the classification of the cancer tumors based on automatically measured cytological and histological features. Among them, some notable works are by Choi (1996), Nordin (1989), Preston Jr. et al., (1988), Firestone et al., (1996), etc..

Broders (1988) was the first to point out that grade of a cancer correlate with prognosis when he stated "The time is not far distant when not only physicians but also the patients and their relatives as well as life insurance companies will be interested in the grade of the malignancy of a cancer in addition to its size and situation, he is certainly in a better position to render more efficient treatment, and more accurate prognosis than one without such knowledge".

Till today, the classification of prostate tumor specimen images into different grades is done based on visual inspection of the 2-D tissue specimen images. Normally the prostate tumor specimen grading is done based on Gleason studies (Gleason, 1988; Gleason et al., 1977). Gleason grading system grades the tissue architecture into crisp-classes based on qualitative approach or visual decision making. During Gleason grading of prostate tumor, pathologists implicitly threshold diagnostic continua and hypothesize classes corresponding to different segments of these continua. Firestone et al., (1996) has shown that the assignment to crisp classes by visual analysis leads to ambiguity when the cases fall near the boundary of two classes. They have proposed continuous-class classification to avoid this ambiguity. Though continuous-class classification or grading of tumor results in less error, there is an inherent difficulty in defining the grade of the tumor under continuous class. Continuous-class classification does not explicitly attribute a particular grade to the tumor or quantify how far away the features of the tumor from its nearest possible class center. The doctors are familiar with the crisp classes or grades, which can be easily communicated or recorded.

In this chapter we have shown how automatic classification tools can be efficiently used to map the feature values of the specimen to the different sub-classes of diseases such as prostate cancer tumor. The results are presented based on weighted combination of all the major features. We have also tried to show that the cytological features that can be measured accurately by automatic image analysis tools are sufficient to grade the prostate cancer. The results are compared with the manual grading. From this, we can also make a list of the important quantifiable features that have a major influence on grading the prostate tumor tissue.

Another important section is the one that deals with the design of the Graphical User Interface (GUI). Many of the algorithms developed and/or implemented by an image analyst are normally difficult to use by a pathologist or a medical expert. This is because these algorithms are made more friendly to the image analyst than the ultimate users. We have designed a GUI with simple press buttons and sliders to click start different algorithms. Most of the intermediate results are also displayed.

7.2 Tumor Grade

Tumor grade is a term used to describe how closely a tumor resembles normal tissue of the same type. Based on the microscopic appearance of the tumor specimen, pathologists use discrete numbers to assign a grade to the tumor. Differentiation is another name used to describe how closely tumor cells resemble their normal counterparts. Tumor cells are described as, well differentiated when they look much like normal cells of the same type and are able to carryout some functions of normal cells. Poorly differentiated and undifferentiated tumor cells are de-organized and abnormal looking compared to normal tissue and cells. Generally, the grade of the tumor corresponds to its rate of growth or aggressiveness. Although grading is used by pathologists to describe most cancers, it plays a more important role in treatment planning for certain types than for others. An example is the Gleason grading system that is specific for the prostate cancer, which uses the grade numbers and grade score to describe the degree of differentiation.

Gleason Grading of Prostate Tumor: The Gleason system is based exclusively on the architectural pattern of the glands of cell nuclei in the tumor tissue specimen. It evaluates how effectively the cells of a cancerous tissue are able to structure themselves into glands resembling those of the normal prostate. The principle of grading is fairly simple. Gleason grading from very well differentiated (grade1) to very poorly differentiated grade (grade5) is usually done by viewing the low magnification microscopic images of the tissue. There are important additional details that require higher magnification. An ability to accurately grade the tumor can be achieved only through rigorous training and experience in pathology. For automatic grading, high magnification images are more useful. In case of glandular tissues such as prostate, the disruption in the glandular architecture can be studied in detail by using high magnification images. But, the measurements have to be done on more than one data set of the specimens collected from the same tumor since the high magnification images represent smaller portion of the tumor specimen.

The specimens belonging to Gleason grade 1 and 2 are composed of very pale glands that grow closely together. They represent healthy tissue specimens. In grade 1 they form a compact mass; in grade 2 they are more loosely aggregated, and some glands wander (invade) into surrounding muscle (stroma). The specimen of grade three also closely resembles grade 1 and grade 2. This is because both grades have a normal "gland unit" like that of normal prostate, i. e., every cell is a part of a circular row that forms the lining of a central space called lumen. The lumen contains prostatic secretion and each gland unit is surrounded by prostate muscle keeping the gland units apart. In grade 3, wandering of glands into the stroma is very prominent and is the main defining feature. The cells are dark rather than pale and the glands often have more variable shapes.

Gleason grade 4 is probably the most important grade because it is fairly common and because of the fact that if a lot of it is present, patient prognosis is usually worsened by a considerable degree. In this case there is a big jump in architecture. For the first time we see disruption and loss of normal gland unit. In fact grade four is identified almost entirely by loss of ability to form individual separate gland unit, each with its separate lumen. Each cancer has its own practical set of tools with which it builds part of the normal structure. Much experience is required for this diagnosis and not all patterns are easily distinguished from grade 3.

The grade 5 predicts another significant step towards the poor prognosis. Its overall importance for the general population is reduced by the fact that it is less common than grade 4. This grade too shows a variety of patterns, all of which demonstrate no evidence of any attempt to form gland units. Fig. 7.1 shows low magnified images of the five Gleason grades of the prostate tissue specimen. Fig. 7.2 shows another set of 2-D images in color, depicting the possible five grades of prostate tumor.

7.3 Partitioning the Data into a Design Set and a Test Set: A leave-one-out Method

One of the most important factor to be considered before designing a classifier is partitioning the data into test set and design set. In designing a practical classifier such as pathological specimen classification, the amount of data available is so limited that it is difficult to divide the data into two equal halves and use them as a design set and test set. This calls for special partitioning procedures which does maximum exploitation of the data. Such procedures are often necessary when, m_i the number of feature vectors in the data for class C_i, is less than 1000, for every class i and feature vector of dimension d. We were using around 160 data sets, which are not symmetrically distributed among all the classes. Among these forty-four images show low grade of carcinoma and sixty-five data sets show higher grades. Remaining images belong to middle grade of the carcinoma. This is a poor amount of data to build any reliable classification system. To circumvent this situation, there are two types of approaches (Skalansky and Wassel, 1981).

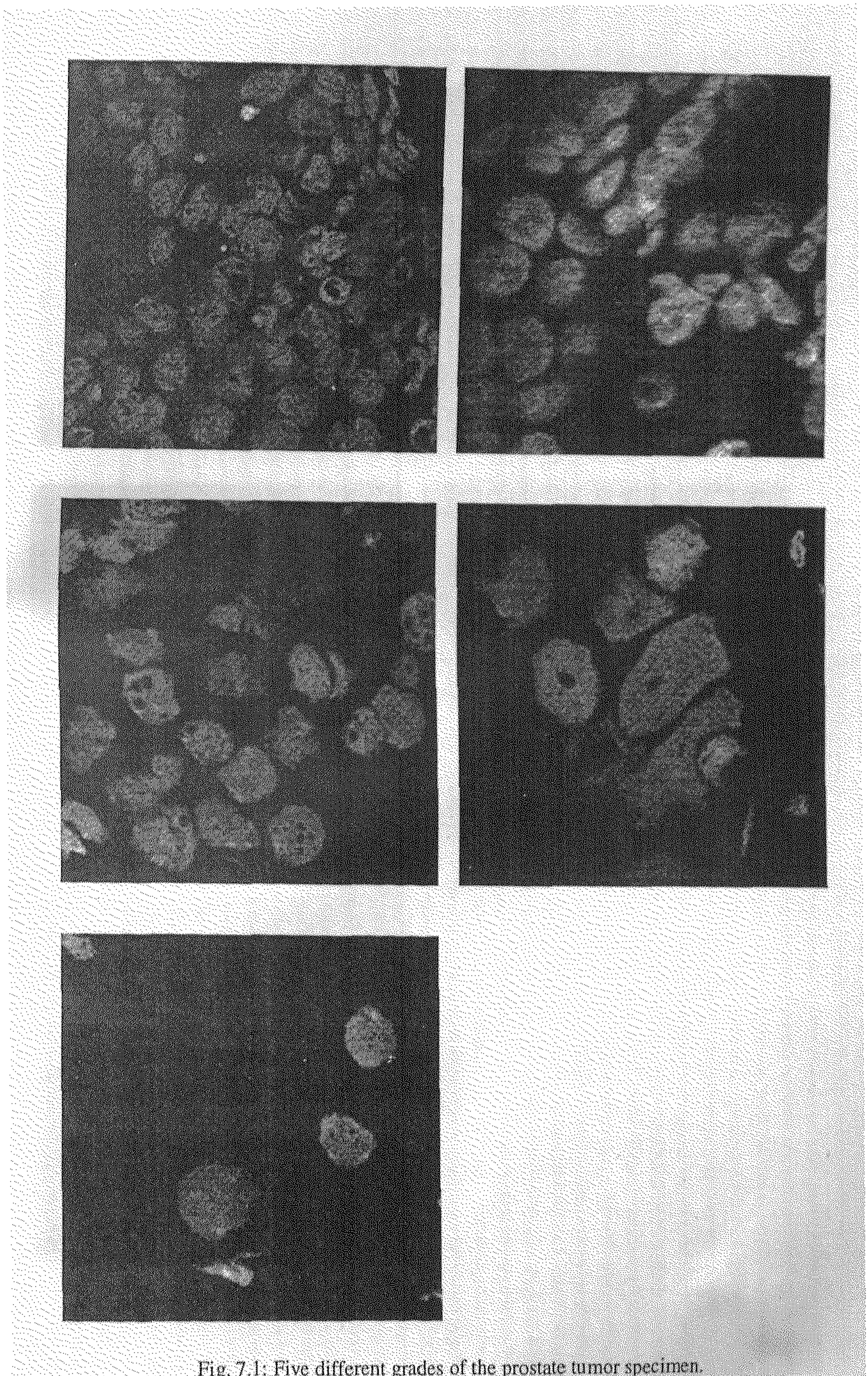

Fig. 7.1: Five different grades of the prostate tumor specimen.

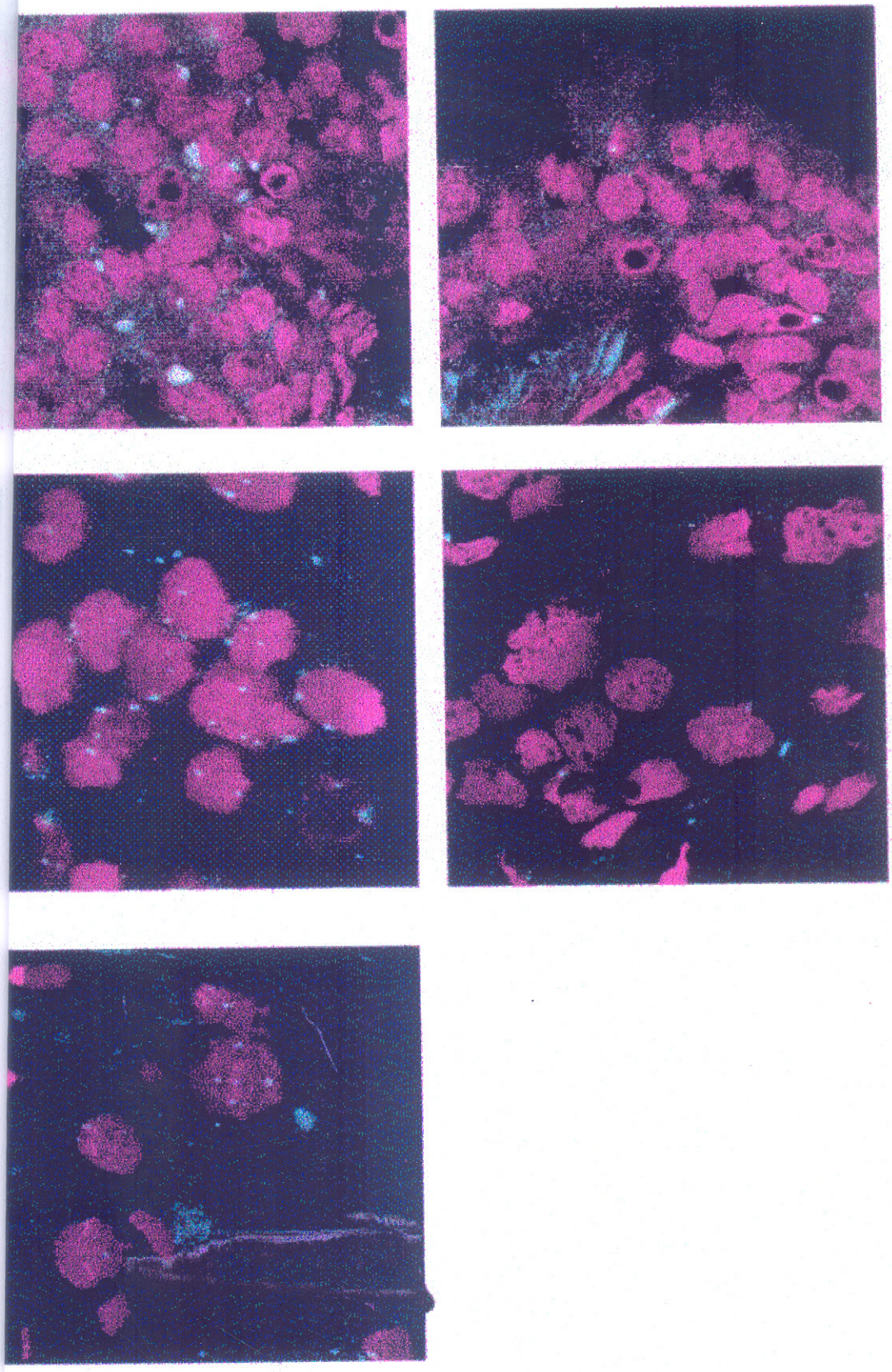

Fig. 7.2: Another set of images showing five grades of prostate tumor specimen.

A rotation procedure (also known as leave-k-out or jack-knife procedure) and a U-procedure (also known as leave-one-out procedure). Leave-one-out procedure is nothing but a rotation procedure where $k=1$. In this procedure, all but one of the data vectors is used in the design set (also called as training set) , and only the single withheld feature vector (single data set) is used as a test set. The design process is repeated such that each feature vector or data set acts as a test set at least once. Though this method is computationally expensive, it gives one of the best solutions when we face with less number of data sets per class.

Another step to improve the efficiency of the classification process is to use multi-stage method. If we try to classify the data into five grades in one step, the number of features that should be considered becomes too high thereby increasing the complexity of the classifier design. So we can divide the classification process into more than one step based on number of classes into which the data are divided. In the present system, we have divided the classification into two-step process. In the first step, the data are classified into only three classes. Then each sub class is further classified as per the need.

7.4 Classification

Pattern recognition theory provides us with the fundamental mathematical tools that facilitates to solve the grading problem of a cancerous tissue specimen, given a set of measured cell and tissue features. Let F be the normalized feature vector consisting of d features measured automatically from the 3-D image data. Then the normalized feature vector can be written as,

$$F=\left[f_1, f_2, \ldots, f_d\right]^T$$

If there are p classes $C_1, C_2, C_3, \ldots, C_p$, the goal of classification is to map the vector F in into class specific regions $C_1, C_2, C_3, \ldots, C_p$. A good set of features is the one that provide wide separation among the classes. Separation increases as the difference between class average increases and standard deviations for each class decreases.

Many of the classifiers designed in earlier attempts for automatic classification of histo-pathological are one-step decision classifiers. This needs a selection of "best" feature vector that is not too large. It is well known that a multi-stage or sequential, hierarchical classifiers with small feature vector in each stage can give a better performance than by employing a single best set of features in a one step decision. We have followed a two-stage classifier where the feature vector in individual stages is not too large but a combined feature vector is large enough for precise classification. We have chosen six major features which shows wide variation in their feature values in different carcinomic grades. These features are 1. Variation in the size of the cells, 2. Eccentricity of the cell shape 3. Ability to form a glandular unit or Disruption in the glandular pattern as given by the tissue architecture measurement, 4. Cell density, 5. Inter Nuclear Distance, 6. Solidity. Additionally we have used a minor feature vector, which can be used to reduce the ambiguity in classification in

certain cases. The minor feature vector consists of features like, 1. Loss of directionality, 2. Variation in cell cluster size, 3. Cell enlargement, 4. Deviation in the shape factor of the cells, 5. Histogram features. We call the major feature vector as deciding feature vector F_d and the minor feature vector as supporting feature vector F_s . All the features are normalized prior to considering it for decision making. The grading system implemented here may not emulate Gleason method as the cytological features are given more importance. Though we have implemented algorithms to quantify histological features also, most of it is limited to measure the disruption in glandular unit of the prostate cells based on inter-nuclear distance, cell density, and other heuristic methods.

Each feature has different weight in influencing the classification. The vector that shows the weight of different features of the feature vector is called weight vector. We have decided upon the weight of different features based on the experiments. The data are classified into three groups based on each features individually. Then the weight factor for each feature is decided based on the ability of the feature to increase the difference between class average of neighboring grades and to decrease the standard deviation within each grade. This is done by comparing the automatic classification based on each feature with the manual classification result.

The basic principle of classification is as follows. Let us call the weight vector as $W = \left[w_1, w_2, w_3, \ldots, w_d\right]^T$ where $w_1, w_2, \ldots, w_d$ are the individual feature weights. If $T_j(F)$ is the linear discriminant function that maps the normalized feature vector to real numbers, it can be written as ,

$$T_j(F) = w_{j0} + W_j^T \cdot F \ .$$

$T_j(F)$ can be viewed as some macro-feature calculated as a linear combination of the normalized features in feature vector. Now, we simply assign the class C_j to the data with feature vector F iff $T_j(F) \geq T_i(F)$ for all i (Skalansky and Wassel, 1981).

In the present example of prostate cancer grading, we have divided the classification into two-step process. The first step is a three-class classifier $(p = 3)$. The three classes are lower grade, middle grade and the higher grade. The second step of classification consists of two, two-class classifier. Here the lower grade and higher-grade classes are further subject to two-way classification. The lower grade is divided into grade 1 and grade 2, while the higher grade into grade 4 and grade 5. The middle grade takes the position of third grade. Fig. 7.3 shows the classification tree.

In the first step we assign the class 'low' to the data with feature vector F iff $T_{low}(F) \geq T_{mid}(F)$ and $T_{low(F)} > T_{hig}(F)$. In the similar way, the data are assigned to the middle and higher classes.

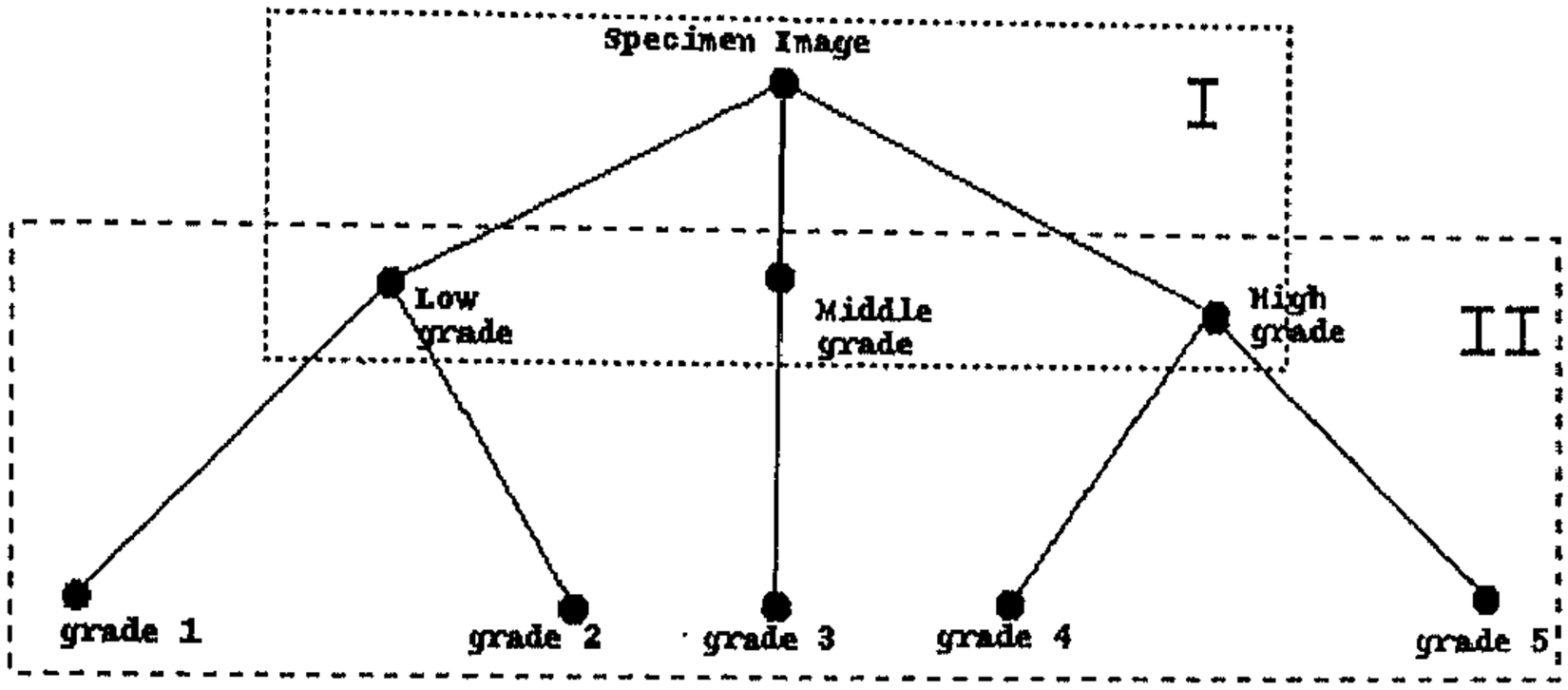

Fig. 7.3: Two step classifier

We have used only major feature vector in the first stage of classification to divide the data into three classes. Minor feature vector and additional features are then used along with the major feature vector to sub-divide the classes into five grades of cancer.

Let μ_l, μ_m and μ_h be the class averages of the macro-features of different data sets belong to lower, middle and higher classes of carcinoma images in training set. Similarly σ_l, σ_m and σ_h are the standard deviations of the macro-feature values within each class. These values are calculated from the results of manual classification of the data sets. Lower and upper bounds for each class are fixed as the lowest and highest macro-feature value within each class. Considering the limited data sets we have to design the classifier, the highest macro-feature value of the lower grade need not be same as the lowest macro-feature value of the next higher grade. This results in a possibility of some part of the continua between different classes being defined as not belonging to either of the neighboring classes. This is diagrammatically shown in Fig. 7.4. When a feature value of the new test data falls on this part of the continua, machine fails to assign a particular class to it.

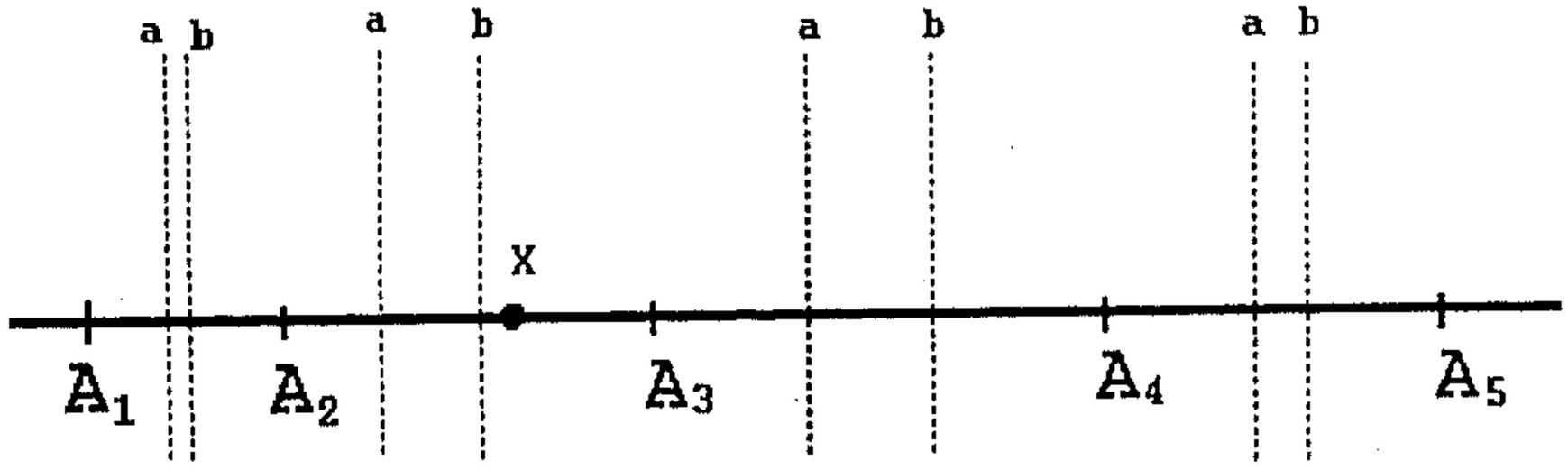

Fig. 7.4: Schematic diagram showing the ambiguity in dividing a continuous scale.

We have used a simple method to assign a class to such data sets. Let a and b be the highest macro-feature value of the lower class and lowest macro-feature value of the next higher class on the scale. We divide the space $|a-b|$ on a continuous scale based on the spread of the classes given by the standard deviation within each class, i. e. a macro-feature

which is less than, $a+|a-b|\cdot\frac{\sigma_l}{(\sigma_l+\sigma_m)}$, is considered as belonging to lower class, otherwise to next higher class, where σ_l and σ_m are the standard deviation of the two neighboring (say, lower and middle) classes on a continuous scale.

In the second phase of classification, the lower class is sub-divided into grade 1 and grade 2. The middle class is assigned grade 3. Higher class is divided into grade 4 and grade 5. Though the process is essentially same as explained above, we have used additional feature vector consisting of minor features to improve the precision in distinguishing the sub-classes in each class.

When we try to classify a new data set into one of these five grades, the macro-feature of the new feature vector need not be placed in a location close to the class average value. In such cases, there is an amount of uncertainty in assigning the data to a particular class. This uncertainty becomes more when the macro-feature lies closer to the class boundary than to the class average. In the practical cases involving the decisions on the prognostic and diagnostic factors of a patient, it is very important to mention this uncertainty factor associated with the automatic classification. We have quantified this uncertainty factor as follows. Let A_1, A_2, A_3, A_4 and A_5 are the grade centers on a continuous scale as obtained by supervised classification. Then, if a macro-feature of the test specimen which lies at point x as shown in Fig. 7.4, which is classified as grade 3, has a percentage of uncertainty defined by,

$$uncertainity = \left(1-\left(\frac{\|x-A_3\|^2}{(\|x-A_3\|+\|x-A_2\|)^2}\right)\right)\times 100$$

7.5 Grading Based on Cytological Features

In a traditional prostate tumor grading, we consider only the histological pattern of the tumor specimen. It has been observed and tested by many that the classification based on cytological features also lead to proper grading of the prostate cancer (Benson, 1988). It is suggested that the cancer grading system should be able to grade the specimen image based on both histological and cytological features. Yatani et al., (1985), have studied the reliability of cytological grading of prostate carcinoma compared with histological grading. According to their study, in no instance were cytological grade 1 cells deemed to be poorly differentiated histologically or grade 3 cells seen as well differentiated. Layfield et al., (1987), have studied the cytological grading of the prostate carcinoma in comparison to the Gleason grading system and have found that there is nearly 75% correlation between three cytological grades and the Gleason score.

Other important and probably the deciding factor in choosing the cytological or histological features is the kind of image data we are dealing with. All the image data we could procure are highly magnified, 3-D multi-spectral images. Most of the image data sets do not cover more than one glandular unit in its image domain. In such cases cytological features play a major role in grading the prostate tumor.

We have attempted to grade the specimen image data sets based on different cytological features using automatic feature extraction methods. Later we have compared the results with grading done by considering all the major features as well as grading done by pathologist. We have used the cytological features such as cellularity, nuclear irregularity, anisonucleosis, macronucleoli, loss of polarity, crowding, cell enlargement, different shape features, etc., for grading purpose. Most of these features are explained in chapter 6. The sub-classification is done in a similar way explained for grading based on major features.

We have conducted the experiment on almost all the volumetric data sets we had. When we classify the features into three carcinomic grades i. e., low grade, middle and high grade, we have found that manual grading and cytological grading is approximately 71% similar for class 1, 80% similar for class 2 and 77% for class 3. The comparison of cytological grading with normal automatic classification has given 72% accurate classification in case of class 1, nearly 70% accuracy in class 2 and 77% accuracy for class 3. Table. 7.1, shows some comparison results of manual classification into three classes and classification based on cytological features only. Table. 7.2, shows similar comparison with the automatic classification considering all the major features and the cytological feature based classification.

When we classify the data into five grades as in Gleason grading system, the percentage of error was as shown in table. 7.3 and table 7.4. The percentage error is not a simple symmetric difference in the number of specimens manually classified and automatically classified. Which specimen is classified into which class is also taken into account i. e., how many false negative and false positive classification is done in the automatic classifier should also be considered for representing the true percentage error. A specimen, which is classified as class I in manual classification, may be incorrectly classified to class II during automatic classification. Similarly, another data from class II may get classified to class I. Though there are two errors made, simple error calculation by finding the difference gives zero error. Thus the percentage error in classification shown in table 7.1, class II, is approximately 20% instead of 8%.

No.	Class	Manual class..	Cytological class..	% Error
1	I	44	56	≈ 29%
2	II	51	47	≈ 20%
3	III	65	57	≈ 23%

Table. 7.1: Similarity of manual grading and cytological grading of the prostate cancer tissue specimens

No.	Class	Automatic class....	Cytological class...	% Error
1	I	46	56	≈ 28%
2	II	60	47	≈ 30%
3	III	54	57	23%

Table. 7.2: Similarity of normal grading with all major features and cytological grading.

No.	Grade	Manual Grading	Cytological Grading	% Error
1	I	21	26	≈ 32%
2	II	23	30	≈ 32%
3	III	51	47	≈ 20%
4	IV	36	28	≈ 28%
5	V	29	24	≈ 24%

Table. 7.3: Comparison of Cytological grades with grading done manually.

No.	Grade	Automatic Grading	Cytological Grading	% Error
1	I	21	26	≈ 38%
2	II	25	30	≈ 36%
3	III	60	47	≈ 30%
4	IV	32	28	≈ 37%
5	V	22	24	≈ 29%

Table. 7.4: Comparison of Cytological grades with automatic grading done considering all the major features.

7.6 Comparison with Manual Classification

One of the main test for any automatic medical diagnosis and prognosis system is to find how close the results are to the actual evaluation by medical experts. If σ_{man} is the standard deviation of the manual classification of a data into a class m, then an automatic system is considered as good if the classification done by the system tends to decrease σ_{man}.

No.	Class	Manual class...	Automatic class...	% Error
1	I	44	46	≈ 21%
2	II	51	60	≈ 20%
3	III	65	54	≈ 21%

Table. 7.5: Comparison of manual classification and automatic classification

No.	Grade	Manual Grading	Automatic Grading	% Error
1	I	21	21	≈ 16%
2	II	23	25	≈ 17%
3	III	51	60	≈ 27%
4	IV	36	32	≈ 23%
5	V	29	22	≈ 28%

Table. 7.6: Comparison of manual grading and the automatic grading.

When we classify the specimen into three classes, there was approximately 79% concurrence while classifying the specimens into class 1 by manual classification and automatic classification, 80% concurrence while classifying into class 2 and 79% concurrence for class 3. Table. 7.5, shows the comparative results when the data is classified into three classes. When we compare the five grades done by pathologist and the machine, approximately 84% concurrence for grade 1, 83% concurrence for grade 2, 73% concurrence for grade 3, 77% concurrence for grade 4 and 72 % concurrence for grade 5 was found. Table. 7.6, shows some of the comparison results and the percentage of error associated with it. It is important to mention here that these percentages may not be representing the true efficiency of the image understanding system we have presented. Even for indicating the near true efficiency, the algorithms have to be tested on large number of data sets of different variety of specimens. The results shown are the ones obtained on the two hundred and odd data sets we are having. The leave-one-out classification procedure also influences the result as it invariably bring down the error in percentage of classification by considering almost all the data sets to design the classifier.

7.7 Graphical User Interface

Graphical User Interface (GUI) is an important module to facilitate the use of different automatic and semi-automatic methods for analysis of histo-pathological images. For a pathologist or a medical expert, the image processing algorithms are of little use unless they are made user-friendly. The best way to make the use of these automatic methods attractive to the medical experts is to design an efficient interface between the user and the computer. Unfortunately, design of a graphical user interface is not an easy problem. There are many advanced computer languages which helps in building proper menus and start buttons for running various algorithms. But, for a pathologist working on a confocal image analysis, the GUI should include facilities for proper visualization of the 3-D images and the maneuver of the images to view through the depth of the image stack at different angles, simultaneous display of XY, YZ and XZ sections of the image stack, separate display of results, display of individual channels of a multi-spectral image, continuous display of the intermediate results when an automatic processing is going on, etc.. Here we have not described the technical details of designing the GUI as it is out of the scope of this thesis. We have described the facilities in the GUI we have built to facilitate the pathologists in using the algorithms we have explained in this thesis.

Fig. 7.5(a) shows GUI we have built for regular use of many enhancement, segmentation and feature extraction purposes. The image stack is displayed in XY, XZ and YZ sections simultaneously. By simply moving the cursor in a corresponding direction, one can view through the depth of the image stack. The results are also displayed in XY, XZ and YZ sections. Individual spectral channels can also be displayed by simply suppressing the display of remaining channels. A 3-D display of the pseudo surface of the cells as shown in Fig. 7.5(b), is also made possible using Interactive Data Language interpreter (IDL, Research Inc., USA).

Fig. 7.5(a): A simple GUI for the quantitative evaluation of the 3-D histo-pathological images

simple push buttons to start different programs and processes as well as to display the results are provided. Separate sections for image enhancement, image segmentation, feature measurement, visualization, etc., is provided within the main frame of the GUI. In case of interactive process, the information has to be displayed on the GUI about what interactive information is needed for the program to proceed further. Facility for interactive --

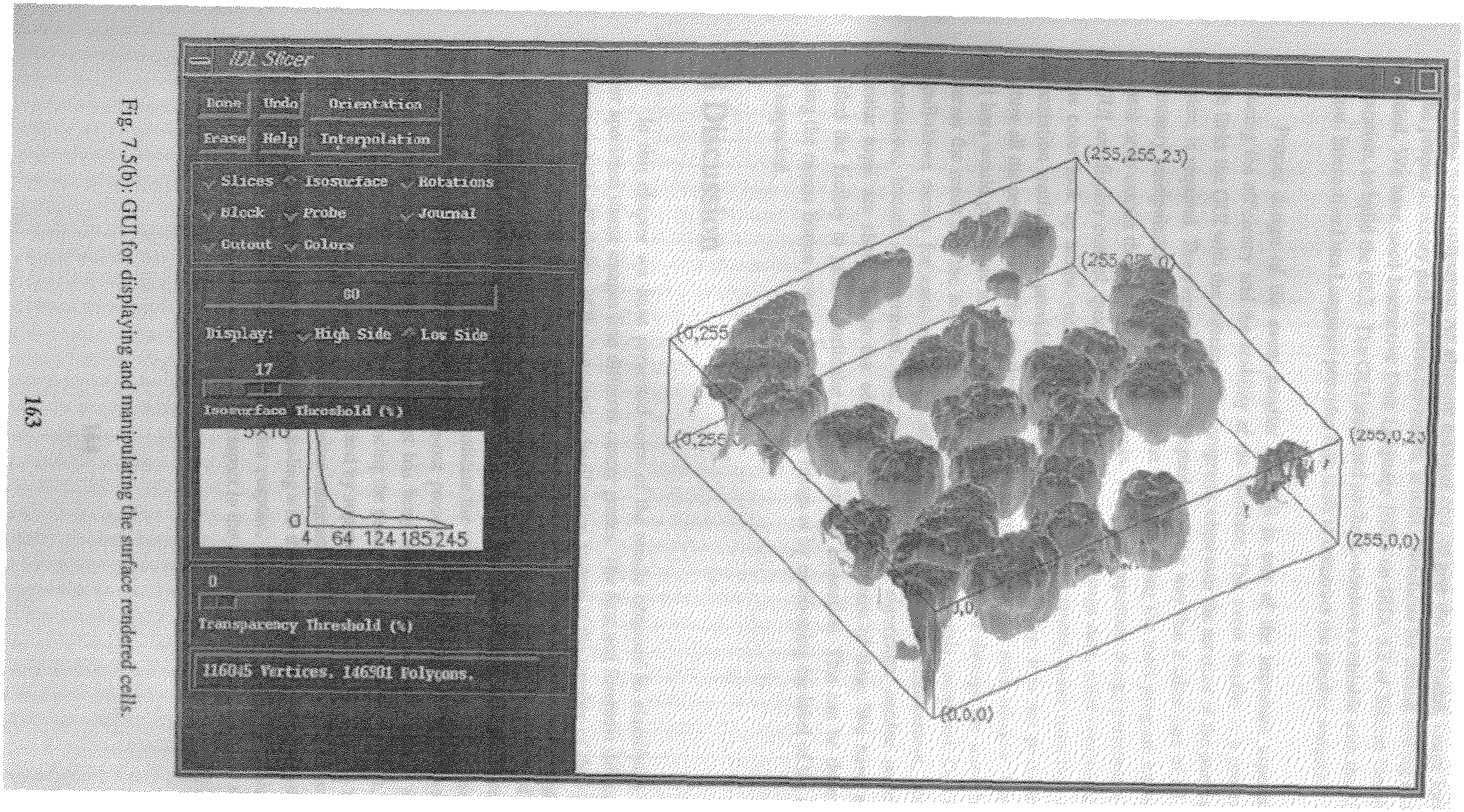

Fig. 7.5(b): GUI for displaying and manipulating the surface rendered cells.

correction of the result is provided. The quantitative measures done on the image may need to be stored and/or displayed. An efficient dialogue box, to give the file name, image format and the proper directory path to store the results, is built. Directions for default storing is also provided. We have used Interactive Data Language (IDL) on IRIX 5.3 of Silicon Graphics workstation, to build the GUI. The GUI are based on the X-windows available with the Unix systems. Interactive Data Language provides easy tools to construct the graphic widgets.

Proper design of the event handler for GUI is one of the important aspects in enhancing the efficiency and the usability of the interface. The event handler is a program, which links the GUI with the corresponding programs when ever the services of the particular program, is required. The event handler is designed in such a way that it takes care of all the preliminary manipulations needed on the data set before applying the main program either to segment or to extract the features from the image. The other important design parameters for the GUI are display control, quick loading and storing of the image data, color control based on the color look up tables, etc.. When there are many enhancement, noise reduction and segmentation methods are provided and the size of the image is big, it is not possible to structure all the press buttons for starting and display areas within one main window. Use of scroll bars would permit us to do this but it is not desirable to move through the scroll bars whenever the result and the input data are needed to be simultaneously compared. One can use pull-down menus for each main topic of image analysis such as enhancement, noise, segmentation, feature measurement, etc., so that only those algorithms needed under a particular topic are shown up in the window at any given point of time. We have also provided the facility to pick a particular cell for detailed inspection. This can be done by clicking the mouse button over such a cell in the image or by mentioning the label of the cell to be inspected.

7.8 Discussion

In this chapter we have presented some of the results obtained in classifying the cancer specimen tissue images into different cancer grades. The first and foremost difficulty in measuring the efficiency of the automatic classification system is the number of data sets available as design sets. For any fruitful application, the classifier should have been designed based on the features measured over a minimum of one thousand data sets at each grade of the cancer. Thus the percentage of error or the percentage of concurrence with the manual classification given in this chapter need not indicate the true efficiency of the whole image understanding system. Second, the leave-one-out procedure has an intrinsic bias towards correct classification as almost every data set has been used as the design set. This may influence the efficiency of the classifier in reducing the percentage of error. Third point is, the class centers and the grade centers marked by supervised classification has taken into account the image data acquired under very similar image acquisition conditions. To make the software more global in nature, the option for dealing with the images taken at different image acquisition set up has to be provided. For this purpose, the software has to be made to normalize certain feature measurements with respect to the image acquisition characters such as resolution, brightness, etc..

Fourth, the supervised classification has to be done by more than one medical expert and we have to observe the variation in their opinion on grading the image data to a particular class. The automatic classifier should be tuned in such a way that the results obtained b it should strengthen the class mean of the supervised classification by different pathologists and should decrease the standard deviation within each class.

Chapter 8
Conclusion

8.1 Summary and Contribution of the Thesis

This work is a part of a bigger and a more general project on *developing algorithms for analysis and quantitative evaluation of multi-dimensional histo-pathological images and an image data base generation*. Though there were many attempts made to automate the histo-pathological image analysis, it is still a challenge for automatic quantitative evaluation.

Our work in design and development of an image understanding system is unique in the sense that such a system on three-dimensional confocal microscopy images is a new development as the interest in confocal images has grown in mid nineties only. In general, the system can be said to be complete, as it incorporates all the major topics of automatic image analysis. More importance is given to the segmentation of the 3-D cells in the images, as it is one of the most critical problems in automatic quantitative evaluation of tissue images. Relatively few studies with practical, biological results from confocal images have been reported and in this regard the present work can be considered as new and extensive.

More specifically, the contribution of this thesis can be listed as follows.

1. A more general introduction to the three dimensional imaging of the histo-pathological images and the difficulties in acquiring the volumetric images is given. Probable sources of instrument noise and the specimen specific noise are also described.

2. A set of noise reduction filters and image enhancement techniques were implemented and its effect on three-dimensional histo-pathological images is studied. A directional Gaussian filter is designed such that it smoothes the fine textural nature of the cell's interior while generally, protect the edges from blurring.

3. A simple method to restore the light intensity along the depth of the image stack is presented and its effect on loss of voxel sensitivity is discussed. A new technique of interpolation based on morphing is described. This has been found to have the advantages of both shape based and contour-based interpolation techniques. A simple logical operation for finding the overall boundary contour of the foreground in the interpolated image slice is presented. These contour pixels are made to work as the control points for morphing.

4. Different edge based and region based segmentation techniques are extended to 3-D and modified to perform efficiently on volumetric histo-pathological images. Simple edge detectors are tested on these images and their applicability is briefly discussed.

5. A new tissue image segmentation technique based on 2-D plane-by-plane approach called layered segmentation is implemented. This is a semi-automatic method which works automatically given one image slice with marked cell boundary.

6. The active model optimization technique is modified and implemented for segmentation of the 3-D cells. Two approaches, namely, a 2-D plane-by-plane approach and a direct 3-D processing based on active models are implemented. Several practical problems and interesting cases are described. It has been shown how the capture range of the potential field can be extended to bring the ill-initialized model within the fold of external forces. We have also shown how region based information can be used to reduce the influence of strong boundary features of nearby objects.

7. A comparative study of different edge based segmentation techniques with respect to segmentation of histo-pathological images is also presented.

8. Several region based image segmentation methods are implemented and their utility in segmentation of volumetric tissue images is discussed. An adaptive similarity measure is implemented to control the seeded volume growing. The classical watershed technique is extended to 3-D and a simple rule based merging technique is proposed to reduce the over segmentation of the cells. It has been shown that for all practical purposes, this method gives acceptable results.

9. An integrated approach for cell segmentation is presented. This can be considered as a step towards complete automation of the segmentation process. Well-established edge based and region based methods are used. Scope for improvement is also discussed.

10. Software is developed for identification and segmentation of FISH signals located within the cell boundary. A Gaussian model based characterization is proposed to solve the problem of overlapped signals. The method is compared to manual evaluation of FISH signals and 2-D evaluation. Several characteristics of FISH signal and the possible causes for error in automatic segmentation and counting of FISH is listed and discussed.

11. A list of criteria for feature selection and standard image acquisition set up is discussed. Many standard and conventional features are described with respect to three-dimensional cells. Some heuristic feature extraction methods for defining the ambiguous features such as tissue architecture, glandular pattern of the cells, etc., are described. Importance and the need of cytological features are also described.

12. Influence of different segmentation, noise reduction and feature enhancement techniques on the measured feature value is discussed. It is shown that image enhancement should be done only for improving the accuracy of segmentation while the features have to be measured by mapping segmentation results to original image stack.

13. A simple leave-one-out classifier is implemented for classifying the handful of data sets into mainly three sub-classes of the prostate cancer. An attempt to grade them into five grades as in Gleason grading system is also presented. Classification of the data based on cytological features only is also given. It is shown that the cytological features are good enough to grade the prostate carcinoma. It enforces the experimental results shown by fine-needle biopsy.

Like all other similar attempts to build the image understanding system for histo-pathological images, this system also has its drawbacks. It is not a complete automatic system but most of the task specific things are solved automatically. For some images the methodologies have given adverse results but it is expected as no single method can be considered as globally successful on all image data. This work, which is a part of the bigger project, appeared to be bit over ambitious when it comes to the design of a classifier based on handful of data sets. No system can be said to complete until and unless it is tested on large number of, different kinds of, data sets from different diseases of various organs and tissues of the human body.

8.2 Scope of the Future Work

This thesis is a development motivated work. Though many image processing algorithms are discussed, most of them are already available in the literature. We have extended and modified several of these algorithms to suit for volumetric histo-pathological images. Most of the algorithms are semi-automatic in nature. There is always a scope to improve in this area to reduce the human interaction with image processing algorithms.

Most of the studies are done on prostate specimen images acquired in a similar microscope set-up. Work has to be done to stabilize the system to give acceptable results on images obtained by different image acquisition set up features by making system to be robust to the variation in image acquisition process.

There is always a scope for improvement in the design of noise reduction and feature enhancement filters. Development of adaptive edge protecting smoothing filters, intensity restoration with a minimum loss of pixel sensitivity, etc., are to name a few.

Segmentation of the real life images is an open problem. Though one can not expect to design a single global algorithm which can be made to work on all the image data sets, there is always a scope for improving the performance of existing methods by redesigning them or by adding extensions to get better results.

There are various image features that can be calculated from histo-pathological images. There is a large scope for design and development of fast and efficient algorithms to calculate such features. Though the automatic classification in case of bio-medical images should be based on the supervised classification results, scopes is existing for improving the classifier performance and bring it very close to the result of classification or decision making by a group of medical experts.

The classifier designed here and the results presented may not reflect the true performance of the image understanding system we have presented in this thesis. For any reliable evaluation of such systems, it has to be tested on a large number of data sets. More number of human experts should be involved in designing the decision making process. The results shown reflects only the possibility of future development of this system into a useful tool for pathologists, molecular biologists and other medical experts.

References:

1. Abmayer W., Abele L., Kugler J. and Borst H., "Capabilities of non-linear gradient and thresholding algorithms for the segmentation of cervical cells", *Analytical Quantitative Cytology*, Vol. 2, (1980), pp. 221-233.

2. Abrantes A. J. and Marques J. S., "Class of constrained clustering algorithms for object boundary extraction", IEEE Trans. on Image Processing, Vol. 5, (1996), pp. 1507-1521.

3. Acharya R. S., Cogswell C. J. and Goldgof D. B.(Eds.) Biomedical Image Processing and Three-Dimensional Microscopy , SPIE Proceedings, Vol. 16660, (1995).

4. Acharya R. S., Cheng P. C., Samarabandu J. K., Summers R. G., Chen L. H., Musial C.E., "Multi-dimensional image analysis of confocal images", Trans. Royal Microscopical Society, Vol. 1, (1990), pp. 289-292.

5. Acharya R. S., "Mathematical Morphology for Multi-dimensional Image Analysis", In: Image Processing, Vol. 1902 of Medical Imaging III, SPIE, (1989), pp. 338-350.

6. Acharya R. S., Wasserman R., Stevens J. and Hinjosa C., "Biomedical Imaging Modalities: A tutorial", *Computerized Medical Imaging and Graphics*, Vol. 1, (1995), pp. 3-25.

7. Acharya R. S., "3-D Segmentation algorithms", In: Signal Processing and Pattern Recognition in non-destructive evaluation of materials (Chen, C. H. Eds.), Heidelberg: Springer Verlag, (1987), pp. 225-291.

8. Adams R. and Bischof L., "Seeded region growing", *IEEE trans. on Patt. Anal. and Mac. Intel.*, PAMI-16, (1994), pp. 641-647.

9. **Adiga P. S. U. and Chaudhuri B. B.,** "An Efficient Cell Segmentation Tool for Confocal Microscopy Tissue Images for Quantitative Evaluation of FISH Signals", Int. J. of Microscopy Research and Technique, Vol. 44, (1999), pp. 49-68.

10. **Adiga P. S. U. and Chaudhuri B. B.,** "Segmentation of Volumetric Tissue Images Using Constrained Active Contour Models", Accepted Subject to Revision in Int. J. of Image and Vision Computing (revised and submitted) (1999).

11. **Adiga P. S. U. and Chaudhuri B. B.,** "Deformable Models for Segmentation of CLSM Images and Its Application in FISH Signal Analysis", Accepted subject to revision in Int. J. of Analytical Cellular Pathology (revised and submitted) (1998).

12. **Adiga P. S. U. and Chaudhuri B. B.,** "Segmentation and Counting of FISH signals in Confocal Microscopy Images", Accepted for publication in MICRON, Int. J. for microscopy research and review (1998).

13. **Adiga P. S. U. and Chaudhuri B. B.,** "Region based Techniques for the Segmentation of Volumetric Histo-Pathological Images Obtained using Confocal Microscope", Accepted subject to minor revision in Int. J. of Computer Methods and Programs in Biomedicine (1999).

14. **Adiga P. S. U., Chaudhuri B. B. and Rodenacker K.,** "Semi-automatic Segmentation of Tissue Cells from Confocal Microscopy Images", In: Proceedings of 13 th Int. Conf. on Pattern Recognition, ICPR-96, 3, (1996), pp. 494-497.

15. **Adiga P. S. U. and Chaudhuri B. B.,** "Segmentation of Histo-Pathological Images by Surface Following Using Constrained Snakes", In: Proceedings of 14 th International Conference on Pattern Recognition, ICPR-98, (1998), pp. 1674-1676.

16. **Adiga P. S. U. and Chaudhuri B. B.,** "Analysis of Volumetric Images of Filamentous Bacteria in Industrial Sludge", In: Proceedings of 14 th International Conference on Pattern Recognition, ICPR-98, (1998), pp. 1735-1737.

17. **Adiga P. S. U. and Chaudhuri B. B.,** "Segmentation of 3-D Histo-Pathological Images Using Snakes and Its Application in Quantitative Evaluation of FISH Signal", In Proceedings of 2 nd International Conference on Medical Image Understanding and Analysis, MIUA-98, (1998).

18. **Adiga P. S. U. and Chaudhuri B. B.,** "Automatic Prostate Cancer Grading System Based on 3-D Histo-Pathological Images", In: Proceedings of IAPR workshop on Machine Vision and Applications, MVA-98 to be held in Chiba, Japan, (1998).

19. **Adiga P. S. U. and Chaudhuri B. B.,** "Automatic Segmentation of 3-D Cells from Confocal Microscopy Images and Its Application in FISH Signal Evaluation", In: Proceedings of 16 th International CODATA Conference, CODATA-98, (1998).

20. **Adiga P. S. U. and Chaudhuri B. B.,** "Classification of Prostate Tumor Specimen based on Cyto and Histological Features Measured from 3D Images", In: Proceedings of 16 th International CODATA Conference, CODATA-98, (1998).

21. **Adiga P. S. U. and Chaudhuri B. B.,** "Quantitative Evaluation of Bacteria in Industrial Sludge by 3-D Image Analysis", In: Proceedings of 16 th International CODATA Conference, CODATA-98, (1998).

22. **Adiga P. S. U. and Chaudhuri B. B.,** "Active Surfaces for the segmentation of the Volumetric Histo-pathological Images", In: Proceedings of Indian Conf. on CVGIP, 1998, pp. 28-34.

23. **Adiga P. S. U. and Chaudhuri B. B.,** "Active Surfaces as a Direct 3-D approach for Segmentation of Volumetric Histological Images and Its Application in Molecular Pathology", for IEEE trans. on Image Processing (In Preparation) (1999).

24. **Adiga P. S. U. and Chaudhuri B. B.,** "Comparative Study of Different Segmentation Techniques for the 3-D Histo-pathological Images" for IEEE Biomedical Engineering (In Preparation) (1999).

25. Alers J. C., Krijtenburg P. J., Vissers K. J., Krishnadath S. K., Bosman F. T., Van Dekken H., "Interphase in situ Hybridization to disagregated and intact tissue specimens of prostatic adeno carcinomas", *Histochem Cell Biol*, Vol. 104, (1995), pp. 479-486.

26. Alexander J. C. and Thaler A. I., "The boundary count of digital pictures", *J. of Assoc. Comp.* Mach., Vol. 18, (1971), pp. 105-112.

27. Amini A. A., Waymouth T. E. and Jain R. C., "Using Dynamic programming for solving variational problems in Vision", *IEEE trans. on PAMI*, Vol. 12, (1990), pp. 855-867.

28. Amos W. B., White J. G., and Fordham M., "Use of Confocal Imaging in the Study of Biological Structures", *Appl. Opt.* Vol. 26, (1987), pp. 3239-3243.

29. Anderson H. L., Bajesy R. and Mintz M., "A modular feedback system for image segmentation", Tech. Report-110, University of Pensylvania, GRASP Lab, (1987).

30. Aslund N., Liljeborg A., Forsgren P. O., and Wahlesten S., "Three dimensional digital microscopy using the PHOIBOS scanner", *Scanning*, Vol. 9, (1987), pp. 227-235.

31. Aslund N. Liljeborg A., "Compensating for depth-dependent light attenuation at 3-D imaging with a confocal microscope", In: Biomedical Image Processing and Three-Dimensional Microscopy (Acharya R. S., Cogswell C. J. and Goldgof D. B. Eds.), SPIE Proceedings, Vol. 16660, (1995), pp. 221-232.

32. Aubele M., Zitzelberger H. Szucs S., Werner M., Brasselman H., Hutzler P., Rodenacker K., Lehmann L., Minkus G., Hofler H., "Comparative FISH analysis of numerical chromosome and abnormalities in 5μm and 15μm paraffin embedded tissue sections from prostate carcinoma", *Int. J. of Histochem. cell. Biol.*, Vol. (1996), pp. 121-126.

33. Baak J.P.A., Kurver P.H.J., Boon M.E., "Computer aided applications of quantitative microscopy in diagnostic pathology", *Pathol. Annal.*, Vol. 17, (1982), pp. 287-306.

34. Babu, V.R., Miles, B.J., Cerny, J.C., Weiss, L., van Dyke, D.L., "Cytogenetic study of four cancers of prostate", *Cancer Genet. Cytogenet.*, Vol. 48, (1990), pp. 83-87.

35. Bamford P. and Lovell B., "Bayesian Analysis of Cell Nucleus Segmentation by Viterbu search Based Active Contour", In: Proceedings of 14th Int. Conf. On Pattern Recognition, ICPR-98, (1998), pp. 133-135.

36. Baretton G. B., Valina C., Vogt T., Schneiderbanger K., Diebold J., Lohrs U, "Interphase cytogenetic analysis of prostatic carcinomas by use of nonisotopic in situ hybridization", *Cancer Research*, Vol. 54, (1994), pp. 4472-4480.

37. Barkenhoff G. J., Blom P., and Barends P., "Confocal Scanning light microscopy with high aperture immersion lenses", *J. Microscopy*, Vol. 117, (1979), pp. 219-232.

38. Bartels P. H., Bahr G. F., Bellamy J. C., "A self-learning computer program for cell recognition", *Acta Cytol.*, Vol. 14, (1970), pp. 486-494.

39. Bengtsson E., "The measuring of the cell features", *Analyt. Quant. Cytol.*, Vol. 9, (1987), pp.497-503.

40. Bengtsson E., Erricsson O., Holmquist J., Nordin B. and Stenkvist B., "High resolution segmentation of cervical cells", *J. of Hystochemistry and Cytochemistry*, Vol. 27, (1979), pp. 621-628.

41. Benson M. C., "Fine Needle Aspiration of the Prostste", *NCI Monographs*, Vol. 7, (1988), pp. 19-24.

42. Beucher S. and Meyer F., "The Morphological approach to segmentation: The watershed transformation", In Mathematical Morphology in Image Processing, E. R. Doughert (Eds.), Morcel Dekker Inc., New York, (1993).

43. Beucher S., "The watershed transformation applied to image segmentation"., *Scanning Microscopy* , Vol. 6, (1992), pp. 299-314.

44. Binford T. O., "Inferring surface from images", *Artificial Intelligence*, Vol. 17, (1981), pp. 205-244

45. Boissonat J. D., "Shape reconstruction from planar cross sections", Computer Vision Graphics and Image Processing, Vol. 44, (1988), pp. 1-29.

46. Borgefors G., "On digital distance transforms in three dimensions", Comp. Vis. Graph. Im. Process., Vol. 64, (1996), pp. 368-376.

47. Brady J. M., "Computational approaches to image understanding", *Computing Servey*, Vol. 14, (1982), pp. 3-71.

48. Broders A. C., "Carcinoma: Grading and practical application", *Arch. Pathol.*, Vol. 3, (1926), pp. 376-381.

49. Bron C. and Gremillet P., "3-D Reconstructions by Image Processing of serial sections in Electron Microscopy", In: In: Visualization in Biomedical Microscopies: 3-D Imaging and Computer Applications, (Kriete A. (Eds.)), VCH, NewYork, (1992), pp. 75-108.

50. Brooks R. A., "Model based three dimensional interpretations of two dimensional images", *IEEE trans. on Patt. Anal. Mac. Intel.*, Vol. PAMI-5, (1983), pp. 140-149.

51. Canny J., "A Computational approach to edge detection", *IEEE trans. on Patt. Anal. Mach. Intell.* Vol. PAMI-8, (1986), pp. 679-698.

52. Carlson K., Danielsson P., Lenz R., Liljeborg A., Majlof L., and Aslund N., "Three-dimensional Microscopy Using a confocal laser scanning microscope", *Optical Letters*, Vol. 10, (1976), pp. 53-55.

53. Carter H. B., Riehle R.A., Koizumi J.H., "Fine needle aspiration of the prostate: Acytohistological correlation", *J. Urology*, Vol. 135, (1986), pp. 294-299.

54. Carvajal-Gonzalez S., Rigaut J.P., Delisle N., Vassy J., Herlin P., "Confocal image cytometry- new developments in direct 3-D image processing and data treatments", *Cytometry*, 5, abstract 3, (1991), pp. 26-26.

55. Castleman K.R., White B.S., "Optimizing cervical specimen classifier", *IEEE trans. on Patt. Anal. and Mach. Intel.*, Vol. 2, (1980), pp. 451-457.

56. Chassery J. M. and Garbay C., "An iterative segmentation method based on a contextual color and shape criterion", *IEEE trans. Pattern Analysis and Machine Intelligence*, Vol. 6, (1984), pp. 165-172.

57. Chaudhuri B. B. and Dutta Majumder D., Two-Tone Image Processing and Recognition, Wiley-Eastern Ltd., New Delhi, (1993).

58. Chaudhuri B. B., "Hierarchical decomposition techniques in pattern classification", In: Clinical Cytometry and Histometry (Burger G., Ploem J. S. and Goerttler K. (Eds.)), Academic Press, London, (1987), pp. 112-114.

59. Chen H., Jason R. S., Marcus G., Sedat J. W. and Agard D. A., "The collection Processing and display of digital three dimensional images of biological specimens", In: Handbook of Biological Confocal Microscopy (Pawley J., eds.), Plenum press, New York, (1995), pp. 197-210.

60. Choi K. H., New Methods for Image Analysis of Tissue Sections, Ph.D. Thesis, Uppsala University, (1996).

61. Cohen L. D. and Cohen I., "Finite element methods for active contour models and balloons for 2-D and 3-D images", *IEEE trans. on Pattern Analysis and Machine Intelligence,* Vol. 15, (1993), pp.1131-1147.

62. Cogswell C. J., and Larkin K. G., "The Specimen Illumination Path and Its Effect on Image Quality", In: Handbook of Biological Confocal Microscopy (Pawley J., eds.), Plenum press, New York, (1995), pp. 197-210.

63. Cooper D. B., Elliot H., Cohen F., Reiss L. and Symosek P., "Stochastic Boundary Estimation and Object Recognition", In: Image Modelling (Rosenfeld A. (Eds.)), Academic Press, New York, 1981.

64. Cramer C., and Cramer T., "Considerations on a laser-scanning-microscope with high resolution and depth of field", *Microsc. Acta.* Vol. 81, (1978), pp. 31-44.

65. Davidovits P. and Egger M. D., U. S. patent #3643015, Scanning Optical Microscope.

66. Davies E. R., "On the noise suppression and Image Enhancement Charecteristics of the median, truncated median and mode filters", *Pattern Recognition Letters*, Vol. 7, (1988), pp. 87-97.

67. Delingette H., "Intialization of deformable Models from 3D data", in *Proceedings of Int. Conf. on Computer Vision, ICCV-98,* (1998), pp. 311-317.

68. Dhingra K., Sneige N., Pandita T. K., Johnston D. A., Lee J. S., Emami K., Hortobagyi G. N., Hittelman W. N., "Quantitative analysis of chromosomes in situ hybridization signal in paraffin-embedded tissue sections", *Cytometry*, Vol. 16, (1994), pp. 100-112.

69. Duda R. O. and Hart P., Pattern Recognition and Scene Analysis, Wiley, NewYork, (1967).

70. Esposti P. L., "Cytologic Malignancy Grading of Proststic Carcinoma by Transrectal Aspiration Biopsy", *Scand. J. Urol. Nephrol.*, Vol. 5, (1971), pp. 199-209.

71. Firestone, L. M., Preston K. Jr., Nathwani, B.N., "Continuous class pattern recognition for pathology, with applications to non-Hodgkin's follicular lymphomas", *Pattern Recognition*, Vol. 29, (1996), pp. 2061-2078.

72. Fram J. R., and Deustch E. S., "On the quantitative evaluation of edge detection schemes and their comparison with human performance', *IEEE Trans. On Computers,* Vol. 24, (1975), pp. 616-628.

73. Fu K. S., Mui J. K., "A Servey on Image Segmentation", *Pattern Recognition*, Vol. 13, (1981), pp. 3-16.

74. Fua P. and Brechbuhler C., "Imposing hard constraints on deformable models through optimization in orthogonal subspaces", *Int. J. of Computer Vision and Image Understanding*, 65, (1997), pp. 148-162.

75. Garbay C., "Knowledge Acquisition and Representation", In: Biomedical Engineering Handbook, Section XVIII, Artificila Intelligence, Chapter 187, (Bronzino J. Eds.), CRC Press, (1995), pp. 2731-2745.

76. Garbay C., "Image structure representation and processing : A discussion of some segmentation methods in Cytology", *IEEE trans. on Pattern Analysis and Machine Intelligence*, Vol. 8, (1986), pp.140-146.

77. Garbay C., "A colour metric as a tool for cytologic image analysis", In: Proceedings of the Int. Symposium on Medical Imaging and Interpretation, Germany, (1982), pp. 311-315.

78. Garbay C., Brugal G., Choquet C., "Application of coloured image analysis to bone marrow cell recognition", Anal. Quant. Cytol., Vol. -3, (1981), pp. 272-280.

79. Gleason D. F. and the Veterans Administration Cooperative Urological Research Group, "Histologic Grading and Clinical staging of Prostatic Carcinoma", Urologic Pathology:The Prostate (Tannenbaum M. eds.), Lea & Febiger, Philadelphia, (1977), pp. 171-197.

80. Gleason D. F., "Histologic grade, Clinical stage, and Patient Age in Prostate Cancer", *NCI Monogr.* Vol. 7, (1988), pp. 15-18.

81. Grinacker S., "Edge based segmentation and texture separation", In: Proceedings of 5 th Int. Conf. on Pattern Recognition, ICPR-80, (1980), pp. 554-557.

82. Haralick R. M. and Shapiro L., Computer and Robot Vision., Addison-Wesley Publishing Company, New York, (1992).

83. Heath M., Sarkar S., Sanocki T., Bowyer K., "Comparison of edge detectors : A methodology and intial study", *Computer Vision Graphics and Image Undurstanding*, Vol. 69, (1998), pp. 38-54.

84. Henke R. P., Kruger E., Ayhan N., Hubner D., Hammerer P., "Frequency and distribution of numerical chromosomal aberrations in prostate cancer", *Human Pathology*, Vol. 25, (1994), pp. 476-484.

85. Herrington C. S., Cooper K., McGee J. O. D., "Interphase Cytogenetics: analysis of numerical chromosome aberrations in isolated cells", *J. of Pathology*, Vol. 175, (1995), pp. 283-295.

86. Hiraoka Y., Sedat J. W., and Agard D. A., "Determination of three-dimensional imaging properties of a light microscope system", *J. of Biophysics*, Vol. 57, (1990), pp. 325-333.

87. Holmquist J., Bengtsson E., Erriksson O. and Stenkvist B., "A program System for Interactive Measurements on Digitized Cell Images", *J of Histochem Cytochem*, Vol. 25, (1977), pp. 641-654.

88. Hopman A.H.N., van Hooren E., van de kaa C. A., Voojis P.G.P., Ramaekers F.C.S., "Detection of Numerical Chromosome aberrations using in situ hybridization in paraffin sections of routinely processed bladder cancers", *Mol. Pathol.*, Vol. 4, (1991), pp. 503-513.

89. Huang T. S., "A fast two-dimensional median filtering algorithm", *IEEE Trans. ASSP*, Vol. 27, (1979), pp. 13-18.

90. Jain A. K., Fundamentals of Digital Image processing, Prentice-Hall of India Pvt. Ltd., New Delhi (1995).

91. Jain R., Kasturi R. and Schunk B. G. Machine Vision , McGrawhill Inc., NewYork, (1995).

92 Jain R., and Binford T., "Ignorance, myopia and naivete in computer vision systems", *CVGIP: Image Understanding*, Vol. 53, (1991), pp. 112-117.

93. Jean R. Weaver and Jessie L. S. Au., "Comparative scoring by visual and image analysis of cells in human solid tumors labelled for proliferation markers". *Cytometry*, vol. 27, (1997), 189-199.

94. Johnson G. D., de Nogueira A G M., "A simple method of reducing fading of immuno-fluorescence during microscopy", *Immunol. Methods*, vol. 43, (1981), pp.349-350.

95. Kass M., A. Witkin, Terzopoulos D., "Snakes: Active contour models", In: proceedings 1 st Int. Conf. on Computer. Vision., ICCV-87, (1987), pp. 259-269.

96. Kinder J., Reuter B., Hutzler P., "Real time multichannel processing in a microscope", in The Automation of Cancer Cytology and Cell Image Analysis, (Pressman NJ, Wied GL eds.), Tutorials of Cytology, Chicago, (1979), pp. 69-73.

97. Kline T. S. and Kannan V., "Prostatic aspirates. A Cytomorphometric analysis with emphasis on well differentiated carcinoma", *Diagnostic Pathology*, Vol 3., (1976), pp. 161-169.

98. Kohler R., "A Segmentation System Based on Thresholding", *Computer Graphics and Image Processing*, Vol. 15, (1981), pp. 319-338.

99. Kriete, A., Visualization in Biomedical Microscopies: 3-D Imaging and Computer Applications, VCH, NewYork, (1992).

100. Lai K. F., Deformable Contours Modeling, Extraction, Detection, and Classification, Ph.D. thesis. University of Wisconsin-Madison, (1994).

101. Layfield L.J., Mukamel E., Hilborne L.H., "Cytologic grading of prostatic aspiration biopsy: A comparison with the Gleason grading system", *J. of Urology*, Vol. 137, (1987), abstract 362.

102. Lee U. S., Chung Y. S., Park H. R., "A Comparative Performance Study of Several global thresholding techniques for segmentation", *Computer Vision Graphics and Image Processing*, Vol. 52, (1990), pp. 171-190.

103. Leroy B., Herlin I. and Cohen L. D., "Multi-resolution algorithms for active contour models", In: Proceedings of 12 th Int. Conf. on Analysis and Optimization of systems", (1996), pp. 58-65.

104. Leymarie F. and Levine M. D., "Tracking deformable objects in the plane using an active contour model", *IEEE trans. on Pattern Analysis and Machine Intelligence*, Vol. 15, (1993), pp. 617-635.

105. Lockett S. J. and Herman B., "Automatic detection of clustered fluorescent stained nuclei by digital image based cytometry", Cytometry, Vol. 17, (1994), pp. 1-12.

106. Malpica N., Solorzano C. O., Vaquero J. J., Santos A., Vallcobra I., Sagredo J. M. G., del Pozo F., "Applying watershed algorithms to the segmentation of clustered nuclei", Cytometry, Vol. 28, (1997), pp. 289-297.

107. Marko M. and Leith A., "Contour based 3-D surface reconstruction using stereoscopic contouring and digitized images", In: Visualization in Biomedical Microscopies: 3-D Imaging and Computer Applications, (Kriete A. (Eds.)), VCH, NewYork, (1992), pp. 45-72.

108. Marr D. and Hilderth E., "Theory of edge detection", *Proc. Royal. Soc. London Ser.* Vol. B207, (1980), pp. 187-217.

109. Mellors R. C., Glassman A., Papanicolaou G. N., "A micr-fluorometric scanning method for detection of cancer cells in smears of exfoliated cells", *Cancer*, Vol. 5, (1952), pp. 458-468.

110. Mastin G. A., "Adaptive filters for digital image noise smoothing: an evaluation", *Computer Vision Graphics and Image Processing*, Vol. 35, (1985), pp. 102-121.

111. Mendelsohn M. L., Mayall B. H., Perry B. H., "Chromosome identification by image analysis and quantitative cyto-chemistry", in Human Chromosome Methodology (Yunis J. (Eds.)), Academic press, NewYork, (1974), pp. 311-346.

112. Micale M.A., Mohammed A., Sakr W., Powell I.J., Wolman S.R., "Cytogenetics of primary adenocarcinoma", *Cancer Genet. Cytogenet.*, Vol. 61, (1992), pp.165-173

113. Minsky M. U. S. patent #3013467, Microscopy Apparatus.

114. Mitchel C. Benson, "Fine needle aspiration of the Prostate", *NCI Monograms*, Vol. 7, (1988), pp.19-24.,

115. Mostofi S. K., "Problems of grading carcinoma of prostate", *Semin Oncol*, Vol. 3, (1976), 161-169.

116. Najman L. and Schimitt M., "Geodesic Saliency of Watershed Contours and Hierachical Segmentation", *IEEE trans. on Patt. Anal. and Mach. Intell.*, Vol. 18, No. 2, (1996).

117. Nardin B., The Development of Automatic Prescreener for the Early Detection of Cervical Cancer: Algorithms and Implementation, Ph.D. Thesis, Department of Scientific Computing, Uppasala University, Sweden, (1989).

118. Nordin B., Bengtsson E., Dehlquist B., Errikson O., Jarkrans T. and Stenkvist B., "Object Oriented Cell Image Segmentation", In: Proceedings of the Int. Symposium on Medical Imaging and Interpretation, Berlin, (1982), pp. 140-145.

119. Nastar C., Ayache N.J., "Fast segmentation, Tracking, and analysis of deformable objects", *Proceedings of Int. Conf. on Computer Vision, ICCV-93*, (1993), pp. 275-279.

120. Netten H., Young I.T., van Vliet L.J., Tanke J.H., Vroljik H., Sloos C.R.W., "FISH and Chips :Automation of Fluorescence dot Counting in Interphase Cell Nuclei", *Cytometry*, Vol. 28, (1997), pp.1-10.

121. Niemen A., Heinonen P. and Nuevo Y., "A new class of detail preserving filters for image processing", *IEEE Trans. on Pattern Analysis and Machine Intelligence*, Vol. 9, (1987), pp. 74-90.

122. Noordmans H. J. and Smeulders A. W. M., "Detection and Charecterization of isolated and overlapping spots", *Computer Vision Graphics and Image Understanding*, Vol. 70, (1998), pp. 23-25.

123. Park D. J., Nam K, N. and Park R. H., "Multiresolution edge detection techniques", Pattern Recognition, Vol. 11, (1993), pp. 45-61.

124. Parui S. K., Jutting U., Burger G., "Methods for Classification of two thyroid follicular tumor classes", *Int. J. Systems Sciences*, Vol. 22, (1991), pp. 1985-1991.

125. Pavlidis T. and Liow Y., "Integrating Region Growing and Edge Detection", *IEEE Trans. on Pattern Analysis and machine Intelligence,* Vol. 12, (1990), pp. 225-233.

126. Pawley J., Handbook of Confocal Microscopy, Academic press, London, 1995.

127. Pawley J., "Sources of noise in three-dimensional microscopic data sets", In: Three-dimensional confocal microscopy: Volume Investigation of Biological Specimens (J. Stevens (Eds.)), Academic Press, San Diego, (1994), pp. 47-94.

128. Peterfreund N., "Robust Tracking with Spatio-Velocity Snakes: Kalman Filtering Approach", In: *Proceedings of Int. Conf. on Computer Vision*, ICCV-98, (1998), pp.433-439.

129. Pratt W. K. Digital Image Processing, Wiley, NewYork, (1991).

130. Preston K. Jr. , Bartels P.H., "Automated image processing for cells and tissue", In: Progress in Medical Imaging (Newhouse eds.), Springer Verlag, (1988), pp. 1-121.

131. Preston K. Jr., "Tissue section analysis: Features selection and Image processing", *Pattern Recognition*, Vol. 13, (1981), pp. 17-36.

132. Preston K. Jr. and Onoe M., Digital Processing of Bio-medical Images, Plenum Press, NewYork, (1976).

133. Prewitt J. M. S. and Mendelsohn M. L., "The analysis of cell images", *Ann. NewYork Acad. Sci.*, Vol. 128, (1966), pp. 1035-1053.

134. Prewitt J. M. S., "Parametric and non-parametric recognition by computer: An application to leukocyte image processing", *Adv. Computing.*, Vol. 12, (1972), pp. 285-414.

135. Raya S. P. and Udupa J. K., "Shape based interpolation of multi-dimensional objects", *IEEE trans. on Medical Imaging*, Vol. 9, (1990), pp. 32-42.

136. Rigaut J. P., "What is new from the field: A new technology is born-Confocal image cytometry", *Anal. cell. Pathol.*, 3, (1991) 137-141.

137. Rigaut J. P., Carvajal-Gonzalez S., Vassy J., "3-D Cytometry", in Visualization in Biomedical Microscopies: 3D Imaging and Computer Applications (Kreite A. eds.), VCH, NewYork, (1992), pp. 205-248.

138. Rodenacker K., "Featuring of Cellular Objects", *Clinical Cytometry and Histometry*, (1987), pp. 91-96.

139. **Rodenacker K., Aubele M., Hutzler P. and Adiga P. S. U.,** "Groping for Quantitative 3D Image Analysis: an Approach to Quantitative Evaluation of Fluorescence in situ Hybridization in Thick Tissue Sections of Prostate Carcinoma", Anal. Cell. Pathol., Vol. 15, (1997), pp. 19-29.

140. Ronfard R., "Region based strategies for active contour models", *Int. J. of Computer Vision*, Vol. 13, (1994), pp. 229-251.

141. Rosenfeld A., "Connectivity in Digital Pictures", *J. Assoc. Comput. Mach.*, Vol. 17, (1970), pp. 146-160.

142. Rosenfeld A., (Eds.), Image Modelling, Academic Press, New York, 1981.

143. Rosenfeld A. and A. C. Kak, Digital Picture Processing, Vol I and Vol II, Academic Press, NewYork, (1982).

144. Rosenfeld A. and Thurston M., "Edge and curve detection for visual scene analysis", *IEEE trans. comput.* Vol. C-20, (1971), pp. 562-569.

145. Rosenfeld A. and De La Torre P., "Histogram Concavity Analysis as an aid in Threshold Selection", *IEEE trans. on System. man. and Cybernetics.*, Vol. SMC-13, (1983), pp. 231-235.

146. Rosenfeld A., "Segmentation: pixel based methods.", In Fundamentals in Computer Vision (Faugeras O. P. Eds..), Cambridge University Press, Cambridge, (1983), pp. 225-238.

147. Roysam B., Bhattacharya A. K., Srinivas C., Szarowski D. H., and Turner J. N., "Unsupervised noise removal algorithms for 3-D confocal fluorescence microscopy", In: Biomedical Image Processing and Three-Dimensional Microscopy (Acharya R. S., Cogswell C. J. and Goldgof D. B. (Eds.)), SPIE Proceedings, Vol. 16660, (1995), pp. 250-261.

148. Roysam B. Maffitt D. R., Miller M. I., Saffitz J. E., and Thomas Jr. L. J., "A PC based Implementation of the Maximum likelyhood Method of Analysis of Electron Microscope Autoradiographs", *Int. J. of Microscopy Research and Technique*, Vol. 20, (1992), pp. 73-86.

149. Roysam B. Cohen A., Getto P. H. and Boyce P. R., "A numerical approach to the computation of light propogation through turbid media: Application to the evaluation of lighted exit signs", *IEEE trans. on Industry Applications*, Vol. 29, (1993), pp. 661-669

150. Roysam B. Bhattacharya A. K., Srinivas C., Turner J. N., "Unsupervised Noise Removal Algorithms for 3-D Confocal Fluorescence Microscopy", *Micron and Microscopica Acta*, Vol. 23, (1992), pp. 447-461.

151. Roysam B., Ancin H., Bhattacharya A. K., Chisti M. A., Seegal R. and Turner J. N., "Algorithms for Automated Cell Population Analysis in Thick Specimens from 3-D Confocal Fluorescence Microscopy data", *J. of Microscopy*, Vol. 173, (1994), pp. 2.

152. Russ J. C., The Handbook of Image Processing, CRC Press, London, (1995).

153. Sadjadi F. A. and Hall E. L., "Three-dimensional moment invariants", *IEEE trans. on Pattern. Analysis. and Machine. Intelligence.*, Vol. 2, (1980), pp. 127-136.

154. Sahoo P. K., Soltani S., Wong A. K. C., Chen Y. C., "A Servey of thresholding techniques", *Computer Vision Graphics and Image Processing*, Vol. 41, (1988), pp. 233-260.

155. Sandison D. R., Williams R. M., Wells K. S., Strickler J., Webb W. W., "Quantitative Fluorescence Confocal Laser Scanning Microscopy (CLSM)" in Handbook of Biological Confocal Microcsopy (Pawley J. (Eds.)), Plenum Press, NewYork, (1995), pp. 39-53.

156. Saraga P. and Wavish P. R., "Edge-coding operators for pattern recognition", *Electron letters*, Vol. 7, (1971), pp. 736-738.

157. Scardino P.T., Weaver R., Hudson M.A., "Early detection of prostate cancer", *Hum. Pathol.*, Vol. 23, (1992), pp. 211-222

158. Schwarz H., Exner H. E., "The charecterization of the arrangement of feature centroids in planes and volumes", J. of Microscopy, (1983), pp. 129-155.

159. Shaw P. J., "Comparison of Wide field/Deconvolution and Confocal Microscopy for 3D imaging", In: Handbook of Biological Confocal Microscopy, (Pawley J. eds.), Plenum press, NewYork, (1995), pp:373-387.

160. Sheppard C. J. R. and Chaudhury A., "Image formation in the scanning microscope", Optica, Vol. 24, (1977), pp. 1051-1051.

161. Sheppard C. J. R., Gunnaway J. N., Walsh D. and Wilson T., "Scanning Optical Microscope for the inspection of the electronic devices", In: *Proceedings of Micocircuit Engineering Conf.* Cambridge, (1978).

162. Shih W.S.V., Lin W.C., Chen C.T., "Contour Model Guided Image Warping for Image Interpolation", In: *Proceedings of Int. Conf. on Pattern Recognition, ICPR-96*, (1996), pp. 396-400.

163. Skalansky J., Wassel G. N., Pattern Classifiers and Trainable Machines, Springer-Verlag, NewYork, (1981).

164. Smyth P. P., Taylor C.J., Adams J.E., "Automatic measurement of vertebral shape using active shape models", *Int. J. Image and Vision computing*, Vol. 15, (1997), pp. 575-581.

165. Sobel I., Camera models and machine perception, *Stanford AI Memo*-121, (1970).

166. Suh O., Weiss L., "The development of technique for morphometric analysis of invasion cancer", *J. Theo. Biol.*, Vol. 108, (1984), pp. 547-562.

167. Tek H. and Kimia B. B., "Image segmentation by reaction diffusion bubles", In: *Proceedings of 5 th International Conf. on Computer Vision*, ICCV-96, (1996), pp. 156-162.

168. Tekola, P., Baak, J.P.A., Beli"en, J.A.M., Brugghe, J., "Highly sensitive, specific, and stable new fluorescent DNA stains for confocal laser microscopy and image processing of normal paraffin sections", *Cytometry*, Vol. 17, (1994), pp. 191-195

169. Thurfjell L., Bengtson E. and Nordin B., "A new three dimensional connected components labeling algorithm with simultaneous object feature extraction capability", *Int. J. of Graphical Models and Image Understanding*, Vol. 54, (1992), pp. 357-364.

170. Torre V. and Poggio T. A., "On Edge Detection", IEEE Trans. On Pattern Analysis and machine Intelligence, Vol. 8, (1986), pp. 147-163.

171. Tucker J.H., Burger G., Husain O.A.N., Ploem J.S., Schenk U., Schwarzmann P., Stenkvist B., "Medicine: Measuring the accuracy of automated cervical cytology prescreening systems based on image analysis", Report prepared by working group 1: *Quality control of cervical cancer prescreening, Commision of European Communities*, October, (1987).

172. Udupa J.K., Ajjanagadde V.G., "Boundary and object labeling in three dimensional images", *Comp. Vis. Graph. Im: Process.: Image Understanding*, Vol. 3, (1990), pp. 355-369.

173. van der Voort H. T. M., Brackenhoff G. J., Baarslag M. W., "Three dimensional visualization methods for confocal microscopy", *J. Microsc*, 158, (1989) 43-54.

174. Vincent L., "Morphological grayscale reconstruction in image analysis: Applications and efficient algorithms", IEEE Trans. On Image Processing, Vol. 2, (1993), pp. 176-201.

175. Vincent L. and Soille P., "Watershed in digital spaces : An efficient algorithm based on immersion simulation", *IEEE Trans. on Pattern. Analysis. and Machine. Intelligence.*, Vol. 13, (1991) pp. 583-598.

176. White J. G., Amos W. B., and Fordham M., "An evaluation of Confocal versus conventional imaging of biological structure by conventional fluorescence light microscopy", J. Cell. Biol., Vol. 105, (1987), pp. 41-48.

177. Willems J. S., Lowhagen T., "Transrectal fine needle aspiration biopsy for cytologic diognosis and grading of prostatic carcinoma", *Prostate*, Vol. 2, (1981), pp. 381-395.

178. Wilson T., Gannaway J. N., and Johnson P., "A scanning optical microscope for the inspection of semiconductor materials and devices", *J. Microscopy.,* Vol. 118, (1980), pp. 390-414.

179. Xu C., Prince J.L., "Snakes, Shapes and Gradient Vector Flow", *IEEE Trans. on Image Processing.*, Vol. 7, (1998), pp. 359-369.

180. Yasnoff W. A. and Bacus J. W., "Scene segmentation algorithm development using error measures", *Anal. Quant. Cytol.*, Vol. 6, (1984), pp. 45-58.

181. Yatani R., Schiraishi T., Soga T., "Reliability of Cytological grading of prostate carcinoma compared with histological grading", *Pathol. Res. Pract.*, Vol. 180, (1985), pp. 68-73.

182. Young G. J., and Huang T. S., "The effect of median filtering on edge location estimation", Computer Graphics and Image Processing, Vol. 15, (1981), pp. 224-245.

183. Young I. T., "Image fidelity: characterizing the image transfer function", *Methods. Cell. Biol.*, Vol. 30, (1989), pp. 2-47.

184. Zhang Y.J., "Influence of segmentation over feature measurement", *Pattern Recognition Letters*, Vol. 16, (1995), pp. 201-206.

185. Zhu Q., Tekola P., Baak J.P.A., Beli"en J.A.M., "Measurement by confocal laser scanning microscopy of the volume of epidermal nuclei in thick skin sections"., *Anal. Quant. Cytol. Histol.*, Vol. 16, (1994), pp. 145-152

186. Ziou D., and Tabbone S., "A multiscale edge detector", Pattern Recognition, Vol. 26, (1993), pp. 127-135.

187. Zitzelberger H., Szucs S., Weier H. U., Lehmann L., Braselmann H., Enders S., Schilling A., Breul J., Hofler H., Bauchinger M., "Numerical abnormalities of chromosome 7 in human prostate cancer detected by fluorescence in situ hybridization (FISH) on paraffin-embedded tissue sections with centromere-specific DNA probes", *J. Pathol.*, Vol. 172, (1994), pp. 325-335.

188. Zucker S., "Region Growing: childhood and adolescence", *Computer Graphics and Image Processing*, Vol. 5, (1976), pp. 382-399.